Robust control and contact recovery of rotor/magnetic bearing systems

Schlotter, Michael

Award date:
2007

Awarding institution:
University of Bath

Robust Control and Contact Recovery of Rotor/Magnetic Bearing Systems

Michael Schlotter

A thesis submitted for the degree of Doctor of Philosophy

University of Bath
Department of Mechanical Engineering

April 2007

ProQuest LLC
789 East Eisenhower Parkway
P.O. Box 1346
Ann Arbor, MI 48106-1346

Abstract

A basis for modern controller design is an accurate model of the plant. A detailed finite element modelling (FEM) framework for rotor/magnetic bearing systems is presented, and the derived FEM model of the flexible rotor test rig is then used for robust H_∞ control design. A novel, versatile LMI based design method is introduced, which takes the physical structure of the system into account. This facilitates the specification of design criteria and allows for the formulation of multiple design objectives in one unified framework. Conventional linear time invariant (LTI) H_∞ controllers are designed for one particular rotational speed only. When applied to different speeds, plant variations may lead to closed loop instability. The applied LMI gain-scheduling techniques, however, guarantee robust stability when the system operates at varying rotational speeds. All derived H_∞ controllers are tested by simulations and experiments. Their stability and performance is examined and compared with decentralised proportional-derivative (PD) control.

In the second part of this thesis, rotor-stator contact dynamics are investigated, and new control strategies for contact recovery are developed. It is shown that rotors subject to constant synchronous excitation can adopt stable periodic contact modes. For recovery, synchronous forces are calculated based on the contact dynamics model, and applied through the magnetic bearings. These forces reduce the excitation causing the contact to a level at which the modes become unstable and the rotor can progress to a contact-free orbit. The procedure is demonstrated by simulations of a simple disk system before it is applied to an experimental flexible rotor test facility. Error margins are investigated and possible limitations are discussed. Although the method is developed for PD controlled systems only, it is shown experimentally that it can also be successfully applied to H_∞ controlled rotors.

Acknowledgements

This thesis is the result of the research work I carried out at the Department of Mechanical Engineering, University of Bath. I would like to thank all who supported me during this project. In particular, I am grateful to my supervisor Patrick Keogh, for his guidance, encouragement and valuable advice.

I was fortunate to have many friends in Bath, who made the past three years most enjoyable. Special thanks to my parents, for their love and support, and for giving me the freedom to explore my interests. This thesis is dedicated to Gertrud Richter.

I acknowledge the receipt of a University scholarship, and funding from the Royal Academy of Engineering.

Contents

1 Introduction

The demands on rotating machinery with respect to performance, precision, safety, etc. are continuously rising. However, the potential to optimise conventional passive systems is limited, so that design specifications may only be met by active or mechatronic systems under intelligent control. An example of such a mechatronic system is an active magnetic bearing (AMB) supported rotor.

1.1 Overview

Magnetic bearings are increasingly used in specialised applications, which take advantage of the contact-free force transmission. Because the rotation is frictionless, there is no wear, no lubrication is required, and very high rotation frequencies are achievable. The service life of magnetic bearings is higher compared to conventional journal or ball bearings, and through life maintenance and running costs are potentially low. The latter is true despite the power requirement during operation. The energy consumption of AMB's is usually much lower than friction losses which would occur in equivalent passive systems.

Electromagnetic bearings can only be operated with a closed loop control system, because the force between a magnet and a ferromagnetic body increases with decreasing distance. This behaviour resembles a non-linear spring with negative stiffness, which destabilises states of equilibrium without appropriate control action. The control loop of a typical magnetic bearing system is shown in Figure 1.1. The aim is to hold the rotor in a certain position. The sensors measure the position and transmit the information to the controller in form of a voltage signal. A control voltage is then calculated, based on a linear or non-linear control law, and passed to the power amplifier. This provides the current for the electromagnets, which exert forces on the rotor. Usually, auxiliary bearing are fitted for emergency operation in case of a system failure or temporary overload. This prevents the rotor making contact with the magnets or sensors, which could cause severe damage to the machine.

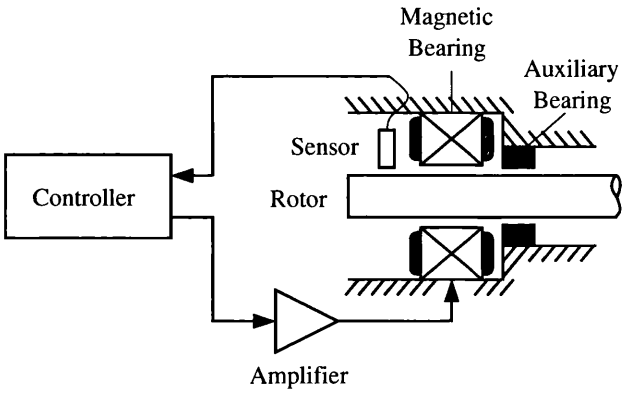

Figure 1.1: Principle of an active magnetic bearing system.

1.2 Application Examples for Magnetic Bearings

Magnetic bearings were first used in the early 1970's for *satellite fly wheels*, and *gyro stabilisers*. The particular advantages of AMB's in these applications are low power consumption and long service life. Since these early days, magnetic bearings have become increasingly popular for the use in industrial machines. One of the most successful applications is in *turbomolecular pumps*. They run at high speeds and produce a high vacuum, which is very sensitive to contamination. Turbomachinery is another example for the use of magnetic bearings. *Turbogenerators*, *turbocompressors* and *turboexpanders* often run at over-critical speeds. Hence, the rotor has to pass through at least one resonance region. Unbalance induced displacement amplitudes in these resonance zones can become quite large in conventional passive systems. If magnetic bearings are used, however, active control can be utilised to reduce these vibrations significantly resulting in increased safety and efficiency. A particularly interesting application area are high speed *milling and grinding spindles*, which often run at speeds in excess of 100,000 rpm. The rotor is not always centred in the stator, but made to follow certain trajectories. This can be very useful when manufacturing unsymmetric parts. Besides these main applications, magnetic bearings can also be found in *blood pumps*, *centrifuges*, *x-ray devices* and more recently in *gas turbines* for transport applications [1].

The main disadvantages of magnetic bearing systems are their relatively high complexity, weight, and high initial cost. Furthermore, there is a certain scepticism in industry regarding this technology, which is proving hard to overcome.

Therefore, for the foreseeable future, their use will be limited to special applications with a high demand on performance where implementation effort and cost play a minor role.

1.3 Current State of Research

The mechanical design of a standard radial magnetic bearing is simple, and offers limited scope for improvement. In order to achieve better performance e.g. by increasing the load capacity, more complex designs are being developed [2]. Most research, however, focuses not on the bearing hardware but on the control algorithm. With intelligent control, the desired magnetic bearing characteristics can be optimised for the particular application. Milling and grinding spindles, for example, must be positioned precisely, and must be insensitive to disturbances from external loads. Bearings for turbomachinery should have a large stiffness and damping, in order to reduce vibrations due to a wide range of excitations, ranging from synchronous unbalance forces to aerodynamic influences. In transport applications, base motion must be considered, and reliability in the priority in aerospace systems. For turbomolecular pumps, vibrations transmitted to the base are often minimised. This can be achieved by letting the (rigid) rotor rotate around a principal axis. The same applies to flywheels, where energy consumption of the bearings is an important design criterium, too.

Simple decentralised proportional-derivative (PD) controllers can be found in most systems mainly because they are simple to implement and exhibit sufficient performance [3]. Much research has been undertaken to enhance PD controllers with the objective of minimum rotor displacements, especially in the resonance zones. A common strategy is to apply synchronous forces through the active magnetic bearings, which compensates for the unbalance excitation. The amplitude and phase of these compensation forces is calculated online based on a dynamic model of the system and displacement measurements in the rotating frame. Burrows et al. [4] describe this method. A single magnetic bearing was used to reduce the vibrations of a large rotor suspended by a pair of journal bearings. Although originally developed for rotors running at a stationary speed, the method can be modified to work for instationary systems by iteratively adopting the compensation forces to the operating conditions [5].

Another strategy to reduce unbalance vibrations is based on the fact that res-

onance regions shift depending on the bearing stiffness. Zhang [6] showed how optimisation techniques can be used to compute an adaptive controller, which adjusts the bearing parameters so that the rotor operates in an anti-resonance zone at all running speeds up to the fourth eigenfrequency of the system. In order to achieve a force-free rotation, notch filters are often inserted into the closed loop. Herzog et al. [7] presented a design approach, and verified the results by experiments with a large turboexpander. Vibrations and transmitted forces could be significantly reduced at a high operating speed. The disadvantage of notch filters, however, is that they only work if the plant dynamics do not change with time. A sudden change in rotational speed, or a short contact of the rotor with the housing will often cause instability.

As PD control has inherent limitations, current research is concerned with the application of modern robust control techniques to rotor/magnetic bearing systems in order to improve reliability and performance. The availability of affordable high performance computers was a driver for the development of robust control theory in the 1980's. One of the most popular robust control strategies is based on H_∞ optimisation. In their pioneering work, Glover and Doyle [8, 9] showed that state-space descriptions of all stabilising controllers can be found by solving two algebraic Riccati equations.

In the 1990's, the first H_∞ algorithms were developed in which the design constraints are reformulated in terms of linear matrix inequalities (LMI). This approach is applicable to a wider range of plants, and it can be computationally advantageous by utilising efficient convex optimisation algorithms. Explicit solutions to the LMI H_∞ problem are given by Gahinet and Apkarian [10, 11].

An interesting application of LMI methods is multi-objective feedback control. This combines the benefits of the H_∞ method such as robustness to model uncertainty and explicit expression of closed-loop frequency domain specifications with the strengths of the H_2 method in handling stochastic aspects. Furthermore, transient responses and minimum closed-loop damping can be specified by time-domain and pole placement constraints. Scherer et al. [12] show how these design objectives can be formulated as LMI constraints used to synthesise a single LTI controller.

The linear matrix inequality (LMI) framework allows the derivation of gain scheduled controllers, which increase robustness and/or performance for feedback systems with linear parameter dependent plants. In ordinary LTI H_∞ design,

time-varying plant characteristics are treated as plant uncertainty, which often leads to overly conservative controllers. If the state-space matrices of the plant are fixed functions of time-varying physical parameters, which can be measured, LMI synthesis methods allow the computation of gain-scheduled controllers as functions of the measured parameters. The derivations of LMI controller synthesis algorithms for two classes of parameter-varying plants are shown in the papers of Packard, Becker, Apkarian, and Gahinet [13–16]. These techniques offer great potential for rotor/magnetic bearing systems as their properties depend on the rotational speed due to gyroscopic effects.

Simulation studies of systems with small rigid rotors have been performed by Sivrioglu and Nonami [17], and Tsiotras and Mason [18]. In the standard LMI gain-scheduling approach, the time varying parameter is allowed to change at an arbitrarily fast rate. In rotordynamic applications, however, the rotor acceleration is within certain bounds due to limited available torque. Tsiotras and Knospe [19] show how a priori known bounds of the parameter change rate can be considered in the controller design to improve the closed loop performance.

A single rotor/magnetic bearing system must usually fulfil several, often conflicting, performance specifications. The H_∞ design method allows the formulation of these constraints in a unified framework. Research in the field of multi-objective control design was undertaken by Cole et al. [20], who investigated the vibration control of a system subject to direct forcing and base motion. If base motion occurs, it is desirable to switch from a soft controller, which minimise actuator forces during normal operation, to a hard controller, which minimises displacements in the presence of disturbances.

Even with the most advanced controllers, rotors levitated by magnetic bearings can come into contact with auxiliary bearings, housings, or seals. This might be caused by failure cases such as power loss or malfunctioning of the bearings where all control capability is lost. However, it can also happen due to temporary overload, increased unbalance, or base motion. The failure cases have been the subject of much research with the aim to optimise auxiliary bearing design for safe rundown. Recent publications in this area are the thesis of Fumagalli [21], who performed extensive measurements to improve the understanding of the non-linear contact dynamics, and that of Bartha [22], who examined the special and potentially very damaging case of dry friction backward whirl in some detail. The dynamics during a rotor drop into auxiliary bearings after a complete failure of the

magnetic bearings is subject of papers from Kirk et al. [23, 24], and Schmied and Pradetto [25]. Analytical methods are presented and measurements performed with full-size machinery are evaluated. Extensive theoretical and experimental studies on the various types of rotor motion in the contact case were also carried out by Ehehalt, Markert and Hahn [26, 27]. Their test facility consists of a very flexible rotor with one disk, which contacts a flexibly mounted nearly rigid ring with damping. A similar test rig was used by Ginzinger and Ulbrich [28], who tried successfully to reduce the often damaging contact forces by actively controlling the auxiliary bearings with magnetic actuators.

There is limited published material relating to rotor-stator contact with fully functioning bearings where there is still scope to return the rotor to a non-contacting orbit without machine shutdown. Keogh and Cole [29, 30] investigated the resulting contact dynamics. A very simple contact recovery control strategy for flexible rotors based on a modified unbalance compensation algorithm is presented in [31], and robust control methods for the contact recovery of a disk system are derived in [32]. Contact recovery control is not a trivial task as the resulting rotor motion depends on many parameters and is generally governed by highly non-linear dynamics. Nevertheless, it is important to master these problems should magnetic bearings be used in future transport and manufacturing applications.

1.4 Structure and Scope of the Thesis

This thesis covers the modelling of rotor/magnetic bearing systems, their control under normal operation conditions and in the presence of rotor-stator contact.

A good mathematical model of the real system is the basis for any successful controller design and therefore much attention was drawn towards this step. Chapter 2 presents the experimental equipment and introduces the theoretical background used to derive a completely new simulation model of the existing test rig.

Chapter 3 gives an introduction to H_∞ feedback theory and describes a new design framework for robust H_∞ controllers, which allows the formulation of multiple design objectives in an intuitive manner. In contrast to the well known mixed sensitivity formulation, this method takes the physical structure of a rotor/magnetic bearing system into account, which facilitates the design process.

LMI gain scheduling techniques are presented, which allow the speed dependence of rotor systems to be embedded within the controller. In the past, LMI based gain-scheduled controllers have been developed for rigid rotors only. Furthermore, the stability and performance of these controllers was verified mainly by simulations; experimental data are rare. In this thesis, LMI based gain-scheduled controllers are developed for a flexible rotor system. The design is verified experimentally and the achieved stability and performance is compared with classical LTI and PD controllers.

Perhaps the biggest concern when using magnetic bearings is possible damage caused by rotor-stator contact. Although transient contact dynamics shortly after the initial impact have been studied extensively, there is a lack of knowledge about stable, periodic contact behaviour of complex flexible rotors with fully functional magnetic bearings. In this project, an analytical procedure to assess these cases is presented in Chapter 4. Possible contact modes of a simple disk system and a more complex flexible rotor are discussed and analytical descriptions are derived. The theory is then verified not only by simulations, but also by extensive experimental tests.

A verified theoretical description of contact dynamics is the basis for Chapter 5 where a new contact recovery strategy for flexible rotors is presented. It is examined how a flexible rotor can be returned from a persistent contacting to a non-contacting state through appropriate control forces applied by the magnetic bearings. Control strategies are developed for various contact modes and their effectiveness is tested in simulations and experiments.

Chapter 6 summarises the results obtained during this PhD project and gives an outlook on possible future research.

2 Rotor System Model

Controller design relies on a sufficiently accurate mathematical description of the physical system in question. The test rig is presented in this chapter, reliable methods to model rotor/magnetic bearing systems are described, and the governing equations are derived. Finally, the resulting model is compared with the experimental rig.

2.1 The Test Rig

The test rig used in this project is shown schematically in Figure 2.1. The rotor is approximately 2 m long, has a shaft diameter of 50 mm, and weighs 100 kg. It is supported in the radial direction by two magnetic bearings, each with a peak control force of 1500 N. Six auxiliary journal bearings provide support if the power is switched off or if the load capacity of the magnetic bearings is exceeded. Axial rotor constraint is provided by an electric motor through a universal coupling, which allows free radial displacement between the rotor shaft and the motor. The base is mounted on two pairs of isolators. It is attached to a shaker, which can excite horizontal base motion.

The maximum rotational speed is 6000 rpm. Four resonant frequencies lie in the operation range: a rotational and a translational "rigid body" mode, and the first two elastic bending modes. Radial displacements are measured by four pairs of

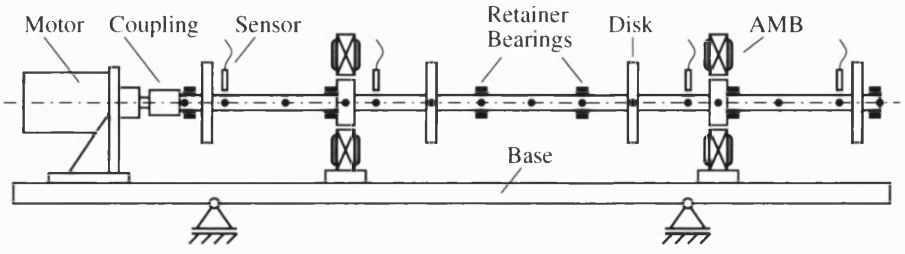

Figure 2.1: Schematic of the test rig.

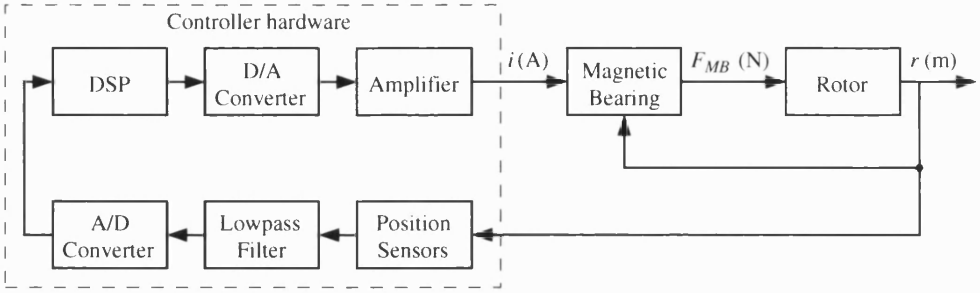

Figure 2.2: Control loop of an active magnetic bearing system.

Shaft	Young's modulus	$E_S = 206400\,\mathrm{N/mm^2}$
	Mass	$m_S = 32.98\,\mathrm{kg}$
	Diameter	$d_S = 50\,\mathrm{mm}$
	Length	$l_S = 2.14\,\mathrm{m}$
Disks	Mass	$m_D = 12.95\,\mathrm{kg}$
	Diameter	$d_D = 0.25\,\mathrm{m}$
	Axial Moment of Inertia	$\Theta_{aD} = 49.9\,\mathrm{g/m^2}$
	Polar Moment of Inertia	$\Theta_{pD} = 97.1\,\mathrm{g/m^2}$
AMB Cores	Mass	$m_D = 7.99\,\mathrm{kg}$
	Diameter	$d_D = 0.175\,\mathrm{m}$
	Axial Moment of Inertia	$\Theta_{aD} = 28.2\,\mathrm{g/m^2}$
	Polar Moment of Inertia	$\Theta_{pD} = 16.5\,\mathrm{g/m^2}$

Table 2.1: Rotor parameters.

Number of poles	$n_p = 8$
Half angle between two poles	$\alpha_M = 22.5°$
Cross section of poles	$A_{Fe} = 13.99\,\mathrm{cm^2}$
Turns per magnet	$n_C = 316$
Average air gap	$s_0 = 1.2\,\mathrm{mm}$
Max. current	$i_{max} = 10\,\mathrm{A}$
Bias current	$i_0 = 5\,\mathrm{A}$
Gravity compensation current	$i_g = 0.65\,\mathrm{A}$
Saturation force limit	$F_{MB,sat} = 2000\,\mathrm{N}$
Cut-off frequency	$\omega_{cut} = 500\,\mathrm{Hz}$

Table 2.2: Magnetic bearing parameters.

eddy current displacement sensors. Each sensor pair is arranged orthogonally at ± 45 degrees to the vertical, which aligns them with the pole pairs in the magnetic bearings.

Due to the inherent instability, magnetic bearings must be operated with feedback control, which is shown in Figure 2.2. The controller is implemented using dSPACE real-time hardware. Together with Matlab/ Simulink software, dSPACE provides a fully integrated development environment for control design, code generation, and real-time processing. Tables 2.1 and 2.2 give important parameters of the experimental equipment. More details can be found in [33] and [34].

2.2 Active Magnetic Bearing Model

The active magnetic bearing model presented in this section is based on the "zero leakage" assumption, which says that the magnetic flux in a high permeability magnetic structure with small air gaps is confined to the iron and the gap volumes. Hysteresis effects are neglected and saturation effects approximated. These simplifications give rise to some errors but the results are usually sufficiently accurate in the operating range of the bearing.

2.2.1 Principles of Active Magnetic Bearings

The electromagnetic forces of a "horse shoe" magnet as shown in Figure 2.3 can be derived from energy conservation. The magnetic field energy in the air gap with volume V_A is

$$W_A = \frac{1}{2} \int_{V_A} B_A H_A \, dV_A \tag{2.1}$$

where the magnetic flux density B_A and the magnetic field strength H_A can be calculated via magnetic circuit analysis as

$$B_A = \frac{n_C i}{\frac{l_{Fe}}{\mu_{Fe}} \frac{A_A}{A_{Fe}} + \frac{l_A}{\mu_A}} \quad \text{and} \quad H_A = \frac{n_C i}{\frac{\mu_A}{\mu_{Fe}} \frac{A_L}{A_{Fe}} l_{Fe} + l_A} \tag{2.2}$$

The magnetic force F_M results from the change of the magnetic field energy in the gap as a function of $s = \frac{1}{2} l_A$. It is a potential force given by

$$F_M = -\frac{\partial W_A}{\partial s} = \frac{\mu_0 A_A n_C^2}{4} \cdot \frac{\left(s - \frac{l_{Fe}}{2\mu_r}\right) i^2}{\left(s + \frac{l_{Fe}}{2\mu_r}\right)^3} \tag{2.3}$$

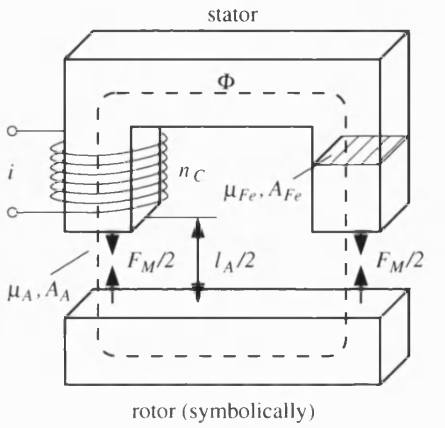

Figure 2.3: Schematic of an electromagnetic actuator.

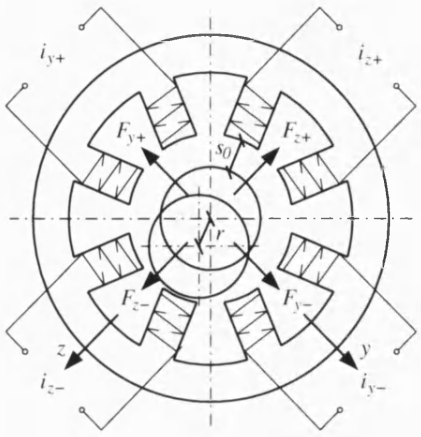

Figure 2.4: Geometry of the stator and forces in a magnetic bearing.

where the assumptions $A_A = A_{Fe}$, $\mu_A = \mu_0 = 4\pi \cdot 10^{-7} \frac{\mathrm{N}}{\mathrm{A}^2}$ are made and μ_r is defined as $\mu_r = \mu_{Fe}/\mu_0$. Equation (2.3) can only be solved if the non-linear relationship between the permeability and the magnetic field strength of the iron core is known. If the bearing is operated below the saturation point, however, μ_r is large (> 1000) and (2.3) can be simplified to

$$F_M = \frac{\mu_0 A_A n_C^2}{4} \cdot \left(\frac{i}{s}\right)^2 \tag{2.4}$$

If the magnets in a radial magnetic bearing are arranged as in Figure 2.4, the forces in the z- and y-direction are (almost) decoupled and can be calculated separately[1]. Two opposing magnets in z- or y-directions cause the force

$$F_{MB} = F_+ - F_- = k_M \left(\left(\frac{i_+}{s_0 + r}\right)^2 - \left(\frac{i_-}{s_0 - r}\right)^2 \right) \tag{2.5}$$

on the rotor, where s_0 is the nominal air gap length, and r is the displacement of the rotor, as shown in Figure 2.4. The magnetic bearing constant is

$$k_M = \frac{\mu_0 A_A n_C^2}{4} \cos \alpha_M \tag{2.6}$$

[1]Details about coupling effects are described in [35].

with α_M denoting the angle between a pole and the magnet centreline. Note that the force F_{MB} is defined as reaction force at the magnetic bearing, i.e. a positive force F_{MB} excites a force in the negative coordinate direction on the rotor.

The non-linearities of the magnetic force are generally reduced by adding a high bias current i_0 to the control current i_s, and in static applications the gravitational forces are sometimes compensated by a constant current i_g. The resulting actuator currents are therefore given by

$$i_+ = i_0 + i_g + i_s \quad \text{and} \quad i_- = i_0 - i_g - i_s \tag{2.7}$$

which leads to

$$F_{MB} = F_+ - F_- = k_M \left(\left(\frac{i_0 + i_g + i_s}{s_0 + r} \right)^2 - \left(\frac{i_0 - i_g - i_s}{s_0 - r} \right)^2 \right) \tag{2.8}$$

The magnetic bearing force can be linearised about the operating point as

$$F_{MB,lin} = F_{MB}|_{OP} + \left. \frac{\partial F_{MB}}{\partial i_s} \right|_{OP} (i_s - i_{s\,OP}) + \left. \frac{\partial F_{MB}}{\partial r} \right|_{OP} (r - r_{OP}) \tag{2.9}$$

Hence, with $i_{s\,OP} = 0$ and $r_{OP} = 0$, the linearised magnetic force of the bearing for small control currents and small displacements is given by

$$F_{MB,lin} = F_{MB,g} + k_i i_s - k_s r \tag{2.10}$$

with the actuator gain k_i and the negative open loop stiffness $-k_s$ defined as

$$k_i = 4 k_M \frac{i_0}{s_0^2} \quad \text{and} \quad k_s = 4 k_M \frac{i_0^2 + i_g^2}{s_0^3} \tag{2.11}$$

The constant force $F_{MB,g}$ vanishes if no gravity compensation is applied:

$$F_{MB,g} = 4 k_M \frac{i_0\, i_g}{s_0^2} \tag{2.12}$$

2.2.2 Improvements of the Magnetic Bearing Model

The model above does not take the frequency response characteristics of the magnetic bearings, amplifiers, or sensors into account. The peak actuator force magnitude of a magnetic bearing decreases above a certain frequency ω_{cut} due to

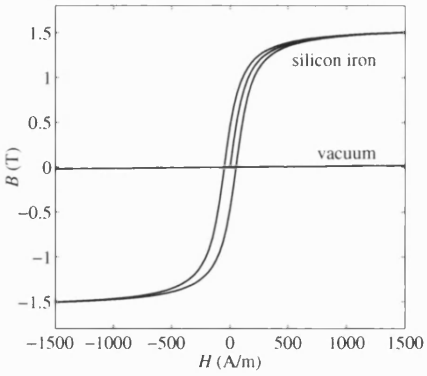

Figure 2.5: Saturation and hysteresis effects of a typical core material for electromagnets.

inductance effects. This low-pass characteristic is mainly influenced by the peak control voltage of the amplifiers, and also depends on the position of the rotor in the bearing. It is shown in [34] that a first order filter is a reasonable approximation:

$$F_{MB,lp}(s) = F_{MB}\frac{\omega_{cut}}{s + \omega_{cut}} \tag{2.13}$$

Usually, ω_{cut} is determined experimentally. If necessary, similar formulations can be used for the amplifier and sensor gains.

If the displacements and coil currents are large, saturation effects should not be neglected. As shown in Figure 2.5, the ratio $\mu = \frac{B}{H}$ is constant up to a certain magnetic field strength, if hysteresis effects are ignored. If B is increased beyond the saturation point, μ decreases rapidly and approaches μ_0, the ratio for a vacuum, asymptotically. This effectively puts an upper limit on the maximum achievable electromagnetic force. To include this effect in the model, the magnetic bearing force can be limited as

$$F_{MB,lim} = F_{MB,sat}\tanh(F_{MB}/F_{MB,sat}) \tag{2.14}$$

where $F_{MB,sat}$ must be set to an appropriate value based on measurements.

Figure 2.6 illustrates the differences between the non-linear force-current and force-displacement relationships of equations (2.8) and (2.14), and the linearised relationships of equation (2.10) with $i_g = 0$. Despite a high bias current, the deviations are considerable especially for large displacements or large currents. Under normal operating conditions, however, all three models lead to similar results during simulation. More details about non-linearities in magnetic bearing systems can be found in [36]. Measurements for the bearings of the test rig are

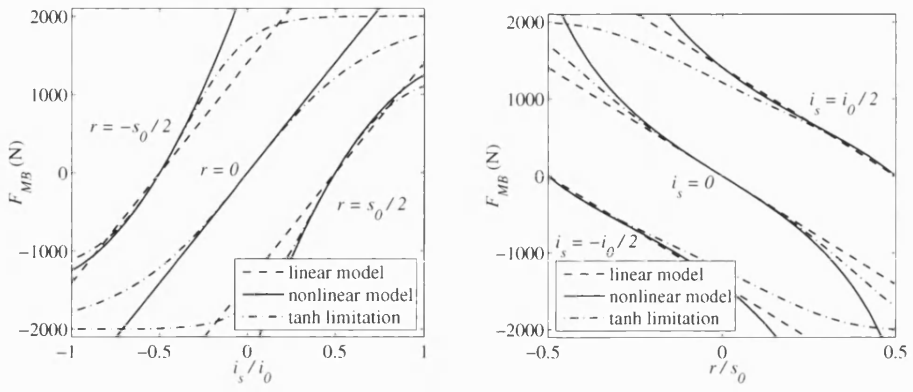

Figure 2.6: Linearised force-current and force-displacement relationships of a pair of electromagnets with high bias current i_0.

presented in [37].

2.2.3 Stabilising Active Magnetic Bearings with PD Control

Uncontrolled magnetic bearings are unstable because of the negative open loop stiffness in equation (2.10). It is common to achieve inherent stability by using decentralised PD-control for the z- and y-directions. With the displacement and the velocity errors $r_e = r_0 - r$ and $\dot{r}_e = \dot{r}_0 - \dot{r}$, the control current is

$$i_s = -\left(k_P r_e + k_D \dot{r}_e\right) \tag{2.15}$$

Substituting (2.15) into (2.10) with $F_{MB,g} = 0$ leads to

$$\begin{aligned} F_{MB,PD} &= -\left(k_i(k_P r_e + k_D \dot{r}_e) - k_s r_e\right) \\ &= -\left((k_i k_P - k_s) r_e + k_i k_D \dot{r}_e\right) \end{aligned} \tag{2.16}$$

which is equivalent to the force of a linear spring-damper system with the stiffness $k_{MB} = k_i k_P - k_s$ and the damping ratio $d_{MB} = k_i k_D$.

In practice, an integrator gain is added to reduce the steady state error. It is usually switched on temporarily in order to prevent windup. The high-frequency gain of the derivative part is limited to make it realisable for controller implementation and to avoid excessive amplification of measurement noise.

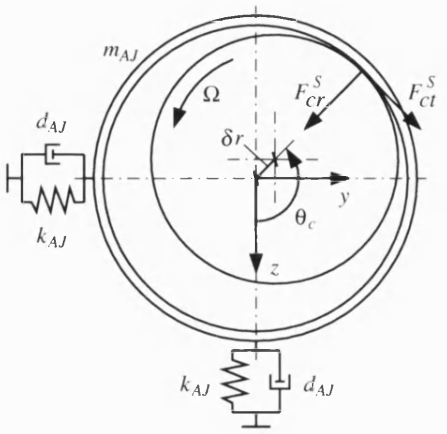

Figure 2.7: Contact between the shaft and the auxiliary bearing with $r_z^{AJ} = r_y^{AJ} = 0$.

2.2.4 Auxiliary Bearings

Most magnetic bearings are equipped with auxiliary bearings. They provide support if the power is switched off and limit the displacements if the load exceeds the magnetic force capacity. The description of contact dynamics is a complex problem subject to many recent papers. Keogh and Cole [29] derived a non-linear contact model in which the bearing is considered to remain rigid apart from local distortion over an Hertzian contact patch connecting with the rotor.

Contact occurs if $\delta r = \sqrt{(r_z^S - r_z^{AJ})^2 + (r_y^S - r_y^{AJ})^2} \geq s_c$, where s_c is the difference between the rotor and the auxiliary bearing radius. Then, the amplitude of the radial contact force F_{cr} between the shaft and the bearing is given by the implicit equation

$$\delta r - s_c = \frac{2F_{cr}(1-\nu)}{\pi E\, l_{AJ}} \left(\frac{2}{3} + \ln \frac{8E\, s_c\, l_{AJ}}{2.15^2\, F_{cr}} \right) \tag{2.17}$$

E is Young's modulus, ν is Poisson's ratio, and l_{AJ} is the length of the contact patch. The values of the constants are defined by the shape of the contacting bodies. With the contact angle

$$\theta_c = \operatorname{atan2}\left((r_y^S - r_y^{AJ}), (r_z^S - r_z^{AJ}) \right) \tag{2.18}$$

the relative velocity between rotor and auxiliary bearing at the contact point is

$$v_{rel} = R_S\Omega - (\dot{r}_z^S - \dot{r}_z^{AJ}) \sin\theta_c + (\dot{r}_y^S - \dot{r}_y^{AJ}) \cos\theta_c \tag{2.19}$$

If dry friction is assumed, the tangential force can be defined as

$$F_{ct} = \mu F_{cr} \operatorname{sgn}(v_{rel}) \tag{2.20}$$

The contact force applied from the rotor on the bearing is then given by

$$F_{cz} = F_{cr} \cos\theta_c - F_{ct} \sin\theta_c \tag{2.21a}$$

$$F_{cy} = F_{ct} \cos\theta_c + F_{cr} \sin\theta_c \tag{2.21b}$$

2.3 Finite Element Method for Elastic Rotor Systems

The dynamics of continuous systems such as flexible rotors are described by partial differential equations for which closed form solutions exist only in the most simple cases. By applying discretisation methods, the partial differential equations are approximated by sets of n ordinary differential equations, which can be written in matrix notation as

$$\mathbf{M}\ddot{\mathbf{q}} + \mathbf{B}\dot{\mathbf{q}} + \mathbf{K}\mathbf{q} = \mathbf{f} \tag{2.22}$$

where $\mathbf{M}$, $\mathbf{B}$, $\mathbf{K}$ are the system mass, damping and stiffness matrices of size $n \times n$, $\mathbf{q}$ is a vector of n generalised coordinates, and $\mathbf{f}$ is the generalised force vector.

The Finite Element Method (FEM) became the standard discretisation technique in structural dynamics during the last decades mainly because it is highly structured and can be implemented very easily in computer programs. The structure is divided into finite elements whose displacements are approximated by local trial functions. The global displacement field is then obtained by simple superposition of the element solutions [38]. The FEM allows the modelling of almost arbitrary structures, which is a great advantage compared to other discretisation techniques such as the methods of Galerkin and Rayleigh-Ritz [39] where global trial functions are used.

2.3.1 Finite Element Choice

Various different element types exist for the description of rotor systems. Two were implemented in this project, namely the Euler-Bernoulli beam element described in [40] and a Timoshenko element. The main difference between the two is that the latter considers shear forces in the element, which makes it more suitable for thick shafts. In both methods the following simplifying assumptions are made:

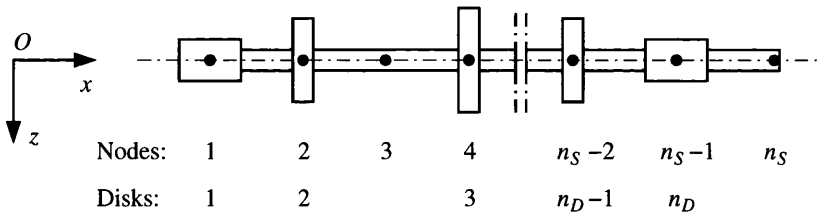

Figure 2.8: Numbering of nodes and disks of a rotor.

- the deformations of the rotor axis are small
- there are no axial nor torsional displacements
- the rotor system is rotationally symmetric except for small unbalances
- the disks are rigid and thin, and they do not affect the bending stiffness of the shaft

Element nodes are defined at points where disks are attached, where external forces act on the rotor, where sensors are mounted and at intermediate points to improve the quality of the model. The numbering is illustrated in Figure 2.8.

2.3.2 Equation of Motion for a Single Element

Figure 2.9 shows a shaft element in the xz-plane, lying parallel to the x-axis. The two translational and two rotational displacements and the according nodal forces can be combined in the vectors

$$\mathbf{q}^e_{zi} = \left[r^e_{zi}, \varphi^e_{yi}, r^e_{zi+1}, \varphi^e_{yi+1}\right]^T \quad \text{and} \quad \mathbf{f}^e_{zi} = \left[F^e_{zi}, \tau^e_{yi}, F^e_{zi+1}, \tau^e_{yi+1}\right]^T \tag{2.23a}$$

The nodal displacements and force vectors in the xy-plane are defined in an analogous way:

$$\mathbf{q}^e_{yi} = \left[r^e_{yi}, \varphi^e_{zi}, r^e_{yi+1}, \varphi^e_{zi+1}\right]^T \quad \text{and} \quad \mathbf{f}^e_{yi} = \left[F^e_{yi}, \tau^e_{zi}, F^e_{yi+1}, \tau^e_{zi+1}\right]^T \tag{2.23b}$$

The shape functions are third order polynomials in s, which represent unity

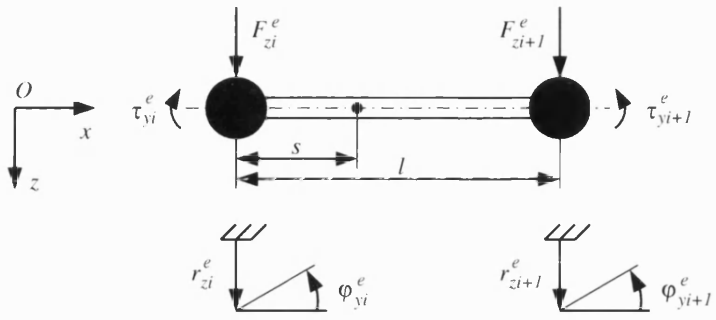

Figure 2.9: Finite beam element in xz-plane.

displacement for each particular coordinate with the other three set to zero:

$$N_{t1} = \frac{1}{1+\phi}\left(1+\phi-\phi\frac{s}{l}-3\left(\frac{s}{l}\right)^2+2\left(\frac{s}{l}\right)^3\right) \tag{2.24a}$$

$$N_{t2} = \frac{l}{1+\phi}\left(\frac{s}{l}+\frac{\phi}{2}\frac{s}{l}-2\left(\frac{s}{l}\right)^2-\frac{\phi}{2}\left(\frac{s}{l}\right)^2+\left(\frac{s}{l}\right)^3\right) \tag{2.24b}$$

$$N_{t3} = \frac{1}{1+\phi}\left(\phi\frac{s}{l}+3\left(\frac{s}{l}\right)^2-2\left(\frac{s}{l}\right)^3\right) \tag{2.24c}$$

$$N_{t4} = \frac{l}{1+\phi}\left(-\frac{\phi}{2}\frac{s}{l}-\left(\frac{s}{l}\right)^2+\frac{\phi}{2}\left(\frac{s}{l}\right)^2+\left(\frac{s}{l}\right)^3\right) \tag{2.24d}$$

The transverse shear factor $\phi = 0$ for an Euler-Bernoulli beam element and $\phi = 24EI(1+\nu)/\kappa EAl^2$ for a Timoshenko element. With the relations

$$\varphi_y(s,t) = -\frac{\partial r_z(s,t)}{\partial s} \quad \text{and} \quad \varphi_z(s,t) = \frac{\partial r_y(s,t)}{\partial s} \tag{2.25}$$

and the shape function matrices

$$\mathbf{N}_z = [N_1, -N_2, N_3, -N_4] \quad \text{and} \quad \mathbf{N}_y = [N_1, N_2, N_3, N_4] \tag{2.26}$$

the inner displacements of an element follow as

$$r_z(s) = \mathbf{N}_z(s)\mathbf{q}^e_z \qquad \varphi_y(s) = -\mathbf{N}'_z(s)\mathbf{q}^e_z \tag{2.27a}$$

$$r_y(s) = \mathbf{N}_y(s)\mathbf{q}^e_y \qquad \varphi_z(s) = \mathbf{N}'_y(s)\mathbf{q}^e_y \tag{2.27b}$$

where $'$ denotes the derivative d/ds.

The equations of motion can be derived with Lagrange's method. The elastic

bending, axial load, and kinetic energy expressions of a beam element element are [41]

$$U_b^e = \frac{1}{2}\int_0^l \begin{bmatrix} -\varphi_y' \\ \varphi_z' \end{bmatrix}^T \begin{bmatrix} EI & 0 \\ 0 & EI \end{bmatrix} \begin{bmatrix} -\varphi_y' \\ \varphi_z' \end{bmatrix} ds \tag{2.28a}$$

$$U_a^e = \frac{1}{2}\int_0^l \begin{bmatrix} -\varphi_y \\ \varphi_z \end{bmatrix}^T \begin{bmatrix} F_a & 0 \\ 0 & F_a \end{bmatrix} \begin{bmatrix} -\varphi_y \\ \varphi_z \end{bmatrix} ds \tag{2.28b}$$

$$V^e = \int_0^l \frac{1}{2} \begin{bmatrix} \dot{r}_z \\ \dot{r}_y \end{bmatrix}^T \begin{bmatrix} \rho A & 0 \\ 0 & \rho A \end{bmatrix} \begin{bmatrix} \dot{r}_z \\ \dot{r}_y \end{bmatrix} + \frac{1}{2}\dot{\varphi}_x^2 \Theta_p^e + \\ + \frac{1}{2} \begin{bmatrix} \dot{\varphi}_y \\ \dot{\varphi}_z \end{bmatrix}^T \begin{bmatrix} \Theta_d & 0 \\ 0 & \Theta_d \end{bmatrix} \begin{bmatrix} \dot{\varphi}_y \\ \dot{\varphi}_z \end{bmatrix} - \dot{\varphi}_x \dot{\varphi}_z \varphi_y \Theta_p \, ds \tag{2.28c}$$

where $\Theta_d = \frac{\rho A R^2}{4}$ and $\Theta_p = \frac{\rho A R^2}{2}$. Substituting (2.27) into (2.28) yields

$$U_b^e = \frac{1}{2}\int_0^l EI \begin{bmatrix} \mathbf{q}_z^e \\ \mathbf{q}_y^e \end{bmatrix}^T \begin{bmatrix} \mathbf{N}_z'' & \mathbf{0} \\ \mathbf{0} & \mathbf{N}_y'' \end{bmatrix}^T \begin{bmatrix} \mathbf{N}_z'' & \mathbf{0} \\ \mathbf{0} & \mathbf{N}_y'' \end{bmatrix} \begin{bmatrix} \mathbf{q}_z^e \\ \mathbf{q}_y^e \end{bmatrix} ds \tag{2.29a}$$

$$U_a^e = \frac{1}{2}\int_0^l F_a \begin{bmatrix} \mathbf{q}_z^e \\ \mathbf{q}_y^e \end{bmatrix}^T \begin{bmatrix} \mathbf{N}_z' & \mathbf{0} \\ \mathbf{0} & \mathbf{N}_y' \end{bmatrix}^T \begin{bmatrix} \mathbf{N}_z' & \mathbf{0} \\ \mathbf{0} & \mathbf{N}_y' \end{bmatrix} \begin{bmatrix} \mathbf{q}_z^e \\ \mathbf{q}_y^e \end{bmatrix} ds \tag{2.29b}$$

$$V^e = \int_0^l \frac{1}{2}\rho A \begin{bmatrix} \dot{\mathbf{q}}_z^e \\ \dot{\mathbf{q}}_y^e \end{bmatrix}^T \begin{bmatrix} \mathbf{N}_z & \mathbf{0} \\ \mathbf{0} & \mathbf{N}_y \end{bmatrix}^T \begin{bmatrix} \mathbf{N}_z & \mathbf{0} \\ \mathbf{0} & \mathbf{N}_y \end{bmatrix} \begin{bmatrix} \dot{\mathbf{q}}_z^e \\ \dot{\mathbf{q}}_y^e \end{bmatrix} + \frac{1}{2}\dot{\varphi}_x^2 \Theta_p + \\ + \frac{1}{2}\Theta_d \begin{bmatrix} \dot{\mathbf{q}}_z^e \\ \dot{\mathbf{q}}_y^e \end{bmatrix}^T \begin{bmatrix} -\mathbf{N}_z' & \mathbf{0} \\ \mathbf{0} & \mathbf{N}_y' \end{bmatrix}^T \begin{bmatrix} -\mathbf{N}_z' & \mathbf{0} \\ \mathbf{0} & \mathbf{N}_y' \end{bmatrix} \begin{bmatrix} \dot{\mathbf{q}}_z^e \\ \dot{\mathbf{q}}_y^e \end{bmatrix} - \\ + \dot{\varphi}_x \Theta_p \begin{bmatrix} \dot{\mathbf{q}}_z^e \\ \dot{\mathbf{q}}_y^e \end{bmatrix}^T \begin{bmatrix} \mathbf{0} & \mathbf{N}_y' \end{bmatrix}^T \begin{bmatrix} -\mathbf{N}_z' & \mathbf{0} \end{bmatrix} \begin{bmatrix} \mathbf{q}_z^e \\ \mathbf{q}_y^e \end{bmatrix} ds \tag{2.29c}$$

Applying Lagrange's equation

$$\frac{d}{dt}\frac{\partial L}{\partial \dot{q}_i} - \frac{\partial L}{\partial q_i} = f_i \tag{2.30}$$

with $L = V - U$ and the constant spin speed restriction $\dot{\varphi}_x = -\Omega$ finally leads to

the equation of motion for an element

$$\left(\begin{bmatrix} \mathbf{M}^e_{tz} & \mathbf{0} \\ \mathbf{0} & \mathbf{M}^e_{ty} \end{bmatrix} + \begin{bmatrix} \mathbf{M}^e_{rz} & \mathbf{0} \\ \mathbf{0} & \mathbf{M}^e_{ry} \end{bmatrix}\right) \begin{bmatrix} \ddot{\mathbf{q}}^e_z \\ \ddot{\mathbf{q}}^e_y \end{bmatrix} + \Omega \begin{bmatrix} \mathbf{0} & -(\mathbf{G}^e)^T \\ \mathbf{G}^e & \mathbf{0} \end{bmatrix} \begin{bmatrix} \dot{\mathbf{q}}^e_z \\ \dot{\mathbf{q}}^e_y \end{bmatrix} + \\ + \left(\begin{bmatrix} \mathbf{K}^e_{bz} & \mathbf{0} \\ \mathbf{0} & \mathbf{K}^e_{by} \end{bmatrix} + \begin{bmatrix} \mathbf{K}^e_{az} & \mathbf{0} \\ \mathbf{0} & \mathbf{K}^e_{ay} \end{bmatrix}\right) \begin{bmatrix} \mathbf{q}^e_z \\ \mathbf{q}^e_y \end{bmatrix} = \begin{bmatrix} \mathbf{f}^e_z \\ \mathbf{f}^e_y \end{bmatrix} \tag{2.31}$$

where the mass, stiffness, and gyroscopic matrices are given by

$$\mathbf{M}^e_{tz} = \int_0^l \rho A\, \mathbf{N}_z^T \mathbf{N}_z \, ds \qquad \mathbf{M}^e_{ty} = \int_0^l \rho A\, \mathbf{N}_y^T \mathbf{N}_y \, ds \tag{2.32a}$$

$$\mathbf{M}^e_{rz} = \int_0^l \Theta_d\, (-\mathbf{N}_z'^T)(-\mathbf{N}_z') \, ds \qquad \mathbf{M}^e_{ry} = \int_0^l \Theta_d\, \mathbf{N}_y'^T \mathbf{N}_y' \, ds \tag{2.32b}$$

$$\mathbf{K}^e_{bz} = \int_0^l EI\, \mathbf{N}_z''^T \mathbf{N}_z'' \, ds \qquad \mathbf{K}^e_{by} = \int_0^l EI\, \mathbf{N}_y''^T \mathbf{N}_y'' \, ds \tag{2.32c}$$

$$\mathbf{K}^e_{az} = \int_0^l F_a\, \mathbf{N}_z'^T \mathbf{N}_z' \, ds \qquad \mathbf{K}^e_{ay} = \int_0^l F_a\, \mathbf{N}_y'^T \mathbf{N}_y' \, ds \tag{2.32d}$$

$$\mathbf{G}^e = \int_0^l \Theta_p\, \mathbf{N}_y'^T (-\mathbf{N}_z') \, ds \tag{2.32e}$$

A full listing of the beam element matrices can be found in Appendix B. The force vector $\mathbf{f}$ includes bearing forces, unbalance forces, and other external effects. Element unbalance forces can be calculated if the distributed mass centre eccentricity for $\varphi_x = 0$ is given as a function of s by the coordinates $(\varepsilon_z(s), \varepsilon_y(s))$. With

$$\mathbf{u}^e_{cz} = \int_0^l \rho A\, \mathbf{N}_z^T \varepsilon_z \, ds \qquad \mathbf{u}^e_{sz} = -\int_0^l \rho A\, \mathbf{N}_z^T \varepsilon_y \, ds \tag{2.33a}$$

$$\mathbf{u}^e_{cy} = \int_0^l \rho A\, \mathbf{N}_y^T \varepsilon_y \, ds \qquad \mathbf{u}^e_{sy} = \int_0^l \rho A\, \mathbf{N}_y^T \varepsilon_z \, ds \tag{2.33b}$$

the element unbalance force vector is

$$\begin{bmatrix} \mathbf{f}^e_{uz} \\ \mathbf{f}^e_{uy} \end{bmatrix} = \Omega^2 \left(\begin{bmatrix} \mathbf{u}^e_{cz} \\ \mathbf{u}^e_{cy} \end{bmatrix} \cos \Omega t + \begin{bmatrix} \mathbf{u}^e_{sz} \\ \mathbf{u}^e_{sy} \end{bmatrix} \sin \Omega t \right) \tag{2.34}$$

2.3.3 Internal Friction

The effect of structural damping in shafts is neglected in most rotor dynamic problems because the forces are very small in most engineering materials and an

exact description is very difficult. Magnetic bearing rotors, however, are often operated at high rotational speeds where internal friction forces can destabilise the system.

The destabilising effect at high rotation speeds has been known for some time [42]. Dimentberg [43] analyses the stability of a Jeffcot rotor subject to internal friction in detail, and Zorzi and Nelson [40] derive a finite element description.

The simplest formulation of internal friction is based on the viscous friction model. Here, the friction forces are proportional to the rate of deformation. A more accurate description is obtained by taking the hysteresis loop into account where it is assumed that area of the loop is proportional to square of the amplitude of the deviation and independent from the speed of deformation.

In this thesis, the model of Zorzi and Nelson [40] is adapted, which takes both friction effects into account. Without showing derivations, the equations of motion for a shaft element with viscous and hysteretic friction are given by

$$\begin{aligned}
&\left(\begin{bmatrix} \mathbf{M}^e_{tz} & \mathbf{0} \\ \mathbf{0} & \mathbf{M}^e_{ty} \end{bmatrix} + \begin{bmatrix} \mathbf{M}^e_{rz} & \mathbf{0} \\ \mathbf{0} & \mathbf{M}^e_{ry} \end{bmatrix}\right) \begin{bmatrix} \ddot{\mathbf{q}}^e_z \\ \ddot{\mathbf{q}}^e_y \end{bmatrix} + \\
&\quad + \left(\eta_v \begin{bmatrix} \mathbf{K}^e_{bz} & \mathbf{0} \\ \mathbf{0} & \mathbf{K}^e_{by} \end{bmatrix} + \Omega \begin{bmatrix} \mathbf{0} & -(\mathbf{G}^e)^T \\ \mathbf{G}^e & \mathbf{0} \end{bmatrix}\right) \begin{bmatrix} \dot{\mathbf{q}}^e_z \\ \dot{\mathbf{q}}^e_y \end{bmatrix} + \\
&\quad + \left(\frac{1+\eta_h}{\sqrt{1+\eta_h^2}} \begin{bmatrix} \mathbf{K}^e_{bz} & \mathbf{0} \\ \mathbf{0} & \mathbf{K}^e_{by} \end{bmatrix} + \begin{bmatrix} \mathbf{K}^e_{az} & \mathbf{0} \\ \mathbf{0} & \mathbf{K}^e_{ay} \end{bmatrix} - \right. \\
&\quad \left. + \left(\eta_v \Omega + \operatorname{sgn}\Omega \frac{\eta_h}{\sqrt{1+\eta_h^2}}\right) \begin{bmatrix} \mathbf{0} & -(\mathbf{K}^e_c)^T \\ \mathbf{K}^e_c & \mathbf{0} \end{bmatrix}\right) \begin{bmatrix} \mathbf{q}^e_z \\ \mathbf{q}^e_y \end{bmatrix} = \begin{bmatrix} \mathbf{f}^e_z \\ \mathbf{f}^e_y \end{bmatrix}
\end{aligned} \tag{2.35}$$

with the viscous damping coefficient η_v, the hysteretic loss factor η_h and the circulatory stiffness matrix

$$\mathbf{K}^e_c = \int_0^l EI\, \mathbf{N}''^T_y \mathbf{N}''_z \, ds \tag{2.36}$$

2.3.4 Rigid Disks

The equations of motion of rigid disks attached to the shaft are developed with Lagrange's method. The kinetic energy of a disk without static and dynamic

unbalance mounted on node i of the shaft is given by

$$V^d = \frac{1}{2}\begin{bmatrix}\dot{r}_{zi} - l_*\dot{\varphi}_{yi}\\ \dot{r}_{yi} + l_*\dot{\varphi}_{zi}\end{bmatrix}\begin{bmatrix}m^d & 0\\ 0 & m^d\end{bmatrix}\begin{bmatrix}\dot{r}_{zi} - l_*\dot{\varphi}_{yi}\\ \dot{r}_{yi} + l_*\dot{\varphi}_{zi}\end{bmatrix} + \\ + \frac{1}{2}\begin{bmatrix}\ddot{\varphi}_{zi}\\ \ddot{\varphi}_{yi}\end{bmatrix}\begin{bmatrix}\Theta_d & 0\\ 0 & \Theta_d\end{bmatrix}\begin{bmatrix}\ddot{\varphi}_{zi}\\ \ddot{\varphi}_{yi}\end{bmatrix} - \dot{\varphi}_x\dot{\varphi}_y\varphi_z\Theta_p \quad (2.37)$$

if the displacements are small. The constant l_* is the distance of the disk centre of mass in x-direction from the node at which the disk is mounted. Substituting (2.37) into Lagrange's equation (2.30) and defining

$$\mathbf{q}_z^d = \left[r_{zi}^e, \varphi_{yi}^e\right]^T \qquad \mathbf{f}_z^d = \left[F_{zi}^e, \tau_{yi}^e\right]^T \quad (2.38a)$$

$$\mathbf{q}_y^d = \left[r_{yi}^e, \varphi_{zi}^e\right]^T \qquad \mathbf{f}_y^d = \left[F_{yi}^e, \tau_{zi}^e\right]^T \quad (2.38b)$$

leads to

$$\begin{bmatrix}\mathbf{M}_z^d & \mathbf{0}\\ \mathbf{0} & \mathbf{M}_y^d\end{bmatrix}\begin{bmatrix}\ddot{\mathbf{q}}_z^d\\ \ddot{\mathbf{q}}_y^d\end{bmatrix} + \Omega\begin{bmatrix}\mathbf{0} & -(\mathbf{G}^d)^T\\ \mathbf{G}^d & \mathbf{0}\end{bmatrix}\begin{bmatrix}\dot{\mathbf{q}}_z^d\\ \dot{\mathbf{q}}_y^d\end{bmatrix} = \begin{bmatrix}\mathbf{f}_z^d\\ \mathbf{f}_y^d\end{bmatrix} \quad (2.39)$$

with the mass matrices

$$\mathbf{M}_z^d = \begin{bmatrix}m^d & -m^d l_*\\ -m^d l_* & \Theta_d + m^d l_*^2\end{bmatrix} \quad \text{and} \quad \mathbf{M}_y^d = \begin{bmatrix}m^d & m^d l_*\\ m^d l_* & \Theta_d + m^d l_*^2\end{bmatrix} \quad (2.40a)$$

and the gyroscopic matrix

$$\mathbf{G}^d = \begin{bmatrix}0 & 0\\ 0 & \Theta_p\end{bmatrix} \quad (2.40b)$$

Static and dynamic unbalance forces can be derived via Newton's law and Euler's equation, respectively. For $\varphi_x = 0$, the centre of mass eccentricity, and the angular displacement of the centre axis of the disk towards the centre axis of the shaft around the z- and y-axis are assumed to be $(\varepsilon_z, \varepsilon_y)$ and (α_z, α_y), respectively. With

$$\mathbf{u}_{cz}^d = \left[m^d\varepsilon_z, -m^d l_*\varepsilon_z - (\Theta_a + m^d l_*^2 - \Theta_d)\alpha_z\right]^T \quad (2.41a)$$

$$\mathbf{u}_{sz}^d = \left[-m^d\varepsilon_y, m^d l_*\varepsilon_y + (\Theta_a + m^d l_*^2 - \Theta_d)\alpha_y\right]^T \quad (2.41b)$$

$$\mathbf{u}_{cy}^d = \left[m^d\varepsilon_y, m^d l_*\varepsilon_y + (\Theta_a + m^d l_*^2 - \Theta_d)\alpha_y\right]^T \quad (2.41c)$$

$$\mathbf{u}_{sy}^{d} = \left[m^{d}\varepsilon_{z}, m^{d}l_{*}\varepsilon_{z} + (\Theta_{a} + m^{d}l_{*}^{2} - \Theta_{d})\alpha_{z}\right]^{T} \tag{2.41d}$$

the disk unbalance force vector is

$$\begin{bmatrix}\mathbf{f}_{uz}^{d}\\ \mathbf{f}_{uy}^{d}\end{bmatrix} = \Omega^{2}\left(\begin{bmatrix}\mathbf{u}_{cz}^{d}\\ \mathbf{u}_{cy}^{d}\end{bmatrix}\cos\Omega t + \begin{bmatrix}\mathbf{u}_{sz}^{d}\\ \mathbf{u}_{sy}^{d}\end{bmatrix}\sin\Omega t\right) \tag{2.42}$$

2.3.5 Bearing Forces

As mentioned in Section 2.2.3, the force-displacement relationship of a PD-controlled magnetic bearing can be approximated by a linear spring-damper system. If the bearing force acts on node i, and its sensor measures the displacement at node k, the equations for a magnetic bearing "element" can be written as

$$\begin{bmatrix}\mathbf{D}_{z}^{pd} & \mathbf{0}\\ \mathbf{0} & \mathbf{D}_{y}^{pd}\end{bmatrix}\begin{bmatrix}\dot{\mathbf{q}}_{z}^{pd}\\ \dot{\mathbf{q}}_{y}^{pd}\end{bmatrix} + \begin{bmatrix}\mathbf{K}_{z}^{pd} & \mathbf{0}\\ \mathbf{0} & \mathbf{K}_{y}^{pd}\end{bmatrix}\begin{bmatrix}\mathbf{q}_{z}^{pd}\\ \mathbf{q}_{y}^{pd}\end{bmatrix} = \mathbf{0} \tag{2.43}$$

with the displacement vectors and the element matrices

$$\mathbf{q}_{z}^{pd} = [r_{z\,i}^{e}, r_{z\,k}^{e}]^{T} \quad \text{and} \quad \mathbf{q}_{y}^{pd} = [r_{y\,i}^{e}, r_{y\,k}^{e}]^{T} \tag{2.44}$$

$$\mathbf{K}_{z,y}^{pd} = \begin{bmatrix}-k_{s(z,y)} & k_{i(z,y)}\,k_{P(z,y)}\\ 0 & 0\end{bmatrix} \quad \text{and} \quad \mathbf{D}_{z,y}^{pd} = \begin{bmatrix}0 & k_{i(z,y)}\,k_{D(z,y)}\\ 0 & 0\end{bmatrix} \tag{2.45}$$

where k_i and k_s are the actuator gain and negative open loop stiffness of the magnetic bearing presented in equation (2.11), and k_P and k_D are the proportional and derivative gains of the PD controller. In the special case of sensor-actuator collocation $i = k$, the displacement vectors are scalars and the bearing stiffness and damping matrices are given by

$$\mathbf{K}_{z,y}^{pd} = k_{i(z,y)}\,k_{P(z,y)} - k_{s(z,y)} \quad \text{and} \quad \mathbf{D}_{z,y}^{pd} = k_{i(z,y)}\,k_{D(z,y)} \tag{2.46}$$

2.3.6 Assembly Process

The element matrices for the z- and y-directions are superposed to get the global nodal displacement vector $\mathbf{q} = [\mathbf{q}_{z}^{T}, \mathbf{q}_{y}^{T}]^{T}$ with

$$\mathbf{q}_{z} = [r_{z1}, \varphi_{y1}, r_{z2}, \varphi_{y2}, \ldots, r_{z\,n_S}, \varphi_{y\,n_S}]^{T} \tag{2.47a}$$

$$\mathbf{q}_{y} = [r_{y1}, \varphi_{z1}, r_{y2}, \varphi_{z2}, \ldots, r_{y\,n_S}, \varphi_{z\,n_S}]^{T} \tag{2.47b}$$

The global mass matrices, as well as the bending and axial loading stiffness matrices are symmetric and have band structure. The gyroscopic and circulatory stiffness matrices are skew-symmetric with skew symmetric band matrices in the lower left and upper right quadrant. The stiffness and damping matrices of a PD-controlled magnetic bearing are diagonal only if sensors and actuators are collocated.

The equations of motion of the whole system are

$$\mathbf{M}\ddot{\mathbf{q}} + \mathbf{B}\dot{\mathbf{q}} + \mathbf{K}\mathbf{q} = \mathbf{f}_u + \mathbf{f}_{MB} \tag{2.48}$$

with

$$\mathbf{M} = \begin{bmatrix} \mathbf{M}_{tz}^S & \mathbf{0} \\ \mathbf{0} & \mathbf{M}_{ty}^S \end{bmatrix} + \begin{bmatrix} \mathbf{M}_{rz}^S & \mathbf{0} \\ \mathbf{0} & \mathbf{M}_{ry}^S \end{bmatrix} + \begin{bmatrix} \mathbf{M}_{z}^D & \mathbf{0} \\ \mathbf{0} & \mathbf{M}_{y}^D \end{bmatrix} \tag{2.49a}$$

$$\mathbf{B} = \eta_v \begin{bmatrix} \mathbf{K}_{bz}^S & \mathbf{0} \\ \mathbf{0} & \mathbf{K}_{by}^S \end{bmatrix} + \Omega \begin{bmatrix} \mathbf{0} & -(\mathbf{G}^S + \mathbf{G}^D)^T \\ \mathbf{G}^S + \mathbf{G}^D & \mathbf{0} \end{bmatrix} + \begin{bmatrix} \mathbf{D}_{z}^{PD} & \mathbf{0} \\ \mathbf{0} & \mathbf{D}_{y}^{PD} \end{bmatrix} \tag{2.49b}$$

$$\begin{aligned} \mathbf{K} = {} & \frac{1+\eta_h}{\sqrt{1+\eta_h^2}} \begin{bmatrix} \mathbf{K}_{bz}^S & \mathbf{0} \\ \mathbf{0} & \mathbf{K}_{by}^S \end{bmatrix} + \begin{bmatrix} \mathbf{K}_{az}^S & \mathbf{0} \\ \mathbf{0} & \mathbf{K}_{ay}^S \end{bmatrix} + \\ & + \left(\eta_v \Omega + \operatorname{sgn}\Omega \frac{\eta_h}{\sqrt{1+\eta_h^2}} \right) \begin{bmatrix} \mathbf{0} & -(\mathbf{K}_c^S)^T \\ \mathbf{K}_c^S & \mathbf{0} \end{bmatrix} + \begin{bmatrix} \mathbf{K}_{z}^{PD} & \mathbf{0} \\ \mathbf{0} & \mathbf{K}_{y}^{PD} \end{bmatrix} \end{aligned} \tag{2.49c}$$

$$\mathbf{f}_u = \left[\mathbf{f}_{uz}^{ST}, \mathbf{f}_{uy}^{ST}\right]^T + \left[\mathbf{f}_{uz}^{DT}, \mathbf{f}_{uy}^{DT}\right]^T \tag{2.49d}$$

The force vector $\mathbf{f}_{MB}$ contains all forces applied from the magnetic bearings on the shaft excluding the linear elastic forces (2.43) arising from PD-control.

2.3.7 Base Motion

Magnetic bearing rotor systems used in manufacturing or transport applications are affected by base motion. The equations on motion (2.22) are formulated in a Newtonian reference frame N, but control variables are usually measured in a reference frame B fixed on the base. The relationship between the modal displacement of the shaft in B and N is

$${}^B\mathbf{q}^S = {}^N\mathbf{q}^S - {}^N\mathbf{q}^B \tag{2.50}$$

where ${}^{N}\mathbf{q}^{B}$ contains the translational and rotational displacements of the base reference frame in N at all rotor nodes.

The base has two translational and two rotational degrees of freedom ${}^{N}r_{z}^{B}$, ${}^{N}r_{y}^{B}$ and ${}^{N}\varphi_{y}^{B}$, ${}^{N}\varphi_{z}^{B}$, respectively. The rotations are defined around an axis passing through node 1 of the undeformed shaft. If the rotations are small, the translational and rotational displacements at node i are given by

$$
\begin{aligned}
{}^{B}r_{zi}^{S} &= {}^{N}r_{zi}^{S} - \left({}^{N}r_{z}^{B} - l_{xi}\sin{}^{N}\varphi_{y}^{B}\right) & {}^{B}\varphi_{yi}^{S} &= {}^{N}\varphi_{yi}^{S} - {}^{N}\varphi_{y}^{B} && \text{(2.51a)}\\
{}^{B}r_{yi}^{S} &= {}^{N}r_{yi}^{S} - \left({}^{N}r_{y}^{B} + l_{xi}\sin{}^{N}\varphi_{z}^{B}\right) & {}^{B}\varphi_{zi}^{S} &= {}^{N}\varphi_{zi}^{S} - {}^{N}\varphi_{z}^{B} && \text{(2.51b)}
\end{aligned}
$$

where l_{xi} is the distance in x-direction between node 1 and node i.

If base motion is present, the equations of motion of the rotor (2.48) become

$$\mathbf{M}\,{}^{N}\ddot{\mathbf{q}}^{S} + \mathbf{B}\,{}^{N}\dot{\mathbf{q}}^{S} + \mathbf{K}\,{}^{N}\mathbf{q}^{S} = \mathbf{f}_{u} + \mathbf{f}_{MB} + \mathbf{f}_{B} \tag{2.52}$$

with

$$\mathbf{f}_{B} = \left(\mathbf{D}^{PD}\,{}^{N}\dot{\mathbf{q}}^{B} + \mathbf{K}^{PD}\,{}^{N}\mathbf{q}^{B}\right) \tag{2.53}$$

and $\mathbf{M}$, $\mathbf{B}$, $\mathbf{K}$, $\mathbf{f}_{u}$, and $\mathbf{f}_{MB}$ defined as in (2.49).

2.3.8 State-Space Formulation and Modal Reduction

For the purpose of simulation and control design, the system equations of motion are transformed into state space form

$$
\begin{aligned}
\dot{\mathbf{x}}(t) &= \mathbf{A}\mathbf{x}(t) + \mathbf{B}\mathbf{u}(t) && \text{(2.54a)}\\
\mathbf{y}(t) &= \mathbf{C}\mathbf{x}(t) + \mathbf{D}\mathbf{u}(t) && \text{(2.54b)}
\end{aligned}
$$

where $\mathbf{x}$ is the model state vector, $\mathbf{u}$ the input, and $\mathbf{y}$ the output vector. If equation (2.52) is rearranged as

$${}^{N}\ddot{\mathbf{q}}^{S} = \mathbf{M}^{-1}\left(\mathbf{f} - \mathbf{B}{}^{N}\dot{\mathbf{q}}^{S} - \mathbf{K}{}^{N}\mathbf{q}^{S}\right) \tag{2.55}$$

with $\mathbf{f} = \mathbf{f}_{u} + \mathbf{f}_{MB} + \mathbf{f}_{B}$, it can be readily seen that its state-space description is given by

$$\begin{bmatrix} {}^{N}\dot{\mathbf{q}}^{S} \\ {}^{N}\ddot{\mathbf{q}}^{S} \end{bmatrix} = \begin{bmatrix} \mathbf{0} & \mathbf{I} \\ -\mathbf{M}^{-1}\mathbf{K} & -\mathbf{M}^{-1}\mathbf{B} \end{bmatrix} \begin{bmatrix} {}^{N}\mathbf{q}^{S} \\ {}^{N}\dot{\mathbf{q}}^{S} \end{bmatrix} + \begin{bmatrix} \mathbf{0} \\ \mathbf{M}^{-1} \end{bmatrix} \begin{bmatrix} \mathbf{f} \end{bmatrix} \tag{2.56a}$$

$$\begin{bmatrix} {}^{B}\mathbf{q}^{S} \\ {}^{B}\dot{\mathbf{q}}^{S} \end{bmatrix} = \begin{bmatrix} \mathbf{I} & \mathbf{0} \\ \mathbf{0} & \mathbf{I} \end{bmatrix} \begin{bmatrix} {}^{N}\mathbf{q}^{S} \\ {}^{N}\dot{\mathbf{q}}^{S} \end{bmatrix} - \begin{bmatrix} \mathbf{I} & \mathbf{0} \\ \mathbf{0} & \mathbf{I} \end{bmatrix} \begin{bmatrix} {}^{N}\mathbf{q}^{B} \\ {}^{N}\dot{\mathbf{q}}^{B} \end{bmatrix} \tag{2.56b}$$

For controller design it is highly desirable to reduce the order of the state-space system (2.56). A good starting point is simple modal reduction, where only the lower frequency eigenmodes are retained. The first step is to transform the system matrix $\mathbf{A}$ into a block-diagonal real modal matrix $\mathbf{A}_m$ with either 1×1 or 2×2 blocks on the diagonal containing the real and imaginary eigenvalues in ascending order based on their magnitude. For a complex eigenvalue pair $\lambda = \alpha \pm \mathrm{j}\omega$ the block is $\left[\begin{smallmatrix} \omega & \alpha \\ -\alpha & \omega \end{smallmatrix}\right]$.

Mathematically, the ordered, real eigenstructure decomposition can be expressed by the similarity transformation

$$\boldsymbol{\Psi}_r^{-1}\mathbf{A}\boldsymbol{\Psi}_r = \mathbf{A}_m \tag{2.57a}$$

where $\boldsymbol{\Psi}_r$ is a set of ordered real eigenvectors spanning the same eigenspace as the complex ones. With $\boldsymbol{\Psi}_r$, the remaining state-space matrices in (2.54) can be transformed as

$$\mathbf{B}_m = \boldsymbol{\Psi}_r^{-1}\mathbf{B} \qquad \mathbf{C}_m = \mathbf{D}\boldsymbol{\Psi}_r \qquad \mathbf{D}_m = \mathbf{D} \tag{2.57b}$$

Once the modal representation is obtained, all states with eigenvalue magnitudes $|\lambda| > |\lambda_{cut}|$ are deleted in order to get the reduced model.

2.4 System Dynamics and Identification

The theoretical eigenmodes and critical frequencies of the experimental rotor system shown in Figure 2.10 can be found by solving the polynomial eigenvalue problem

$$\left(\mathbf{M}\lambda^2 + \mathbf{B}\lambda + \mathbf{K}\right)\boldsymbol{\psi} = \mathbf{0} \tag{2.58}$$

where $\mathbf{M}$, $\mathbf{B}$, and $\mathbf{K}$ are defined in equation (2.49). Figure 2.11 shows the first five eigenmodes for zero rotational speed together with the corresponding eigenfrequencies. It is assumed that the magnetic bearings are PD-controlled with stiffness and damping values of $k_{MB} = 1\,\mathrm{MN/m}$ and $d_{MB} = 3500\,\mathrm{Ns/m}$, respectively. Internal friction effects are neglected. With these parameters, the first two modes correspond to near "rigid body" motion of the rotor. The third

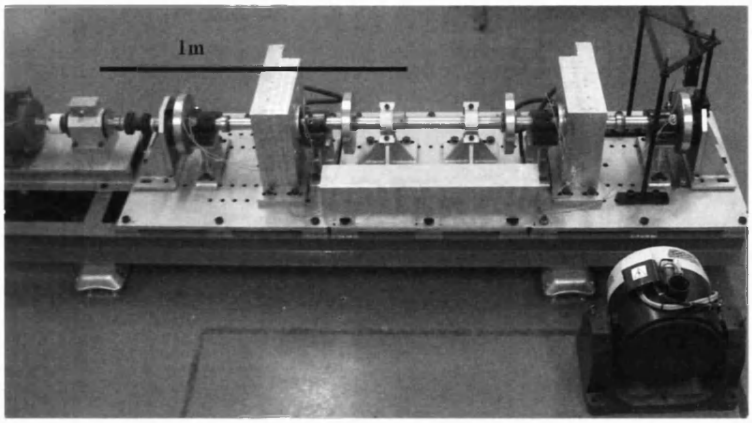

Figure 2.10: Photograph of the test rig.

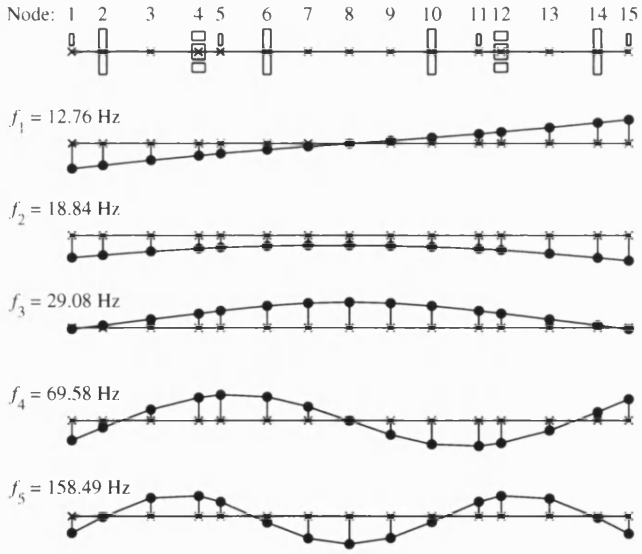

Figure 2.11: Eigenmodes and -frequencies of the rotor with a bearing stiffness $k_{MB} = 1\,\mathrm{MN/m}$ and damping $d_{MB} = 3500\,\mathrm{Ns/m}$. The motor (not shown) is connected to node 1.

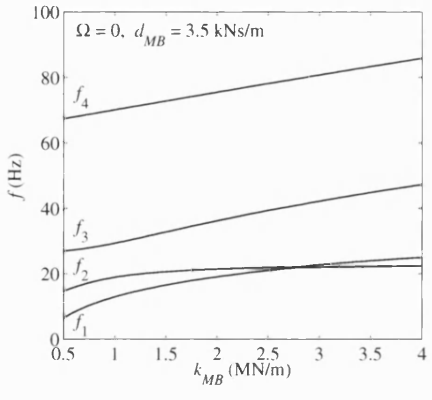

Figure 2.12: Relation of eigenfrequencies f_k to bearing stiffness k_{MB}.

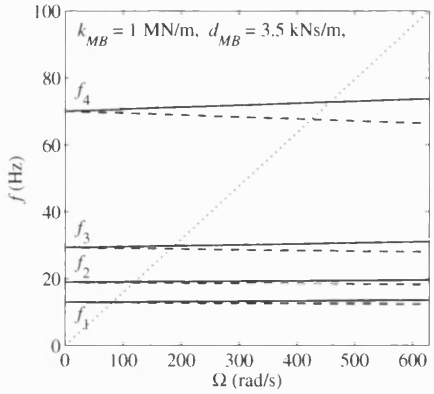

Figure 2.13: Relation of eigenfrequencies f_k to rotational speed Ω.

and fourth mode are the first symmetric and antisymmetric bending modes. The fifth mode has a eigenfrequency higher than the maximum rotation speed, so that it will not be excited by synchronous unbalance forces.

The eigenfrequencies (and eigenmodes) change significantly if the bearing stiffness is varied or if the rotational speed increases. This fact is illustrated in Figures 2.12 and 2.13 where the magnitudes of the eigenvalues are plotted over bearing stiffness and rotational speed, respectively.

All modes in the operating range can be well damped by the magnetic bearings, because the displacement amplitudes at the bearing nodes $(4, 12)$ are relatively large as shown in Figure 2.11. The magnitudes of the transfer function from magnetic bearing forces at node 4 to displacements at sensor nodes 5 and 11 for various values of d_{MB} are shown in Figure 2.14. It is tempting to increase the damping to a high value in order to reduce vibration amplitudes in the resonant zones. In practice, however, large values for d_{MB} lead to high noise amplification, large actuator forces, and reduced system stability so that a compromise has to be found.

An experimental system identification has been performed to verify the theoretical results. The magnetic bearings were used to excite the rotor with a sweep-sine force

$$F(t) = \widehat{F} \sin\left(2\pi \frac{f_{max}}{t_{sweep}} t^2\right) \tag{2.59}$$

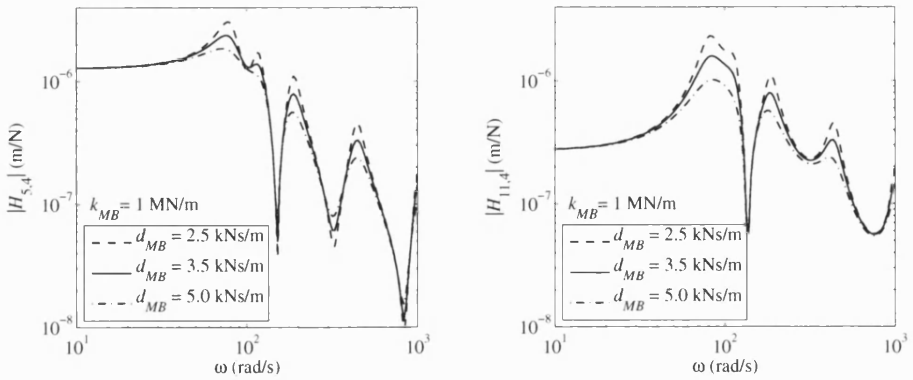

Figure 2.14: Magnitudes of the displacement frequency response at the inner sensor nodes 5 and 11 to forces applied through the magnetic bearing at node 4 for different bearing damping parameters d_{MB}.

with the amplitude $\widehat{F} = 120\,\mathrm{N}$, the maximum frequency $f_{max} = 200\,\mathrm{Hz}$, and the sweep time $t_{sweep} = 24\,\mathrm{s}$. The rotor was excited separately at both magnetic bearings in z- and y-directions and the responses were measured at all sensor nodes.

The system input $\mathbf{u}(t) = F(t)$ and measured output $\mathbf{y}(t) = \mathbf{r}(t)$ were transferred element-wise into the frequency domain via the Fast Fourier transformation (FFT):

$$U_k(\omega_m) = \frac{1}{n_{fft}} \sum_{i=1}^{n_{fft}} u_k(t_i) \mathrm{e}^{\mathrm{j}\omega_m t_i} \quad \text{and} \quad Y_l(\omega_m) = \frac{1}{n_{fft}} \sum_{i=1}^{n_{fft}} y_l(t_i) \mathrm{e}^{\mathrm{j}\omega_m t_i} \tag{2.60}$$

With the power spectra

$$S_{uu}(\omega) = \frac{1}{n_{avg}} \sum_{i=1}^{n_{avg}} U_i^*(\omega) U_i(\omega) \quad \text{and} \quad S_{yy}(\omega) = \frac{1}{n_{avg}} \sum_{i=1}^{n_{avg}} Y_i^*(\omega) Y_i(\omega) \tag{2.61}$$

and the cross power spectral densities

$$S_{uy}(\omega) = \frac{1}{n_{avg}} \sum_{i=1}^{n_{avg}} U_i^*(\omega) Y_i(\omega) \quad \text{and} \quad S_{yu}(\omega) = \frac{1}{n_{avg}} \sum_{i=1}^{n_{avg}} Y_i^*(\omega) U_i(\omega) \tag{2.62}$$

which are averaged over $n_{avg} = 32$ tests, the frequency response from input chan-

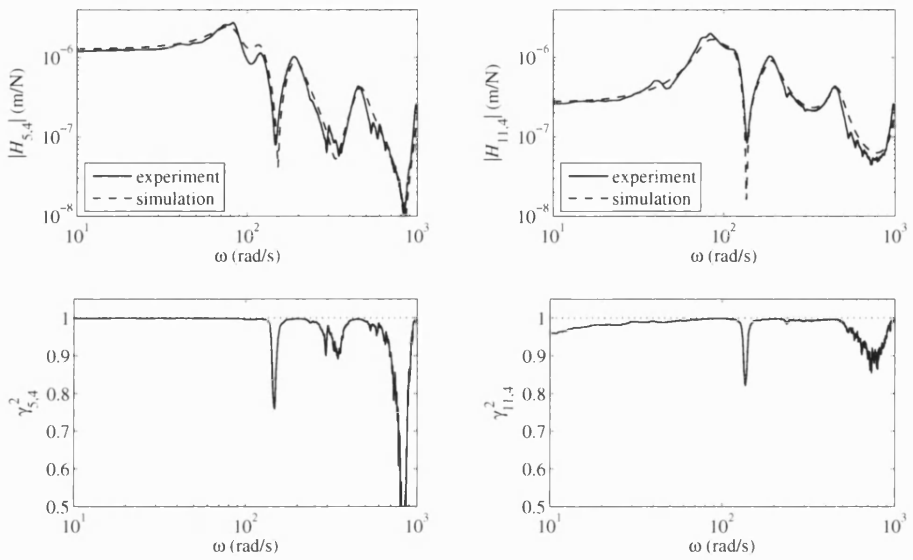

Figure 2.15: Measured frequency response and coherence from forces in z-direction at node 4 to displacements at nodes 5 and 11 with $k_{MB} = 1\,\mathrm{MN/m}$ and $d_{MB} = 3500\,\mathrm{Ns/m}$.

nel u to output channel y can be estimated as [44], [45]

$$H(\omega) = \frac{1}{2}\left(\frac{S_{uy}(\omega)}{S_{uu}(\omega)} + \frac{S_{yu}(\omega)}{S_{yy}(\omega)}\right) \tag{2.63}$$

The coherence

$$\gamma^2(\omega) = \frac{S_{yu}(\omega)S_{uy}(\omega)}{S_{yy}(\omega)S_{uu}(\omega)}, \qquad 0 \leq \gamma^2 \leq 1 \tag{2.64}$$

is a measure for the quality of the estimation. The closer the value is to 1, the smaller is the uncertainty in the estimated frequency response. It generally deteriorates in anti-resonance zones where the output values are small, and at high frequencies due to the influence of noise.

Figure 2.15 shows the estimated frequency response of the rotor system from forces applied by the driven end magnetic bearing (node 4) to displacements at the inner sensors (nodes 5 and 11), together with the coherence. A coherence close to unity in the first four resonance zones shows that the quality of the measurement is acceptable. The very close match between the measured and the theoretical values could be achieved by tuning the parameters of the FEM model slightly and

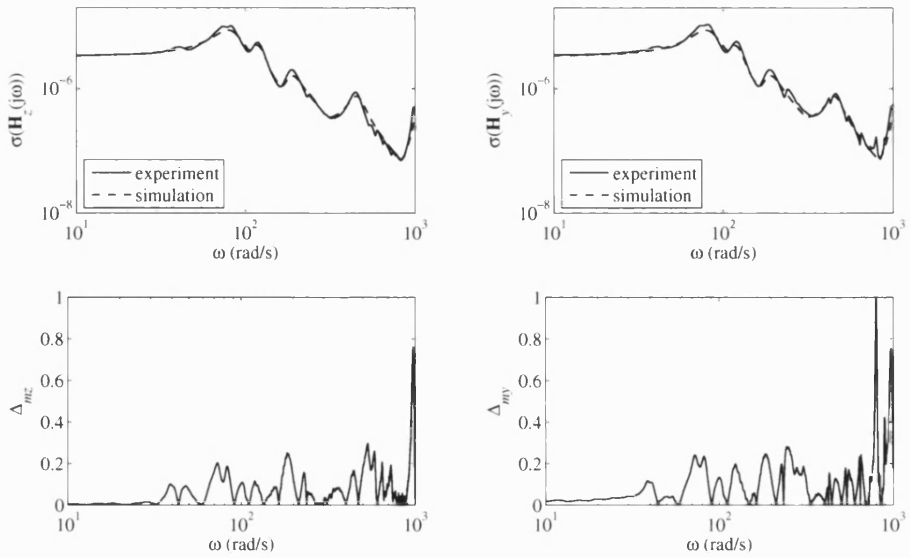

Figure 2.16: Measured largest singular values of the frequency response matrix from magnetic bearing forces to displacements at sensor nodes in z- and y-directions with $k_{MB} = 1\,\mathrm{MN/m}$ and $d_{MB} = 3500\,\mathrm{Ns/m}$.

implementing the magnetic bearing with a low-pass characteristic as described by (2.13) with $\omega_{cut} = 3000\,\mathrm{rad/s}$. If the low-pass characteristic is neglected, the simulation model underestimates the amplitudes in the resonance zones.

Figure 2.16 shows the largest singular values of the measured and the calculated frequency response matrix from forces at the magnetic bearing to displacements at the sensor nodes in z- and y-directions together with the multiplicative error

$$\Delta_m = \left| \frac{\overline{\sigma}_{meas}}{\overline{\sigma}_{calc}} - 1 \right| \tag{2.65}$$

which is an important measurement in robust control design. In the frequency range $[0, \Omega_{max}]$ of interest, the maximum multiplicative error is smaller than 30%.

2.5 Closure

This chapter presented an approach to derive a mathematical model of rotor/-magnetic bearing systems. It was shown that the basic FEM framework can easily be extended to incorporate internal friction effects, non-linear magnetic

bearing characteristics, and dynamics of sensors, amplifiers, etc, if high accuracy is required. A model for the flexible rotor test rig was derived. It was compared with an experimental system and an estimate for the model error was given.

3 Robust Control of Rotor/AMB Systems

Decentralised single-input-single-output PD feedback is the most commonly used control strategy for commercial rotor/magnetic bearing systems. It can be implemented very easily, is reliable, and provides reasonable stability and performance for most applications. It does not, however, exploit the whole potential of magnetic bearing technology. There may also be high gain stability problems, which are usually overcome by using notch filters.

As outlined in Section 2.2.3, a PD-controlled bearing behaves like a linear spring-damper system with stiffness and damping as tunable parameters. Modern multi-variable control methods offer undoubtly more possibilities to improve the system performance. Not only do they provide a direct means to assess stability and robustness of the closed loop, they also allow the formulation of various control objectives in one unified framework. Such objectives may be the minimisation of displacements at other points than the magnetic bearings, the limitation of actuator forces, robustness against parameter variations, and attenuation of external disturbance forces and noise, to name only a few.

This chapter focuses on H_∞ control. This is a very powerful feedback design method especially suitable for multi-objective control of MIMO systems. After some theoretical aspects are presented, the mixed sensitivity problem is discussed as a practical application. This standard formulation is then modified to represent the physical structure of rotor/magnetic bearing systems in an improved manner. Conventional linear time invariant (LTI) H_∞ controllers may lead to instability when the rotational speed varies. To overcome his problem, a linear matrix inequality (LMI) approach is presented, which allows the designer to implement gain scheduled robust H_∞ controllers. They consider the measured rotational speed as a system parameter, and guarantee stability over the whole operating range. The performance and stability of the derived robust time-invariant and gain-scheduled controllers for flexible rotor/magnetic bearing systems is examined and compared to PD control in simulations and experiments.

3.1 Modern Control Strategies

A control engineer can choose between a vast number of well-developed MIMO design techniques these days. Popular ones include pole placement, Nyquist--like techniques, linear quadratic Gaussian methods (LQG) with or without loop transfer recovery (LTR), and the more recent H_2 and H_∞ optimisation methods.

The most straightforward method is pole placement, where the designer can place the poles of the closed loop system anywhere in the complex plane provided that the plant is controllable. By moving poles, the influences on time response characteristics such as rise time, settling time, and transient oscillations are achieved. Although it is sometimes possible to meet design objectives with pole placement, the tuning of system performance usually involves a tedious trial-and-error process as the optimal pole positions are not known beforehand. The achieved stability margins and robustness of the closed loop are generally poor for the same reason. Model error may also lead to instability if the loop gain is too high.

"Nyquist-like" techniques [46] are basically an extension of classical SISO design methods to multi-variable systems. As with pole-placement, stability and robustness are not addressed directly, but must be examined after the controller is synthesised. These difficulties are overcome by optimal LQG/LTR feedback design methods, which take process disturbances and measurement noise into account, and also allow to trade off regulation performance and control effort.

A modern approach to MIMO control design is to describe closed loop performance objectives by the "size" of closed loop transfer function matrices. The size can be assessed by various operator norms, which provide a measure of how large the output signals can get for certain classes of input signals. Minimisation of the norms over the set of all stabilising controllers is the basis for recent H_2 and H_∞ optimal robust control theories.

3.2 H_∞ Control in a Nutshell

A complete derivation of H_∞ control theory is beyond the scope of this thesis. Only several aspects directly related to the following practical applications are shown here. A good introduction, which covers more detail, can be found in [46].

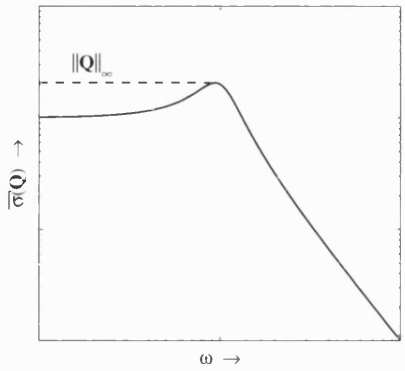

Figure 3.1: Reading off $\|\mathbf{Q}\|_\infty$ from a plot of largest principal gain.

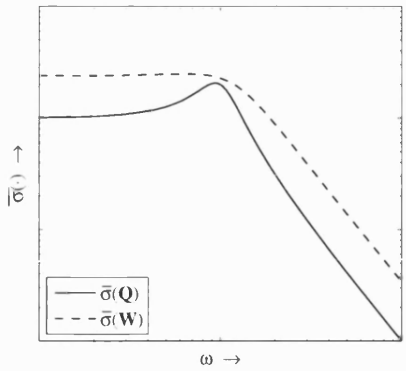

Figure 3.2: Fulfilled constraint $\overline{\sigma}(\mathbf{Q}(\mathrm{j}\omega)) \leq \overline{\sigma}(\mathbf{W}(\mathrm{j}\omega))$.

3.2.1 The Use of Operator Norms to Specify Performance

H_∞ control theory builds upon a measure of the maximum gain of a linear dynamic system. Such a measure is given by the *infinity norm*

$$\|\mathbf{Q}\|_\infty = \sup_\omega \overline{\sigma}\left(\mathbf{Q}(\mathrm{j}\omega)\right) \tag{3.1}$$

which is simply the least upper bound of the largest singular value of the transfer function matrix $\mathbf{Q}$ over all frequencies ω, as shown in Figure 3.1.

With the H_∞ norm, design objectives can be formulated as inequalities

$$\|\mathbf{Q}\|_\infty \leq \gamma \tag{3.2}$$

or optimisation problems such as

$$\text{minimise} \|\mathbf{Q}\|_\infty \tag{3.3}$$

where $\mathbf{Q}$ is some closed loop system.

Just constraining the peak gain of a plain closed loop transfer function is mostly not particularly useful, however. The true potential of the $\|\cdot\|_\infty$ formulation is exploited by augmenting closed loop transfer functions of interest with appropriate weighting functions. For example, the constraint $\overline{\sigma}(\mathbf{Q}(\mathrm{j}\omega)) \leq \overline{\sigma}(\mathbf{W}(\mathrm{j}\omega))$, which is

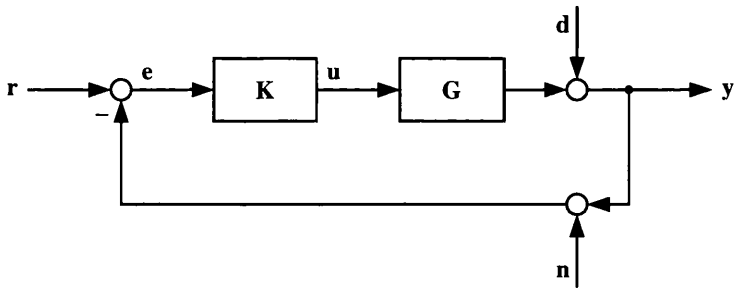

Figure 3.3: Classical feedback configuration.

illustrated in Figure 3.2, can be specified by

$$\frac{\overline{\sigma}(\mathbf{Q}(\mathrm{j}\omega))}{\overline{\sigma}(\mathbf{W}(\mathrm{j}\omega))} \leq \|\mathbf{W}^{-1}\mathbf{Q}\|_\infty \leq \|\mathbf{W}^{-1}\|_\infty \|\mathbf{Q}\|_\infty = \|\mathbf{W}\|_\infty^{-1} \|\mathbf{Q}\|_\infty \leq 1 \tag{3.4}$$

3.2.2 Feedback Loop Representation

Controller design usually involves the creation of a block diagram, which visualises the interconnection of systems (plant, controller, filter, etc.), and external in- and outputs. A classical formulation is shown in Figure 3.3. The blocks $\mathbf{G}$ and $\mathbf{K}$ are the plant and the controller. The inputs $\mathbf{r}$, $\mathbf{d}$, and $\mathbf{n}$ represent the reference input, plant output disturbance, and measurement noise. The remaining signals are the error $\mathbf{e}$, and the plant in- and outputs $\mathbf{u}$, and $\mathbf{y}$.

Various closed loop transfer functions in this system are of interest for robust controller design as shown later. Of particular importance are the *output and input sensitivity functions*

$$\mathbf{S}_o = (\mathbf{I} + \mathbf{GK})^{-1} \quad \text{and} \quad \mathbf{S}_i = (\mathbf{I} + \mathbf{KG})^{-1} \tag{3.5}$$

and the *output and input complementary sensitivity functions*[1]

$$\mathbf{T}_o = \mathbf{GK}\,(\mathbf{I} + \mathbf{GK})^{-1} \quad \text{and} \quad \mathbf{T}_i = \mathbf{KG}\,(\mathbf{I} + \mathbf{KG})^{-1} \tag{3.6}$$

The output sensitivity functions can also be interpreted as the following closed loop transfer functions:

$$\mathbf{y} = \mathbf{S}_o\mathbf{d} \qquad \mathbf{e} = \mathbf{S}_o\mathbf{r} \qquad \mathbf{y} = \mathbf{T}_o\mathbf{r} \tag{3.7}$$

[1]Sometimes $\mathbf{T}_o(s)$ is also referred to as *closed loop transfer function*

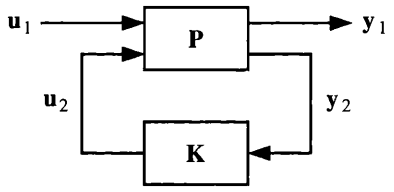

Figure 3.4: Feedback configuration for robust controller design.

Another block diagram representation, which is popular for robust controller design is shown in Figure 3.4. Here, $\mathbf{K}$ stands for the controller and $\mathbf{P}$ is the plant which is usually augmented with weighting functions.

The plant $\mathbf{P}$ can be partitioned as

$$\mathbf{P} = \begin{bmatrix} \mathbf{P}_{11} & \mathbf{P}_{12} \\ \mathbf{P}_{21} & \mathbf{P}_{22} \end{bmatrix} \tag{3.8}$$

so that

$$\mathbf{y}_1 = \mathbf{P}_{11}\mathbf{u}_1 + \mathbf{P}_{12}\mathbf{u}_2 \quad \text{and} \quad \mathbf{y}_2 = \mathbf{P}_{21}\mathbf{u}_1 + \mathbf{P}_{22}\mathbf{u}_2 \tag{3.9}$$

After eliminating $\mathbf{u}_2$ and $\mathbf{y}_2$ using $\mathbf{u}_2 = \mathbf{K}\mathbf{y}_2$ one obtains

$$\mathbf{y}_1 = \left(\mathbf{P}_{11} + \mathbf{P}_{12}\mathbf{K}(\mathbf{I} - \mathbf{P}_{22}\mathbf{K})^{-1}\mathbf{P}_{21}\right)\mathbf{u}_1 := \mathrm{F}_l(\mathbf{P}, \mathbf{K})\mathbf{u}_1 \tag{3.10}$$

where $\mathrm{F}_l(\mathbf{P}, \mathbf{K})$ is called the *lower linear fractional transformation* of $\mathbf{P}$ and $\mathbf{K}$. If the controller is drawn above $\mathbf{P}$ one needs the *upper linear fractional transformation* defined as

$$\mathbf{y}_2 = \left(\mathbf{P}_{22} + \mathbf{P}_{21}\mathbf{K}(\mathbf{I} - \mathbf{P}_{11}\mathbf{K})^{-1}\mathbf{P}_{12}\right)\mathbf{u}_2 := \mathrm{F}_u(\mathbf{P}, \mathbf{K})\mathbf{u}_2 \tag{3.11}$$

3.2.3 Representation of Uncertainty

The motivation for robust feedback design is the inherent uncertainty in the mathematical models of real plants. In classical control theory, rather crude stability margins are used to deal with this problem.

However, in robust control design, explicit uncertainty models are formulated. The most popular ones are

$$\mathbf{P}(s) = \mathbf{P}_0(s) + \mathbf{\Delta}_a(s) \tag{3.12a}$$

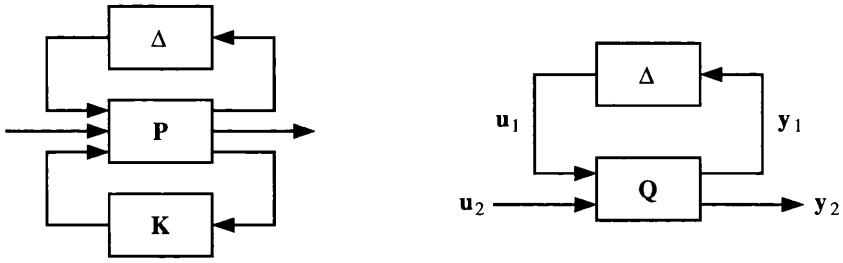

Figure 3.5: Block diagram representations of structured uncertainty. In the right diagram, the plant **P** and the compensator **K** are combined to a single system **Q**.

$$\mathbf{P}(s) = \mathbf{P}_0(s)(\mathbf{I} + \mathbf{\Delta}_i(s)) \tag{3.12b}$$

$$\mathbf{P}(s) = (\mathbf{I} + \mathbf{\Delta}_o(s))\mathbf{P}_0(s) \tag{3.12c}$$

where $\mathbf{\Delta}_a$ represents an additive perturbation, $\mathbf{\Delta}_i$ an input- and $\mathbf{\Delta}_o$ an output multiplicative perturbation, respectively. The perturbations are constrained by their size, usually measured by $\overline{\sigma}(\mathbf{\Delta}(\mathrm{j}\omega))$. By introducing scaling transfer matrices $\mathbf{W}_1(s)$ and $\mathbf{W}_2(s)$, which characterise the spatial and frequency structure of an uncertainty $\mathbf{\Delta}$:

$$\mathbf{\Delta}(s) = \mathbf{W}_1(s)\widetilde{\mathbf{\Delta}}(s)\mathbf{W}_2(s) \tag{3.13}$$

it is always possible to take

$$\|\widetilde{\mathbf{\Delta}}\|_\infty \leq 1 \tag{3.14}$$

which will be convenient for stability and robustness analysis.

Sometimes detailed information about the plant uncertainty structure are available, e.g. disturbances might only act on a subset of plant inputs or outputs, or some plant parameters can be identified much better than others. In these cases it is likely that the models in (3.12) are too conservative for satisfactory robust feedback design. The solution is to use a *structured* uncertainty model whose block diagram representation is shown in Figure 3.5.

Whenever there is uncertainty in a part of the plant or the controller it is represented locally by one of the models (3.12). All n of those local $\mathbf{\Delta}$ blocks can then be "pulled out" and put into a block-diagonal transfer function matrix

$$\mathbf{\Delta}(s) = \mathrm{diag}\,(\mathbf{\Delta}_1(s), \mathbf{\Delta}_2(s), \ldots, \mathbf{\Delta}_n(s)) \tag{3.15}$$

which is connected to a set of plant inputs and outputs by means of an upper linear fractional transformation. As before, weighting functions can be introduced to quantify frequency dependence and to normalise $\|\widetilde{\mathbf{\Delta}}\|_\infty$.

3.2.4 Small Gain Theorem

Arguably the most important application of the H_∞ norm is the *small gain theorem*. It states that if $\mathbf{Q}$ and $\mathbf{\Delta}$ are stable, robust internal stability of the right system in Figure 3.5 is guaranteed for

$$\text{a)} \quad \|\mathbf{\Delta}\|_\infty \leq 1/\gamma \quad \text{if and only if} \quad \|\mathbf{T}_{y_1,u_1}\|_\infty < \gamma \tag{3.16a}$$

$$\text{b)} \quad \|\mathbf{\Delta}\|_\infty < 1/\gamma \quad \text{if and only if} \quad \|\mathbf{T}_{y_1,u_1}\|_\infty \leq \gamma \tag{3.16b}$$

where, in line with the current convention in literature, $\mathbf{T}_{y_1,u_1}$ denotes the closed loop transfer function from $\mathbf{u}_1$ to $\mathbf{y}_1$ and should not be confused with the complementary sensitivity function.

Robust stability conditions for various assumptions of unstructured plant uncertainty can be derived from (3.16). For structured uncertainty, a less conservative formulation can be used. The basic concepts are the same, but stability conditions will involve the *structured singular value*, a matrix function denoted by $\mu(\cdot)$. A good introduction to μ-synthesis and analysis is given in [47].

3.2.5 The Mixed Sensitivity Problem

A popular approach to H_∞ control design is the so-called *mixed sensitivity* formulation. The two main objectives are good disturbance rejection and robustness against errors in the plant model. They can be directly accessed by constraining the output sensitivity and complementary sensitivity function of the closed loop plant:

For good disturbance rejection, the transfer function between $\mathbf{d}$ and $\mathbf{y}$, $\mathbf{S}_o$, should be as small as possible. By choosing a suitable weight $\mathbf{W}_1(s)$, the designer can put a constraint on $\mathbf{S}_o$ as

$$\overline{\sigma}(\mathbf{S}_o(\mathrm{j}\omega)) \leq \overline{\sigma}(\mathbf{W}_1^{-1}(\mathrm{j}\omega)) \tag{3.17}$$

If all plant uncertainties are expressed by the output multiplicative model (3.12c)[2],

[2]Similar derivations exist for the other models in (3.12)

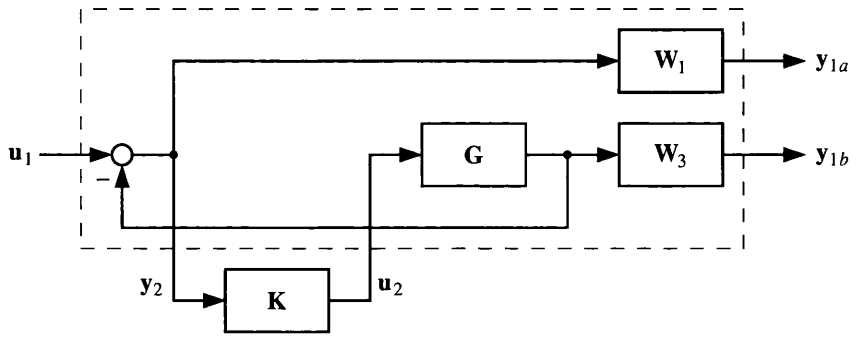

Figure 3.6: Block diagram of mixed sensitivity problem.

it follows from the small gain theorem that robust stability of the closed loop plant is guaranteed if

$$\overline{\sigma}(\mathbf{\Delta}_o(\mathrm{j}\omega)) < \frac{1}{\overline{\sigma}(\mathbf{T}_o(\mathrm{j}\omega))} \tag{3.18}$$

Hence, a robustly stable system can be obtained by choosing a weighting function $\mathbf{W}_3(s)$ so that

$$\overline{\sigma}(\mathbf{\Delta}_o(\mathrm{j}\omega)) < \overline{\sigma}(\mathbf{W}_3(\mathrm{j}\omega)) \tag{3.19}$$

and constraining the complementary sensitivity function by

$$\overline{\sigma}(\mathbf{T}_o(\mathrm{j}\omega)) \leq \overline{\sigma}(\mathbf{W}_3^{-1}(\mathrm{j}\omega)) \tag{3.20}$$

Using equation (3.7), the constraints can be visualised by the block diagram in Figure 3.6. This diagram can be transferred into a representation as in Figure 3.4 by combining the part within the dashed lines to a single partitioned augmented plant

$$\mathbf{P} = \begin{bmatrix} \mathbf{P}_{11} & \mathbf{P}_{12} \\ \mathbf{P}_{21} & \mathbf{P}_{22} \end{bmatrix} = \left[\begin{array}{c|c} \mathbf{W}_1 & -\mathbf{W}_1\mathbf{G} \\ \mathbf{0} & \mathbf{W}_3\mathbf{G} \\ \hline \mathbf{I} & -\mathbf{G} \end{array}\right] \tag{3.21}$$

It follows from (3.10) that

$$\mathbf{y}_1 = \mathrm{F}_l(\mathbf{P}, \mathbf{K})\mathbf{u}_1 = \begin{bmatrix} \mathbf{W}_1\mathbf{S}_o \\ \mathbf{W}_3\mathbf{T}_o \end{bmatrix} \mathbf{u}_1 \tag{3.22}$$

Therefore, the constraints (3.17) and (3.20) can be written as

$$\|\mathrm{F}_l(\mathbf{P},\mathbf{K})\|_\infty \leq 1 \tag{3.23}$$

which is an expression that can be solved for $\mathbf{K}$ [9].

It should be noted that $\mathbf{K}$ is generally of at least the same order as $\mathbf{P}$. To keep the complexity of the controller low, the plant should be reduced if possible, and the order of the weighting functions kept small. After $\mathbf{K}$ is derived, it might be necessary to apply further model reduction techniques to the controller in order to increase the computational performance.

It is tempting to make $\mathbf{W}_1$ and $\mathbf{W}_3$ large to achieve good disturbance rejection and robustness over the whole frequency range. This, however, is not possible as it follows from $\mathbf{S}_o + \mathbf{T}_o = \mathbf{I}$ that

$$1 \leq \overline{\sigma}(\mathbf{W}_1^{-1}(\mathrm{j}\omega)) + \overline{\sigma}(\mathbf{W}_3^{-1}(\mathrm{j}\omega)) \tag{3.24}$$

The common approach is therefore to shape $\mathbf{W}_3$ first so that (3.19) holds. Then, $\mathbf{W}_1$ is made as large as allowed by (3.24) in frequency regions where good disturbance rejection and performance is required.

3.3 Application of H_∞ Control to the Rotor

The previous section gave an overview about some H_∞ control concepts, and showed how the theory can be applied in practice using the mixed sensitivity formulation. H_∞ methods are utilised to design controllers for the rotor/magnetic bearing test rig.

3.3.1 Feedback Loop Formulation

Common objectives when designing a controller for a rotor/magnetic bearing system are the minimisation of displacements or the minimisation of actuator forces in the presence of disturbances. Furthermore, robustness against plant uncertainty and measurement noise should be achieved. Although the mixed sensitivity strategy outlined in Section 3.2.5 could be followed, it is not ideal as it assumes disturbances at the plant output instead of the input, nor does it provide measures to specify measurement noise and it is not suitable to constrain actuator action.

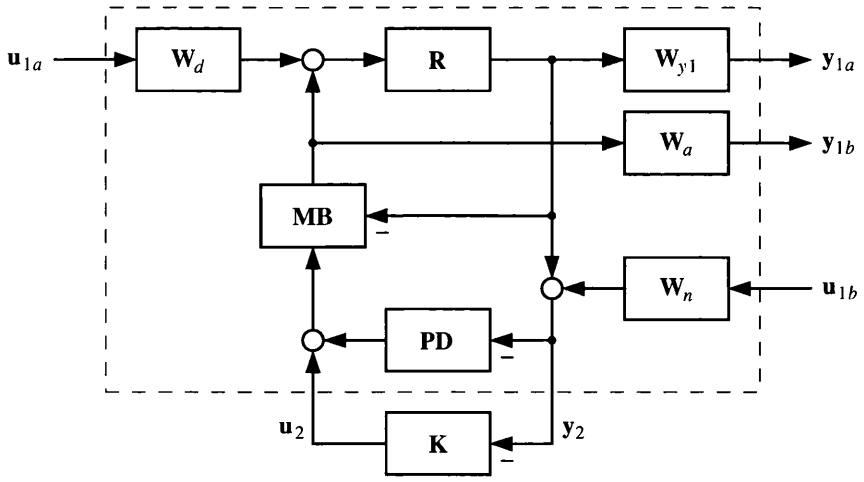

Figure 3.7: Block diagram of augmented plant with PD controller.

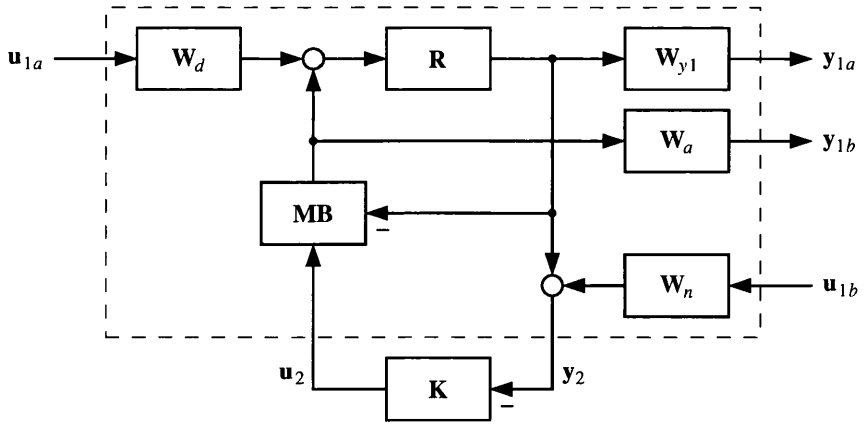

Figure 3.8: Block diagram of augmented plant without PD controller.

Two better formulations, which closely resemble the physical system and allow all desired robustness and performance objectives to be defined are shown in Figures 3.7 and 3.8. In both block diagrams, **K** represents the controller, and **R** the rotor with nodal forces as input and nodal displacements at the sensor locations as output. For controller design and simulation, **R** is reduced to the first 5 modes shown in Figure 2.11. **MB** represents the linear magnetic bearing model (2.10), which can be augmented with a low-pass filter as shown in (2.13). The size and frequency content of disturbance forces acting at the input of the plant, and measurement noise acting on the output are expressed by the weighting function matrices $\mathbf{W}_d$ and $\mathbf{W}_n$. Rotor displacements and actuator effort are penalised by $\mathbf{W}_{y_1}$ and $\mathbf{W}_a$, respectively.

The difference between the two block diagrams in Figures 3.7 and 3.8 is the PD controller, which is omitted in the second formulation. The main reason to permanently include a PD controller in the feedback loop is that it stabilises the augmented plant prior to H_∞ design. Although most H_∞ algorithms can deal with unstable plants, virtually all achieve better results if the plant is sufficiently damped. This is obvious as the H_∞ norm is extremely sensitive to "spikes" in the frequency response. Lightly damped poles have to be cancelled in order to make the norm small and achieve good performance. If the plant dynamics are uncertain, however, the exact position of the poles is unknown and any attempts to cancel poles will almost certainly reduce robustness. Furthermore it is advisable to keep the bearing stiffness low. Otherwise the H_∞ controller has to work against the PD controller, which might reduce robustness due to measurement noise and uncertainties in the PD frequency response.

The main reasons for a design without a PD controller is the clearer layout of the block diagram and the lower order of the augmented plant. It also facilitates stability and robustness analysis as no parallel connection between two controllers with different inputs[3] has to be formed. For simplicity, this model will be considered in the main for the rest of the chapter.

3.3.2 Choice of Weight Functions

The most important step apart from the design of the augmented plant is the choice of weighting functions. They determine the properties of the closed loop

[3] **K** considers all eight sensor outputs while **PD** uses the four displacements signals at the magnetic bearings only.

system. The closer the augmented plant resembles the physical system, the easier is it generally to assign suitable values. In the current system, $\mathbf{W}_d$ and $\mathbf{W}_n$ have a physical meaning: they represent the power spectra of disturbance forces and measurement noise. They can be found by actually measuring these parameters on the real system. If such data is unavailable, realistic assumptions must be made.

The output weights $\mathbf{W}_{y_1}$ and $\mathbf{W}_a$ are used to achieve stability and performance requirements. Their ratio determines the trade-off between small rotor displacements and small actuator forces in the presence of disturbances.

In practice, care must be taken to limit the high frequency gain, hence the noise amplification, of $\mathbf{K}$. This is achieved by increasing the high frequency gain of the dominant input and output weights. A suitable transfer function template for this task is

$$\mathbf{W}(s) = \mathbf{P}\mathbf{w}\frac{(s+a)}{(s+ab)}, \qquad a \in \mathbb{C}, b > 1 \tag{3.25}$$

so that $\lim_{\omega\to 0}|\mathbf{W}_n(\mathrm{j}\omega)| = \lim_{\omega\to\infty}|\mathbf{W}_n(\mathrm{j}\omega)|/b$. Here, $\mathbf{P}$ is a Bool position matrix and $\mathbf{w}$ is a diagonal static scaling matrix.

The interpretation of $\mathbf{W}_d$ and $\mathbf{W}_n$ as measures for physical disturbances and noise, and $\mathbf{W}_{y_1}$ and $\mathbf{W}_a$ as constraints on nominal performance is straightforward. It is less obvious, however, how robust stability constraints can be specified in the current formulation. This will be now be shown.

If $\mathbf{G}$ is defined as

$$\mathbf{G} = \mathrm{F}_l(\mathbf{R}, -\mathbf{MB}) \tag{3.26}$$

and the plant exhibits a multiplicative output uncertainty

$$\mathbf{G} = (\mathbf{I} + \mathbf{W}_1\widetilde{\mathbf{\Delta}}_o\mathbf{W}_2)\mathbf{G}_0, \qquad \|\widetilde{\mathbf{\Delta}}_o\|_\infty \leq 1 \tag{3.27}$$

the small gain theorem states that the closed loop system is stable if and only if

$$\|\mathbf{W}_2\mathbf{T}_o\mathbf{W}_1\|_\infty < 1 \tag{3.28}$$

How can this be guaranteed? Close inspection of the block diagram of Figure 3.8 reveals that the closed loop transfer function from $\mathbf{u}_{1b}$ to $\mathbf{y}_{1a}$ is given by

$$\mathbf{T}_{y_{1a},u_{1b}} = \mathbf{W}_{y_1}\mathbf{GK}\left(\mathbf{I} + \mathbf{GK}\right)^{-1}\mathbf{W}_n = \mathbf{W}_{y_1}\mathbf{T}_o\mathbf{W}_n \tag{3.29}$$

Hence, if two weights $\mathbf{W}_{y_1}$ and $\mathbf{W}_n$ are specified that fulfil the performance objectives and

$$\overline{\sigma}(\mathbf{W}_1\widetilde{\mathbf{\Delta}}_o\mathbf{W}_2) \leq \overline{\sigma}(\mathbf{W}_{y_1}\widetilde{\mathbf{\Delta}}_o\mathbf{W}_n) \tag{3.30}$$

robust stability and nominal performance is guaranteed if a controller can be found that leads to

$$\|\mathbf{T}_{y_1,u_1}\|_\infty \leq \gamma, \qquad \gamma < 1 \tag{3.31}$$

If the plant multiplicative uncertainty is assumed to be at the input of $\mathbf{R}$, analogous closed loop stability studies can be performed, which lead to the requirement

$$\overline{\sigma}(\mathbf{W}_1\widetilde{\mathbf{\Delta}}_i\mathbf{W}_2) \leq \overline{\sigma}(\mathbf{W}_a\widetilde{\mathbf{\Delta}}_i\mathbf{W}_d) \tag{3.32}$$

instead of (3.30).

3.3.3 Controller Synthesis

Two different weight function configurations for each of the augmented plants in Figures 3.7 and 3.8 were used to compute H_∞ optimised controllers with the Matlab `hinfsyn` function [48]. This implements a two-Riccati formula algorithm with standard γ-iteration.

The aim of the first design is to derive a hard controller, which minimises the maximum rotor displacements due to unbalance forces and base motion. In the second design, a soft controller is derived, which minimises actuator forces and reduces the sensitivity to sensor noise.

A performance measure for the hard controller is the H_∞ norm of the transfer function from nodal disturbance forces to displacements at the sensor locations $\mathbf{H}$. To make it small, the product $\overline{\sigma}(\mathbf{W}_{y1})\overline{\sigma}(\mathbf{W}_d)$ should be large. If output multiplicative plant uncertainty (3.27) is assumed, $\mathbf{W}_n$ must be chosen so that the condition (3.30) is met. The gain of $\mathbf{W}_a$ must be small for low frequencies to achieve good performance. At high frequencies, however, the gain should increase to limit noise amplification. After several iterations, the input weights were set to static gains

$$\mathbf{W}_d = 120\,\mathbf{P}_d \quad \text{and} \quad \mathbf{W}_n = 3 \cdot 10^{-4}\,\mathbf{P}_n \tag{3.33a}$$

and the output weights were chosen to be diagonal first order transfer functions

$$\mathbf{W}_{y1} = 1000\,\frac{\frac{s}{2\pi 50}+1}{\frac{s}{2\pi 1000}+1}\,\mathbf{I} \quad \text{and} \quad \mathbf{W}_a = 6\cdot 10^{-5}\,\frac{\frac{s}{2\pi 50}+1}{\frac{s}{2\pi 1000}+1}\,\mathbf{I} \tag{3.33b}$$

Robust stability is guaranteed if a controller with $\gamma < 1$ can be computed, because the product of $\mathbf{W}_{y1}$ and $\mathbf{W}_n$ provide an upper bound for the output multiplicative error of the plant model (c.f. Figure 2.16 and equation (3.30)).

A soft controller reduces the transfer function from disturbance forces or measured displacements to actuator forces. As the plant uncertainty is unchanged, $\mathbf{W}_{y1}$ and $\mathbf{W}_n$ were not altered. $\mathbf{W}_d$ was reduced to relax the constraints on $\mathbf{H}$. The DC gain of $\mathbf{W}_a$ was increased, and the poles and zeros were shifted towards lower frequencies in order to penalise actuator action in the operating range of the rotor. A suitable set of weights for soft controller design is given by

$$\mathbf{W}_d = 80\,\mathbf{P}_d \quad \text{and} \quad \mathbf{W}_n = 3\cdot 10^{-4}\,\mathbf{P}_n \tag{3.34a}$$

and

$$\mathbf{W}_{y1} = 1000\,\frac{\frac{s}{2\pi 50}+1}{\frac{s}{2\pi 1000}+1}\,\mathbf{I} \quad \text{and} \quad \mathbf{W}_a = 1.8\cdot 10^{-4}\,\frac{\frac{s}{2\pi 12}+1}{\frac{s}{2\pi 250}+1}\,\mathbf{I} \tag{3.34b}$$

A major problem with controller design for magnetic bearing/rotor systems is the change of system parameters with the rotation speed due to gyroscopic effects. Even for relatively slow speed machinery, eigenfrequencies can change significantly as illustrated in Figure 2.13. Stability in the whole operating range is therefore not guaranteed with controllers designed at $\Omega = 0$. If a plant is operated at only a few nominal rotational speeds, an option is to take a plant model at these speeds for the derivation of the controller and switch between them as required. If the rotation speed is continuously variable, however, more complex gain-scheduling techniques should be applied. Here, the first approach is followed and the "adaptive" controllers derived for each rotational speed $\Omega = \omega$ are compared to a nominal controller derived at $\Omega = 0$.

3.3.4 Stability and Performance Analysis

H_∞ controllers were derived with the two augmented plants shown in Figures 3.7 and 3.8. The results were almost identical so that only those for pure H_∞ control

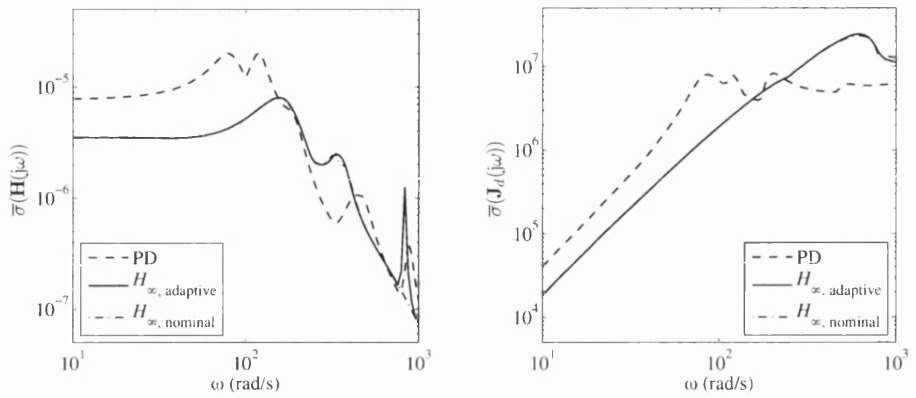

Figure 3.9: Largest singular value plots for closed loop transfer functions $\mathbf{H}$ and $\mathbf{J}_d$ with a hard controller.

are presented. The PD controller used as a reference leads to a magnetic bearing stiffness and damping of $k_{MB} = 1\,\mathrm{MN/m}$ and $d_{MB} = 3500\,\mathrm{NS/m}$, respectively. These values were found to be a good compromise between stiffness, closed loop stability, damping and noise rejection.

As mentioned before, the main objective of a hard control design is the minimisation of the maximum displacements in the presence of synchronous unbalance forces in the operating range. A measure for this characteristic is the largest singular value plot of $\mathbf{H}$. The smaller $\overline{\sigma}(\mathbf{H}(\mathrm{j}\omega))|_\Omega$ the smaller are the displacement due to disturbance forces. Equivalently, a soft controller should minimise the largest singular values of the transfer function $\mathbf{J}_d$, which relates actuator forces to rotor displacements and/or sensor noise.

Figure 3.9 shows the singular value plots of $\mathbf{H}$ and $\mathbf{J}_d$ for the closed loop system with a hard H_∞ controller. As expected, the H_∞ norm of $\mathbf{H}$ is greatly reduced, whereas $\|\mathbf{J}_d\|_\infty$ is increased. From $150 - 400\,\mathrm{rad/s}$, $\overline{\sigma}(\mathbf{H}(\mathrm{j}\omega))$ is actually larger with H_∞ control than with PD action due to an eigenmode in that frequency range. Such local performance deterioration compared to other designs is hard to avoid with H_∞ synthesis unless very complex (hence not practicable) weights are used. It is noted that the actuator forces are decreased at low frequencies.

The singular value plots in Figure 3.10 for the plant with a soft controller reveal that the displacement amplitudes due to disturbance forces are generally increased compared to the hard design. The actuator forces due to rotor displacement are smaller than for the PD controlled system except in the frequency range

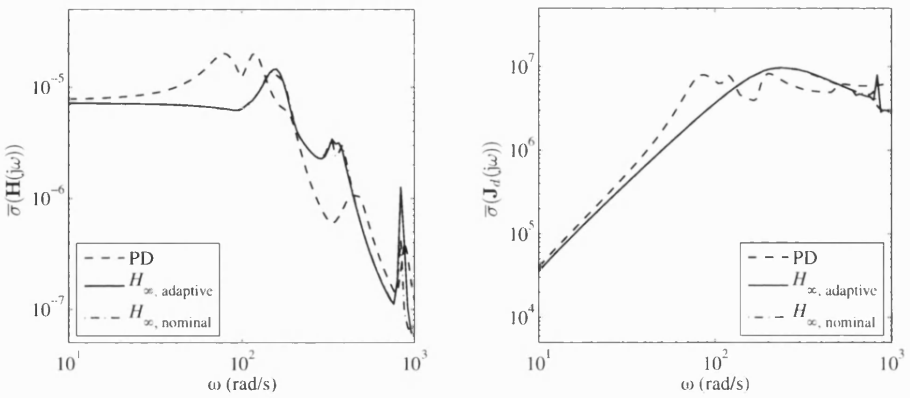

Figure 3.10: Largest singular value plots for closed loop transfer functions $\mathbf{H}$ and $\mathbf{J}_d$ with a soft controller.

150−400 rad/s. $\|\mathbf{J}_d\|_\infty$ is smaller than that for the hard H_∞ system, and $\overline{\sigma}(\mathbf{J}_d(j\omega))$ is reduced at high frequencies, which implies better noise rejection.

Good robustness against multiplicative plant uncertainty is achieved if $\|\mathbf{T}_o(j\omega)\|_\infty$ is small as stated in (3.28). Figure 3.11 shows that both the hard and the soft controllers reduce the output complementary sensitivity function significantly, which implies better stability margins for H_∞ controlled plants compared to their PD controlled counterparts.

Robust stability of the closed loop system was checked by using the Matlab `loopmargin` function [48]. It calculates the multi-loop output disk margin, which is the largest region for simultaneous, independent variations in the individual output channels of a loop transfer function $\mathbf{Q}$ such that for all gain and phase variations inside that region the closed loop is stable. The multi-loop output disk margin is a non-conservative robustness measure derived from the structured singular value of the balanced output sensitivity function $\mu(\mathbf{S}_o + \mathbf{T}_o)$. Figure 3.12 shows the results for the hard and soft controllers. The most important observations are that the loop with the nominal H_∞ controller designed at $\Omega = 0$ is not stable over the whole operating range, and that the hard adaptive controller has far better stability margins than the soft one. Both are superior to the simple PD controller over the whole frequency range.

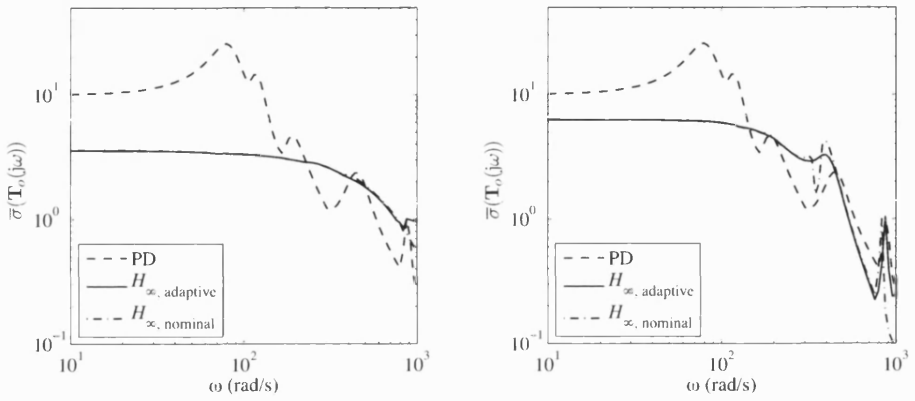

Figure 3.11: Output complementary sensitivity functions for closed loops with hard (left) and soft (right) controller.

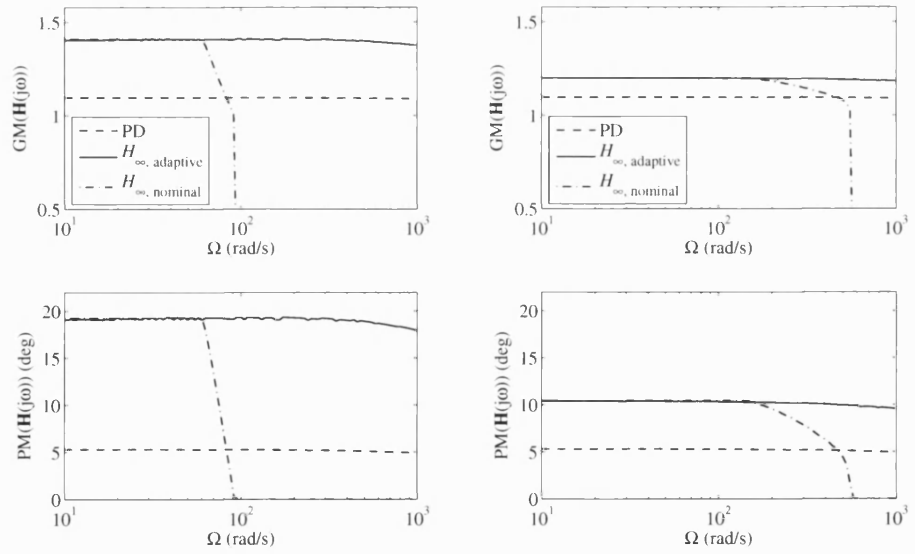

Figure 3.12: Gain and phase margins for the closed loop plants with hard (left) and soft (right) controller.

3.4 Experimental Results for Robust Control

The hard and soft H_∞ controllers were implemented on the flexible rotor test rig described in Section 2.1 in order to compare their performance with conventional PD control experimentally. The continuous controller state-space equations used in the previous section were discretised with the zero-order hold method for a sampling frequency of 8192 Hz. It is possible to run the full order controller with 32 to 40 states[4] on the available dSPACE hardware in real time. However, it was found out that controllers can be reduced to 24 to 28 states with Hankel singular value reduction methods without loss of performance.

H_∞ controllers derived with the augmented plants in Figures 3.7 and 3.8 were tested, and no significant differences could be observed. The measurements presented in the next sections were all performed with the plain H_∞ controller (no underlying PD control).

3.4.1 Impulse Response

In the first experiment, the transient displacement response of the stationary rotor due to an impulsive force input (400 N for 0.015 s) applied by the non-driven end magnetic bearing was measured. The results are a good indicator for the disturbance rejection performance of the system. The displacements at the non-driven end magnetic and auxiliary bearing are compared for PD and hard/soft H_∞ control in Figure 3.13 and 3.14.

The left plots show the superior performance of the hard H_∞ controller. The maximum displacement amplitude is 15–20% smaller than with PD control and the settling time is reduced by a factor of four. The disturbance rejection properties of the soft H_∞ controller are comparable with PD control. The maximum rotor displacement at the magnetic bearing, which applies the force, is slightly larger due to the "softness" of the system. The settling time is approximately the same. However, the response at the auxiliary bearing node is slightly superior to the PD controlled system, because the H_∞ controller takes the displacements at the rotor ends into account whereas the PD controller only uses the displacement at the magnetic bearings.

[4]The order of the controller depends on the choice of the augmented plant (with or without PD) and on the number of modes in the reduced FE model of the rotor.

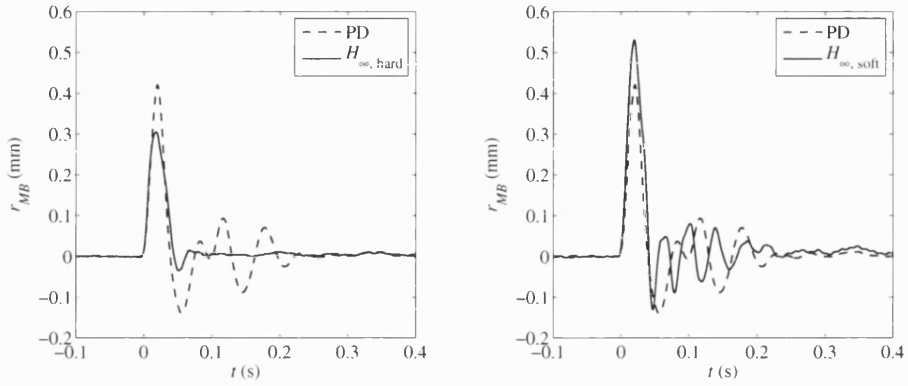

Figure 3.13: Measured displacement response due to an impulse force input at the non-driven end magnetic bearing.

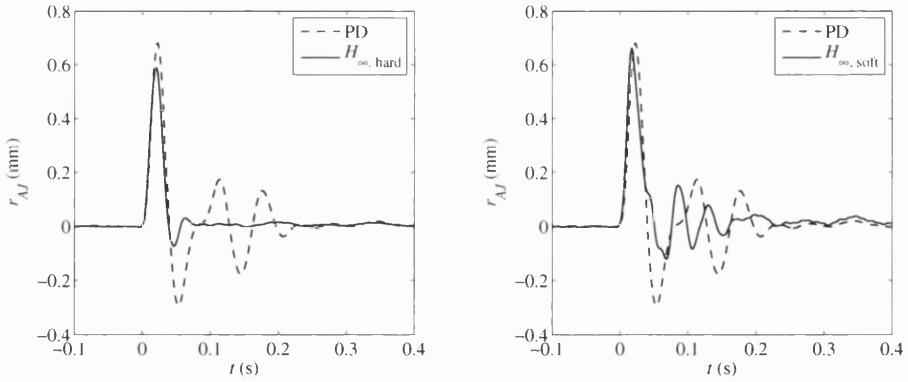

Figure 3.14: Measured displacement response at the non-driven end auxiliary bearing node due to an impulse force applied by the adjacent magnetic bearing.

3.4.2 Mass Loss Test

After performing impulse response tests with a stationary rotor, it was examined how the controllers perform at a non-zero rotational speed. Mass loss experiments at $\Omega = 125\,\text{rad/s}$ and $\Omega = 151\,\text{rad/s}$ were undertaken. An unbalance of $200\,\text{g cm}$ was attached to the non-driven end disk. It was reduced by a smaller mass tied on the opposite circumferential point of the same disk using a Kevlar chord, which could be cut by a solenoid controlled blade. The performance of hard and soft H_∞ controllers was assessed by comparing the displacement response at the non-driven end magnetic and auxiliary bearings with the PD controlled system.

It was expected that the H_∞ controllers would perform significantly better than the PD controller at the lower rotational speed due to the smaller singular values of the system at that frequency (c.f. Figures 3.9 and 3.10). At $\omega = 151\,\text{rad/s}$, $\overline{\sigma}(\mathbf{H}(\mathrm{j}\omega))$ is roughly the same for all three controllers, which means that the steady state responses should be similar.

The results shown in Figure 3.15 verify these predictions. At $\Omega = 125\,\text{rad/s}$, the displacements with PD control are indeed much larger than with H_∞ control. Noticeable is that the steady state responses of the hard and soft H_∞ controllers have very similar magnitudes. However, the overshoot just after the mass loss at $t = 0.5\,\text{s}$ is larger with the soft controller, as predicted by the impulse response examined above.

It is this overshoot that makes the difference at $\Omega = 151\,\text{rad/s}$. Although the steady state amplitudes are similar for all three controllers, rotor-stator contact is most likely for the PD controlled system with an overshoot of roughly 25% compared to nearly 0% for the hard and less than 10% for the soft H_∞ controller. As shown in the following chapters, damaging persistent rotor-stator contact modes can become established after only one initial impact even if the contact-free orbit is significantly smaller than the clearance. Hence, overshoot after a transient force input should be an important performance measure for certain applications.

3.4.3 Run-Up Experiment

Vibration amplitudes reached during run-up or run-down are often the main problem in turbo machinery operation. This is true especially for large flexible rotors with small clearances such as in modern gas turbines. To test the quality of the derived controllers at various rotation speeds, slow run-ups from 2–30 Hz were

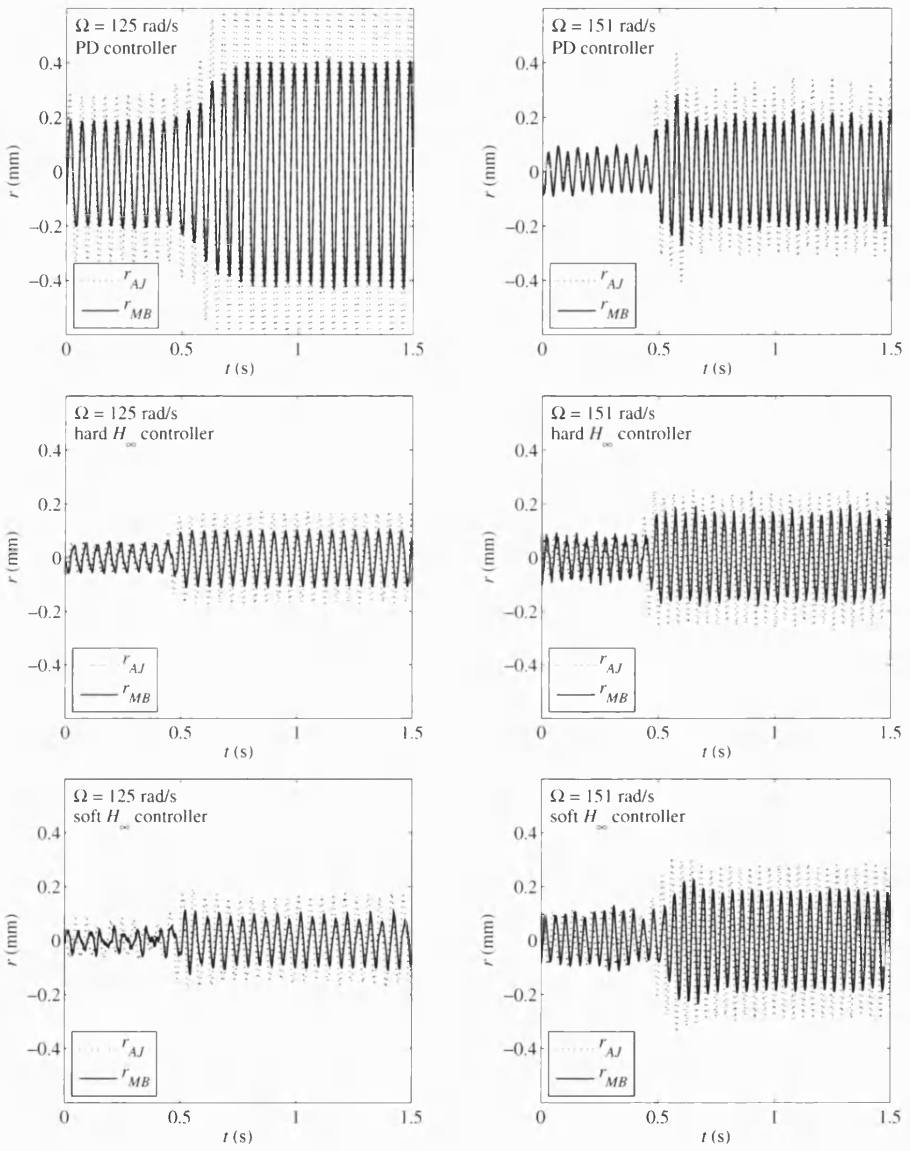

Figure 3.15: Measured mass loss displacement response with PD and hard/soft H_∞ controllers operating at $\Omega = 125\,\mathrm{rad/s}$ and $\Omega = 151\,\mathrm{rad/s}$.

performed. To get a significant amplitude, an unbalance of 200 g cm was added to the non-driven end disk. The response was measured at the non-driven end magnetic and auxiliary bearings.

The inherent problem of H_∞ LTI controllers is that they are guaranteed to be robustly stable for the design rotational speed only. Here, H_∞ controllers computed for $\Omega = 151$ rad/s were used, which proved to be stable at all rotational speeds reached during run-up.

The measured data presented in Figure 3.16 verifies the theoretical predictions in Figures 3.9 and 3.10. The PD controlled plant reaches the largest maximum displacements in the observed frequency range between 120 rad/s and 130 rad/s. The maximum displacement at the end auxiliary bearing is more than 2.5 times larger than that obtained with the hard H_∞ controller, which performs better at all speeds. Compared with PD, the soft H_∞ controller gives rise to larger displacements at speeds above 140 rad/s. However, the maximum displacement amplitude during run-up is a factor of two less.

It is noticeable that the H_∞ controllers are particularly good in keeping the displacements at the end auxiliary bearings small. That is because they use the information provided by the sensors at the rotor ends. The only way this could be achieved with PD control is to implement synchronous unbalance compensation at the expense of reduced stability and possibly larger displacements at the magnetic bearings and/or larger transmitted forces.

3.5 Gain-Scheduled H_∞ Control

As mentioned before, the plant dynamics of rotor/magnetic bearing systems change with the rotational speed due to gyroscopic effects. Therefore, H_∞ controllers designed at a single speed usually achieve robustness and good performance over a small speed range only. One way to solve this problem is to model the frequency varying part as plant uncertainty. Although this approach can be applied successfully to simple systems, it is likely to be too conservative for complex flexible rotors. Another possible solution is to switch between controllers designed for specific speeds, as outlined in Section 3.3.3. The major drawback of this method, however, is that generally stability cannot be guaranteed, as switching might excite higher order modes.

A more sophisticated way of dealing with this problem is to design gain-scheduled

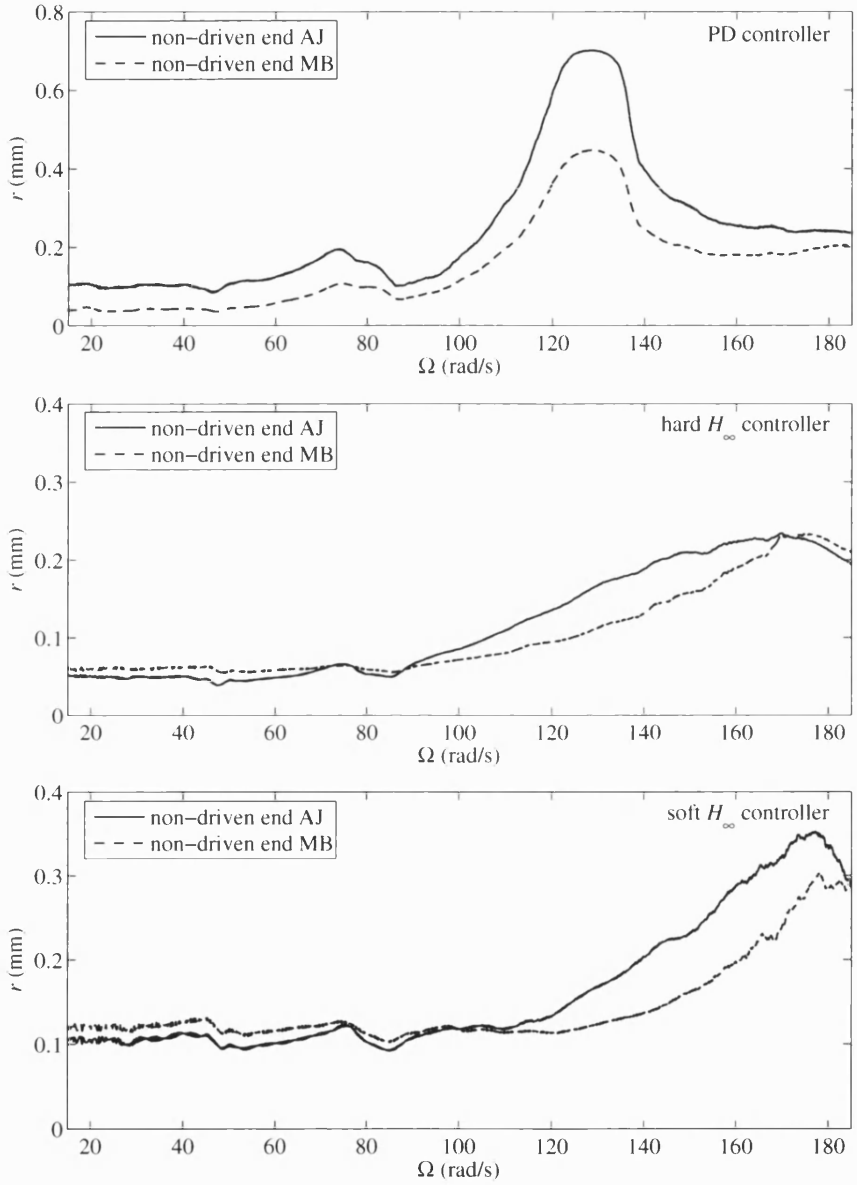

Figure 3.16: Measured vibration amplitudes at the non-driven end auxiliary and magnetic bearings during a run-up from 2–30 Hz with PD and H_∞ controllers.

H_∞ controllers, which use the real-time measurement of the rotation speed to optimise the performance and robustness of the closed loop system. The controller is computed at each rotation speed as an affine combination of two vertex systems. It adjusts to the variations in the plant dynamics in order to provide stability and good performance over the whole speed range.

3.5.1 Linear Parameter Varying Systems

In contrast to linear time-invariant (LTI) systems, the state-space matrices of linear parameter varying (LPV) plants are functions of a parameter vector $\boldsymbol{\theta}(t)$

$$\dot{\mathbf{x}}(t) = \mathbf{A}(\boldsymbol{\theta}(t))\mathbf{x}(t) + \mathbf{B}(\boldsymbol{\theta}(t))\mathbf{u}(t) \tag{3.35a}$$

$$\mathbf{y}(t) = \mathbf{C}(\boldsymbol{\theta}(t))\mathbf{x}(t) + \mathbf{D}(\boldsymbol{\theta}(t))\mathbf{u}(t) \tag{3.35b}$$

If $\boldsymbol{\theta}(t)$ is unknown, it must be considered as time-varying uncertainty. If it can be measured in real-time, however, it can be used to adapt the controller to the varying plant dynamics in order to improve robustness and performance.

3.5.2 LFT Formulation

The formulation in (3.35) is very general. For tractability reasons, certain restrictions are usually placed on how the plant depends on $\boldsymbol{\theta}(t)$. One way is to assume that $\mathbf{A}, \mathbf{B}, \mathbf{C}, \mathbf{D}$ are linear fractional functions of the varying parameter. The linear fractional transformation (LFT) be expressed by (c.f. equations (3.10) and (3.11))

$$\mathbf{y} = \mathrm{F}_l(\mathbf{P}, \boldsymbol{\Theta})\mathbf{u} \tag{3.36a}$$

with

$$\boldsymbol{\Theta} = \mathrm{diag}(\theta_1\mathbf{I}_1, \theta_2\mathbf{I}_2, \ldots, \theta_k\mathbf{I}_k) \tag{3.36b}$$

The corresponding block diagram is shown in Figure 3.17.

Consistent with the plant, the controller also has a LFT dependence on $\boldsymbol{\Theta}$, so that the overall closed loop transfer function from input $\mathbf{u}$ to output $\mathbf{y}$ is given by

$$\mathbf{T}_{y,u}(\mathbf{P}, \mathbf{K}, \boldsymbol{\Theta}) = \mathrm{F}_l(\mathrm{F}_u(\mathbf{P}, \boldsymbol{\Theta}), \mathrm{F}_l(\mathbf{K}, \boldsymbol{\Theta})) \tag{3.37}$$

The special interconnection structure of $\mathbf{P}$ and $\boldsymbol{\Theta}$ enables solution for a gain-scheduled controller $\mathbf{K}(\boldsymbol{\theta})$, which stabilises the plant and guarantees some closed

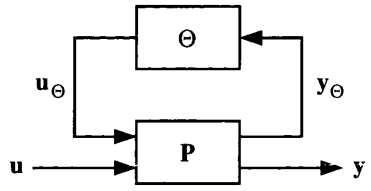

Figure 3.17: LFT representation of a parameter-varying plant.

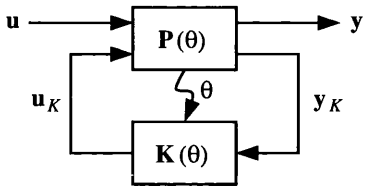

Figure 3.18: Feedback loop with gain-scheduled polytopic controller.

loop performance γ for all parameter variations. Apkarian's and Gahinet's paper [15] presents the detailed derivations and LMI-based algorithms for the continuous and discrete time case.

3.5.3 Affine Parameter Dependent Plants

Another way to find a gain-scheduled controller for a system (3.35) is to assume that the state-space matrices depend affinely on the time-varying measured parameter. $\boldsymbol{\theta}(t)$ is restricted to vary in a polytope $\boldsymbol{\Theta}$ of vertices $\boldsymbol{\theta}_1, \boldsymbol{\theta}_2, \ldots, \boldsymbol{\theta}_n$ as

$$\boldsymbol{\theta} \in \boldsymbol{\Theta} := \mathrm{Co}\{\boldsymbol{\theta}_1, \boldsymbol{\theta}_2, \ldots, \boldsymbol{\theta}_n\} \tag{3.38}$$

where

$$\mathrm{Co}\{\boldsymbol{\theta}_1, \boldsymbol{\theta}_2, \ldots, \boldsymbol{\theta}_n\} = \left\{ \sum_{i=1}^{n} \alpha_i \boldsymbol{\theta}_i : \alpha_i \geq 0, \sum_{i=1}^{n} \alpha_i = 1 \right\} \tag{3.39}$$

Then, the state-space matrices of the LPV plant range in a convex hull whose vertices are the images of the vertices of the parameter polytope $\boldsymbol{\Theta}$:

$$\begin{bmatrix} \mathbf{A}(\boldsymbol{\theta}) & \mathbf{B}(\boldsymbol{\theta}) \\ \mathbf{C}(\boldsymbol{\theta}) & \mathbf{D}(\boldsymbol{\theta}) \end{bmatrix} \in \mathrm{Co} \left\{ \begin{bmatrix} \mathbf{A}(\boldsymbol{\theta}_i) & \mathbf{B}(\boldsymbol{\theta}_i) \\ \mathbf{C}(\boldsymbol{\theta}_i) & \mathbf{D}(\boldsymbol{\theta}_i) \end{bmatrix}, i = 1, 2, \ldots, n \right\} \tag{3.40}$$

For these plants, Apkarian et al. [16] describe a LMI-based method to derive a gain-scheduled controller $\mathbf{K}(\boldsymbol{\theta})$. The strategy is to calculate LTI H_∞ controllers at the vertices $\boldsymbol{\theta}_i$ of the parameter polytope first. For a measured parameter vector $\boldsymbol{\theta} \in \boldsymbol{\Theta}$, $\mathbf{K}(\boldsymbol{\theta})$ can then be computed online as a convex combination of the vertex controllers:

$$\mathbf{K}(\boldsymbol{\theta}) = \sum_{i=1}^{n} \alpha_i \mathbf{K}_i = \sum_{i=1}^{n} \alpha_i \begin{bmatrix} \mathbf{A}_i^K & \mathbf{B}_i^K \\ \mathbf{C}_i^K & \mathbf{D}_i^K \end{bmatrix} \tag{3.41}$$

The reason why this approach leads to guaranteed stable gain-scheduled control, and naive interpolation between independent LTI controllers at the parameter vertices does not, is that a single Lyapunov function is used to establish asymptotic stability of all controllers over the whole parameter range $\boldsymbol{\Theta}$.

The state-space description of the plant in Figure 3.18 is

$$\begin{bmatrix} \dot{\mathbf{x}} \\ \mathbf{y} \\ \mathbf{y}_K \end{bmatrix} = \begin{bmatrix} \mathbf{A}(\boldsymbol{\theta}) & \mathbf{B}_1(\boldsymbol{\theta}) & \mathbf{B}_2(\boldsymbol{\theta}) \\ \mathbf{C}_1(\boldsymbol{\theta}) & \mathbf{D}_{11}(\boldsymbol{\theta}) & \mathbf{D}_{12}(\boldsymbol{\theta}) \\ \mathbf{C}_2(\boldsymbol{\theta}) & \mathbf{D}_{21}(\boldsymbol{\theta}) & \mathbf{D}_{22}(\boldsymbol{\theta}) \end{bmatrix} \begin{bmatrix} \mathbf{x} \\ \mathbf{u} \\ \mathbf{u}_K \end{bmatrix} \tag{3.42}$$

Certain assumptions on the plant must be made in order to be able to derive a gain-scheduled H_∞ controller:

- $\mathbf{D}_{22}(\boldsymbol{\theta}) = \mathbf{0}$
- $\mathbf{D}_{22}(\boldsymbol{\theta}), \mathbf{B}_2(\boldsymbol{\theta}), \mathbf{C}_2(\boldsymbol{\theta}), \mathbf{D}_{12}(\boldsymbol{\theta}), \mathbf{D}_{21}(\boldsymbol{\theta})$ are constant, i.e. parameter independent
- $(\mathbf{A}(\boldsymbol{\theta}), \mathbf{B}_2)$ and $(\mathbf{A}(\boldsymbol{\theta}), \mathbf{C}_2)$ are quadratically stabilisable and detectable over $\boldsymbol{\Theta}$, respectively[5]

Most models of real plants fulfil these conditions. If not, the model structure can usually be modified so that the assumptions are valid.

With the state-space description of the closed loop system

$$\begin{bmatrix} \dot{\mathbf{x}}^{cl} \\ \mathbf{y} \end{bmatrix} = \begin{bmatrix} \mathbf{A}^{cl} & \mathbf{B}^{cl} \\ \mathbf{C}^{cl} & \mathbf{D}^{cl} \end{bmatrix} \begin{bmatrix} \mathbf{x}^{cl} \\ \mathbf{u} \end{bmatrix} \tag{3.43}$$

where

$$\begin{bmatrix} \mathbf{A}^{cl} & \mathbf{B}^{cl} \\ \mathbf{C}^{cl} & \mathbf{D}^{cl} \end{bmatrix} = \begin{bmatrix} \mathbf{A}_0 + \overline{\mathbf{B}}\mathbf{K}\overline{\mathbf{C}} & \mathbf{B}_0 + \overline{\mathbf{B}}\mathbf{K}\overline{\mathbf{D}}_{21} \\ \mathbf{C}_0 + \overline{\mathbf{D}}_{21}\mathbf{K}\overline{\mathbf{C}} & \mathbf{D}_{11} + \overline{\mathbf{D}}_{12}\mathbf{K}\overline{\mathbf{D}}_{21} \end{bmatrix} \tag{3.44}$$

[5] A matrix function $\mathbf{A}(\boldsymbol{\theta})$ is called quadratically stable over $\boldsymbol{\Theta}$ if for some $\mathbf{P} = \mathbf{P}^T > 0$ and $\mathbf{Q} = \mathbf{Q}^T > 0$: $\mathbf{P}\mathbf{A}(\boldsymbol{\theta}) + \mathbf{A}(\boldsymbol{\theta})^T\mathbf{P} \leq -\mathbf{Q}$, $\forall \boldsymbol{\theta} \in \boldsymbol{\Theta}$. A pair of matrix functions $(\mathbf{A}(\boldsymbol{\theta}), \mathbf{B}(\boldsymbol{\theta}))$ is said to be quadratically stabilisable over $\boldsymbol{\Theta}$ if there exists a matrix $\mathbf{K}$ such that $\mathbf{A}(\boldsymbol{\theta}) + \mathbf{B}(\boldsymbol{\theta})\mathbf{K}$ is quadratically stable over $\boldsymbol{\Theta}$. $\mathbf{A}(\boldsymbol{\theta})$ and $\mathbf{C}(\boldsymbol{\theta})$ are said to be quadratically detectable over $\boldsymbol{\Theta}$ if there exists a matrix $\mathbf{L}$ such that $\mathbf{A}(\boldsymbol{\theta}) + \mathbf{L}\mathbf{B}(\boldsymbol{\theta})$ is quadratically stable over $\boldsymbol{\Theta}$.

and

$$\left[\begin{array}{ccc} \mathbf{A}_0 & \mathbf{B}_0 & \overline{\mathbf{B}} \\ \mathbf{C}_0 & \mathbf{D}_{11} & \overline{\mathbf{D}}_{12} \\ \overline{\mathbf{C}} & \overline{\mathbf{D}}_{21} & \mathbf{K} \end{array}\right] = \left[\begin{array}{cc|c|cc} \mathbf{A} & \mathbf{0} & \mathbf{B}_1 & \mathbf{0} & \mathbf{B}_2 \\ \mathbf{0} & \mathbf{0} & \mathbf{0} & \mathbf{I} & \mathbf{0} \\ \hline \mathbf{C}_1 & \mathbf{0} & \mathbf{D}_{11} & \mathbf{0} & \mathbf{D}_{12} \\ \hline \mathbf{0} & \mathbf{I} & \mathbf{0} & \mathbf{A}^K & \mathbf{B}^K \\ \mathbf{C}_2 & \mathbf{0} & \mathbf{D}_{12} & \mathbf{C}^K & \mathbf{D}^K \end{array}\right] \tag{3.45}$$

it can be shown [10] that the H_∞ suboptimal control problem is equivalent to the existence of a positive definite solution $\mathbf{X} > 0$ to the inequality

$$\left[\begin{array}{ccc} \mathbf{A}^{cl\,T}\mathbf{X} + \mathbf{X}\mathbf{A}^{cl} & \mathbf{X}\mathbf{B}^{cl} & \mathbf{C}^{cl\,T} \\ \mathbf{B}^{cl\,T}\mathbf{X} & -\gamma\mathbf{I} & \mathbf{D}^{cl\,T} \\ \mathbf{C}^{cl} & \mathbf{D}^{cl} & -\gamma\mathbf{I} \end{array}\right] < 0 \tag{3.46}$$

For LPV systems, this can be reformulated as the problem to find two symmetric matrices $\mathbf{R}, \mathbf{S} \in \mathbb{R}^{n^P \times n^K}$ satisfying the system of $2n + 1$ LMI's [16]:

$$\left[\begin{array}{cc} \mathcal{N}_R & \mathbf{0} \\ \mathbf{0} & \mathbf{I} \end{array}\right]^T \left[\begin{array}{ccc} \mathbf{A}_i\mathbf{R} + \mathbf{R}\mathbf{A}_i^T & \mathbf{R}\mathbf{C}_{1i}^T & \mathbf{B}_{1i} \\ \mathbf{C}_{1i}\mathbf{R} & -\gamma\mathbf{I} & \mathbf{D}_{11i} \\ \mathbf{B}_{1i}^T & \mathbf{D}_{11i}^T & -\gamma\mathbf{I} \end{array}\right] \left[\begin{array}{cc} \mathcal{N}_R & \mathbf{0} \\ \mathbf{0} & \mathbf{I} \end{array}\right] < 0 \tag{3.47a}$$

$$\left[\begin{array}{cc} \mathcal{N}_S & \mathbf{0} \\ \mathbf{0} & \mathbf{I} \end{array}\right]^T \left[\begin{array}{ccc} \mathbf{A}_i^T\mathbf{S} + \mathbf{S}\mathbf{A}_i & \mathbf{S}\mathbf{B}_{1i} & \mathbf{C}_{1i}^T \\ \mathbf{B}_{1i}^T\mathbf{S} & -\gamma\mathbf{I} & \mathbf{D}_{11i}^T \\ \mathbf{C}_{1i} & \mathbf{D}_{11i} & -\gamma\mathbf{I} \end{array}\right] \left[\begin{array}{cc} \mathcal{N}_S & \mathbf{0} \\ \mathbf{0} & \mathbf{I} \end{array}\right] < 0 \tag{3.47b}$$

$$\left[\begin{array}{cc} \mathbf{R} & \mathbf{I} \\ \mathbf{I} & \mathbf{S} \end{array}\right] \geq 0 \tag{3.47c}$$

where $i = 1, \ldots, n$, and $\mathcal{N}_R, \mathcal{N}_S$ denote orthonormal bases of the null spaces of $[\mathbf{B}_2^T \mathbf{D}_{12}^T]$ and $[\mathbf{C}_2 \mathbf{D}_{21}]$, respectively. Reduced order controllers with rank $n^K < n^P$ exist, if $\text{rank}(\mathbf{I} - \mathbf{RS}) = n^K \leq n^P$.

With two full column-rank matrices $\mathbf{M}, \mathbf{N} \in \mathbb{R}^{n^P \times n^K}$ chosen such that $\mathbf{M}\mathbf{N}^T = \mathbf{I} - \mathbf{RS}$, $\mathbf{X}$ can be computed as the unique solution of

$$\left[\begin{array}{cc} \mathbf{S} & \mathbf{I} \\ \mathbf{N}^T & \mathbf{0} \end{array}\right] = \mathbf{X} \left[\begin{array}{cc} \mathbf{I} & \mathbf{R} \\ \mathbf{0} & \mathbf{M}^T \end{array}\right] \tag{3.48}$$

The result is substituted into (3.46), which can then be solved for the controller state-space matrices. Global stability of the solution over the whole parameter

range Θ is established by the single Lyapunov function

$$V(\mathbf{x}) = \mathbf{x}^T \mathbf{X} \mathbf{x} \tag{3.49}$$

which fulfils the conditions

$$V(\mathbf{x}) > 0 \quad \forall \mathbf{x} \neq 0 \tag{3.50a}$$

$$\mathcal{H}V(\mathbf{x}) < 0 \quad \text{(negative definite)} \tag{3.50b}$$

where $\mathcal{H}V(\mathbf{x})$ denotes the Hessian[6] of $V(\mathbf{x})$. Furthermore, the gain in terms of the 2-norm between inputs and outputs is bounded by

$$\|\mathbf{y}\|_2 < \gamma \|\mathbf{u}\|_2 \tag{3.51}$$

3.6 Gain-Scheduled Control of the Rotor System

The LPV system description of the rotor depends on one parameter, namely, the rotational speed Ω. Hence, the two vertices of the parameter polytope are 0 and Ω_{max}. The vertex system matrices of an affine parameter dependent plant model can be derived in several ways where some are more advantageous than others.

3.6.1 Formulation of the LPV Plant and Controller Synthesis

A first attempt might be to substitute $\Omega = 0$ and $\Omega = \Omega_{max}$ into (2.56), reduce the order with (2.57), and take the resulting systems as vertices of the plant polytope. The drawback of this method is that all state-space matrices except $\mathbf{D}$ depend on Ω due to the modal transformation with $\mathbf{\Psi}_r$. In practice, this leads to computational problems with the currently available controller synthesis algorithms if the plant is reasonably complex.

A better way to calculate the vertex systems is to form a feedback connection between the modally reduced nominal plant $\mathbf{R}_0$ at $\Omega = 0$, and a parameter depen-

[6] The Hessian matrix is the square matrix of second partial derivatives of a scalar-valued function:

$$\mathcal{H}(V(x_1, x_2, \ldots, x_n)) = \begin{bmatrix} \frac{\partial^2 V}{\partial x_1^2} & \frac{\partial^2 V}{\partial x_1 \partial x_2} & \cdots & \frac{\partial^2 V}{\partial x_1 \partial x_n} \\ \frac{\partial^2 V}{\partial x_2 \partial x_1} & \frac{\partial^2 V}{\partial x_2^2} & \cdots & \frac{\partial^2 V}{\partial x_2 \partial x_n} \\ \vdots & \vdots & \ddots & \vdots \\ \frac{\partial^2 V}{\partial x_n \partial x_1} & \frac{\partial^2 V}{\partial x_n \partial x_2} & \cdots & \frac{\partial^2 V}{\partial x_n^2} \end{bmatrix}$$

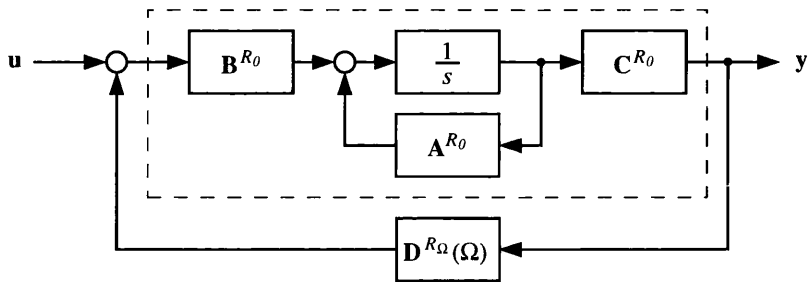

Figure 3.19: Feedback connection of nominal plant with parameter dependent system representing gyroscopic effects.

dent system representing the gyroscopic effects $\mathbf{R}_\Omega(\Omega)$ as shown in Figure 3.19. $\mathbf{R}_\Omega$ is a static gain system with $\mathbf{D}^{R_\Omega}$ as the only non-zero state-space matrix. With $\mathbf{D}^{R_0} = \mathbf{0}$, the state-space equations of the feedback connection are given by

$$\begin{bmatrix} \dot{\mathbf{x}} \\ \mathbf{y} \end{bmatrix} = \begin{bmatrix} \mathbf{A}^{R_0} + \mathbf{B}^{R_0}\mathbf{D}^{R_\Omega}(\Omega)\mathbf{C}^{R_0} & \mathbf{B}^{R_0} \\ \mathbf{C}^{R_0} & \mathbf{0} \end{bmatrix} \begin{bmatrix} \mathbf{x} \\ \mathbf{u} \end{bmatrix} \tag{3.52}$$

where only the system matrix $\mathbf{A}$ depends on Ω, as desired.

Once the LPV system is formed, the formulation of the augmented plant including the choice of the weighting functions proceeds in an analogous manner as in section 3.3 and shall not therefore be repeated here.

3.6.2 Stability and Performance Analysis

The same stability and performance calculations as in Section 3.3.4 were carried out with the gain-scheduled controller $\mathbf{K}(\boldsymbol{\theta})$. $\mathbf{K}(\boldsymbol{\theta})$ evaluated at $\boldsymbol{\theta} = 0$ shall be referred to as the "nominal" controller whereas "adaptive" means that $\boldsymbol{\theta} = \Omega$.

The performance measures $\mathbf{H}$ and $\mathbf{J}_d$ for the hard and the soft controller shown in Figures 3.20 and 3.21, respectively, are all worse compared to the results obtained with time-invariant H_∞ synthesis. This was expected because the controller must now deal with a parameter-varying plant instead of an LTI system. Not surprisingly, the stability margins of the gain-scheduled system are smaller than in the LTI case, indicated by a larger complementary sensitivity function and smaller gain and phase margins as shown in Figures 3.22 and 3.23, respectively.

Whether gain-scheduled control can be used or not depends on the performance and robustness requirements. If the rotational speed varies slowly, switching be-

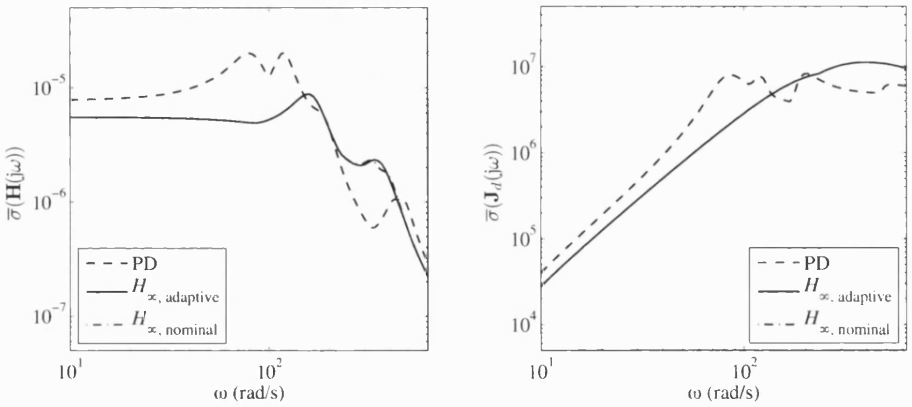

Figure 3.20: Largest singular value plots for closed loop transfer functions $\mathbf{H}$ and $\mathbf{J}_d$ with a gain-scheduled hard controller.

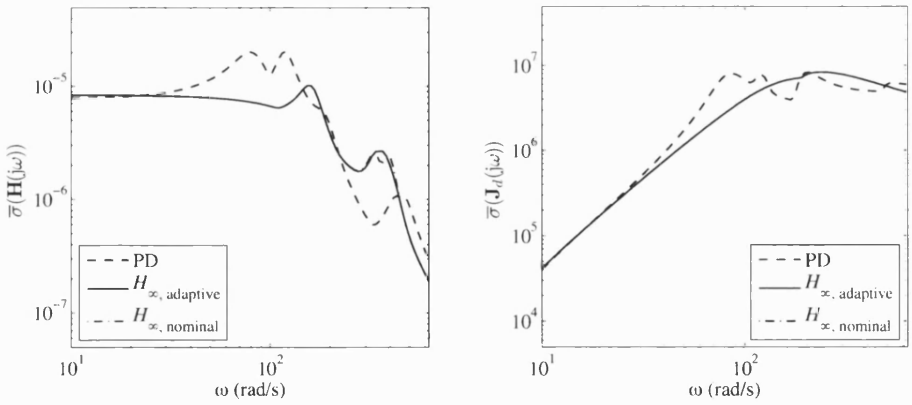

Figure 3.21: Largest singular value plots for closed loop transfer functions $\mathbf{H}$ and $\mathbf{J}_d$ with a gain-scheduled soft controller.

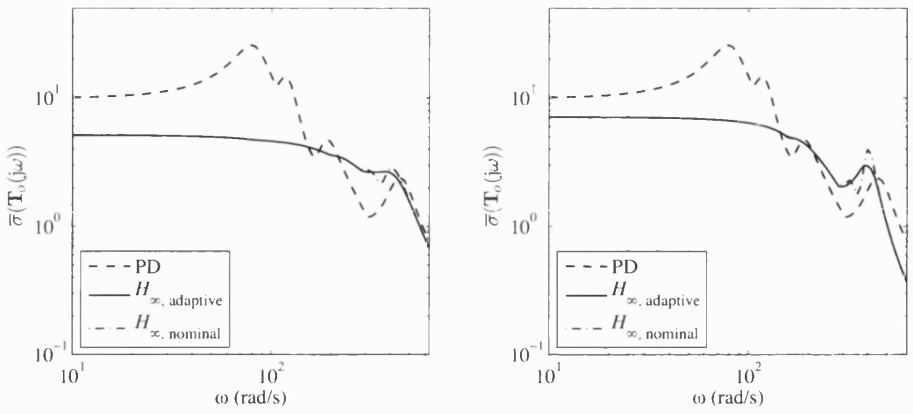

Figure 3.22: Output complementary sensitivity functions for closed loops with hard (left) and soft (right) controller.

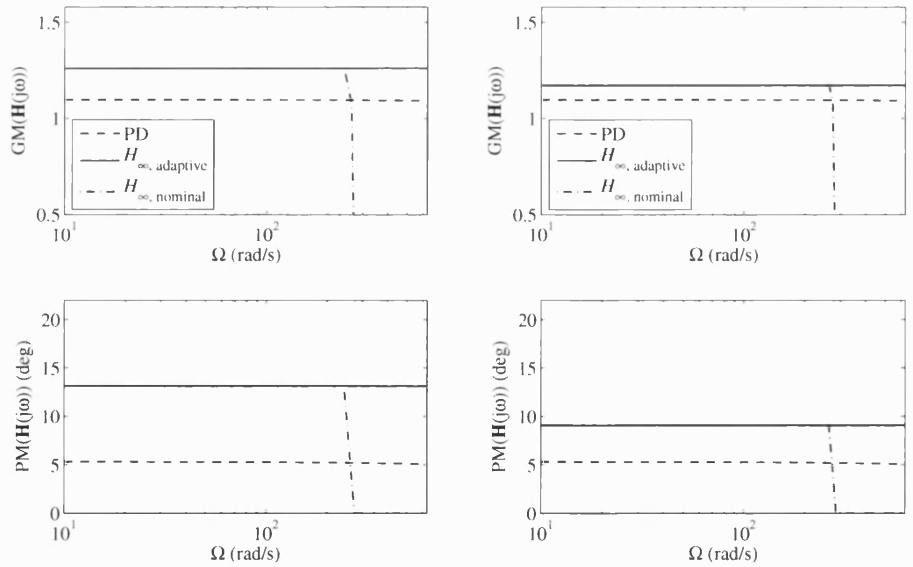

Figure 3.23: Gain and phase margins for the closed loop plants with hard (left) and soft (right) gain-scheduled controller.

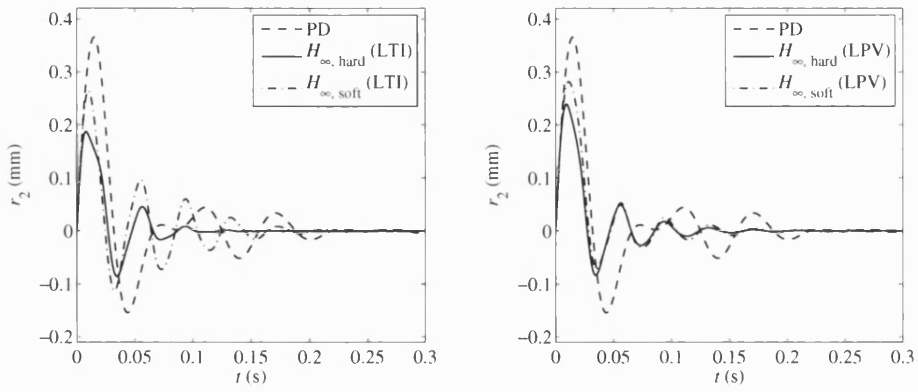

Figure 3.24: Transient displacement response to an impulse force input at node 2 with PD and LTI and LPV H_∞ controllers at $\Omega = 125\,\mathrm{rad/s}$.

tween LTI controller could be considered, although it does not guarantee stability. If the plant runs at a fixed operating speed, it might be advantageous to use (adaptive) PD control for acceleration and deceleration phases and switch on an appropriate H_∞ controller once the operating speed is reached.

3.6.3 Transient Response of LTI and LPV Controllers

Studies to compare the transient responses of PD and LTI/LPV H_∞ controlled plants have been carried out. An impulsive force $f_z(t) = \delta(t) \cdot 1000\,\mathrm{N}$ was applied at the non-driven end disk node of a linearised simulation model. The resulting displacement response was calculated at the same node.

For the first simulation, a LTI controller was derived for $\Omega = 151\,\mathrm{rad/s}$, which coincides with the rotation speed. At that speed, the transfer function matrix $\mathbf{H}$ of the closed loop system has similar largest singular values for each controller as shown in Figures 3.9, 3.10, 3.20, and 3.21. Figure 3.24 reveals that the PD controlled plant has the largest displacement amplitude and the longest settling time. The hard H_∞ controllers have the best performance. The time response characteristics of the LTI and LPV H_∞ controllers are similar.

In the second simulation, the LTI controller derived for $\Omega = 151\,\mathrm{rad/s}$ was used for a rotor with a speed of $\Omega = 314\,\mathrm{rad/s}$. The system became unstable although the initial response is almost identical. The gain-scheduled controller performs equally well at both speeds.

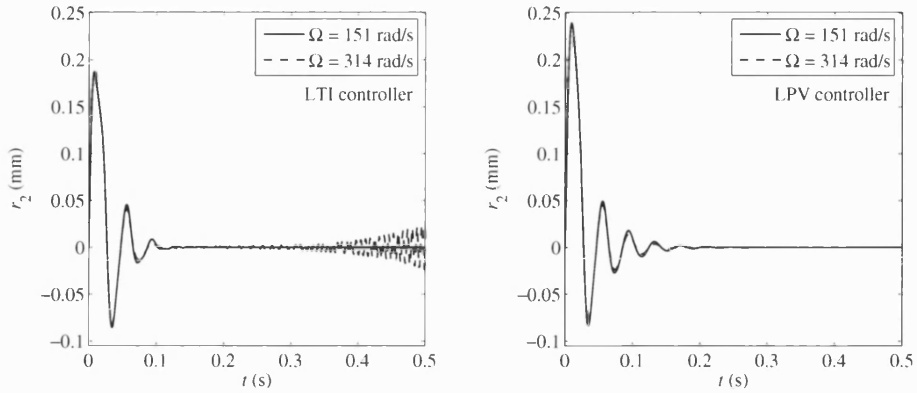

Figure 3.25: Comparison of transient responses of LTI and LPV controllers at $\Omega = 151\,\text{rad/s}$ (LTI design speed) and $\Omega = 314\,\text{rad/s}$.

3.7 Experimental Results of Gain-Scheduled Control

As with the LTI controllers in Section 3.4, some experiments have been performed with the LPV gain-scheduled H_∞ controllers to verify the theoretical predictions. Gain-scheduling with one parameter approximately doubles the computational complexity, so that the sampling frequency of the discrete controller was set to only 4 kHz due to hardware limitations. Non-reduced discretised state-space models of the continuous controllers presented above were used in the experiments, although 8 to 10 states could be removed with appropriate reduction techniques without loss of performance.

3.7.1 Impulse Response

The displacement response of the rotor at the two non-driven end sensors (at node 15) to an impulsive force (400 N pulse with a duration of 0.015 s) applied by the non-driven end magnetic bearing at $\Omega = 0\,\text{rad/s}$ is displayed in Figures 3.26 and 3.27.

Similar to the LTI case examined in Section 3.4.1, the hard LPV H_∞ controller provides superior disturbance rejection compared to the PD controller and the soft H_∞ controller. The maximum displacement of the soft H_∞ controlled system is larger than with PD control especially at the magnetic bearing where the force is applied. However, the settling time is always lower for the robust controllers.

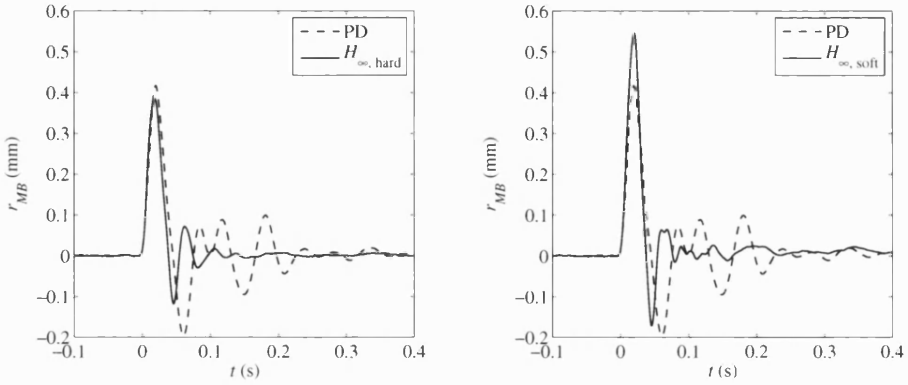

Figure 3.26: Measured displacement response to an impulse force input at the non-driven end magnetic bearing with gain-scheduled controller.

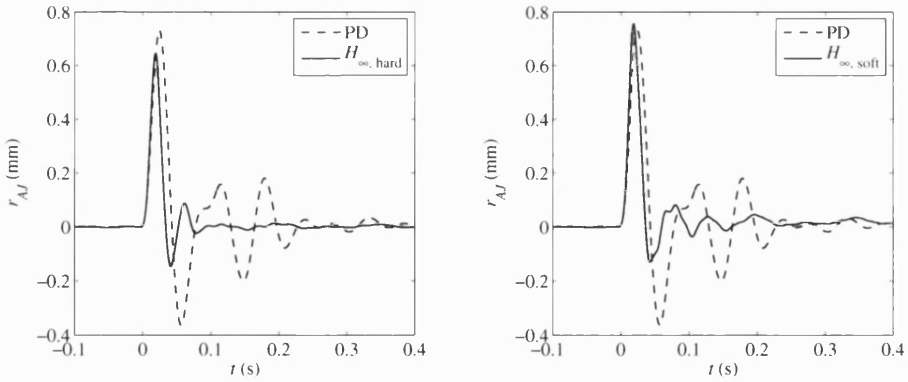

Figure 3.27: Measured displacement response at the non-driven end auxiliary bearing node to an impulse force applied by the adjacent magnetic bearing with gain-scheduled controller.

As predicted by the simulation results shown in Figure 3.24, the gain-scheduled controllers do not perform as well as their LTI counterparts, but the differences are small.

3.7.2 Run-Up Experiment

The unbalanced rotor was run up from 2–30 Hz under gain scheduled H_∞ control. The measured displacement response is compared to the one of a PD controlled system in Figure 3.28. In the observed speed range, there is only a small difference between the hard LPV and LTI controllers (c.f. Figure 3.16). Slightly surprising are the small amplitudes of the soft gain-scheduled controller, which are almost identical to those of the hard system.

Overall, the displacement responses of LTI and LPV controlled systems are similar. However, gain-scheduled control has the major advantage that stability is guaranteed in the whole operating range, whereas the stability region of LTI H_∞ controllers has to be tested experimentally. This can cause problems in practice, due to the potential damage from rotor-stator contact.

3.7.3 Instability due to Parameter Variations

The stability region of LTI controllers, and in particular the onset of instability due to the variation of the rotational speed was examined experimentally on the test rig. The major problem is that gyroscopic effects increase with the rotational speed, but instability should not be caused deliberately above a rotational frequency of 30 Hz to avoid possible damage. It was therefore decided to run the rotor below 30 Hz and vary the controller design frequency in an "equivalent" manner. The idea is based on the fact that the absolute rotational speed does not cause system instability, but the difference between the actual speed and the controller design speed is the important parameter.

In the experiments, the rotor was run at $\Omega = 151\,\text{rad/s}$ and $\Omega = 176\,\text{rad/s}$ with controllers designed for the corresponding *negative* speeds $\Omega = -151\,\text{rad/s}$ and $\Omega = -176\,\text{rad/s}$, respectively. This enables the gyroscopic influences on system stability to be exaggerated without the risk of damaging the test equipment. Figure 3.29 shows the measured orbit at the non-driven end magnetic bearing. The system is stable at $\Omega = 151\,\text{rad/s}$, but at $\Omega = 176\,\text{rad/s}$, the detuned controller starts to excite super-synchronous modes resulting in a severe distortion of the

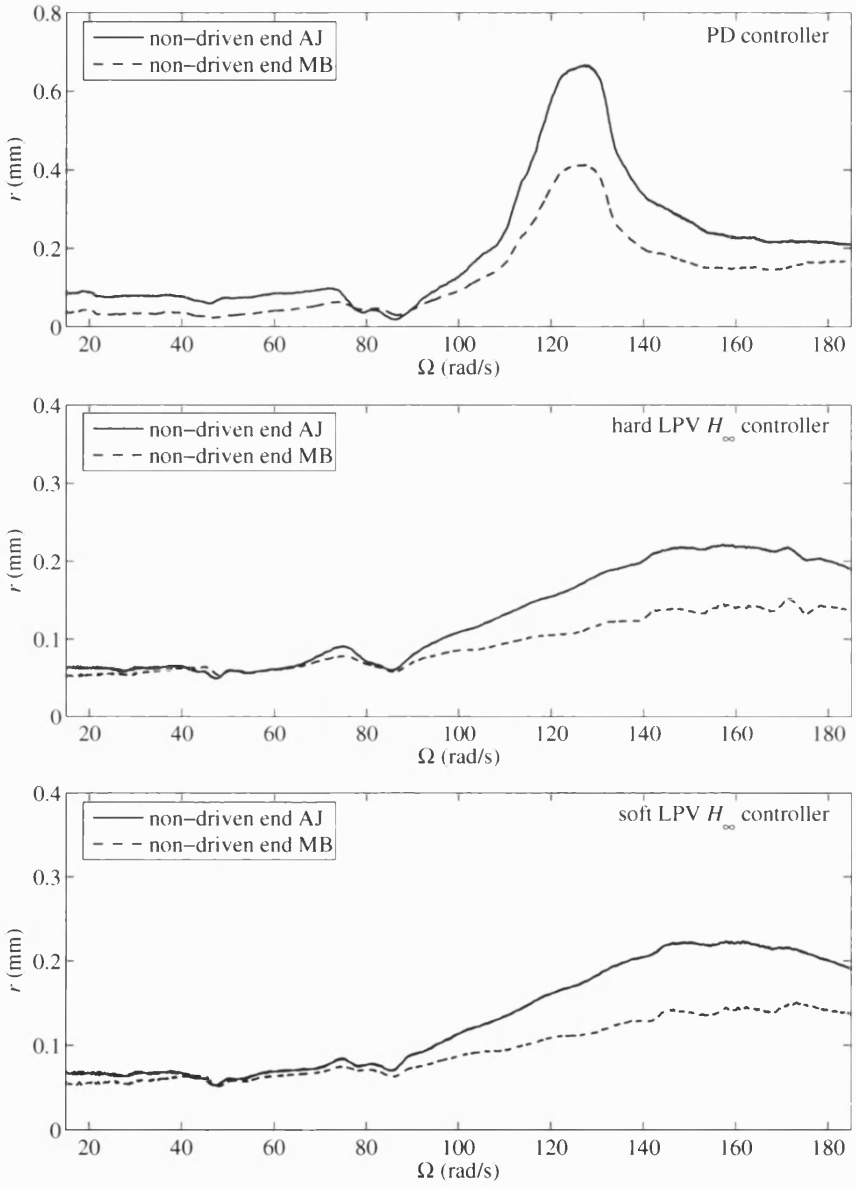

Figure 3.28: Measured vibration amplitudes at the non-driven end auxiliary and magnetic bearings during a run-up with PD and gain-scheduled H_∞ controllers.

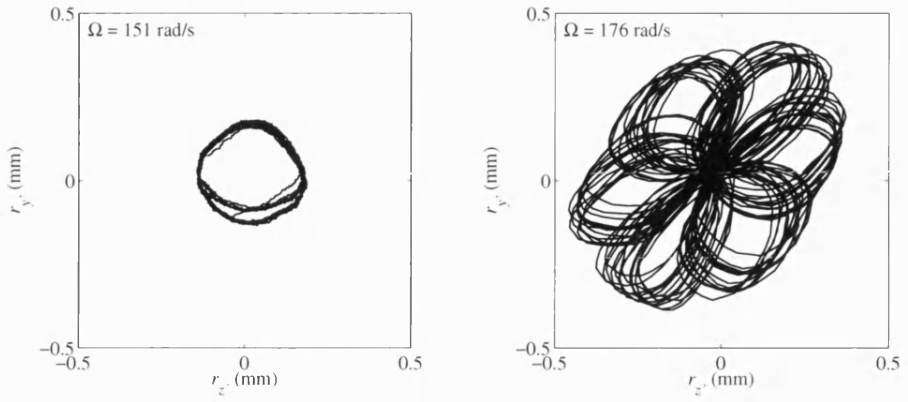

Figure 3.29: Higher modes get excited if the system is operated at a different rotation speed than the design speed for the LTI H_∞ controller.

orbit and audible noise. It must be noted that the orbit is confined within the clearance gap, and the system is still stable. If the difference between controller design speed and actual rotation speed is increased above approximately $\Omega = 190\,\text{rad/s}$, the system will become unstable and the rotor will make contact.

An FFT analysis of the displacement signals shown in Figure 3.30 reveals that there are two distinct peaks at the higher speed. That at $\omega = 176\,\text{rad/s}$ corresponds to the synchronous unbalance response, whereas the other peak at $\omega = 870\,\text{rad/s}$ may correspond to an excited super-synchronous mode or a higher harmonic.

Other experiments in which the controller design speed was chosen to be a multiple of the rotation speed, or where the gain-scheduled controller was fed with erroneous parameters led to similar results. When the difference between the rotation speed and the controller design speed is gradually increased, the rotor passes through a phase in which higher modes become excited before the system goes unstable. This fact can be useful in detecting developing instability due to parameter variations.

3.8 Closure

The H_∞ method was introduced as a means to design robust model based MIMO controllers. The proposed design framework for controllers of rotor/magnetic

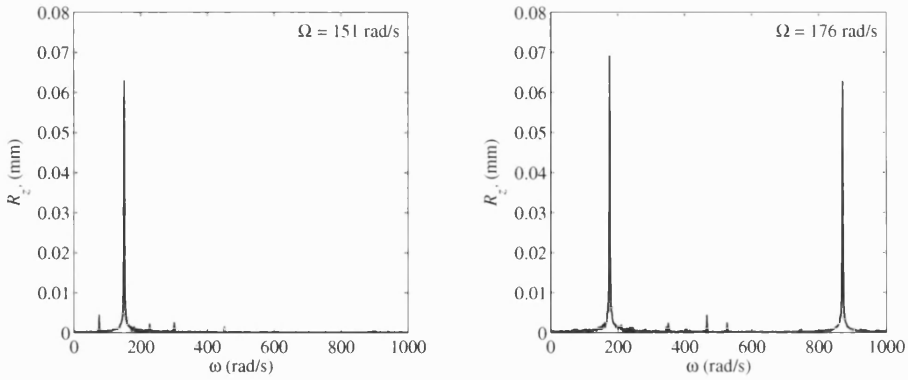

Figure 3.30: FFT of the displacement signals in Figure 3.29 shows two distinct peaks at the higher rotation speed.

bearing systems provided good results. It was shown that gain-scheduling techniques should be used if measurable system parameters change with time in order to guarantee stability and performance in the whole operating range. By considering the rotation speed as parameter, the robustness of H_∞ controlled instationary rotor systems can be increased. LTI and LPV controllers have been derived for the test rig, which offer superior performance compared to simple decentralised PD control. It was shown by simulations and experiments that LMI controllers, which have only been applied to rigid rotors so far, can be successfully applied to flexible systems. However, it must be kept in mind that the order of the controller and therefore the demands on real-time hardware are rather high.

4 Rotor-Stator Contact Dynamics

Usually, controllers for rotor/magnetic bearing systems are based on the linearised dynamics of a levitating rotor, derived for example with the finite element method. Under certain circumstances, however, the rotor can come into contact with auxiliary bearings, housings, or seals, which changes the dynamic characteristics significantly.

The most obvious reason for contact is a rotor drop due to power failure or other fault of the magnetic bearing system. Other possible causes are external forces exceeding the load capacity of the bearings, an increase of synchronous unbalance forces due to mass loss, or base motion. Rotor drop after a power failure or malfunction of bearings, in which all control capability is lost has been studied extensively. If contact occurs due to overload, increased unbalance, or a temporary fault when full control is still available, it is desirable to return the rotor into a non-contacting state in order to avoid machine shutdown.

This chapter discusses rotor dynamics in the presence of contact. Analytical methods are presented to assess possible non-linear motion of multimode rotor-bearing systems. A simple system is used to demonstrate the techniques, which are then applied to the more complex model of the rotor test rig. The theoretical predictions are compared with simulations and experimental results.

4.1 Contact Modes

The response of the rotor after a contact event depends on initial conditions (impact speed, impact angle,...), material properties (friction, stiffness,...) and operational conditions (rotational speed, unbalance,...). The rotor might recover by itself to a non-contacting state, or continue to make subsequent contacts. These may eventually become chaotic [49], or result in a steady state rotor limit cycle response. For a rotor subject to synchronous excitation e.g. due to unbalance, the following steady state responses have been observed:

Type 1: orbit with constant rub

Type 2: periodic impacts at subharmonics of the synchronous frequency

Type 3: rotor whirl with asynchronous periodic impacts

The first case has been studied extensively. Theoretical solutions exist for rigid as well as compliant surrounds [50–52]. The second type occurs with rotors on loose foundations and certain types of rotor-stator system anisotropy due to bearing characteristics, misalignment, or external loading [53–55]. The contact always occurs at fixed locations on the stator as the contact or rub frequency is a subharmonic of the rotation frequency. In the third case, the rotor makes repeated contacts with the surround at asynchronous frequencies. The resulting motion with synchronous excitation is periodic in the synchronously rotating reference frame, but generally not in the stationary reference frame. This type of response can be observed in systems with approximately isotropic rotor and bearing characteristics. The periodic contact produces a forward or backward 'bouncing' whirl, which eventually leads to damaging continuous backward whirl that has to be avoided [22, 56].

4.2 Analytical Description of Asynchronous Periodic Contact Modes

In the following, an analytical procedure to assess Type 3 contact modes for multimode flexible rotors under idealised contact will be presented. This is the most common contact response for typical isotropic systems. Type 1 constant rub modes are also covered by this framework as a borderline case with zero "bounce amplitude".

In general, the rotor motion in a Type 3 contact mode does not inhibit any periodicity in the stationary frame. Spectral analysis reveals that the rotor vibration contains components at the synchronous frequency Ω as well as components at harmonics of the distinct non-synchronous contact frequency ω_c. Therefore, rotor motion becomes periodic when transformed to the synchronous rotating frame.

4.2.1 Rotor Dynamics in the Rotating Frame

In the stationary frame, the equations of motion for a PD controlled rotor system can be expressed as

$$\begin{bmatrix} \mathbf{M}_{zz} & \mathbf{0} \\ \mathbf{0} & \mathbf{M}_{zz} \end{bmatrix} \begin{bmatrix} \ddot{\boldsymbol{q}}_z \\ \ddot{\boldsymbol{q}}_y \end{bmatrix} + \begin{bmatrix} \mathbf{B}_{zz} & \mathbf{B}_{zy} \\ \mathbf{B}_{yz} & \mathbf{B}_{yy} \end{bmatrix} \begin{bmatrix} \dot{\boldsymbol{q}}_z \\ \dot{\boldsymbol{q}}_y \end{bmatrix} + \begin{bmatrix} \mathbf{K}_{zz} & \mathbf{K}_{zy} \\ \mathbf{K}_{yz} & \mathbf{K}_{yy} \end{bmatrix} \begin{bmatrix} \boldsymbol{q}_z \\ \boldsymbol{q}_y \end{bmatrix} = \begin{bmatrix} \mathbf{R}_d & \mathbf{0} \\ \mathbf{0} & \mathbf{R}_d \end{bmatrix} \begin{bmatrix} f_{dz} \\ f_{dy} \end{bmatrix} + \begin{bmatrix} \mathbf{R}_c & \mathbf{0} \\ \mathbf{0} & \mathbf{R}_c \end{bmatrix} \begin{bmatrix} f_{cz} \\ f_{cy} \end{bmatrix} \tag{4.1}$$

The off-diagonal elements $\mathbf{B}_{zy}$, $\mathbf{B}_{yz}$ are gyroscopic terms, and $\mathbf{K}_{zy}$, $\mathbf{K}_{yz}$ are non-zero if internal friction is present (c.f. equation (2.49)). f_d and f_c represent the disturbance and contact forces, respectively, and the matrices $\mathbf{R}_d$ and $\mathbf{R}_c$ determine how these forces are distributed between the nodes.

In order to bring the FEM equations derived in Section 2.3 into a suitable form with the same mass matrices for the z- and y-directions, the displacement state vectors $\mathbf{q}_z$, $\mathbf{q}_y$ in equation (2.47) are redefined as

$$\boldsymbol{q}_z = [r_{z1}, \varphi_{y1}, r_{z2}, \varphi_{y2}, \ldots, r_{z\,n_S}, \varphi_{y\,n_S}]^T \tag{4.2a}$$

$$\boldsymbol{q}_y = [r_{y1}, -\varphi_{z1}, r_{y2}, -\varphi_{z2}, \ldots, r_{y\,n_S}, -\varphi_{z\,n_S}]^T \tag{4.2b}$$

i.e. $\boldsymbol{q}_y$ contains *negative* rotations around the z-axis. This will facilitate the notation in the following derivations.

Synchronous unbalance enters the equation (4.1) via the term for disturbance forces. If unbalance forces are the only external disturbances, f_d and $\mathbf{R}_d$ are given by

$$f_{dz} = \mathrm{Re}\left(\Omega^2 \sum_{i=1}^{n_s} |u_{cz\,i} + \mathrm{j} u_{sz\,i}| \, \mathrm{e}^{\mathrm{j}\Omega t} \right) \tag{4.3a}$$

$$f_{dy} = \mathrm{Im}\left(\Omega^2 \sum_{i=1}^{n_s} |u_{cz\,i} + \mathrm{j} u_{sz\,i}| \, \mathrm{e}^{\mathrm{j}\Omega t} \right) \tag{4.3b}$$

$$\mathbf{R}_d = \frac{\mathbf{u}_{cz} + \mathrm{j}\mathbf{u}_{sz}}{\sum_{i=1}^{n_s} |u_{cz\,i} + \mathrm{j} u_{sz\,i}|} \tag{4.3c}$$

The scalars f_{cz} and f_{cy} are the amplitudes of the contact force in $z-$ and $y-$directions, respectively. $\mathbf{R}_c$ is a $[n_s \times 1]$ Boolean matrix with one non-zero element at the degree of freedom where contact occurs. This is usually a translational displacement, which can be extracted from the full state vector with the

$[1 \times n_s]$ position matrices $\mathbf{P}_c$ as

$$\begin{bmatrix} r_{cz} \\ r_{cy} \end{bmatrix} = \begin{bmatrix} \mathbf{P}_c & \mathbf{0} \\ \mathbf{0} & \mathbf{P}_c \end{bmatrix} \begin{bmatrix} \boldsymbol{q}_z \\ \boldsymbol{q}_y \end{bmatrix} \tag{4.4}$$

The complex displacement vector $\mathbf{w}$ in a coordinate frame (ζ, η) rotating with the rotor at an angular velocity Ω and a phase ψ is defined by the transformation

$$\mathbf{w} = \boldsymbol{q}_\zeta + \mathrm{j}\boldsymbol{q}_\eta = (\boldsymbol{q}_z + \mathrm{j}\boldsymbol{q}_y)\mathrm{e}^{-\mathrm{j}(\Omega t+\psi)} \tag{4.5}$$

which is equivalent to

$$\begin{aligned} \begin{bmatrix} \boldsymbol{q}_z \\ \boldsymbol{q}_y \end{bmatrix} &= \begin{bmatrix} \mathrm{Re}((\boldsymbol{q}_\zeta + \mathrm{j}\boldsymbol{q}_\eta)\mathrm{e}^{\mathrm{j}(\Omega t+\psi)}) \\ \mathrm{Im}((\boldsymbol{q}_\zeta + \mathrm{j}\boldsymbol{q}_\eta)\mathrm{e}^{\mathrm{j}(\Omega t+\psi)}) \end{bmatrix} = \mathrm{Re}\left(\begin{bmatrix} \mathbf{I} \\ -\mathrm{j}\mathbf{I} \end{bmatrix} \mathbf{w}\, \mathrm{e}^{\mathrm{j}(\Omega t+\psi)} \right) \\ &= \frac{1}{2}\left(\begin{bmatrix} \mathbf{I} \\ -\mathrm{j}\mathbf{I} \end{bmatrix} \mathbf{w}\, \mathrm{e}^{\mathrm{j}(\Omega t+\psi)} + \begin{bmatrix} \mathbf{I} \\ \mathrm{j}\mathbf{I} \end{bmatrix} \mathbf{w}^* \mathrm{e}^{-\mathrm{j}(\Omega t+\psi)} \right) \end{aligned} \tag{4.6}$$

The equations of motion in the rotating frame are expressed in terms of harmonically modulated rotor states $\boldsymbol{\xi}$, defined as

$$\begin{bmatrix} \boldsymbol{q}_z \\ \boldsymbol{q}_y \end{bmatrix} = \mathrm{Re}\left(\boldsymbol{\xi}\, \mathrm{e}^{\mathrm{j}(\Omega t+\psi)} \right) = \frac{1}{2}\left(\boldsymbol{\xi}\, \mathrm{e}^{\mathrm{j}(\Omega t+\psi)} + \boldsymbol{\xi}^*\, \mathrm{e}^{-\mathrm{j}(\Omega t+\psi)} \right) \tag{4.7}$$

Equating the last parts of equations (4.6) and (4.7) leads to the following relationship between $\mathbf{w}$ and $\boldsymbol{\xi}$:

$$\mathbf{w} = \frac{1}{2}\begin{bmatrix} \mathbf{I} & \mathrm{j}\mathbf{I} \end{bmatrix}\left(\boldsymbol{\xi} + \boldsymbol{\xi}^*\, \mathrm{e}^{-2\mathrm{j}(\Omega t+\psi)} \right) \tag{4.8}$$

By defining the disturbance and contact forces in the rotating frame as

$$\begin{bmatrix} f_{dz} \\ f_{dy} \end{bmatrix} = \mathrm{Re}\left(\begin{bmatrix} 1 \\ -\mathrm{j} \end{bmatrix} F_d\, \mathrm{e}^{\mathrm{j}\Omega t} \right) \tag{4.9}$$

$$F_c = f_{c\zeta} + \mathrm{j}f_{c\eta} = (f_{cz} + \mathrm{j}f_{cy})\mathrm{e}^{-\mathrm{j}(\Omega t+\psi)} \tag{4.10}$$

and substituting (4.7) into (4.1), the rotating frame dynamics follow as

$$\mathbf{M}_w\ddot{\boldsymbol{\xi}} + \mathbf{B}_w\dot{\boldsymbol{\xi}} + \mathbf{K}_w\boldsymbol{\xi} = \mathbf{R}_{dw}F_d\, \mathrm{e}^{-\mathrm{j}\psi} + \mathbf{R}_{cw}F_c \tag{4.11}$$

with

$$\mathbf{M}_w = \mathbf{M} \qquad \mathbf{B}_w = \mathbf{B} + 2\mathrm{j}\Omega\mathbf{M} \qquad \mathbf{K}_w = \mathbf{K} + \mathrm{j}\Omega\mathbf{B} - \Omega^2\mathbf{M} \tag{4.12a}$$

$$\mathbf{R}_{dw} = \begin{bmatrix}\mathbf{R}_d & -\mathrm{j}\mathbf{R}_d\end{bmatrix}^T \qquad \mathbf{R}_{cw} = \begin{bmatrix}\mathbf{R}_c & -\mathrm{j}\mathbf{R}_c\end{bmatrix}^T \tag{4.12b}$$

where $\mathbf{M}$, $\mathbf{B}$, $\mathbf{K}$, $\mathbf{R}_d$, $\mathbf{R}_c$ denote the full system matrices in the stationary frame as appropriate to equation (4.1). The main benefit from equation (4.11) is that the contact forcing term is the only time-variant excitation (the synchronous disturbance forcing term is now static), so that steady state solutions in a contacting state can be sought.

4.2.2 Periodic Contact Modes

Without loss of generality it is assumed that repeated periodic contacts with a frequency $\omega_c = 2\pi/T_c$ occur at times $t_c = kT_c$ where k is an integer. The phase ψ of the rotating frame is chosen so that the impact takes place at a fixed location:

$$r_{cw}(kT_c) = s_c \tag{4.13}$$

where s_c is real and $r_{cw}(t) = (r_{cz}(t) + \mathrm{j}r_{cy}(t))\,\mathrm{e}^{-\mathrm{j}(\Omega t+\psi)}$. If the contact is instantaneous with an impulse p in radial direction, the impact force can be expressed in terms of the Dirac δ-function as

$$F_c(t) = -(1+\mathrm{j}\mu)p \sum_{k=-\infty}^{\infty} \delta(t_c - kT_c) \tag{4.14}$$

where μ is the sliding dry friction coefficient between the bearing and the shaft at the contact point.

The equations of motion in the rotating frame can be solved by expanding $\boldsymbol{\xi}$ and F_c as complex Fourier series with the fundamental frequency ω_c:

$$\boldsymbol{\xi}(t) = \sum_{i=-\infty}^{\infty} \boldsymbol{\Xi}_i\,\mathrm{e}^{\mathrm{j}i\omega_c t} \tag{4.15}$$

$$F_c(t) = -(1+\mathrm{j}\mu)\,p\,\frac{\omega_c}{2\pi} \sum_{i=-\infty}^{\infty} \mathrm{e}^{\mathrm{j}i\omega_c t} \tag{4.16}$$

and substituting them into (4.11) to give the Fourier coefficients for the rotor

response

$$\boldsymbol{\Xi}_i = \begin{cases} p\boldsymbol{\Upsilon}_i(\omega_c) + \mathbf{K}_w^{-1}\mathbf{R}_{dw}F_d\,\mathrm{e}^{-\mathrm{j}\psi} & i = 0 \\ p\boldsymbol{\Upsilon}_i(\omega_c) & i \neq 0 \end{cases} \tag{4.17}$$

where

$$\boldsymbol{\Upsilon}_i(\omega_c) = (i^2\omega_c^2\mathbf{M}_w - \mathrm{j}i\omega_c\mathbf{B}_w - \mathbf{K}_w)^{-1}\mathbf{R}_{cw}(1+\mathrm{j}\mu)\frac{\omega_c}{2\pi} \tag{4.18}$$

It is apparent that for a fixed contact frequency ω_c, the amplitudes of rotor vibration in the rotating frame are proportional to the contact impulse p.

The displacement in the plane of contact is given by

$$r_{cw}(kT_c) = \mathbf{P}_c\mathbf{w}(kT_c) = s_c \tag{4.19}$$

Using equation (4.8) and defining $\mathbf{P}_{cw} = \frac{1}{2}\mathbf{P}_c[\mathbf{I} \quad \mathrm{j}\mathbf{I}]$, (4.19) can be rewritten as

$$\mathbf{P}_{cw}\sum_{i=-\infty}^{\infty}\left(\boldsymbol{\Xi}_i + \boldsymbol{\Xi}_i^*\,\mathrm{e}^{-2\mathrm{j}(\Omega kT_c+\psi)}\right) = s_c \tag{4.20}$$

Hence, for the contact location to be invariant in the rotating frame, it is required that $T_c = l\pi/\Omega$, $l \in \mathbb{Z}$, so that $\mathrm{e}^{-2\mathrm{j}(\Omega kT_c+\psi)} = \mathrm{e}^{-2\mathrm{j}\psi}$. This leads to Type 2 contact modes involving periodic impacts at synchronous (sub-)harmonics of the rotation frequency. The rotor motion is then also periodic in the stationary frame and the impact period is an integer multiple of the half-synchronous period. These special solutions will not be considered further here, as this type of contact only occurs if there is some sort of anisotropy in the system.

For isotropic systems, $z-$ and $y-$axis frequency responses will be the same so that

$$\begin{bmatrix}\mathbf{I} & \mathrm{j}\mathbf{I}\end{bmatrix}\boldsymbol{\Xi}_i^* = \mathbf{0} \tag{4.21}$$

which makes (4.20) independent of the contact frequency. If equation (4.21) holds, the rotor response is given by

$$\mathbf{w}(t) = \frac{1}{2}\begin{bmatrix}\mathbf{I} & \mathrm{j}\mathbf{I}\end{bmatrix}\sum_{i=-\infty}^{\infty}\boldsymbol{\Xi}_i\mathrm{e}^{\mathrm{j}i\omega_c t} \tag{4.22}$$

At the time of contact $\mathbf{P}_c\mathbf{w}(kT_c) = s_c$, therefore with (4.17)

$$\frac{1}{2}\mathbf{P}_{cw}\begin{bmatrix}\mathbf{I} & \mathrm{j}\mathbf{I}\end{bmatrix}\left(\mathbf{K}_w^{-1}\mathbf{R}_{dw}F_d\,\mathrm{e}^{-\mathrm{j}\psi} + p\sum_{i=-\infty}^{\infty}\boldsymbol{\Upsilon}_i(\omega_c)\right) = s_c \tag{4.23}$$

or

$$F_d\,\mathrm{e}^{-\mathrm{j}\psi} = s_c K_w\left(1 - \alpha\mathbf{P}_{cw}\sum_{i=-\infty}^{\infty}\boldsymbol{\Upsilon}_i(\omega_c)\right) \tag{4.24}$$

where $K_w = (\mathbf{P}_{cw}\mathbf{K}_w^{-1}\mathbf{R}_{dw})^{-1}$ is referred to as "rotating frame complex stiffness", and $\alpha = p/s_c$ is the "bounce amplitude factor". Equation (4.24) can be used to graphically determine the phase and the bounce amplitude factor (hence the contact impulse) for a given synchronous disturbance force F_d and contact frequency ω_c. The locus of the left hand side with variable ψ is a circle in the complex plane with a radius F_d and centre at the origin. The right hand side is a straight line with parameter α, which originates from the point $s_c K_w$. The intersections between the line and the circle are solutions corresponding to particular vibration modes involving contact. The argument of the point of intersection gives the negative phase $-\psi$ of the rotating frame relative to the forcing, and the value of the parameter α determines the vibration amplitude in the rotating frame. In general, there will be a minimum forcing amplitude for a solution to exist. Above this amplitude, there will be either one ($|s_c K_w| < |F_d|$), or two ($|s_c K_w| \geq |F_d|$) solutions for the rotor response.

4.2.3 Periodic Contact Frequency

The contact frequency ω_c must be known in order to calculate possible contact modes with equation (4.24). For simple 2-dof systems it follows directly from the equations of motion [29]. For more complex multi degree of freedom rotors considered here, contact frequencies are found by considering energy changes during impacts.

The kinetic energy of the rotor is a quadratic function of the nodal velocities:

$$V(t) = \frac{1}{2}\left(\dot{\boldsymbol{q}}_z^T\mathbf{M}_{zz}\dot{\boldsymbol{q}}_z + \dot{\boldsymbol{q}}_y^T\mathbf{M}_{zz}\dot{\boldsymbol{q}}_y\right) \tag{4.25}$$

which can be separated into components along the real and imaginary axes of the rotating frame

$$V = V_\zeta + V_\eta \tag{4.26}$$

where

$$V_\zeta(t) = \frac{1}{2}\,\mathrm{Re}\left(\dot{\mathbf{w}}^T + \mathrm{j}\Omega\mathbf{w}^T\right)\mathbf{M}_{zz}\,\mathrm{Re}\left(\dot{\mathbf{w}} + \mathrm{j}\Omega\mathbf{w}\right) \tag{4.27a}$$

$$V_\eta(t) = \frac{1}{2}\,\mathrm{Im}\left(\dot{\mathbf{w}}^T + \mathrm{j}\Omega\mathbf{w}^T\right)\mathbf{M}_{zz}\,\mathrm{Im}\left(\dot{\mathbf{w}} + \mathrm{j}\Omega\mathbf{w}\right) \tag{4.27b}$$

For a perfectly elastic collision, the kinetic energy in the normal direction, V_ζ, will be unchanged by the impact. Generally, however, only a fraction $0 < \beta < 1$ of the kinetic energy will be conserved, so that

$$V_\zeta(0^+) - \beta V_\zeta(0^-) = 0 \tag{4.28}$$

The aim is now to find expressions for $V_\zeta(0^+)$ and $V_\zeta(0^-)$, or, equivalently, for $\dot{\mathbf{w}}(0^+)$, $\dot{\mathbf{w}}(0^-)$, and $\mathbf{w}(0)$. The actual velocity states at $t = 0$ are discontinuous, but the Fourier series solution (4.15) converges to a finite value of

$$\frac{1}{2}\sum_{i=-\infty}^{\infty}\left[\mathbf{I}\quad \mathrm{j}\mathbf{I}\right]\Xi_i\,\mathrm{j}i\omega_c = \frac{1}{2}\left(\dot{\mathbf{w}}(0^+) + \dot{\mathbf{w}}(0^-)\right) \tag{4.29}$$

The velocity states immediately before and after the impact are therefore given by

$$\dot{\mathbf{w}}(0^-) = \frac{1}{2}\sum_{i=-\infty}^{\infty}\left[\mathbf{I}\quad \mathrm{j}\mathbf{I}\right]\Xi_i\,\mathrm{j}i\omega_c - \frac{1}{2}\left(\dot{\mathbf{w}}(0^+) - \dot{\mathbf{w}}(0^-)\right) \tag{4.30a}$$

$$\dot{\mathbf{w}}(0^+) = \frac{1}{2}\sum_{i=-\infty}^{\infty}\left[\mathbf{I}\quad \mathrm{j}\mathbf{I}\right]\Xi_i\,\mathrm{j}i\omega_c + \frac{1}{2}\left(\dot{\mathbf{w}}(0^+) - \dot{\mathbf{w}}(0^-)\right) \tag{4.30b}$$

The step change in the velocity states can be calculated by substituting (4.14) into (4.11) and integrating over $t = [0^-, 0^+]$ with $\mathbf{w}(0^-) = \mathbf{w}(0^+)$:

$$\dot{\mathbf{w}}(0^+) - \dot{\mathbf{w}}(0^-) = -\mathbf{M}_{zz}^{-1}\mathbf{R}_c(1 - \mathrm{j}\mu)p \tag{4.31}$$

Hence,

$$\dot{\mathbf{w}}(0^-) = \frac{1}{2}\sum_{i=-\infty}^{\infty}\left[\mathbf{I}\quad \mathrm{j}\mathbf{I}\right]\Xi_i\,\mathrm{j}i\omega_c + \frac{1}{2}\mathbf{M}_{zz}^{-1}\mathbf{R}_c(1 - \mathrm{j}\mu)p \tag{4.32a}$$

$$\dot{\mathbf{w}}(0^+) = \frac{1}{2}\sum_{i=-\infty}^{\infty}\left[\mathbf{I}\quad \mathrm{j}\mathbf{I}\right]\Xi_i\,\mathrm{j}i\omega_c - \frac{1}{2}\mathbf{M}_{zz}^{-1}\mathbf{R}_c(1 - \mathrm{j}\mu)p \tag{4.32b}$$

The displacement states at $t = 0$ follow from substituting (4.17) and (4.24)

into (4.22) as

$$\mathbf{w}(0) = s_c \frac{1}{2} \begin{bmatrix} \mathbf{I} & \mathrm{j}\mathbf{I} \end{bmatrix} \left(\mathbf{K}_w^{-1} \mathbf{R}_{dw} K_w \left(1 - \alpha \mathbf{P}_{cw} \sum_{i=-\infty}^{\infty} \boldsymbol{\Upsilon}_i \right) + \alpha \sum_{i=-\infty}^{\infty} \boldsymbol{\Upsilon}_i \right) \tag{4.33}$$

so that the radial velocity components in the stationary frame before and after impact are

$$\mathrm{Re}\left(\dot{\mathbf{w}}(0^-) + \mathrm{j}\Omega \mathbf{w}(0)\right) = \frac{1}{2} \alpha s_c \left(\boldsymbol{\aleph}(\omega_c) + \frac{\beth}{\alpha} + \mathbf{M}_{zz}^{-1} \mathbf{R}_c \right) \tag{4.34a}$$

$$\mathrm{Re}\left(\dot{\mathbf{w}}(0^+) + \mathrm{j}\Omega \mathbf{w}(0)\right) = \frac{1}{2} \alpha s_c \left(\boldsymbol{\aleph}(\omega_c) + \frac{\beth}{\alpha} - \mathbf{M}_{zz}^{-1} \mathbf{R}_c \right) \tag{4.34b}$$

with

$$\boldsymbol{\aleph}(\omega_c) = \mathrm{Re}\left(\sum_{i=-\infty}^{\infty} \begin{bmatrix} \mathbf{I} & \mathrm{j}\mathbf{I} \end{bmatrix} \left(\mathrm{j}i\omega_c \mathbf{I} + \mathrm{j}\Omega \left(\mathbf{I} - K_w \mathbf{K}_w^{-1} \mathbf{R}_{dw} \mathbf{P}_{cw} \right) \right) \boldsymbol{\Upsilon}_i \right) \tag{4.35}$$

$$\beth = -\Omega \, \mathrm{Im}\left(\begin{bmatrix} \mathbf{I} & \mathrm{j}\mathbf{I} \end{bmatrix} \mathbf{K}_w^{-1} \mathbf{R}_{dw} K_w \right) \tag{4.36}$$

Substituting these results into (4.28) gives

$$V_\zeta(0^+) - \beta V_\zeta(0^-) = \frac{1}{8} \alpha^2 s_c^2 \, \Pi(\omega_c, \alpha) = 0 \tag{4.37}$$

where

$$\begin{aligned} \Pi(\omega_c, \alpha) = (1 - \beta) \left(\boldsymbol{\aleph}(\omega_c)^T + \frac{\beth^T}{\alpha} \right) \mathbf{M}_{zz} \left(\boldsymbol{\aleph}(\omega_c) + \frac{\beth}{\alpha} \right) + \\ + (1 - \beta) \mathbf{R}_c^T \mathbf{M}_{zz}^{-1} \mathbf{R}_c - 2(1 + \beta) \mathbf{R}_c^T \left(\boldsymbol{\aleph}(\omega_c) + \frac{\beth}{\alpha} \right) \end{aligned} \tag{4.38}$$

Therefore, roots of (4.38) give possible solutions for the contact frequency ω_c. Usually, $\left|\frac{\beth}{\alpha}\right|_2 \ll |\boldsymbol{\aleph}(\omega_c)|_2$, so that the term $\frac{\beth}{\alpha}$ can be neglected in practice. Hence, the contact frequency for a particular mode becomes independent from the vibration amplitude α and we may now write $\Pi(\omega_c, \alpha) = \Pi(\omega_c)$.

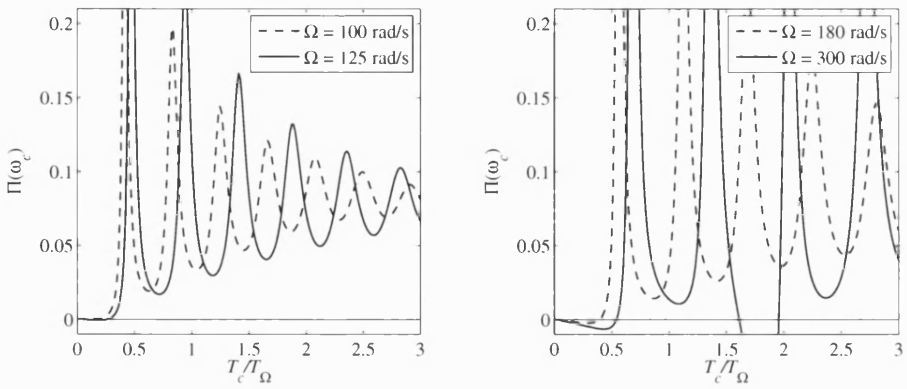

Figure 4.1: Plot of the characteristic equation $\Pi(\omega_c)$ to find possible periodic contact frequencies at two under-critical and two over-critical rotation speeds.

4.3 A Simple Example

A simple 2-dof disk system similar to that shown in Figure 2.7 is used to demonstrate the application of the theory developed in Section 4.2. Assuming that the disk is subject to a synchronous unbalance force with zero phase (F_d real), the equation of motion (4.1) simplifies to

$$\begin{bmatrix} M & 0 \\ 0 & M \end{bmatrix} \begin{bmatrix} \ddot{r}_z \\ \ddot{r}_y \end{bmatrix} + \begin{bmatrix} D & 0 \\ 0 & D \end{bmatrix} \begin{bmatrix} \dot{r}_z \\ \dot{r}_y \end{bmatrix} + \begin{bmatrix} K & 0 \\ 0 & K \end{bmatrix} \begin{bmatrix} r_z \\ r_y \end{bmatrix} = \begin{bmatrix} f_{dz} \\ f_{dy} \end{bmatrix} + \begin{bmatrix} f_{cz} \\ f_{cy} \end{bmatrix} \tag{4.39}$$

The default mass, damping, and stiffness parameters are $M = 50\,\text{kg}$, $D = 1400\,\text{Ns/m}$, $K = 1\,\text{MN/m}$, which leads to a resonance frequency of $141\,\text{rad/s}$ or $22.5\,\text{Hz}$. The clearance between the rotor and the rigid auxiliary bearing is $s_c = 0.8\,\text{mm}$, the coefficient of friction is $\mu = 0.15$, and the energy dissipation coefficient $\beta = 0.98$.

4.3.1 Contact Frequencies

Possible contact frequencies are given by the roots of the energy function $\Pi(\omega_c)$ given by equation (4.38). $\Pi(\omega_c)$ is plotted for two under-critical and two over-critical rotation speeds in Figure 4.1. It can be seen that the number of possible contact frequencies increases with increasing Ω. For $\Omega = 100\,\text{rad/s}$, there are no contact modes. For $\Omega = 125\,\text{rad/s}$ and $\Omega = 180\,\text{rad/s}$, the energy function

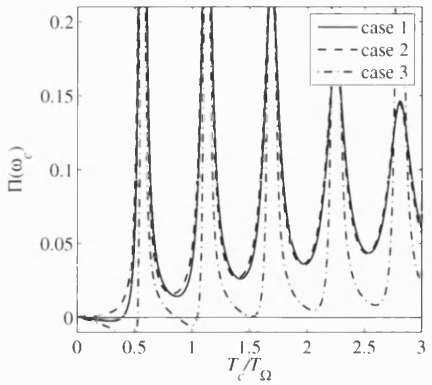

Case	$\Omega\,(\frac{\text{rad}}{\text{s}})$	μ	$D\,(\frac{\text{Ns}}{\text{m}})$
1	180	0.15	1400
2	180	0.05	1400
3	180	0.15	300

Figure 4.2: Contact frequency solution for different friction and damping values.

has two roots at contact frequencies above the synchronous frequency: $T_c/T_\Omega = \{0.0653, 0.2551\}$ and $T_c/T_\Omega = \{0.0336, 0.3923\}$, respectively. Two additional sub-critical periodic contact frequencies exist at the higher rotational speed $\Omega = 300\,\text{rad/s}$, giving the roots $T_c/T_\Omega = \{0.0234, 0.5392, 1.6128, 1.9565\}$.

Figure 4.2 shows the influence of friction and damping parameters. If the dry friction coefficient μ is reduced from 0.15 to 0.05, no periodic contact modes exist at $\Omega = 180\,\text{rad/s}$. If the damping coefficient D is reduced from 1400 Ns/m to 300 Ns/m, with $\Omega = 180\,\text{rad/s}$ and $\mu = 0.15$, two additional possible contact frequencies are introduced near the synchronous frequency.

It can be summarised that periodic contact modes are more likely to exist for lightly damped rotors, at high speeds, with high friction coefficients between rotor and stator and increased unbalance.

4.3.2 Contact Impulse and Phase

Once possible contact frequencies are identified, the contact impulse and phase of the contact mode vibration can be found by plotting both sides of equation (4.24) in the complex plane as described in Section 4.2.2.

Figure 4.3 shows the results for both super-critical contact frequencies at $\Omega = 180\,\text{rad/s}$ and $\Omega = 300\,\text{rad/s}$ with radial unbalance mass offsets $\varepsilon = \{0.133\,\text{mm}, 0.266\,\text{mm}, 0.4\,\text{mm}\}$. This leads to unbalance force amplitudes of $F_d = \{215\,\text{N}, 431\,\text{N}, 646\,\text{N}\}$ at $\Omega = 180\,\text{rad/s}$, and $F_d = \{598\,\text{N}, 1197\,\text{N}, 1795\,\text{N}\}$ at $\Omega = 300\,\text{rad/s}$, respectively. The values for contact impulse and phase read from the plots in Figure 4.3 at the points A–F are listed in Table 4.3.2.

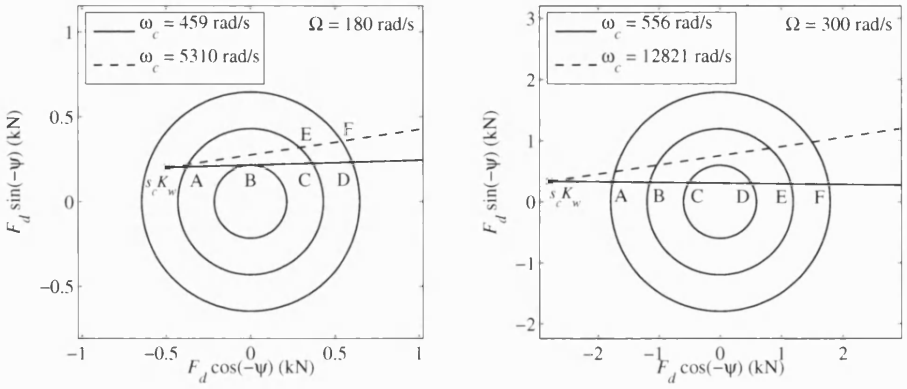

Figure 4.3: Determining the contact impulse p and phase ψ by plotting both sides of equation (4.24) separately with unbalance mass offset $\varepsilon = \{0.133\,\text{mm}, 0.266\,\text{mm}, 0.4\,\text{mm}\}$.

	$\Omega = 180\,\text{rad/s}$			$\Omega = 300\,\text{rad/s}$		
Mode	ψ (rad)	α (Ns/m)	p (Ns)	ψ (rad)	α (Ns/m)	p (Ns)
A	-2.64	1496	1.19	-2.95	4928	3.94
B	-1.59	6290	5.03	-2.87	7846	6.27
C	-0.55	11056	8.84	-2.59	10911	8.72
D	-0.36	14082	11.26	-0.52	15817	12.65
E	-0.83	1150	0.92	-0.24	18881	15.10
F	-0.58	1515	1.21	-0.16	21799	17.43

Table 4.1: Contact impulse and phase for some solutions in Figure 4.3.

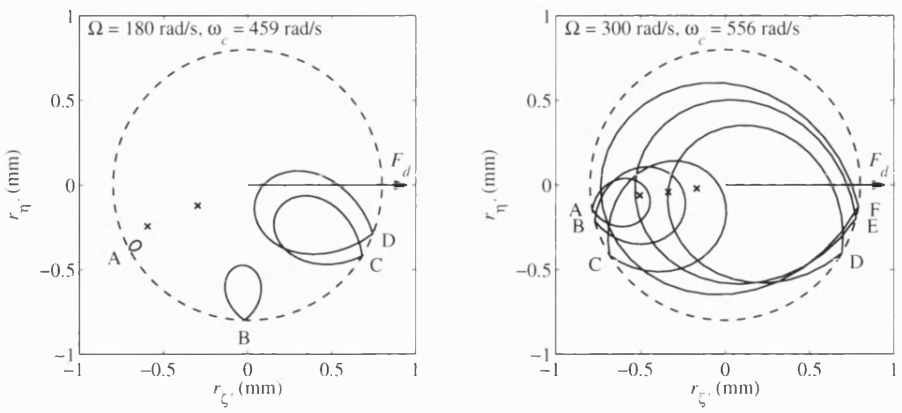

Figure 4.4: Contact mode amplitudes and phase in the rotating frame for $\varepsilon = \{0.133\,\text{mm}, 0.266\,\text{mm}, 0.4\,\text{mm}\}$. $\times$ indicate static non-contact solutions (non-existent for $\Omega = 180\,\text{rad/s}$, $\varepsilon = 0.4\,\text{mm}$).

At $\Omega = 180\,\text{rad/s}$, $\omega_c = 459\,\text{rad/s}$, the curve originating at $s_c K_w$ just touches the circle corresponding to $F_d = 215\,\text{N}$, which means that this is the smallest unbalance force amplitude for which periodic contact modes exist at that rotational speed. For $F_d = 646\,\text{N}$, the point $s_c K_w$ lies within the circle, which implies that the static displacement caused by synchronous unbalance forces is larger than the clearance. Contact-free rotor motion can only exist if the distance between $s_c K_w$ and the origin is larger than the unbalance force amplitude.

4.3.3 Contact Modes

With known values for the contact impulse p and phase ψ, the Fourier coefficients $\boldsymbol{\Xi}_i$ can be calculated and substituted into (4.22) to give the vibrational motion in the rotating frame $\mathbf{w}(t)$. The trajectories corresponding to solutions for the first supercritical contact frequency at $\Omega = 180\,\text{rad/s}$ and $\Omega = 300\,\text{rad/s}$ are depicted in Figure 4.4. The coordinate system (ζ', η') is chosen so that the unbalance force vector is in the direction of the positive ζ' axis for each solution. Synchronous rotor response solutions without contact are static in the rotating frame. They are indicated by a $\times$ if they exist.

It is apparent that, for given unbalance mass offsets, the contact mode amplitudes at $\Omega = 300\,\text{rad/s}$ are significantly larger than at $\Omega = 180\,\text{rad/s}$ although the static displacements in the non-contacting state are much smaller. This shows

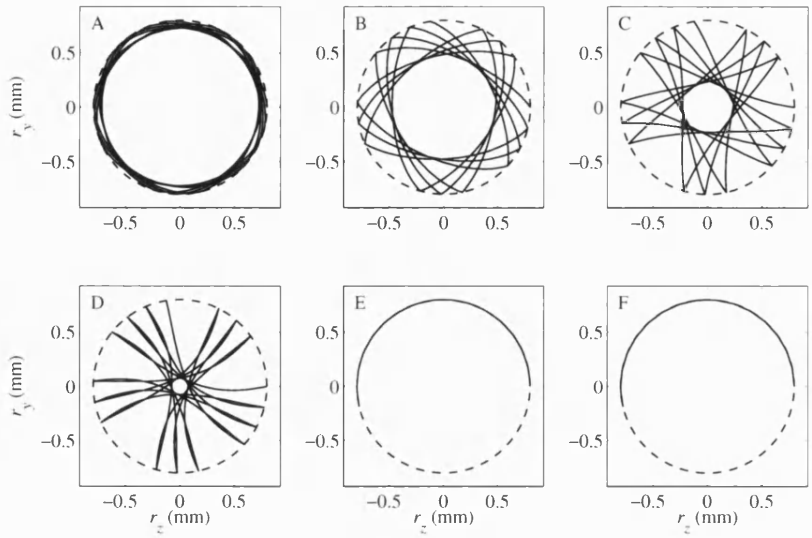

Figure 4.5: Rotor motion in the stationary frame with $\Omega = 180\,\text{rad/s}$, $\omega_c = 459\,\text{rad/s}$ (A-D), and $\omega_c = 5310\,\text{rad/s}$ (E,F). The starting point is at $(r_z, r_y) = (s_c, 0)$.

that rotor-stator contact is particularly problematic in high speed machinery. At $\Omega = 300\,\text{rad/s}$ and $\omega_c = 556\,\text{rad/s}$, the trajectory for mode F is just confined to the clearance circle. This type of contact mode will lead to double contact and is likely to progress to full backward whirl with a slightly higher unbalance or a small transient disturbance.

The analytical method used here cannot exactly describe constant rubbing as contacts are assumed to be instantaneous. However, the contact modes with the highest impact frequencies are good approximations. In the example here, the corresponding frequencies are $\omega_c = 5310\,\text{rad/s}$ and $\omega_c = 12821\,\text{rad/s}$ at $\Omega = 180\,\text{rad/s}$ and $\Omega = 300\,\text{rad/s}$, respectively. The vibration amplitudes in the rotating frame are negligible, so that the only parameter of interest for those contact modes is the phase ψ.

The rotor trajectories in the stationary frame corresponding to modes A–F at $\Omega = 180\,\text{rad/s}$ and $\Omega = 300\,\text{rad/s}$ are shown in Figures 4.5 and 4.6 for the duration of the first 16 impacts. Similar to Figure 4.4, it can be seen that the motion becomes more backward pronounced at high rotation speeds. The interpretation of the highest frequency modes as approximations for constant rubbing becomes

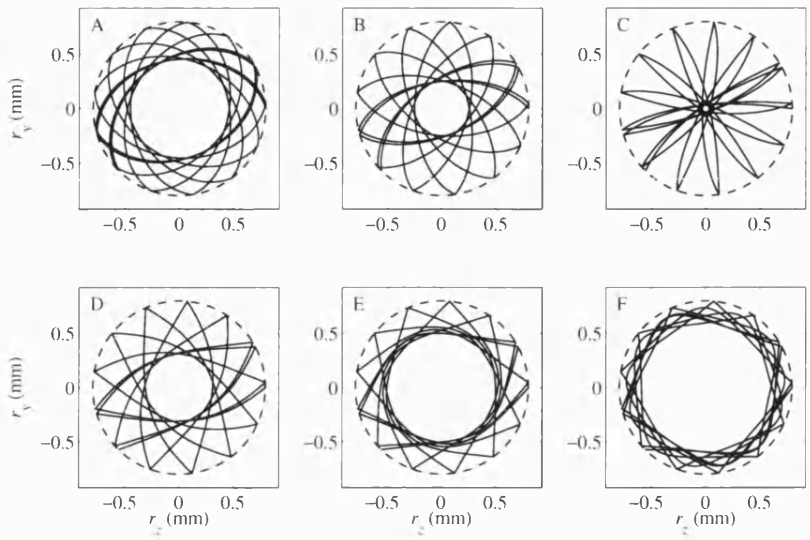

Figure 4.6: Rotor motion in the stationary frame with $\Omega = 300\,\text{rad/s}$, $\omega_c = 556\,\text{rad/s}$. The starting point is at $(r_z, r_y) = (s_c, 0)$.

apparent for trajectories E and F in Figure 4.5.

4.3.4 Contact Mode Existence and Stability

Not all analytical solutions are physically plausible. The boundary value condition $\mathbf{P}_{cw}\mathbf{w}(kT_c) = s_c$, $k = 0, 1, \ldots$ does not put any constraints on the motion between impacts. Hence, the trajectories may contain points outside the clearance circle. This often occurs for low sub-synchronous contact frequencies. Obviously those modes cannot exist.

Even if a mode is physically plausible it might be unstable and does not appear in reality. Stability of the example system's contact modes can be assessed qualitatively with Figure 4.3. For the solutions A, B, C, at $\Omega = 300\,\text{rad/s}$, the contact impulse will decrease with increasing disturbance force amplitudes, which can be interpreted as an unstable negative stiffness property. In contrast, the impulses of modes D, E, F, will increase with increasing unbalance force. Hence, the rotor will rather adopt one of the latter contact modes or progress to a contact-free orbit instead of moving as predicted by solutions A, B, C.

Similarly, for $\Omega = 180\,\text{rad/s}$, the rotor is likely to adopt response C rather than A. Mode D will be very stable as the level of unbalance is too large for a contact-

free orbit to exist. Mode B is far less stable. The rotor will probably loose contact and progress to a contact-free orbit.

It follows from equation (4.24) that stable contact modes fulfil the condition

$$\left| s_c K_w - (p+\delta p) K_w \mathbf{P}_{cw} \sum_{i=-\infty}^{\infty} \Upsilon_i(\omega_c) \right| \geq \left| s_c K_w - p K_w \mathbf{P}_{cw} \sum_{i=-\infty}^{\infty} \Upsilon_i(\omega_c) \right|, \quad \delta p > 0 \tag{4.40}$$

The phase ψ of the stable contact modes of the disk system at $\Omega = 180\,\text{rad/s}$ and $\Omega = 300\,\text{rad/s}$ lies between $-\pi/2$ and 0, even though the phase of the linear unconstrained responses are close to π at these speeds. This fact will be important for the development of control strategies.

4.3.5 Simulation Results

The analytical results are obtained with the simplifying assumptions that the auxiliary bearing is rigid, i.e. acts as a rigid boundary, that the contacts are instantaneous, and that the rotor is suspended by a linear spring/damper system. It is now examined by numerical simulation how a more realistic contact model and non-linear magnetic bearing characteristics influence the dynamics. Two questions are of particular importance: Will the rotor motion be similar to an analytic mode? Also: Can the statements in Section 4.3.4 about stability be verified?

In the first simulation, the rotor was still assumed to be suspended by linear springs/dampers, but the non-linear Hertzian contact model (2.17) replaced the ideal rigid contact model used in the analytical derivations. All other system parameters including the unbalance forces were the same as in the previous section. The initial conditions for position and velocity were set to the values $\mathbf{w}(0^+)$ and $\dot{\mathbf{w}}(0^+)$ calculated in Section 4.3.3 for the examined modes A–F at $\Omega = 180\,\text{rad/s}$ and $\Omega = 300\,\text{rad/s}$.

Figure 4.7 shows the rotor trajectories at $\Omega = 180\,\text{rad/s}$. As predicted, response A is unstable. The rotor makes three contacts with stator and then progresses to a contact-free orbit. The borderline stability of mode B is apparent. The rotor moves as predicted for a few revolutions and then loses contact. The simulated response with parameters and initial conditions set to those of modes C–F all coincide well with the theory.

Encouraging results are also obtained for $\Omega = 300\,\text{rad/s}$ in Figure 4.8. Responses A, B, C are unstable as predicted; the rotor progresses quickly to a

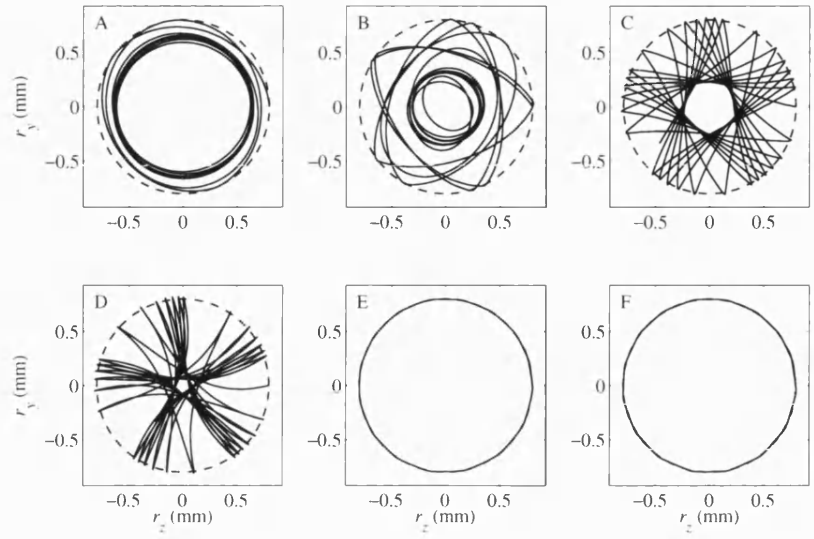

Figure 4.7: Simulated rotor motion in the stationary frame with an ideal linear magnetic bearing and $\Omega = 180\,\mathrm{rad/s}$. The initial displacement is $(r_z, r_y) = (s_c, 0)$.

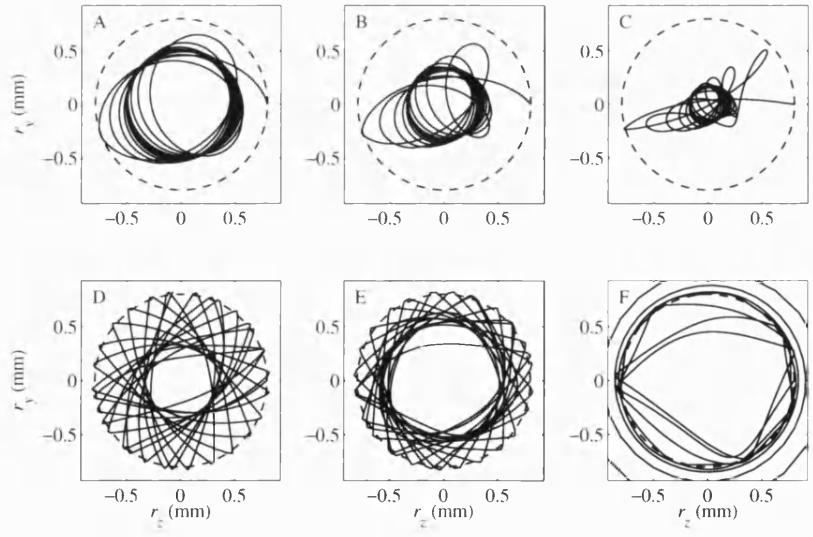

Figure 4.8: Simulated rotor motion in the stationary frame with an ideal linear magnetic bearing and $\Omega = 300\,\mathrm{rad/s}$. The initial displacement is $(r_z, r_y) = (s_c, 0)$.

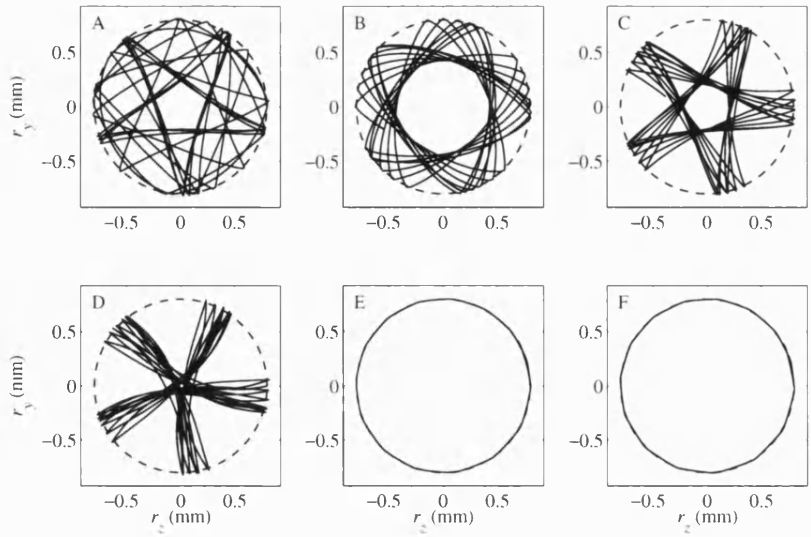

Figure 4.9: Simulated rotor motion in the stationary frame with a non-linear magnetic bearing and $\Omega = 180\,\mathrm{rad/s}$.

contact-free orbit. The trajectories in D and E are virtually the same as the analytical cases. Mode F is not adopted, as the rotor progresses to full backward whirl. Such behaviour was expected as the rotor motion in the rotating frame is just contained within the clearance space. Hence, this mode can be destabilised by a small additional disturbance or change in parameters. In reality, the rotor trace in during backward whirl is "smooth". The simulation output, however, appears slightly jagged due to the extremely high whirl frequencies.

In the second simulation, the linear spring-damper suspension was replaced by the non-linear magnetic bearing model (2.5). As shown in Figure 4.9 and 4.10, the rotor response matches the theoretical results very well again.

At $\Omega = 180\,\mathrm{rad/s}$, the instability of mode A is still apparent. However, the rotor does not progress to a contact-free orbit, but takes up a mode C type response, which is caused by the same unbalance as mode A. This kind of behaviour is covered by the theory and was discussed in Section 4.3.4. With the parameters and initial conditions of mode B, the rotor stays in contact with the auxiliary bearing. The responses C, D, E, F are as predicted.

At $\Omega = 300\,\mathrm{rad/s}$, response A progresses to a mode F type motion, then to full backward whirl. Responses B, C, D are virtually the same as before. Response E

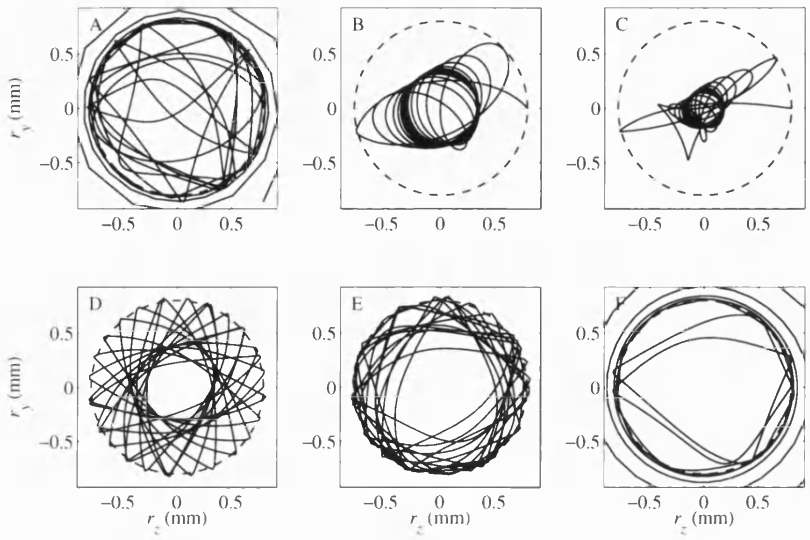

Figure 4.10: Simulated rotor motion in the stationary frame with a non-linear magnetic bearing and $\Omega = 300\,\mathrm{rad/s}$.

is more backward pronounced and could eventually become full backward whirl if a small additional disturbance acts on the rotor, or if the parameters change slightly.

One can summarise that all simulation results are very encouraging. They show that the analytical method is suitable to describe realistic magnetic bearing/-rotor dynamic models with non-linear properties. The qualitative statements about the stability of modes have been verified and it was shown that modes with large amplitudes in the rotating frame can easily progress to full backward whirl, especially at high speeds.

4.4 Bi-stable Rotor Responses

The rotor will always move in a contact-free orbit for unbalance force amplitudes below a certain threshold provided that no further disturbances occur. If the bearings have a linear spring/damper characteristic, and the unbalance force magnitude $|F_d| = |F_u| \geq |s_c K_w|$, contact is inevitable. If $|F_d|$ has a value somewhere in between, the rotor may either move on a contact-free orbit, or adopt a stable contact mode. This bi-stable behaviour will now be examined through

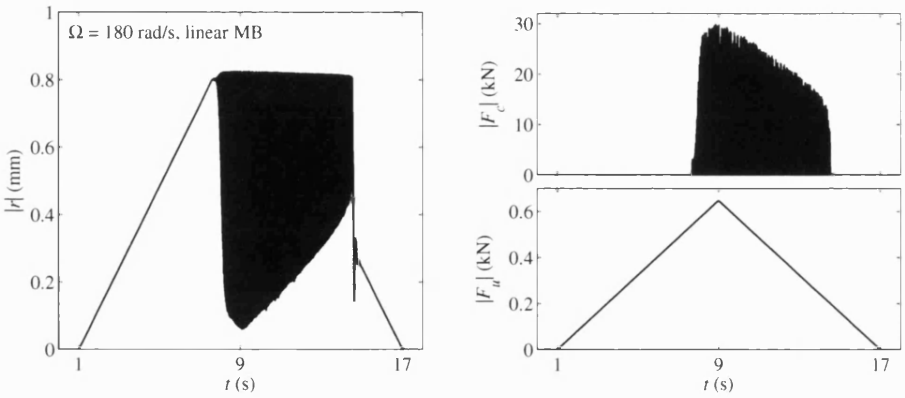

Figure 4.11: Bounce-like rotor response to varying unbalance force.

simulation.

It is assumed that the disk rotates at $\Omega = 180\,\mathrm{rad/s}$ with the unbalance mass offset slowly increasing from $\varepsilon = 0\,\mathrm{mm}$ to $\varepsilon = 0.4\,\mathrm{mm}$ in 8 s. The rotor will stay on a contact-free orbit until the static displacement in the rotating frame becomes larger than the bearing clearance. Then, it will adopt a contact mode according to the level of unbalance. If the unbalance is increased further, there will be a point when the bounce amplitude comes close to $2s_c$, which is when full backward whirl becomes established.

When the unbalance is reduced from the maximum value $\varepsilon = 0.4\,\mathrm{mm}$ (which is well below the backward whirl threshold), the disk will certainly stay in contact until $|F_d| = |F_u| \leq |s_c K_w|$. Then, the rotor might come off or stay in contact with the auxiliary bearing until $\varepsilon = 0.133\,\mathrm{mm}$, which is the smallest unbalance for which contact is possible (c.f. Figure 4.3).

Figures 4.11 and 4.12 show the response for a system with ideal linear magnetic bearings. After the initial contact, the rotor adopts either a bounce-like or a constant rubbing contact mode. Only small numerical perturbations in initial conditions determine which solution is obtained. In practice, both responses are possible. The contact forces in the rubbing case are a factor 10 smaller than for the bounce response. The hysteresis effect is clearly visible in both cases. When $|F_d|$ is reduced, the rotor stays in contact almost until the minimum unbalance for stable contact modes is reached.

Figure 4.13 shows the motion in the rotating frame. The phase change after the initial impact is clearly visible. It is also apparent that the phase of the contact

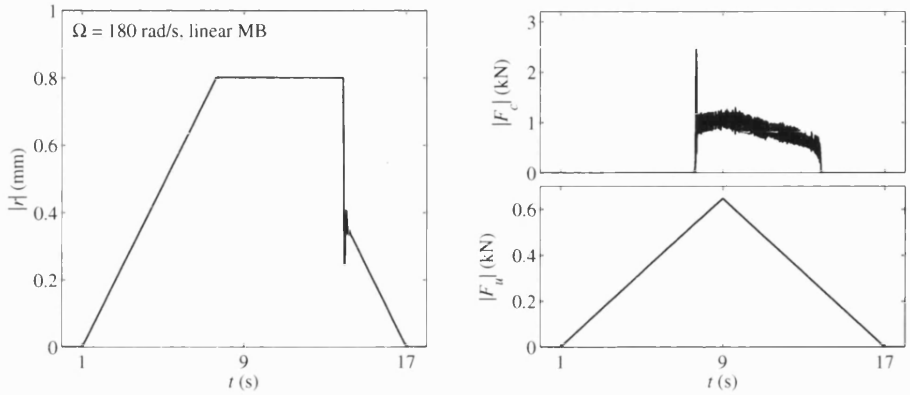

Figure 4.12: Constant rub type rotor response to varying unbalance force.

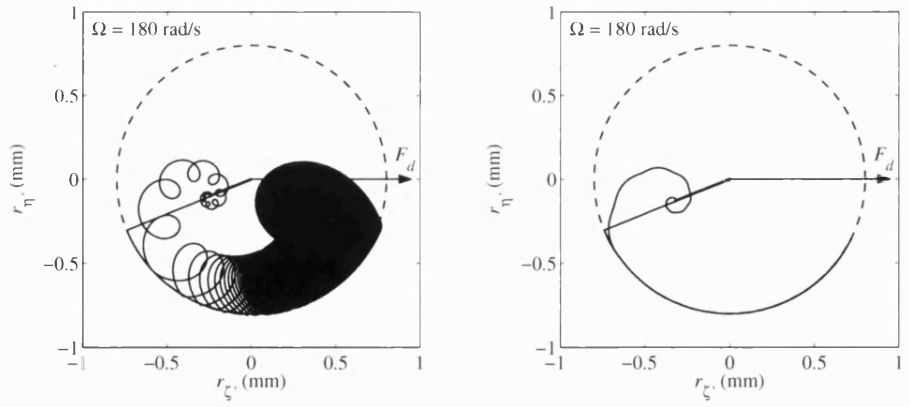

Figure 4.13: Rotor response in the rotating frame for bounce-like and rub mode.

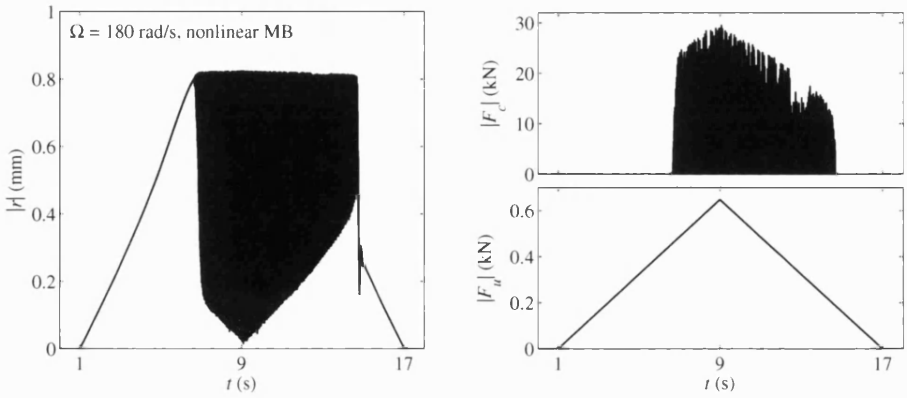

Figure 4.14: Rotor response to varying unbalance force with a non-linear magnetic bearing characteristic.

point progresses towards the stationary phase of contact-free motion when the unbalance is decreased. This validates the theoretical results presented earlier.

Figures 4.14 and 4.15 show the simulated motion and contact forces for a system with a non-linear magnetic bearing. The initial contact occurs at an unbalance very close to $|s_c K_w|$, and the hysteresis effects are similar to the linear case. The main difference compared to the previous results is that the non-contact displacement-unbalance relationship is no longer linear and the rubbing modes are less likely due to the reduced magnetic bearing stiffness near the boundaries.

4.5 Contact Dynamics of the Flexible Rotor

In this section, the contact dynamics of the flexible rotor depicted in Figure 2.1 are examined at the two rotational speeds $\Omega = 151\,\text{rad/s}$ and $\Omega = 226\,\text{rad/s}$. The magnetic bearings are PD controlled with a stiffness of $1\,\text{MN/m}$ and a damping factor of $3500\,\text{Ns/m}$. The nominal clearance between the auxiliary bearings and the rotor is $s_c = 0.825\,\text{mm}$. The coefficients of friction and energy dissipation are $\mu = 0.15$ and $\beta = 0.98$, respectively. It is assumed that the unbalance forces act on the non-driven end disk only, and that the rotor makes contact at the non-driven end auxiliary bearing.

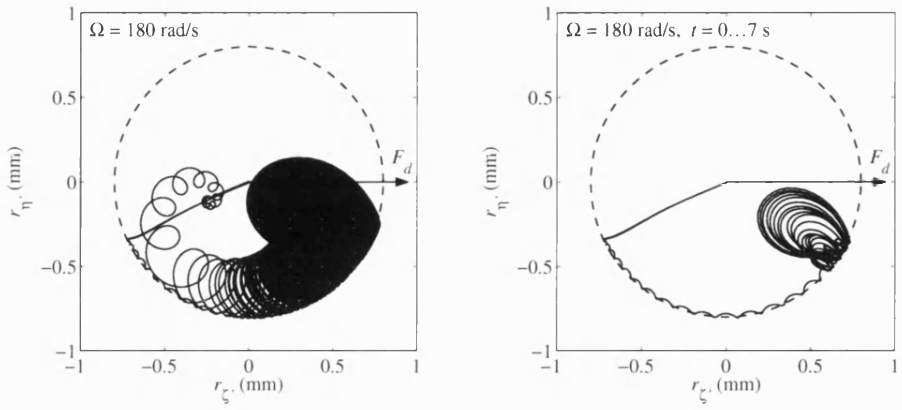

Figure 4.15: Rotating frame displacements for system with non-linear bearings. The right plot shows the response for the first seven seconds only, where $0 \leq \varepsilon \leq 0.3\,\mathrm{mm}$.

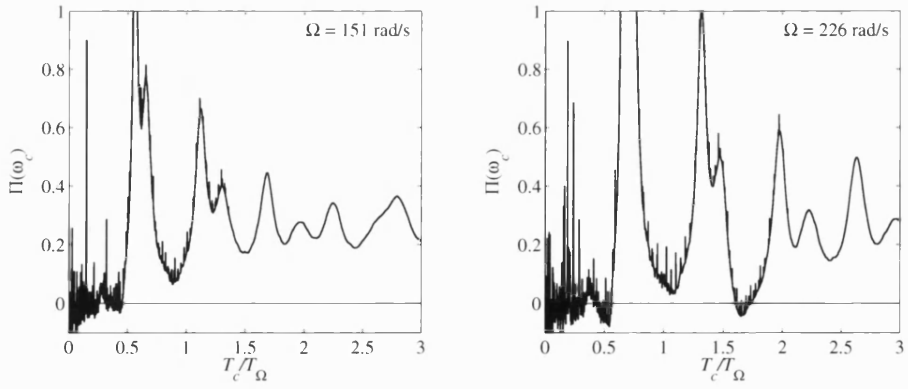

Figure 4.16: Plot of $\Pi(\omega_c)$ whose roots indicate possible contact frequencies.

4.5.1 Contact Frequency and Contact Points

Figure 4.16 shows plots of $\Pi(\omega_c)$ at the two considered rotational speeds. Due to the high flexibility, there are numerous roots at contact frequencies above approximately twice the rotation speed. At $\Omega = 226\,\text{rad/s}$ there are also some subsynchronous roots, which do not become established in practice, because their associated vibration amplitude in the rotating frame is not confined within the clearance circle. In contrast to simple systems, the plot of $\Pi(\omega_c)$ is used to find regions of possible contact frequencies rather than exact solutions.

Key features of the contact modes, namely, the minimum synchronous disturbance force for periodic contact modes, $F_{d\,min}$, and the angular location of the contact point relative to the disturbance force phase, ψ, can be expressed as functions of the contact frequency. The right hand side of equation (4.24) represents a straight line in the complex plane with parameter α , and the left hand side represents a circle with centre at the origin and radius F_d.

With x and y as the real and complex part of points, the line and circle can also be expressed parametrically as

$$y = \kappa x + c \tag{4.41a}$$

and

$$x^2 + y^2 = F_d^2 \tag{4.41b}$$

The slope κ is given by

$$\kappa(\omega_c) = \tan\left(\arg\left(-s_c K_w \mathbf{P}_{cw} \sum_{i=-\infty}^{\infty} \boldsymbol{\Upsilon}_i(\omega_c)\right)\right) \tag{4.42}$$

and the point c at which the line crosses the imaginary (or y-) axis is

$$c(\omega_c) = -\kappa\,\mathrm{Re}(s_c K_w) + \mathrm{Im}(s_c K_w) \tag{4.43}$$

which follows from the fact that (4.41a) goes through $s_c K_w$.

$F_{d\,min}$ is simply the distance of (4.41a) from the origin, which is given by

$$F_{d\,min}(\omega_c) = \left|\frac{c}{\sqrt{\kappa^2 + 1}}\right| \tag{4.44}$$

κ and $F_{d\,min}$ are plotted for $\Omega = 151\,\text{rad/s}$ and $\Omega = 226\,\text{rad/s}$ in Figure 4.17 for

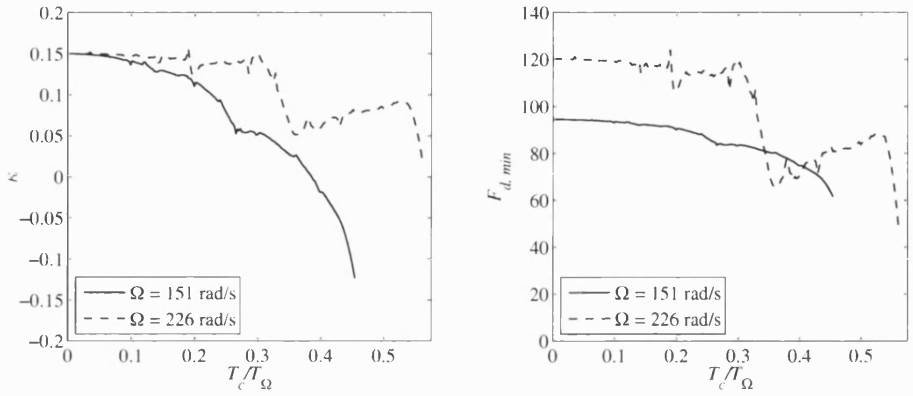

Figure 4.17: Slope κ and minimum required synchronous disturbance force $F_{d\,min}$ for all possible super-synchronous periodic contact mode frequencies.

all contact periods of interest.

The phase difference between angular contact point location and effective disturbance force, ψ, is the negative argument of the intersection point between the straight line and the circle, which follows from substituting (4.41a) into (4.41b) as

$$\psi(\omega_c, F_d) = -\operatorname{atan2}(\kappa v + c, v) \tag{4.45}$$

where

$$v = \frac{\kappa c}{\kappa^2 + 1}\left(-1 \pm \sqrt{1 - \frac{\kappa^2 + 1}{\kappa^2 c^2}\left(c^2 - F_d^2\right)}\right), \qquad v \in \mathbb{R} \tag{4.46}$$

Equation (4.46) can have up to two real solutions. If no solution exists, no contact mode with the chosen contact frequency is possible, because the excitation force is too small. If equation. (4.46) has two solutions, only the one which satisfies the condition (4.40) will correspond to a stable mode as discussed in Section 4.3.4.

The left and right hand sides of equation (4.24) are plotted for two example contact frequencies, one of which is the first super-synchronous root of $\Pi(\omega_c)$. Figure 4.18 reveals that the principal characteristics are the same as for the simple disk system. Again, the value $|s_c K_w|$ gives the maximum force for which the rotor can move on a contact-free orbit. The minimum unbalance force amplitudes for which contact modes are possible are $F_{d\,min} = 61\,\mathrm{N}$ at $\Omega = 151\,\mathrm{rad/s}$ and $F_{d\,min} = 47\,\mathrm{N}$ at $\Omega = 226\,\mathrm{rad/s}$, respectively. The phases of non-contact displacements and contact points are comparable to the disk example, in particular the phase ψ of

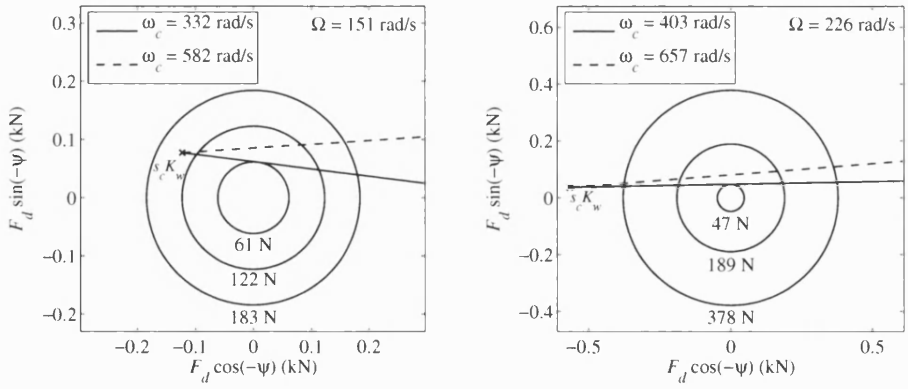

Figure 4.18: Plot of equation (4.24) at $\Omega = 151\,\mathrm{rad/s}$ and $\Omega = 226\,\mathrm{rad/s}$ for two different contact frequencies ω_c.

stable contact modes lies between $-\pi/2$ and 0.

4.5.2 Simulations with Varying Unbalance

The large differences between $|s_c K_w|$ and $F_{d\,min}$ imply that bi-stable rotor responses are possible. This has been checked by simulations in which the unbalance was increased from zero to a maximum value above $|s_c K_w|$, before it was reduced to zero again. Figure 4.19 shows the results, which agree with the predictions, especially at $\Omega = 226\,\mathrm{rad/s}$. The large range of unbalance force magnitudes at which the rotor can adopt either a contact-free or a contact response is noticeable. Bounce-like and rubbing modes are equally likely. Even though contact forces are much lower in the rubbing case, the range of unbalance forces at which contact occurs is very similar.

The motion in the rotating frame for the bounce-like response is plotted in Figure 4.20. At $\Omega = 151\,\mathrm{rad/s}$, the bounce amplitudes and contact forces are relatively small compared to the the results at $\Omega = 226\,\mathrm{rad/s}$. In the latter case, the motion is 'backward pronounced at synchronous disturbance force magnitudes near 800 N.

At the lower rotational speed, the angle between the contact point and the unbalance force varies "smoothly" with the force magnitude. At $\Omega = 226\,\mathrm{rad/s}$, however, the rotor motion becomes "chaotic" at some levels of unbalance as illustrated in Figure 4.21. Up to $t = 7\,\mathrm{s}$, where $|F_d| = 600\,\mathrm{N}$, the rotor adopts periodic

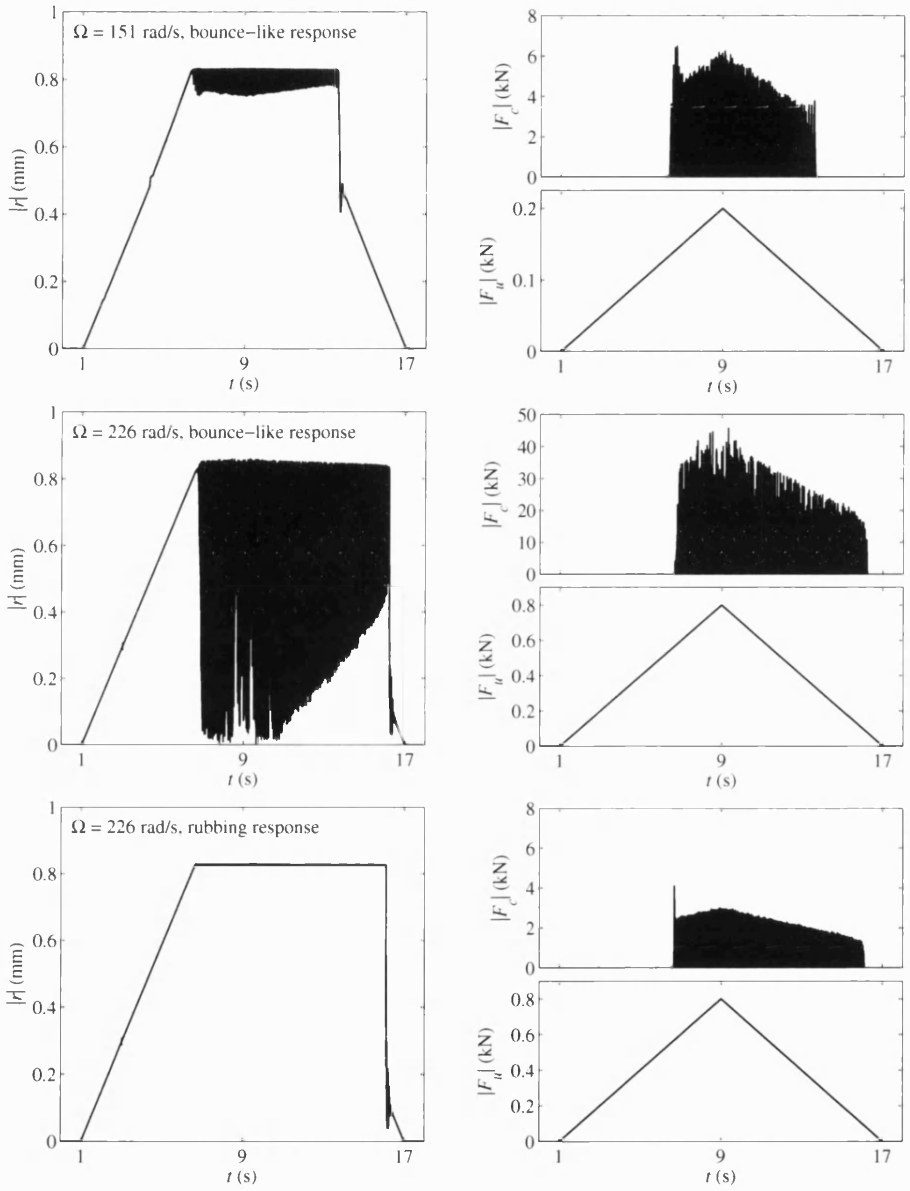

Figure 4.19: Bounce-like and rubbing rotor responses to varying unbalance force on the non-driven end disk at $\Omega = 151\,\mathrm{rad/s}$ and $\Omega = 226\,\mathrm{rad/s}$.

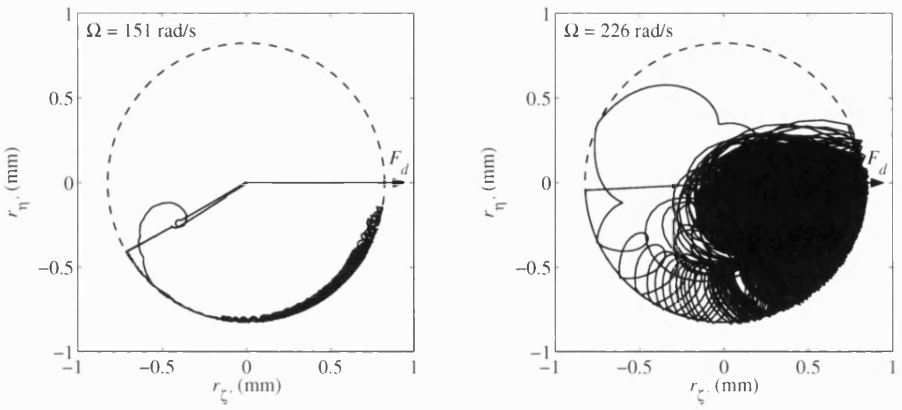

Figure 4.20: Bounce-like rotor response in the rotating frame at $\Omega = 151\,\mathrm{rad/s}$ and $\Omega = 226\,\mathrm{rad/s}$.

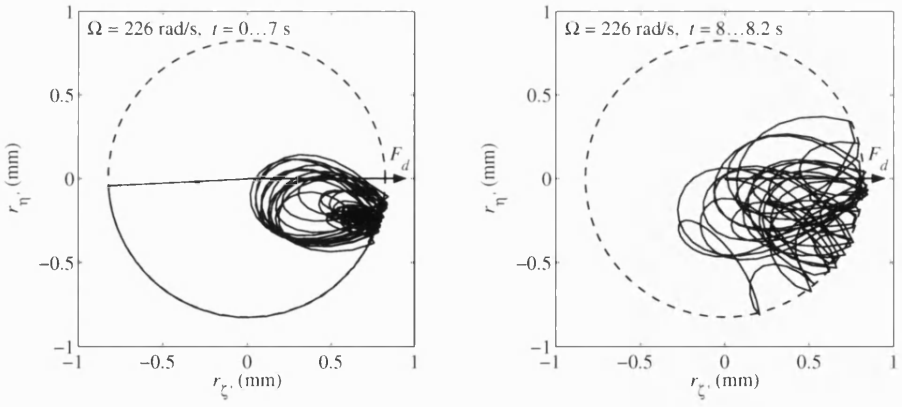

Figure 4.21: Bounce-like rotor response in the rotating frame at $\Omega = 226\,\mathrm{rad/s}$ at selected time intervals.

contact modes according to the level of unbalance. Between $t = 8\,\mathrm{s}$ and $t = 8.2\,\mathrm{s}$, however, rotor motion is chaotic and the contact point in the rotating frame varies significantly.

Thus far, unbalance forces have been assumed to act on the non-driven end disk only. In reality, however, unbalance is distributed over the rotor length. Figure 4.22 shows the results of a simulation in which the unbalance on the non-driven end disk was increased as before, but all other disks had small mass eccentricities of $0.025\,\mathrm{mm} < \varepsilon < 0.01\,\mathrm{mm}$ with random phase as well. It is apparent that this change does not affect the general characteristics of the contact dynamics. The contact force, the hysteresis effects, the bounce amplitude, and the contact point phase are all comparable to the results of simulations with an initially ideally balanced rotor. This implies that distributed unbalance can be replaced by an additional virtual unbalance at the contact node causing the same complex displacement.

In multi-mode systems, not only the nodal motion at the auxiliary bearing but also at other nodes is of interest. Figure 4.23 shows the relationship between the complex displacements at the non-driven end auxiliary bearings and the closest magnetic bearing for bounce-like and rubbing responses. The relationship is constant in the non-contact case only if the unbalance distribution does not change. When the rotor touches the auxiliary bearing, the ratio of displacement magnitudes and differences of phase start to oscillate for bounce-like contact modes. The oscillations are relatively small at $\Omega = 151\,\mathrm{rad/s}$. For large unbalance forces at $\Omega = 226\,\mathrm{rad/s}$, however, the motions at the two nodes are unrelated due to the chaotic behaviour. Interestingly, for rubbing contact, the amplitude ratio and phase difference stay almost constant although the unbalance force on the end disk is varied in a wide range. This fact will be important for contact recovery control where the magnetic bearings are used as actuators to influence the motion at the auxiliary bearings.

4.6 Rotor-Stator Contact Experiments

Mass loss experiments with the flexible rotor rotating at $\Omega = 151\,\mathrm{rad/s}$ have been carried out to verify the simulation results. An unbalance of $520\,\mathrm{g\,cm}$ was added to the non-driven end disk of the initially balanced rotor. This causes a mass eccentricity of $\varepsilon = 0.4\,\mathrm{mm}$. The unbalance was compensated by an equivalent

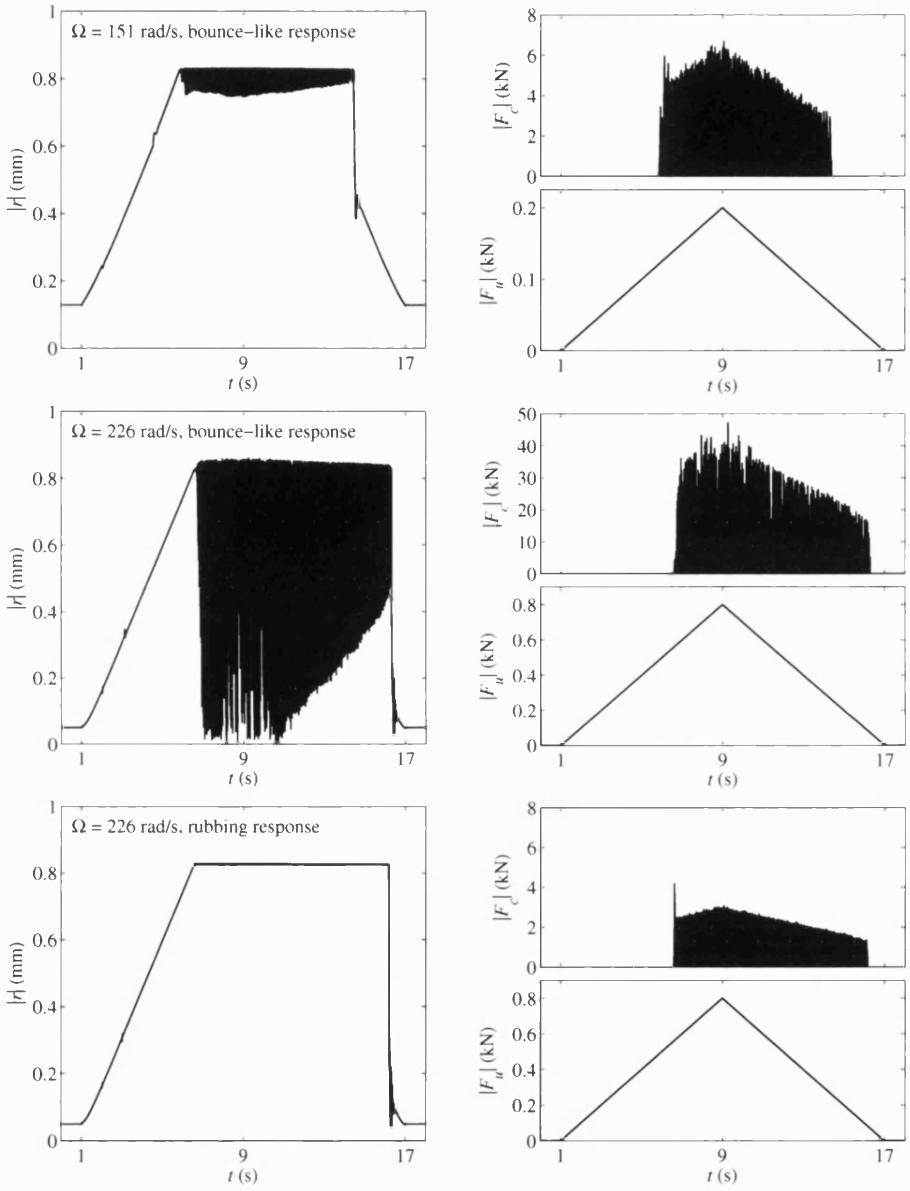

Figure 4.22: Bounce-like and rubbing rotor responses to varying unbalance force on the non-driven end disk and distributed unbalance on the other disks.

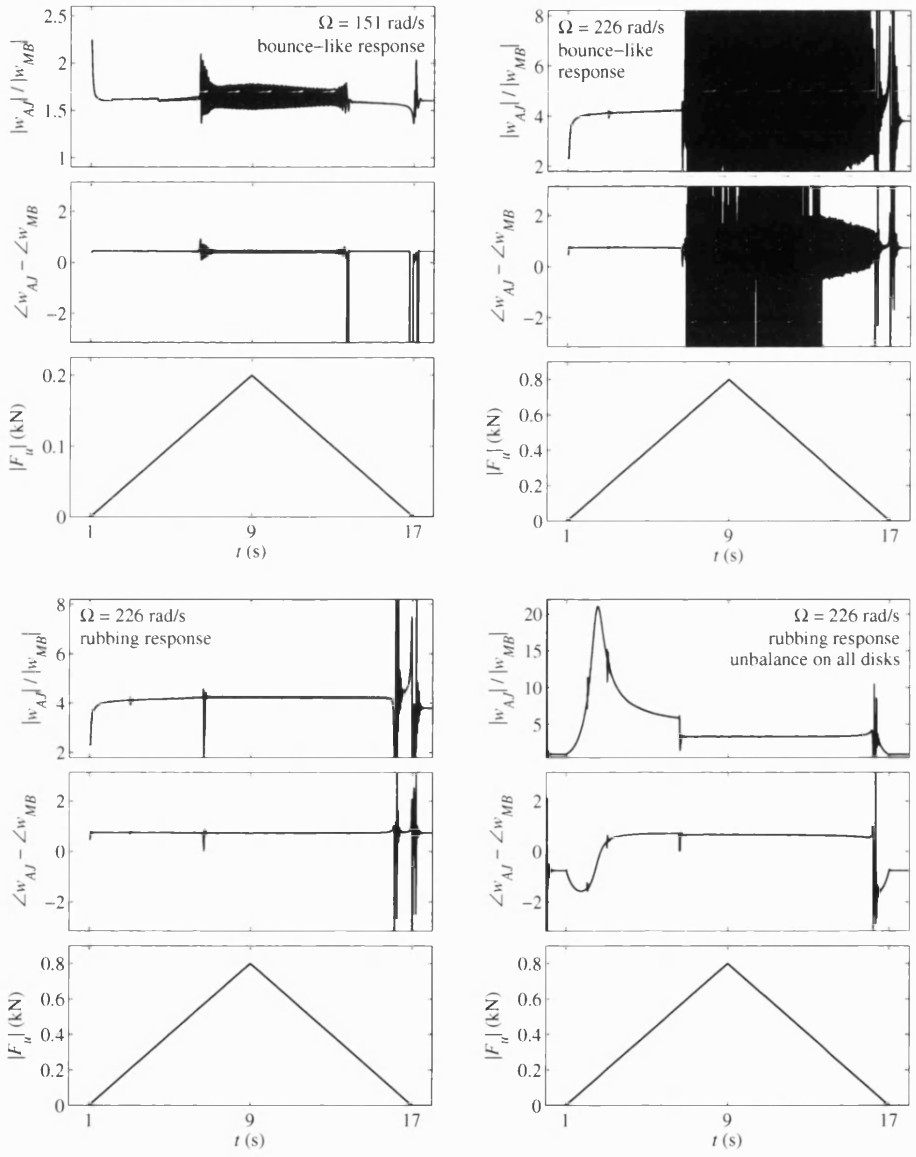

Figure 4.23: Differences of displacement amplitude and phase at the magnetic bearing and the outer auxiliary bearing dependent on level of unbalance.

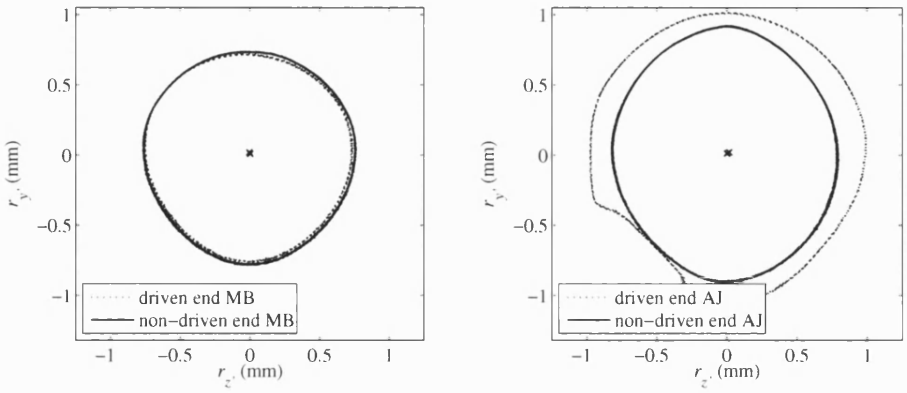

Figure 4.24: Measured geometry of the auxiliary bearings at the magnetic bearings (left), and at both rotor ends (right).

mass tied on the same disk using a Kevlar chord. A solenoid controlled blade was utilised to cut the chord and cause mass loss.

Before the first test has been carried out, the geometry of the auxiliary bearings was measured. The results in Figure 4.24 show that the inner auxiliary bearings have a clearance of $\approx 0.75\,\text{mm}$, which is slightly less than the 0.825 mm used in the simulations. In the contacting and the non-contacting cases, however, displacements at the magnetic bearing nodes are usually much smaller than at the ends so that this difference is not important. The auxiliary bearings at the driven and the non-driven end have approximate clearances of 0.95 mm and 0.825 mm, respectively. The diameter at the driven end auxiliary bearing was purposely chosen large to make contact at that end less likely. The "flat" at the lower left of the measured clearance was caused by sensor saturation. It is not actually a geometric fault.

In the first mass loss experiment, the balanced rotor was run up to $\Omega = 151\,\text{rad/s}$ before the compensation mass was cut off causing a response. Figure 4.25 shows the rotating frame motion shortly before and after the sudden unbalance increase at $t = 0\,\text{s}$. The arrow F_d represents the approximate direction of the synchronous disturbance force, and the dashed circle is the nominal clearance of the auxiliary bearing. It is apparent that the measured motion in general, and the angular contact point location in particular, match the predicted results well.

It can be observed that the rotor motion in the non-contacting case is not a

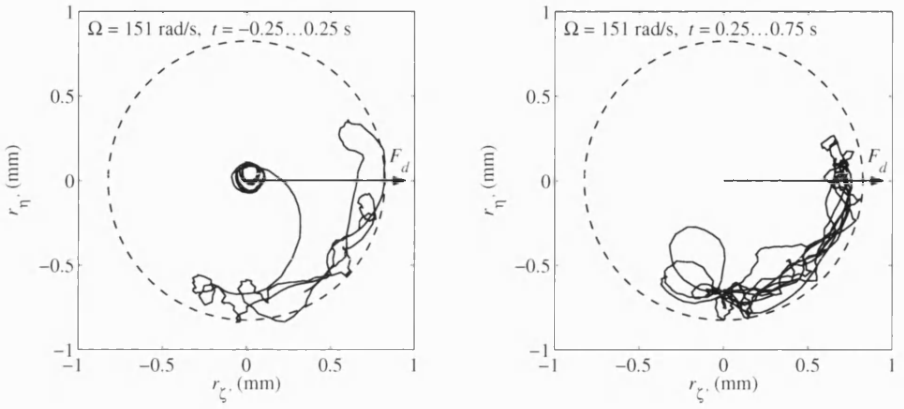

Figure 4.25: Initial rotor response after mass loss at $t = 0\,\mathrm{s}$ where $\varepsilon(t > 0) \approx 0.4\,\mathrm{mm}$.

single point in the rotating frame, but a small circular orbit. This was attributed to the universal joint coupling between the motor and the shaft, which introduces some higher harmonic vibrations. This effect occurs at all rotational speeds and all unbalance levels.

Measurements at around 2 s and 6 s after the mass loss, shown in Figure 4.26, confirm that the contact mode is stable. The contact point oscillations become less after $t = 6\,\mathrm{s}$, which is evident by decaying transient vibrations.

The phase difference between the non-contacting and the contacting rotor is visualised in Figure 4.27. As before, an unbalance of 520 g cm was added to the non-driven end disk, but this time it was not compensated completely by the tied on mass. The rotor moved on an orbit with an average radius of 0.25 mm. The phase lag relative to the disturbance force was close to the predicted 144°. After the sudden mass loss, the phase in the rotating frame swung around to reach similar values as obtained in the first experiment.

4.7 Contact Dynamics of H_∞ Controlled Systems

So far, it has been assumed, that the rotor is suspended by bearings with a linear spring-damper characteristic. As shown earlier, PD magnetic bearings fall into this category under normal operational conditions. If robust model based controllers are used, however, the dynamics of magnetic bearings become more

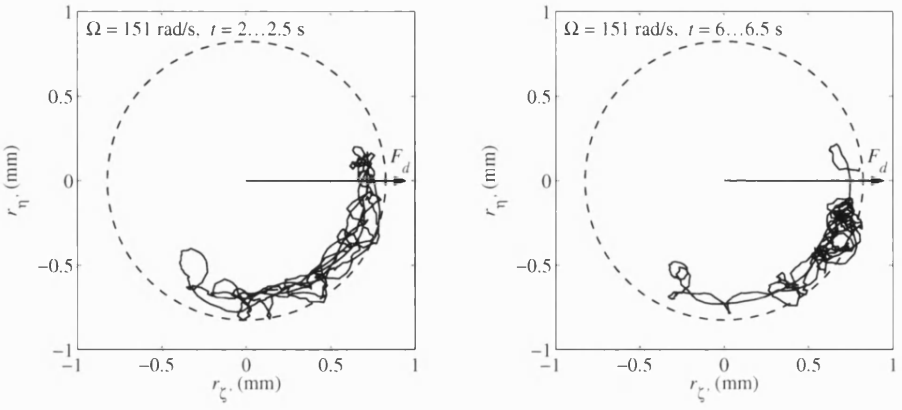

Figure 4.26: Established contact with $\varepsilon(t > 0) \approx 0.4\,\text{mm}$ two and six seconds after the mass loss event with an initially balanced rotor.

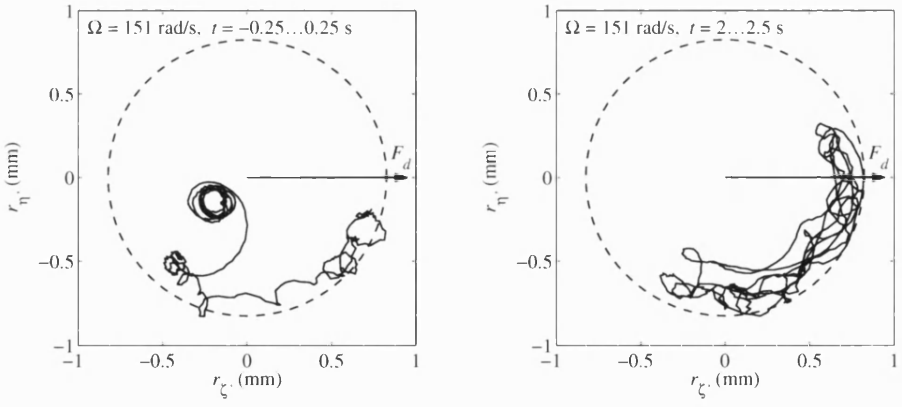

Figure 4.27: Contact response of an initially unbalanced rotor with $\varepsilon(t < 0) \approx 0.2\,\text{mm}$ and $\varepsilon(t > 0) \approx 0.4\,\text{mm}$.

complex.

Robust controllers are usually derived with a linear model of the plant. Stability is guaranteed if the model error lies between certain bounds. If contact occurs, the rotor dynamics become highly non-linear, and it is questionable whether stability is still achievable with model based controllers. Without a detailed non-linear model of a contacting flexible rotor this question is hard to answer.

An analytical examination of H_∞ controlled rotor contact dynamics is also difficult. An approach similar to the one in Section 4.2 could be followed by using a state-space model of the closed loop system in the rotating frame. It must be recognised, however, that H_∞ controllers usually have a high order, which increases the computational effort. Model based controllers can process information from non-collocated sensors, which can lead to complex rotor displacement–actuator force relationships. Each closed loop system has to be assessed separately, thus generally applicable conclusions have not been derived.

4.7.1 Simulation Results

Due to the problems of an analytical description of robustly controlled rotor/-magnetic bearing system contact dynamics, it was decided to perform several simulations in order to find out whether there are similarities to the response of systems with PD controlled magnetic bearings. The hard/soft H_∞ controllers derived in Section 3.3 were used for the tests at a rotational speed of $\Omega = 151\,\mathrm{rad/s}$. An initial unbalance of $65\,\mathrm{g\,cm}$ at the non-driven end disk was increased to $650\,\mathrm{g\,cm}$ and $520\,\mathrm{g\,cm}$ for the hard and the soft system, respectively. The simulated motion at the non-driven end sensor node is shown in Figure 4.28 for the first $0.5\,\mathrm{s}$ after the mass loss.

The hard and the soft system quickly adopt a bounce-like contact mode type response. The contact point in the rotating frame is almost constant; similar to the PD controlled system at that speed. Noticeable is that the maximum displacement at the sensor node is significantly smaller than the auxiliary bearing clearance. This difference is due to the offset between sensor and contact point and the fact that the H_∞ controller keeps the orbit at the magnetic bearing small, even in the contact case. This is shown in Figure 4.29. At the auxiliary bearing, the maximum amplitude obviously equals the clearance.

Another interesting observation is that the H_∞ controlled rotor system does not show significant contact hysteresis effects. In other words, contact due to

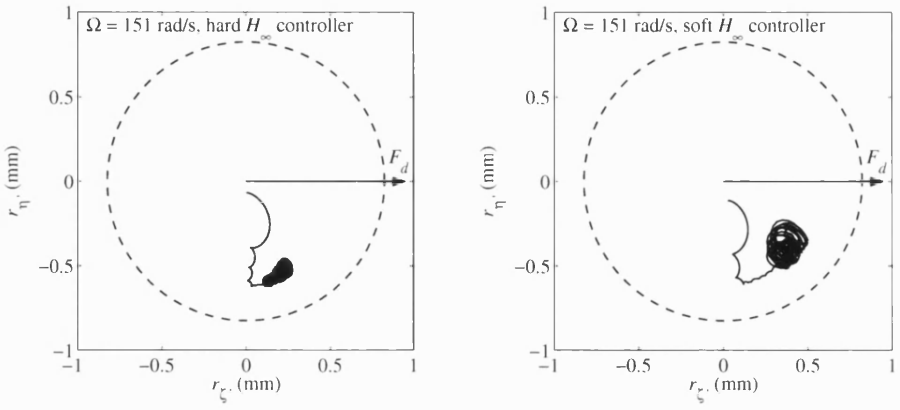

Figure 4.28: Simulated motion in the rotating frame after mass loss with the hard and the soft H_∞ controlled systems at the non-driven end sensor node.

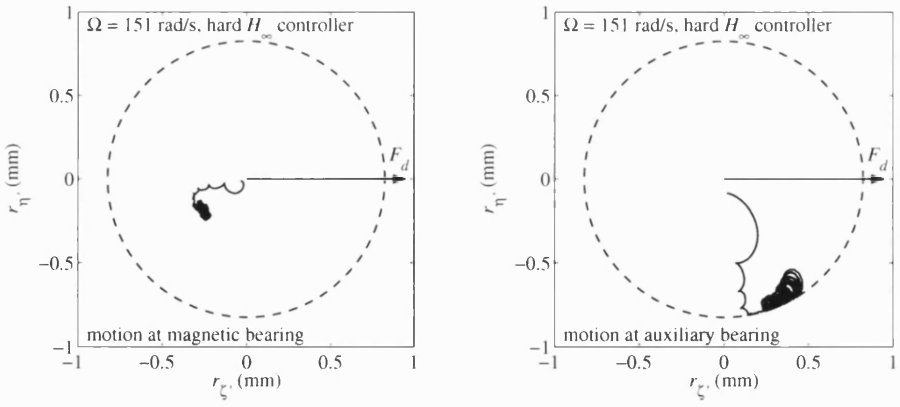

Figure 4.29: Displacements of the hard system at the magnetic and auxiliary bearings.

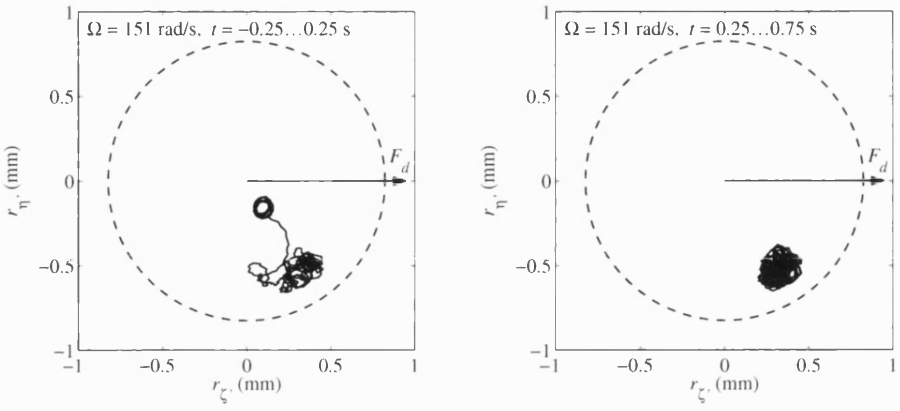

Figure 4.30: Contact response of a system with hard H_∞ controller after a small loss unbalance of $\varepsilon(t > 0) \approx 0.5\,\text{mm}$.

unbalance forces only occurs if the non-contacting orbit is equal to or larger than the clearance. In PD controlled systems, the rotor can "stick" to the stator even if the unbalance is small. This effect did not occur with the designed robust controllers.

4.7.2 Measurements on the Test Rig

The hard and soft H_∞ controllers were implemented on the rig, and mass loss tests were performed with the same parameters as in the simulations. Figures 4.30 and 4.31 show that the measurements match the simulation results well. The small bounce amplitude and the maximum displacements at the sensor node coincide. Also, the predicted compactness of the contact region and the position in the rotating frame are verified by the experiments.

The results imply, that it is possible to assess the contact response qualitatively for some H_∞ controlled rotor systems by simulations. The example shows that stable periodic contact can exist even if magnetic bearings are controlled by robust MIMO controllers. However, these observations cannot be generalised. Other H_∞ controlled rotor systems might show a completely different behaviour. Each individual case has to be examined separately.

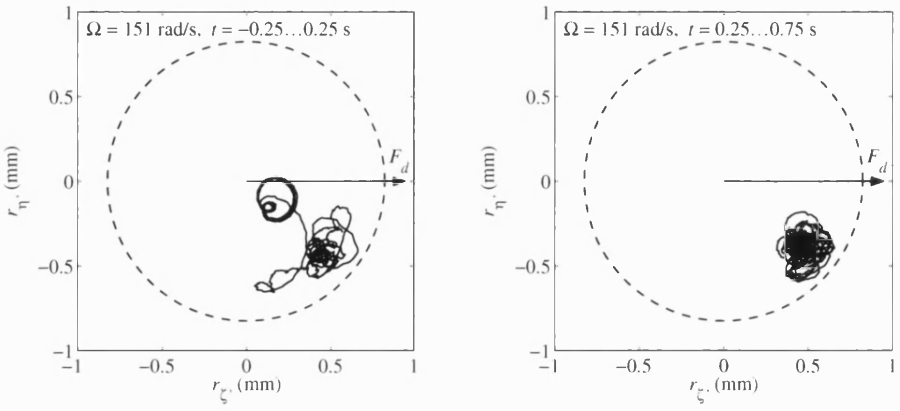

Figure 4.31: Contact response of a system with soft H_∞ controller after a small loss unbalance of $\varepsilon(t > 0) \approx 0.5\,\text{mm}$.

4.8 Closure

An analytical method to calculate contact dynamics of rigid and flexible rotors has been presented. The rotor may adopt asynchronous periodic contact modes with a fixed contact point in the rotating frame. A simple disk system was used to demonstrate the calculations and examine the influence of various system parameters. The more complex contact dynamics of the flexible rotor were then derived. Simulations and experiments showed an excellent match between theory and practice. It was demonstrated experimentally that H_∞ controlled rotor/magnetic bearing systems can present similar contact behaviour to rotors suspended by bearings with a linear spring-damper characteristic. An analytical examination of such systems is regarded as difficult, however, due to the complex dynamics of model based controllers.

5 Feed-forward Control Strategies for Contact Recovery

It has been shown in the previous chapter that rotors subject to synchronous disturbance forces above a certain magnitude can enter stable periodic contact modes. The cause of this can be sudden or high acceleration base motion or mass loss. Due to the stability of the contact modes, the rotor will not progress to a contact-free orbit unless control action is taken. It is therefore common practice to shut a machine down if the rotor makes persistent contact with the stator. However, in transport applications or large power plants, for example, a shutdown is very undesirable if not impossible to undertake quickly. Furthermore, the rotor might pass through several resonance frequencies during run-down, which can lead to even higher contact forces.

In this chapter it is examined how a rotor established in a periodic contact mode can be brought back to a contact free orbit using synchronous control forces applied through the magnetic bearings. The approach is to reduce the total synchronous excitation below a threshold where stable periodic contact modes are not possible. The strategy is related to active unbalance compensation [5, 6], except that the measured displacements during contact cannot be used directly to derive the compensation forces [31]. It is examined whether the linear dynamical properties of the system, in particular transfer functions from nodal forces to nodal displacements, change in the contact case. This question is important if the magnetic bearing and the contact point are not at the same node. The simple disk system is used to demonstrate the discussed techniques before the application to the more complex flexible rotor.

5.1 Simple Rotor with Unbalance Compensation

It is crucial for contact recovery control to know the phase of unbalance forces acting on the rotor. It is much easier to calculate a contact recovery force if the unbalance is measured before contact occurs. The unbalance is known, for

example, in plants such as flywheels, gyros, and certain industrial appliances, where synchronous unbalance compensation is used to reduce the transmitted force between the magnetic bearings and the rotor.

5.1.1 Unbalance Force Compensation

Force-free rotation is achieved by letting the rotor spin around a principal axis rather than the geometric centre. In a PD controlled system, synchronous compensation forces are applied which "cancel" the magnetic bearing forces. For a disk rotor as considered here, these compensation forces can be easily derived.

If the mass, damping, and stiffness parameters are denoted by m, d, and k, respectively, the relationship between displacement and synchronous disturbance force in the frequency domain is

$$\frac{w(\Omega)}{F_d(\Omega)} = \frac{1}{-\Omega^2 m + \mathrm{j}\Omega d + k} \tag{5.1}$$

With $F_d = F_u = \varepsilon m \Omega^2$, one can find the unbalance mass eccentricity ε with

$$\varepsilon = w \frac{-\Omega^2 m + \mathrm{j}\Omega d + k}{-\Omega^2 m} \tag{5.2}$$

where w is the measured complex displacement in the rotating frame. The desired rotor displacement for force-free rotation is $-\varepsilon$, therefore the centre of rotation has to be shifted by

$$\Delta w = -\varepsilon - w = -w \left(\frac{-\Omega^2 m + \mathrm{j}\Omega d + k}{-\Omega^2 m} + 1 \right) \tag{5.3}$$

With (5.1), the necessary compensation force F_a follows as

$$F_a(\Omega) = -w \left(\frac{-\Omega^2 m + \mathrm{j}\Omega d + k}{-\Omega^2 m} + 1 \right) \left(-\Omega^2 m + \mathrm{j}\Omega d + k \right) \tag{5.4}$$

Alternatively, one can say that F_a has to cancel the magnetic bearing force so that $F_a = F_{MB}$[1]. If the disk is spinning around the mass centre

$$F_{MB} = \varepsilon \left(\mathrm{j}\Omega d + k \right) \tag{5.5}$$

[1] F_{MB} is defined as reaction force, so it is positive if it acts in negative coordinate direction on the rotor (c.f. page 22)

Force	$\Omega = 180\,\text{rad/s}$	$\Omega = 300\,\text{rad/s}$
F_u (N)	430	1197
F_a (N)	$274\,e^{-j2.89}$	$288\,e^{-j2.74}$
F_d (N)	$178\,e^{-j0.39}$	$937\,e^{-j0.12}$
$F_{d\,min}$ (N)	215	305

Table 5.1: Unbalance forces and computed compensation forces with $\varepsilon = 0.266\,\text{mm}$.

Hence,

$$F_a(\Omega) = -w\left(\frac{-\Omega^2 m + j\Omega d + k}{-\Omega^2 m}\right)(j\Omega d + k) \tag{5.6}$$

which is equivalent to equation (5.4).

5.1.2 Simulated Contact Recovery with Known Unbalance

For the following calculations, the rotor parameters are the same as in the previous chapter, namely $m = 50\,\text{kg}$, $d = 1400\,\text{Ns/m}$, $k = 1\,\text{MN/m}$, and $s_c = 0.8\,\text{mm}$, $\mu = 0.15$, $\beta = 0.98$. For $\varepsilon = 0.266\,\text{mm}$, the unbalance and compensation forces are listed in Table 5.1.

It can be seen that at $\Omega = 180\,\text{rad/s}$ with applied compensation $|F_a + F_u| = |F_d| < F_{d\,min}$, so that the rotor will not make persistent contact with the stator. At $\Omega = 300\,\text{rad/s}$, however, the amplitude of the sum of synchronous disturbance forces is larger than the minimum force required for stable periodic contact modes so that persistent rotor-stator contact is likely to develop after an initial impact.

Once a contact mode is established, the total synchronous force acting on the disk must be reduced to a value below $F_{d\,min}$ in order to bring the rotor back to a contact-free orbit. Therefore, the optimal recovery force for the disk with unbalance compensation is $F_r = -F_d = -(F_u + F_a)$.

Simulations at $\Omega = 180\,\text{rad/s}$ and $\Omega = 300\,\text{rad/s}$ have been carried out to verify the results. In the first second of the simulation, only unbalance forces are considered to act on the rotor. At $t = 1\,\text{s}$, a compensation force F_a was applied leading to force-free rotation. At $t = 2\,\text{s}$, the base was shaken, which caused contact between the rotor and the auxiliary bearing.

Figure 5.1 shows that, as predicted, no stable contact mode could be established at $\Omega = 180\,\text{rad/s}$. After a few contacts, the rotor returned to a contact-free orbit. Hence, no further control input was required.

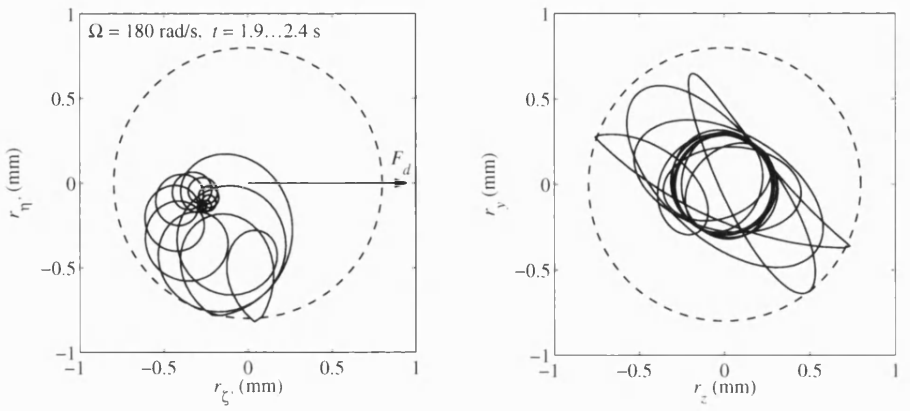

Figure 5.1: Rotor response to base motion at $\Omega = 180\,\mathrm{rad/s}$. No persistent contact is established.

At $\Omega = 300\,\mathrm{rad/s}$, the rotor makes persistent contact after the base motion event as shown in Figures 5.2 and 5.3. After a short initial transient response, the rotor settles to a periodic contact mode. At $t = 3\,\mathrm{s}$, a recovery force $F_r = -F_d$ was applied and the rotor motion became contact-free with an orbit of small amplitude. The magnetic bearing force was large, however, until the recovery force was switched of at $t = 4\,\mathrm{s}$ when the original force-free rotation was adopted again. This example shows, that a rotor can be successfully recovered from stable periodic contact modes by applying synchronous forces through the magnetic bearings.

5.2 Contact after Mass Loss

A sudden increase of unbalance after mass loss is a rather common problem for turbo machinery. After a mass loss event leading to rotor-stator contact, three cases have to be distinguished:

Case 1: Contact is not persistent; the rotor adopts a contact free orbit after a few impacts.

Case 2: Persistent contact is established with non-periodic or chaotic motion.

Case 3: The rotor adopts a periodic contact mode after an initial transient phase.

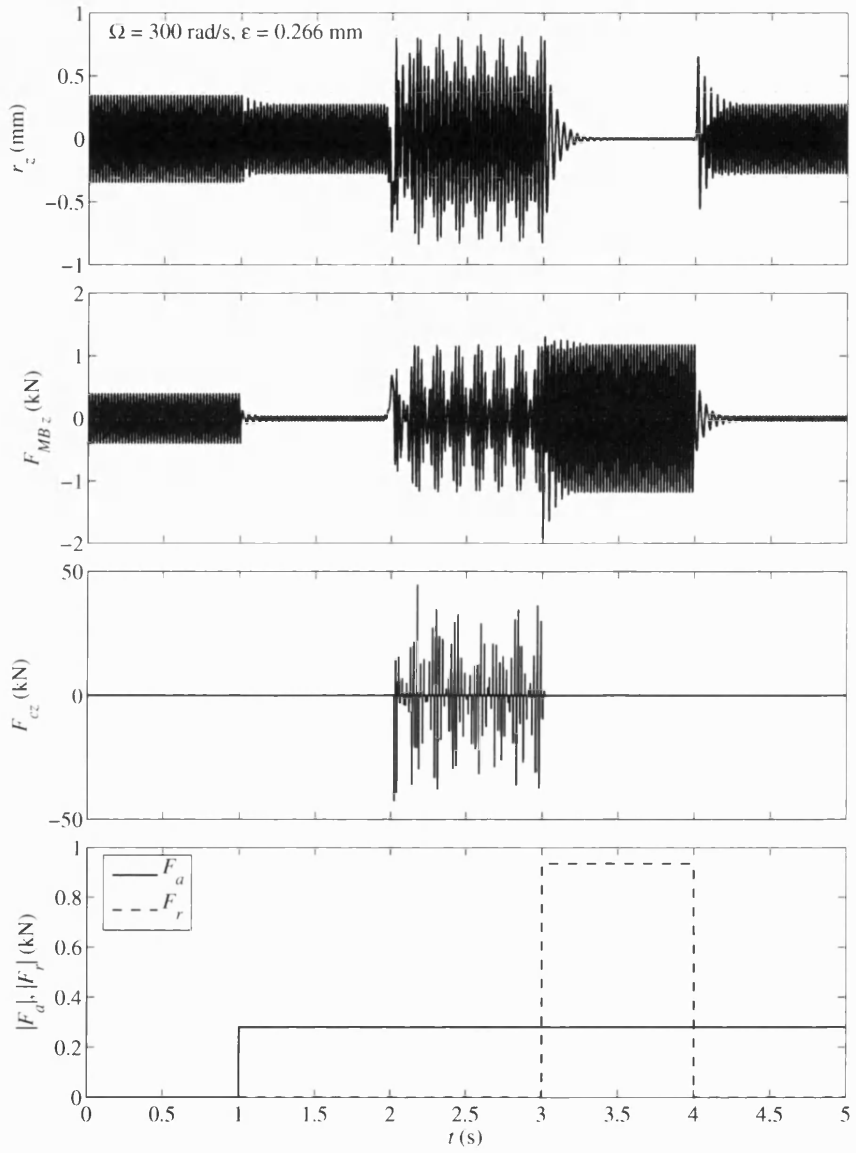

Figure 5.2: Rotor response and applied control and contact forces during contact recovery at $\Omega = 300\,\mathrm{rad/s}$.

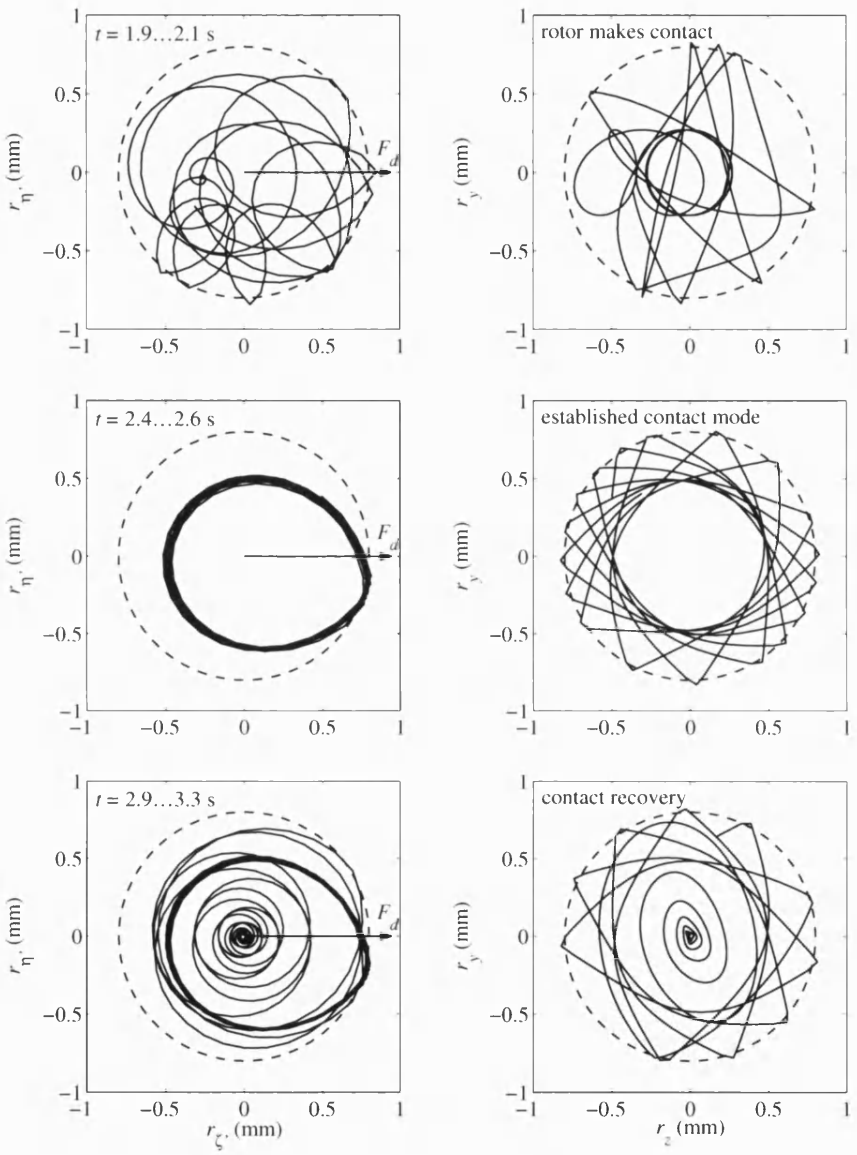

Figure 5.3: Simulated rotor motion at selected times in the rotating and stationary frame.

In Case 1, no further control action is required unless the new contact-free orbit or the transmitted forces are too large. If that happens, conventional synchronous unbalance compensation methods based on a linear rotor model can be applied.

If the rotor makes persistent contact after an initial impact, and the motion stays non-periodic or chaotic, no information about the unbalance causing the contact can be obtained. A machine shutdown or at least a reduction of the rotation speed seems to be the only option. If, however, the rotor adopts a periodic contact mode, the results from Chapter 4 can be used to find the phase of the unbalance force, which is the basis for recovery action.

5.2.1 Estimating the Unbalance Force

First, the contact point has to be determined by measuring the time dependent motion in the rotating frame. All points with a displacement magnitude greater than a certain threshold s_t are extracted and divided into four groups, one for each quadrant of the clearance circle as shown in Figure 5.4. A periodic contact mode is almost certainly not present if there are points in all quadrants or in only two non-consecutive ones. Such a measurement is dismissed and eventually repeated. In all other cases, the phase of the measured complex displacements with appropriate magnitude is calculated, and their median is taken as an estimate for the position of the contact point.

The standard deviation σ of the data is an indicator of confidence for the result. If σ is large, the measured points are well separated, indicating possible transient components in the motion. Therefore, the measurements should be repeated. If σ is small, however, the points are close together and the rotor is likely to be in a periodic contact mode.

It is useful to distinguish whether the contact mode is a rub or bounce type. The easiest way to find out is to divide the number of points with a magnitude greater than the threshold by the total number of samples. A ratio close to unity indicates a rubbing mode.

Obviously, the choice of the amplitude threshold s_t determining which points are used to calculate the contact point is crucial. In practice, it largely depends on the asymmetry and eccentricity of the auxiliary bearing, but a value of $\approx 90\%$ of the nominal clearance is appropriate. The length of the measurement interval is a compromise between speed and accuracy. It should be at least ten times the rotation period to get meaningful statistical results.

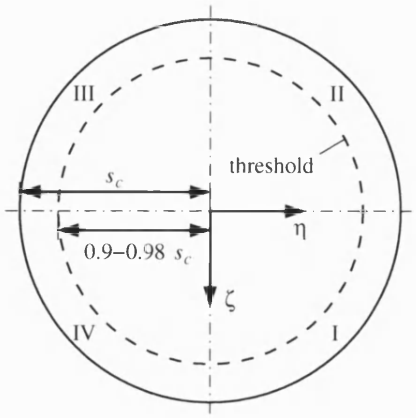

Figure 5.4: Measured displacements with a magnitude greater than a certain threshold are divided into four groups.

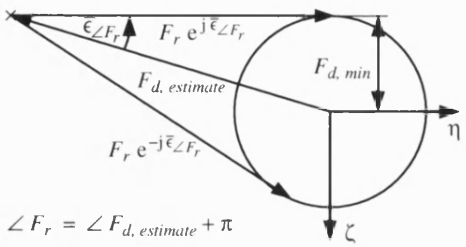

Figure 5.5: The phase of the unbalance must be known with an accuracy of $\pm\epsilon_\phi$ for guaranteed recovery.

Once the contact point is known, the phase of the unbalance force can be estimated from plots of the type in Figure 4.3. For stable contact modes of the disk system, the maximum phase ψ between unbalance force and contact point is 90°. The larger the unbalance, the the smaller the phase.

The rotor is guaranteed to recover from persistent periodic contact if the amplitude of the vector sum of disturbance force and recovery force $|F_d + F_r|$ is smaller than than $F_{d\,min}$, the minimum synchronous disturbance force amplitude for which periodic contact is possible. Therefore, recovery becomes more difficult for large unbalances and/or small values of $F_{d\,min}$. It follows from Figure 5.5 that the phase of the unbalance must be known with an accuracy of $\pm\bar{\epsilon}_{\angle F_r}$ for guaranteed recovery, where

$$\bar{\epsilon}_{\angle F_r} = \arcsin \frac{F_{d\,min}}{|F_d|} \tag{5.7}$$

Although the phase of the unbalance force can be estimated, there is generally no information available about its magnitude. Therefore, the required compensation force magnitude is unknown and has to be found iteratively by increasing it in steps until the rotor progresses to a contact free orbit or the angular contact point location changes significantly (phase change greater 90°). The latter can happen if $|F_d + F_r|$ does not become small enough to pull the rotor off, e.g. because the

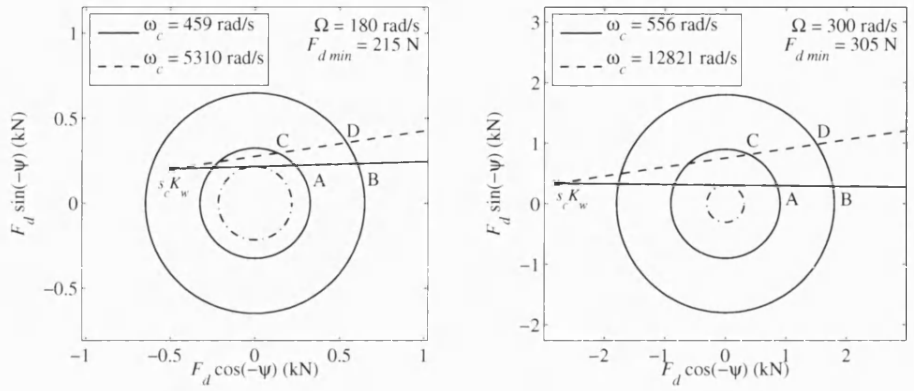

Figure 5.6: Contact mode phases for $\varepsilon = 0.2\,\text{mm}$ and $\varepsilon = 0.4\,\text{mm}$.

phase of the unbalance force was not determined correctly, or $|F_r|$ was increased with excessive increments. In that case, one can either abort or repeat the same process again with updated parameters.

5.2.2 Theoretical Contact Point Locations

The disk system is considered at the rotational speeds $\Omega = 180\,\text{rad/s}$ and $\Omega = 300\,\text{rad/s}$. Figure 5.6 shows possible contact frequencies and related angular contact point locations for unbalance mass eccentricities $\varepsilon = 0.2\,\text{mm}$ and $\varepsilon = 0.4\,\text{mm}$. Cases A and B are bounce-like modes, whereas C and D are indicate rotor-stator rub. In practice, bounce-like responses are more likely after mass loss, because the initial impact angle is usually quite large.

Contact recovery attempts only make sense up to a certain level of unbalance. The maximum mass eccentricity considered for the disk system was $\varepsilon = 0.4\,\text{mm}$. At $\Omega = 180\,\text{rad/s}$, this unbalance is well above the level at which the non-contact orbit is larger than the annual clearance (threshold is $\varepsilon = 0.3305\,\text{mm}$). At $\Omega = 300\,\text{rad/s}$, the theoretical bounce amplitude at $\varepsilon = 0.4\,\text{mm}$ is close to the bearing clearance. Any higher levels of unbalance are likely to lead to damaging backward whirl.

The unbalance phase must be known for recovery, but only the angular contact point location can be measured. Therefore, an important aspect is a good estimate of ψ. Ideally, the estimate should allow the successful recovery for a wide range of unbalance force magnitudes. Table 5.2 lists ψ and $\overline{\epsilon}_{\angle F_r}$ for the contact cases of interest. It was decided to set $\psi_e \approx \psi(\varepsilon = 0.4\,\text{mm})$ for each response type, i.e. for

Case	$\Omega = 180\,\text{rad/s}$			$\Omega = 300\,\text{rad/s}$		
	$\lvert F_d \rvert$ (N)	ψ (rad)	$\bar{\epsilon}_{\angle F_r}$ (rad)	$\lvert F_d \rvert$ (N)	ψ (rad)	$\bar{\epsilon}_{\angle F_r}$ (rad)
A	324	-0.7557	0.7277	900	-0.3362	0.3468
B	648	-0.3672	0.3390	1800	-0.1601	0.1708
C	324	-1.1493	0.7277	900	-1.1283	0.3468
D	648	-0.5828	0.3390	1800	-0.5767	0.1708

Table 5.2: Unbalance force amplitude, contact mode phase, and necessary guaranteed recovery accuracy for the contact cases shown in Figure 5.6.

bounce-like and rubbing modes at $\Omega = 180\,\text{rad/s}$, $\psi_e^{bounce} = -0.36\,\text{rad}$ and $\psi_e^{rub} = -0.58\,\text{rad}$, and at $\Omega = 300\,\text{rad/s}$, $\psi_e^{bounce} = -0.16\,\text{rad}$ and $\psi_e^{rub} = -0.58\,\text{rad}$.

The total error of the recovery force phase, $\epsilon_{\angle F_r}$, is the sum of the errors from the measurement of the contact point location ϵ_ϕ, and the difference between ψ and ψ_e, ϵ_ψ. Recovery in one step is only guaranteed if the recovery force amplitude is chosen correctly, and $\epsilon_{\angle F_r} + \epsilon_\phi + \epsilon_\psi \leq \bar{\epsilon}_{\angle F_r}$.

For the system of interest, a "2-step" recovery might be necessary if the rotor adopts a rubbing mode at $\Omega = 300\,\text{rad/s}$ for small unbalances. In mode C, for example, $|\psi - \psi_e^{rub}| > \bar{\epsilon}_{\angle F_r}$. At an initial recovery attempt with $\angle F_r = \psi_e^{rub} + \pi$, the magnitude of the sum of unbalance and recovery force will eventually be reduced to a value below the minimum unbalance force required for *rubbing* contact $F_{d\,min}^{rub} > F_{d\,min}^{bounce}$. Then, the rotor either comes off, or progresses to a bounce-like mode. If the latter happens, the unbalance force phase must be reassessed by measuring the contact point location and subtracting ψ_e^{bounce}.

5.2.3 Control Parameters for Contact Recovery

During normal operation, the rotor displacements in the rotating frame are measured repeatedly with a sample rate of 2048 Hz for 512 samples. No action is taken if no contact is detected. However, if some points have a magnitude greater than s_t, contact recovery is initialised. During the first measurement with detected contact, the rotor is usually in a transient state, and no action is taken as there is the possibility that the rotor returns unaided to a non-contacting orbit. After 0.125 s, or 256 sample periods, another measurement of 512 samples is started[2]. If contact is detected again, the angular contact point location is evaluated, as

[2]The reason for the delay between measurements is the way the method is implemented on the experimental real-time equipment. It is not necessary for simulations

Threshold	Measurement 2		Measurement 3		Measurement 10	
s_t (mm)	$\phi_{m\,2}$ (rad)	σ_2	$\phi_{m\,3}$ (rad)	σ_3	$\phi_{m\,10}$ (rad)	σ_{10}
0.7	-0.3422	0.4483	-0.3408	0.2912	-0.3228	0.2944
0.75	-0.3375	0.3709	-0.3185	0.1882	-0.3273	0.1885
0.8	-0.2559	0.3559	-0.3203	0.1020	-0.3228	0.0950

Table 5.3: Estimated angular contact point locations together with the standard deviation of the data sets for the second, third and tenth measurement cycle after contact.

described in Section 5.2.1. The data set is considered to be useful only if the standard deviation $\sigma < 0.5$. Otherwise, the measurement is repeated.

The recovery force phase is calculated with the results of the first valid measurement, and the magnitude is increased from zero in steps of 25 N per 0.1 s. The displacement measurements are repeated to check whether the rotor has returned to a contact free state. The increment of $|F_r|$ is stopped after the detection of a contact-free orbit, if the angular contact point location has changed by more than 90°, or if the limit of $|F_r| = 1000\,\mathrm{N}$ is reached. The latter two cases imply that recovery has failed and a new attempt has to be made.

All parameters mentioned above were found by "common sense". They are not optimal in any sense, but seem to be very suitable in practice. Some trial-and-error iterations will always be necessary to find appropriate values for other systems.

A first simulation was performed to find a suitable value for the threshold s_t. If it is too small, too many points are considered to calculate the contact location leading to a large variance and potentially large errors. If s_t is too large, some significant points might be missed and rubbing cannot be detected reliably. The values $s_t \in \{0.7, 0.75, 0.8\}\,\mathrm{mm}$ were tested for $\Omega = 300\,\mathrm{rad/s}$, and a total mass loss unbalance eccentricity of $\varepsilon = 0.2\,\mathrm{mm}$, which occurs in the middle of the first measurement cycle. The measured contact location ϕ_m and the standard deviation for the second, third, and tenth measurement cycle after the mass loss without the application of any recovery force are listed in Table 5.3.

It was expected that the standard deviation would become smaller and the results more accurate for later measurement cycles as the transient response decays to zero. Surprisingly, the standard deviations of the third and tenth measurement are almost identical, and the detected phase changes very little. A comparison with the theoretic value $\phi = -0.3362\,\mathrm{rad/s}$ reveals that the actual error of the

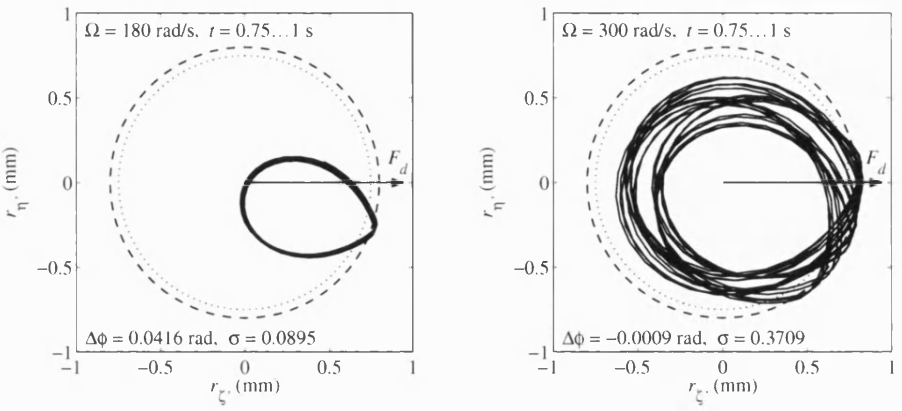

Figure 5.7: Measured motion in the rotating frame used to calculate the phase of the unbalance force.

measured angular contact point location is exceptionally small. This implies that the method is suitable. The threshold $s_t = 0.75\,\text{mm}$ was chosen for the following recovery simulations as it provides the best compromise between accuracy and reliability.

5.2.4 Simulated Contact Recovery with Unknown Unbalance

Simulations have been carried out to verify the methods for contact recovery after mass loss. The initial unbalance eccentricity was $\varepsilon = 0.02\,\text{mm}$, before a sudden mass loss led to an additional unbalance mass offset of $\varepsilon = 0.38\,\text{mm}$ at $\Omega = 180\,\text{rad/s}$, and $\varepsilon = 0.18\,\text{mm}$ at $\Omega = 300\,\text{rad/s}$, respectively. In both cases, the rotor adopted a stable periodic bounce-like contact mode after an initial transient response.

The measurement-evaluation cycle takes, as mentioned above, $0.25\,\text{s} + 0.125\,\text{s} = 0.375\,\text{s}$. The mass loss occurred at $t = 0.5\,\text{s}$ in the middle of the second measurement period. After contact is detected, the displacements in the following measurement period from 0.75 s to 1 s were used to find the contact location. Figure 5.7 shows the acquired data together with the threshold s_t represented by the dotted line.

The periodic contact mode is well established at $\Omega = 180\,\text{rad/s}$, only 0.25 s after the mass loss. At the higher speed of $\Omega = 300\,\text{rad/s}$, however, the transient motion has not fully decayed. Nevertheless, the actual measurement error ϵ_ϕ is

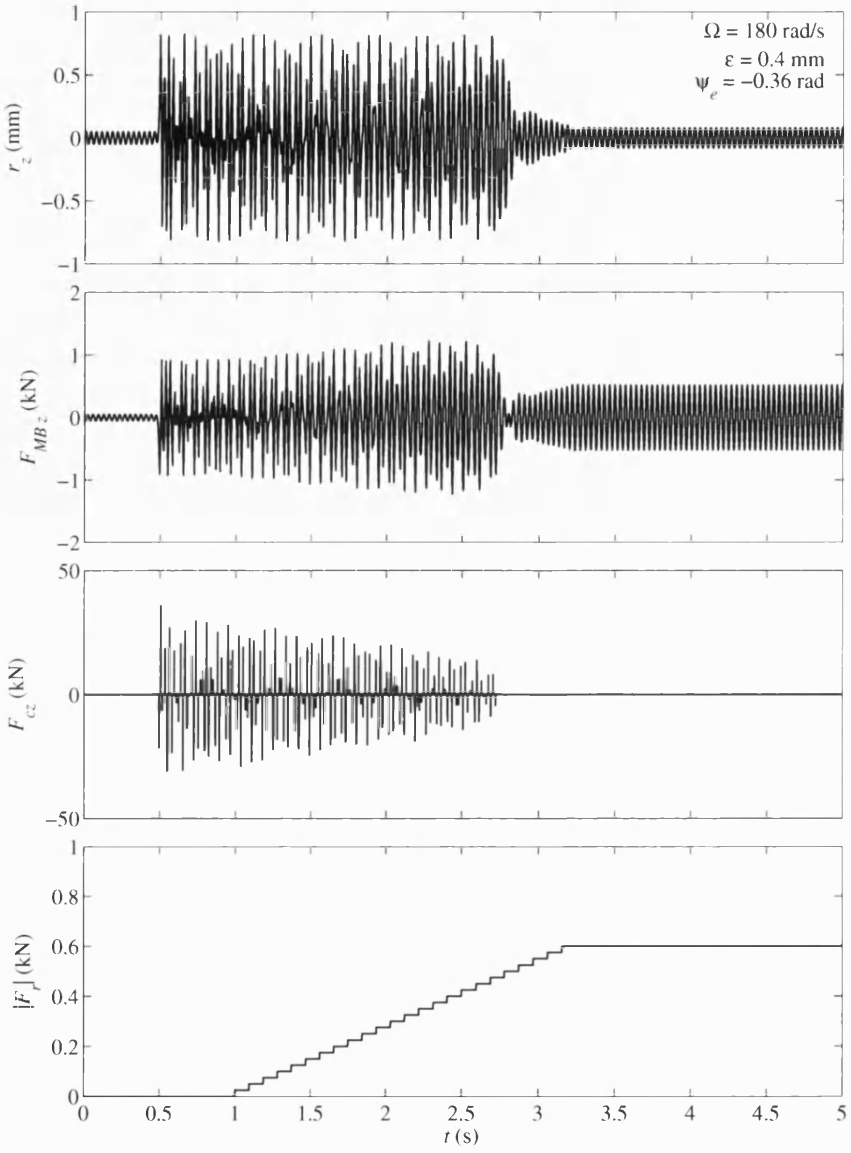

Figure 5.8: Rotor response, applied control and contact forces during contact recovery at $\Omega = 180\,\mathrm{rad/s}$.

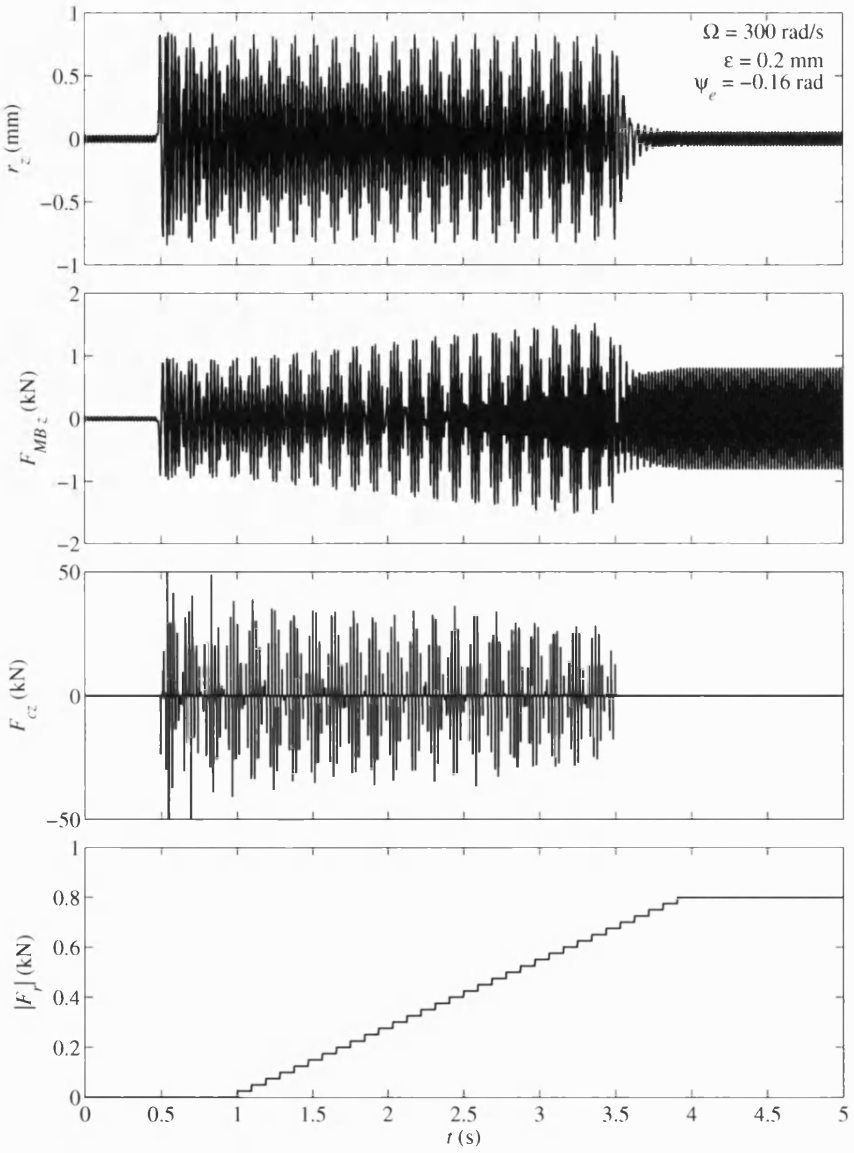

Figure 5.9: Rotor response, applied control and contact forces during contact recovery at $\Omega = 300\,\mathrm{rad/s}$.

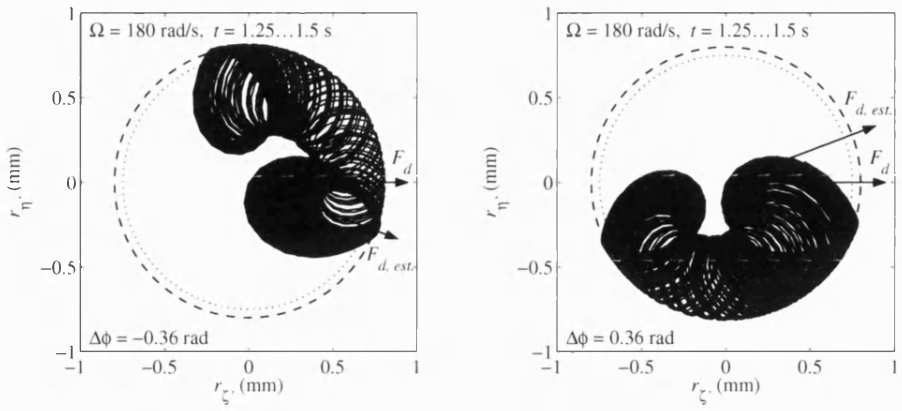

Figure 5.10: Contact recovery fails if the difference between estimated and real phase is larger than $\bar{\epsilon}_{\angle F_r}$.

small, and the standard deviation is within the limit of $\sigma < 0.5$. Therefore, the data shown in Figure 5.7 could be used to calculate the phase of the recovery force.

As soon as the recovery force phase is determined, F_r can be applied on the rotor with $|F_r|$ increasing in steps of 25 N per 0.1 s. Figures 5.8 and 5.9 show the rotor displacement and applied magnetic bearing force, contact force, and recovery force amplitude during the simulations at $\Omega = 180\,\text{rad/s}$ and $\Omega = 300\,\text{rad/s}$. In both cases, the recovery worked reliably. The rotor was brought to a contact-free state after a maximum of 3 s, even though the levels of unbalance were large.

When $|F_r|$ increased, the contact force reduced, but the amplitude of the magnetic bearing force $|F_{MB}|$ increased until the rotor became contact free. The final value of $|F_r|$ is comparable with the total unbalance force after mass loss. Hence, the amplitude of the unbalance is roughly known after recovery, and a decision can be made whether it is safe to let the machine running or whether a shutdown is required. Additionally, synchronous compensation forces which either reduce the rotor displacements or the transmitted magnetic bearing force could be derived with the standard linear methods.

Figure 5.10 shows what happens if the phase of the unbalance force is estimated with a deliberate error $\angle F_{de} - \angle F_d = \epsilon_{F_d} > \bar{\epsilon}_{\angle F_r}$. At this simulation with a rotational speed of $\Omega = 180\,\text{rad/s}$ and an unbalance eccentricity $\varepsilon = 0.4\,\text{mm}$, $\angle F_d$ was estimated with an error of $\epsilon_{F_d} = \pm 0.36\,\text{rad}$. Table 5.2 reveals that

$\overline{\epsilon}_{\angle F_r} = 0.339$, therefore $|F_d + F_r|$ will never be smaller than $F_{d\,min}$ and a failure of the recovery is likely.

In the current case, the location of the contact point changed by more than 90° before the limit of $|F_r| = 1000\,\mathrm{N}$ was reached. After such a recovery failure is detected, a new attempt with modified parameters can be made.

5.3 Flexible Rotor Contact Recovery

The contact recovery principle for flexible rotors is the same as for the simple disk system: Synchronous forces are applied through the magnetic bearings, which cancel the effective synchronous excitation. The major difference is that actuators, sensors, and the contact plane are not usually collocated. Hence, the detection of contact becomes more difficult and the flexible rotor dynamics have to be taken into account.

5.3.1 Unbalance Compensation of Flexible Rotors

The stationary complex displacements in the rotating frame at a node AJ are given by

$$w_{AJ} = H_{AJ,X}(\Omega)F_r + H_{AJ,AJ}(\Omega)F_d \tag{5.8}$$

in the non-contact case. F_r is a synchronous actuator force applied at node X, and F_d is the effective synchronous excitation at node AJ. $H_{AJ,X}$ and $H_{AJ,AJ}$ are appropriate transfer functions obtained from the FEM model and evaluated at the rotation speed Ω.

The aim is to drive $w_{AJ} \to 0$. If $X = AJ$, one gets

$$0 = H_{AJ,MB}(\Omega)F_r + H_{AJ,AJ}(\Omega)F_d \quad \Rightarrow \quad F_r = -F_d \tag{5.9}$$

which is the well known result from the previous section. If the forces are applied at a different node $X = MB$, where $MB \neq AJ$, then

$$0 = H_{AJ,MB}(\Omega)F_r + H_{AJ,AJ}(\Omega)F_d \quad \Rightarrow \quad F_r = -\frac{H_{AJ,AJ}(\Omega)}{H_{AJ,MB}(\Omega)}F_d \tag{5.10}$$

The evaluated transfer functions at $\Omega = 151\,\mathrm{rad/s}$ and $\Omega = 226\,\mathrm{rad/s}$ are listed in Table 5.4, where AJ and MB denote the non-driven end auxiliary and magnetic bearing nodes, respectively, and $H_r = \frac{H_{AJ,AJ}}{H_{AJ,MB}}$.

TF	$\Omega = 151\,\mathrm{rad/s}$	$\Omega = 226\,\mathrm{rad/s}$
$H_{AJ,AJ}$	$5.64 \cdot 10^{-6}\,\mathrm{e}^{-\mathrm{j}2.64}$	$1.39 \cdot 10^{-6}\,\mathrm{e}^{-\mathrm{j}3.07}$
$H_{AJ,MB}$	$1.45 \cdot 10^{-6}\,\mathrm{e}^{-\mathrm{j}3.11}$	$4.32 \cdot 10^{-7}\,\mathrm{e}^{-\mathrm{j}2.94}$
H_r	$3.88\,\mathrm{e}^{\mathrm{j}0.47}$	$3.22\,\mathrm{e}^{-\mathrm{j}0.13}$

Table 5.4: Evaluated transfer functions of the flexible rotor.

5.3.2 Limitations of Contact Recovery for Flexible Rotors

Periodic contact modes of rigid disk-like systems can always be recovered if the synchronous disturbance force magnitude does not exceed the maximum magnetic bearing force. There are more restrictions for flexible rotors.

First of all, the required actuator forces can exceed the unbalance forces significantly, as shown in Table 5.4. In the two example cases, $|H_r| \in [3, 4]$, which implies that the compensation force amplitude applied through the magnetic bearings has to be 3–4 times larger than the effective synchronous excitation at the contact point. In many cases it will not be possible to apply such large forces with magnetic actuators as saturation levels may be exceeded.

Even if that force capacity is available, there is the danger that the rotor will make contact at other auxiliary bearings due to the additional applied forces. Although it may be theoretically possible to return the rotor from such a state with the right recovery forces, a success in practice is questionable due to the large uncertainties. The problem of stable contact modes occurring in multiple planes is outside the scope of this thesis.

5.3.3 Amplitude and Phase of the Recovery Force

So far it has been assumed that transfer functions derived from the linear FEM model are still applicable in the contact case. In other words, if the disturbance force F_d at the contact location is known, one can calculate a magnetic bearing force with equation (5.10), which cancels F_d and guarantees recovery provided that no contacts at other locations are induced.

This is a bold statement considering that the contact dynamics are highly nonlinear and the motion changes dramatically once the rotor touches the stator. However, the results shown in Figure 4.23 are encouraging. It is shown that the phase difference between the displacement at the auxiliary bearings, w_{AJ}, and the magnetic bearing, w_{MB}, does not change if the rotor enters a stable periodic

contact mode.

Simulations have been carried out with the flexible rotor system described in Section 4.5. The non-driven end disk was subject to a mass eccentricity of $\varepsilon = 0.4\,\text{mm}$ at $\Omega = 151\,\text{rad/s}$, and $\varepsilon = 0.285\,\text{mm}$ at $\Omega = 226\,\text{rad/s}$. All other disks were considered to be perfectly balanced. The resulting disturbance forces are $F_d(\Omega = 151\,\text{rad/s}) = 118\,\text{N} \approx 2F_{d\,min}$ and $F_d(\Omega = 226\,\text{rad/s}) = 189\,\text{N} \approx 4F_{d\,min}$ (c.f. Figure 4.18). Contact-free rotation is possible in both cases, although the orbit at $\Omega = 151\,\text{rad/s}$ is just contained within the clearance circle.

A sudden simulated base motion at $t = 0.25\,\text{s}$ led to contact at the non-driven end auxiliary bearing. After an initial transient phase, periodic contact modes were induced. Between $t = 0.75\,\text{s}$ and $t = 1\,\text{s}$, the amplitude of the synchronous compensation force F_r was increased. The rotor motion between $t = 1.5\,\text{s}$ and $t = 1.75\,\text{s}$ was measured and used to assess the success of the recovery attempt.

Figures 5.11 and 5.12 summarise the results obtained with $\Omega = 151\,\text{rad/s}$ and $\Omega = 226\,\text{rad/s}$. The amplitude and phase of F_r are varied over a wide range. Each point represents one simulation, and the symbol indicates which result was obtained. In the first set of simulations, shown in the upper plots, F_r was applied at the contact node. Hence, the theoretically optimal amplitude and phase are $|F_r| = |F_d|$ and $\angle F_r = \pi$. At both rotational speeds, successful recovery is obtained for values around these points, as expected. The lower plots show the results for the more realistic case that the recovery force F_r is applied through the magnetic bearings. The frequency response values listed in Table 5.4 give optimal phases of

$$\angle F_r(\Omega = 151\,\text{rad/s}) = 3.61\,\text{rad} \approx 1.15\pi\,\text{rad} \tag{5.11a}$$

$$\angle F_r(\Omega = 226\,\text{rad/s}) = 3.01\,\text{rad} \approx 0.96\pi\,\text{rad} \tag{5.11b}$$

Again, those theoretical values coincide well with the simulation results. Not only the phase, but also the required amplitude of F_r is predicted correctly by the linear FEM model. The minimum force for which the rotor looses contact is roughly 3–4 times larger if F_r is applied at the magnetic bearing node rather than in the contact plane.

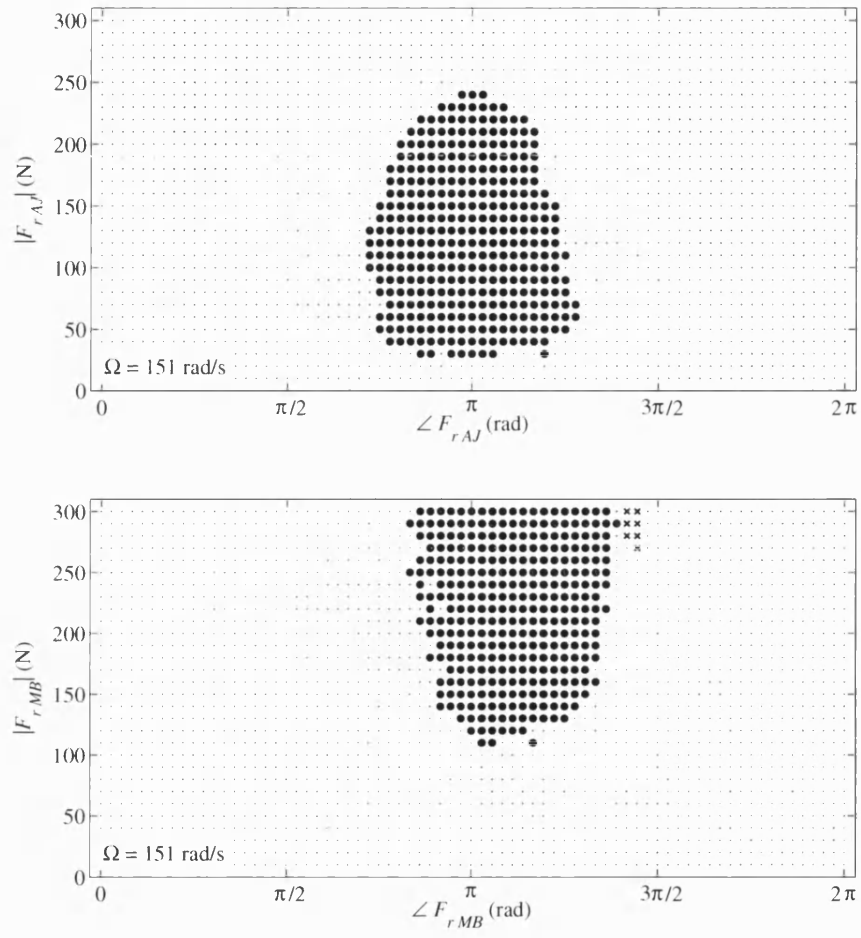

Figure 5.11: Recovery results at $\Omega = 151$ rad/s with F_r applied at the non-driven end contact node 15 (top) and the non-driven end magnetic bearing node 12 (bottom). Each point represents one simulation with the following results:

- $\cdot$ = contact condition has not changed
- $\bullet$ = recovery succeeded
- $\circ$ = contact recovered at original location but new contact at other nodes
- $\times$ = additional contact at other auxiliary bearings.

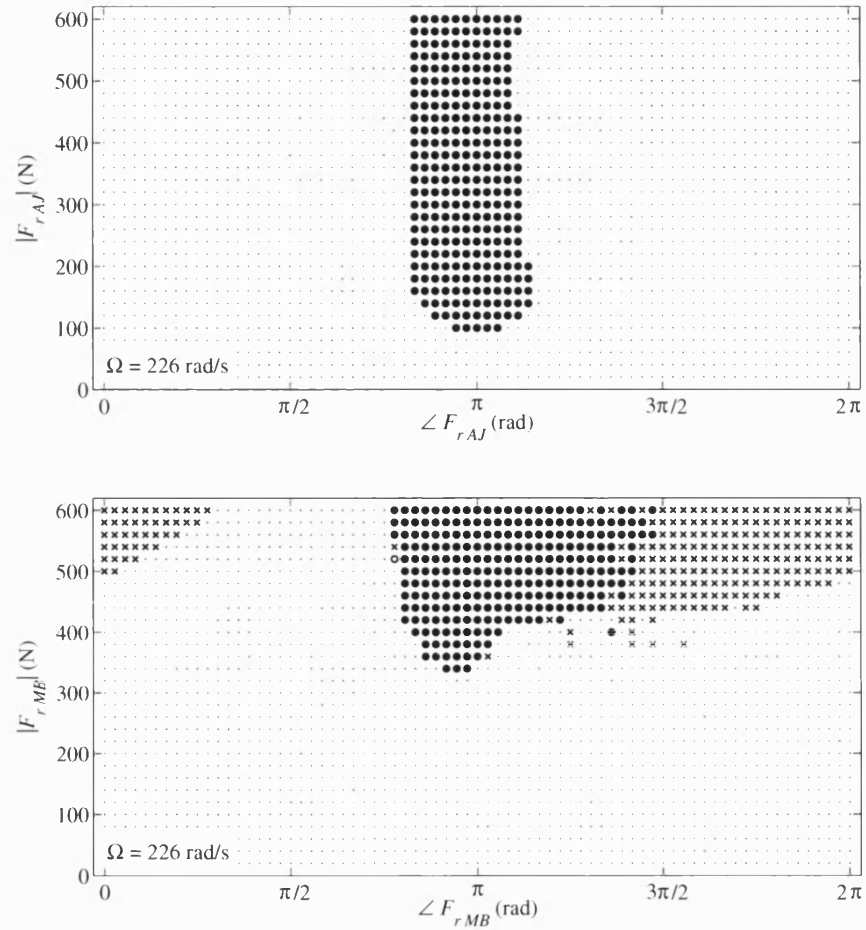

Figure 5.12: Recovery results at $\Omega = 226\,\mathrm{rad/s}$ with F_r applied at the non-driven end contact node 15 (top) and the non-driven end magnetic bearing node 12 (bottom). Each point represents one simulation with the following results:
- · = contact condition has not changed
- • = recovery succeeded
- ○ = contact recovered at original location but new contact at other nodes
- × = additional contact at other auxiliary bearings.

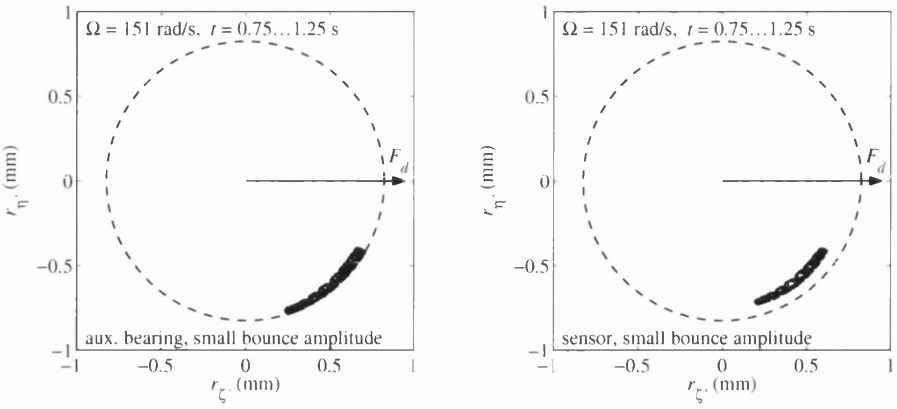

Figure 5.13: Motion with a small bounce amplitude mode at the non-driven end auxiliary bearing and sensor plane at $\Omega = 151\,\mathrm{rad/s}$. Recovery results are displayed in Figure 5.11.

5.3.4 Effects of the Adopted Contact Mode

The flexible rotor can adopt various periodic contact modes, as shown in Figure 4.16. Slight changes in the initial conditions can lead to very different responses. Now, it is examined whether the adopted mode has an influence on the required recovery force.

Figures 5.13 and 5.14 show simulations leading to two possible modes with a small and a large bounce amplitude, respectively. The motion is captured from 0.5 s to 1 s after the initial impact. Figure 5.11 in the previous section presents the recovery results for the contact mode with a small bounce amplitude, whereas Figure 5.15 corresponds to the mode with the larger amplitude.

It is apparent that the induced contact mode does not have a major effect on the required recovery force amplitude and phase. If the bounce amplitude is large, however, it is more likely that contacts at multiple auxiliary bearings will occur if F_r is chosen badly.

5.4 Contact Recovery with Unknown Unbalance

If the rotor makes contact and the unbalance is not known, it must be estimated from the measured displacements. The strategy was outlined in Section 5.2 for a simple disk system. However, some more issues arise for complex flexible systems,

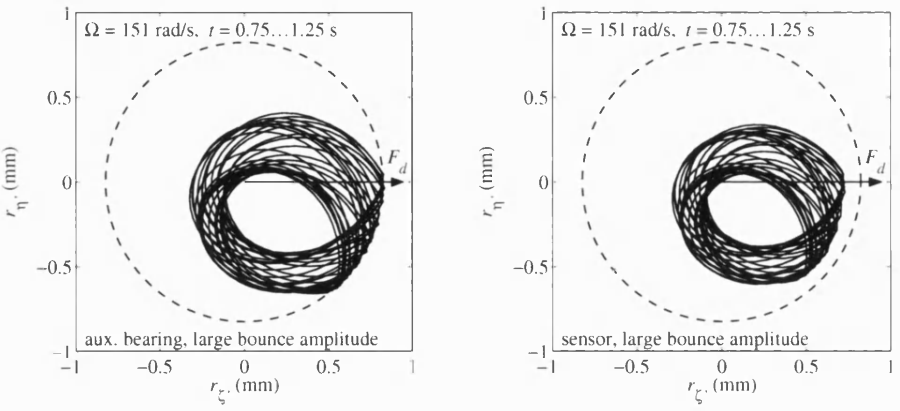

Figure 5.14: Motion with a large bounce amplitude mode at the non-driven end auxiliary bearing and sensor plane at $\Omega = 151\,\mathrm{rad/s}$. Recovery results are displayed in Figure 5.15.

which will now be discussed.

5.4.1 Detecting Contact

Auxiliary bearings and sensor are usually not collocated, so that the exact displacements at the contact location are unknown. Figures 5.13 and 5.14 show that at $\Omega = 151\,\mathrm{rad/s}$ the maximum measured displacement at the sensor location is smaller than at the auxiliary bearing. The threshold s_t has to be chosen accordingly. The optimal value depends on the rotational speed due to the flexibility of the rotor. For simulations, $s_t = 0.75\,\mathrm{mm}$ was found to be suitable at the rotational speeds $\Omega = 151\,\mathrm{rad/s}$ and $\Omega = 226\,\mathrm{rad/s}$.

If contact is a common problem in a particular application, the reliability of contact detection should be increased by accelerometers, force sensors, or microphones at the auxiliary bearings. This is especially so, if the rotor touches the stator at multiple locations since it is difficult to determine the correct state by displacement signals only.

5.4.2 Estimating the Contact Point Location

The angular contact point location in the rotating frame usually oscillates around the theoretical value for all but the most simple systems. One reason for non-constant contact points are the transient vibrations of the flexible structure sub-

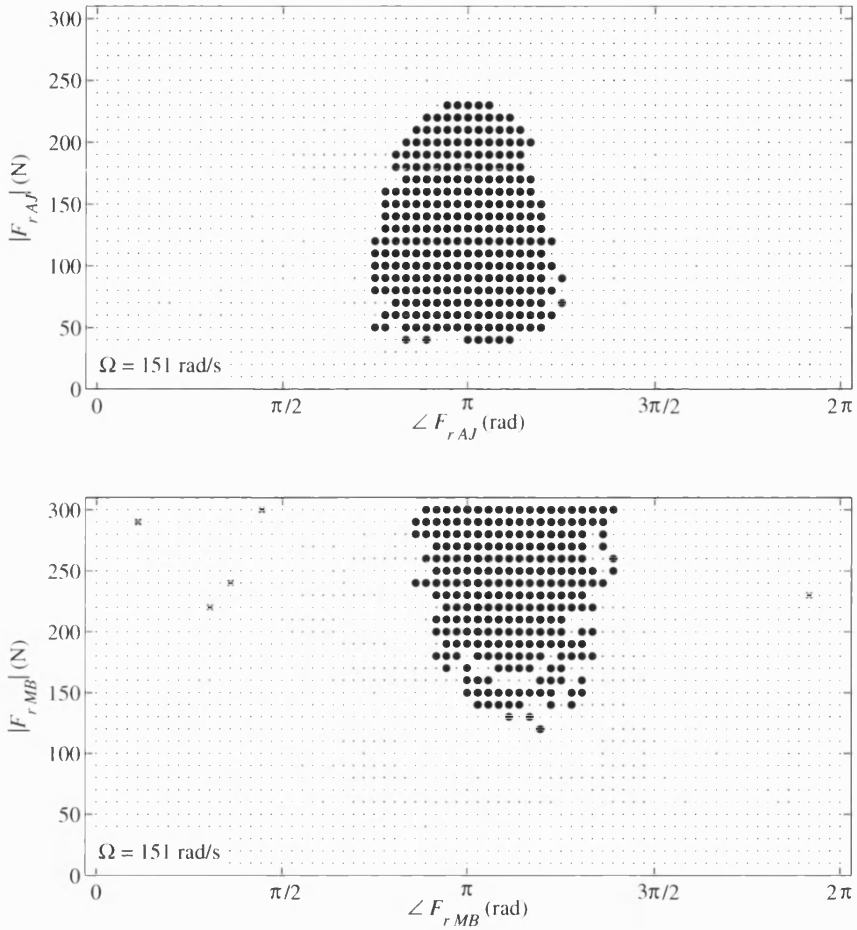

Figure 5.15: Recovery results at $\Omega = 151$ rad/s where the rotor was induced into a mode with a large bounce amplitude as opposed to Figure 5.11 where the amplitude is small. Each point represents one simulation with the following results:

- · = contact condition has not changed
- • = recovery succeeded
- ○ = contact recovered at original location but new contact at other nodes
- × = additional contact at other auxiliary bearings.

ject to excitation with large impulse forces. Oscillations of the angular contact point location around a nominal value can also occur if the rotor alternates between different contact modes. This behaviour can be caused by multiple possible contact modes with similar frequencies.

To keep the error of the contact point measurement in a reasonable range, it is desirable to position the sensors as close to the auxiliary bearings as possible. This is to make sure that the differences between measured and actual displacement magnitudes is small, and to avoid large phase differences. For the actual rotor with unbalance at the non-driven disk only, the theoretical phase difference between the sensor and the auxiliary bearing displacements, $\Delta\varphi = \varphi_{AJ} - \varphi_{SEN}$, for linear oscillations without contact is

$$\Delta\varphi(\Omega = 151\,\text{rad/s}) = 0.0972\,\text{rad} \quad \text{and} \quad \Delta\varphi(\Omega = 226\,\text{rad/s}) = 0.0519\,\text{rad} \tag{5.12}$$

These differences are so small that they can be neglected.

5.4.3 Calculating the Recovery Force Phase

The aim is to cancel the effective synchronous excitation in the contact plane by applying a suitable synchronous force F_r through the magnetic bearings. As information about the unbalance phase must be extracted from the measured angular contact point location, the phase between the contact point and the disturbance force, ψ is important. It is a function of the disturbance force amplitude $|F_d|$ and the contact frequency ω_c given by equation (4.45). Figure 5.16 shows the phase variation at two rotational speeds, $\Omega = 151\,\text{rad/s}$ and $\Omega = 226\,\text{rad/s}$.

In practice, the phase of the recovery force relative to the measured angular contact point location may be chosen as

$$\angle F_r = \phi_m + \angle H_{re} - \psi_e + \pi \tag{5.13}$$

where ϕ_m is the measured angular contact point location, and $\angle H_{re}$ and ψ_e are estimates of $\angle H_r$ and ψ, respectively. For successful recovery, the total error in the estimate of $\angle F_r$ must be smaller than $\bar{\epsilon}_{\angle F_r}$ given by equation (5.7). $\epsilon_{\angle F_r}$ is the sum of:

- the contact point measurement error $\epsilon_\phi = \phi - \phi_m$
- errors in the argument of the transfer function H_r: $\epsilon_{\angle H_r} = \angle H_r - \angle H_{re}$

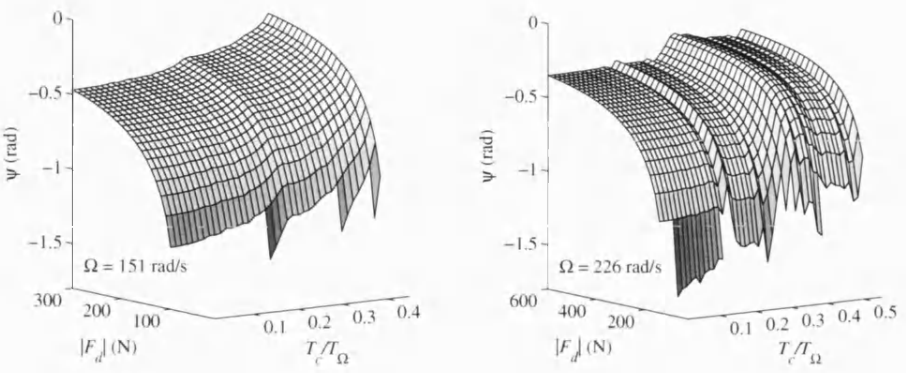

Figure 5.16: Angular contact point location relative to the disturbance force direction as function of $|F_d|$ and the contact mode period ratio T_c/T_Ω.

- the difference between the actual and the estimated phase between the contact point and the disturbance force $\epsilon_\psi = \psi - \psi_e$

Figure 5.17 shows the allowable bounds on $-\psi_e + \pi$, assuming that the contact mode, and therefore $F_{d\,min}$, does not change when F_r is applied. Provided that $|F_r|$ is chosen correctly, recovery is guaranteed if $\angle F_r - \phi - \angle H_r$ lies between the two surfaces for a given contact condition.

Fortunately, ψ changes little with the contact frequency, so that the choice of the recovery force phase can be made independently of ω_c. To find a suitable function for ψ_e, the 3D plots of Figure 5.17 are reorientated so that in Figure 5.18 the T_c/T_Ω axis is perpendicular to the page. This visualises the gap between the surfaces, which confine the region of suitable values for $-\psi_e + \pi$.

A second order polynomial fit may be used to minimise ϵ_ψ at high disturbance forces where the permissible error is small. It is used as the estimate for $-\psi + \pi$, and with the relation (5.13), the phase of the recovery force is given by a function of its amplitude as

$$\angle F_r(\Omega) = a\left(|H_r^{-1}||F_r|\right)^2 + b|H_r^{-1}||F_r| + c + \phi_m + \angle H_{re} \tag{5.14}$$

with the coefficients listed in Table 5.5.

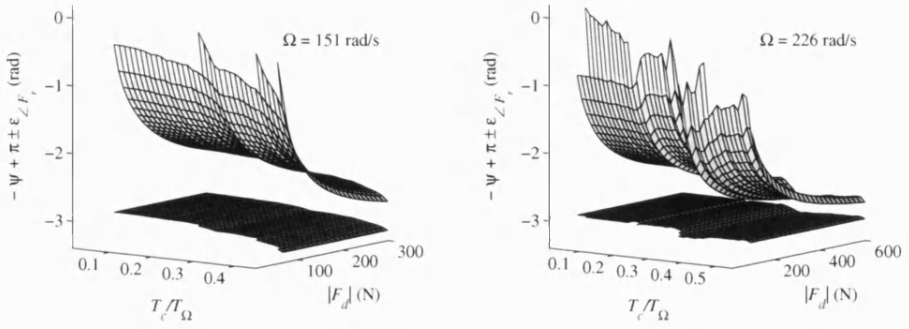

Figure 5.17: Allowable bounds for the estimate of $-\psi + \pi$ as function of the disturbance force amplitude and the contact mode period ratio.

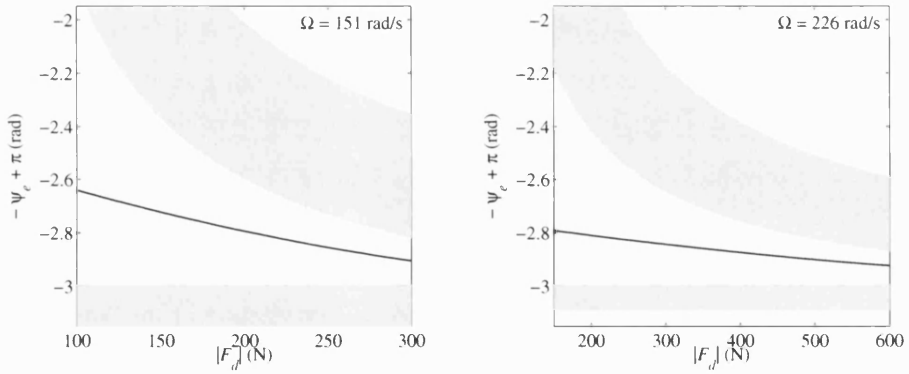

Figure 5.18: Estimate $-\psi_e + \pi$ as function of the disturbance force amplitude only. The gray areas are the error bounds above and below the optimal value (—) for successful recovery.

Ω (rad/s)	a	b	c
151	$2.150 \cdot 10^{-6}$	$-2.185 \cdot 10^{-3}$	-2.443
226	$1.797 \cdot 10^{-7}$	$-4.281 \cdot 10^{-3}$	-2.731

Table 5.5: Polynomial coefficients for equation (5.13).

5.4.4 Summary of the Recovery Procedure

The first step is to detect contact and to find out where it occurs. As mentioned, this can be quite difficult if only displacements are measured. When the contact node has been found, the contact point location in the rotating frame is measured. After a sufficiently accurate ϕ_m is obtained and H_r calculated, the recovery process is started using the magnetic bearing closest to the contact node.

As with the simple disk system, the amplitude of F_r is increased in steps from a start value until the rotor adopts a contact-free orbit or until other conditions are fulfilled. Such conditions include a large ($\approx 90°$) change of the angular contact point location, contact at additional auxiliary bearings, or the reach of a predefined limit of $|F_r|$. Whenever $|F_r|$ is increased, $\angle F_r$ is recalculated with equation (5.14).

When the rotor has come off, the actual unbalance can be calculated with the common linear methods. Based on these results, synchronous compensation forces can be applied, which further reduce displacements and/or actuator forces.

5.5 Contact Recovery Experiments

The procedure outlined above was implemented on the flexible rotor test rig. Contact was initialised by mass loss as described in Section 4.6. At $\Omega = 151\,\text{rad/s}$, an unbalance of $520\,\text{g cm}$ (or $\varepsilon = 0.4\,\text{mm}$) at the non-driven end disk led to a stable contact mode. Contact recovery action is highly desired, as changing the PD control parameters or the rotational speed will not bring the rotor back to a non-contacting orbit. Decreasing Ω even makes the contact forces larger due to the critical speed at 19 Hz.

5.5.1 Contact Recovery Parameters

The control parameters for contact recovery are similar to those used for the disk system in Section 5.2.3. The rotor displacement in the rotating frame is measured with a sample rate of 2048 Hz for 512 samples. The acquired data are evaluated in the following 0.125 s, before the next data set is obtained.

If contact is detected in two subsequent measurements, and $\sigma < \sigma_{max} = 0.6$, a synchronous recovery force F_r is applied. $|F_r|$ is increased in steps of 6.25 N per $\approx 0.1\,\text{s}$. The increment of $|F_r|$ is stopped after the rotor progresses to a non-

contacting orbit, if $|F_r| >= 500\,\mathrm{N}$, or if θ_m changes by more than 90°. In all experiments, mass loss occurred at the non-driven end disk, and the non-driven end magnetic bearing applied the compensation force.

5.5.2 Successful Contact Recovery

In the first experiment, the rotor was initially balanced so that the displacement amplitudes at all sensor nodes were smaller than 0.15 mm. At $t = 1\,\mathrm{s}$, a sudden mass loss occurred.

Figure 5.19 shows that from the displacement data alone, it is difficult to determine at which disk the mass loss actually happened. With additional force sensors or accelerometers at the auxiliary bearings, however, this problem could be solved. Here, it was known that the unbalance was caused by a mass eccentricity of the non-driven end disk, hence the rotational frame displacement at sensor plane 4 was used to estimate $\angle F_d$.

These data are shown in Figure 5.20 for selected time intervals. After the mass loss, the rotor quickly adopts a contact mode with a small bounce amplitude. The contact point varies by about ±45° around the average value. The standard deviation of the arguments of complex displacements with a magnitude greater than 0.8 mm is approximately $\sigma = 0.5$. The arrow F_d indicates the disturbance force caused by the mass loss. It does not take the unbalance distribution along the rotor into account and is therefore only an approximation for the total synchronous excitation which has to be compensated.

The second data set of 512 points, obtained between 0.65 s and 0.90 s after the initial impact, was used to calculate $\angle F_r$. At $\approx 0.95\,\mathrm{s}$ after the first contact, F_r was applied, and only 2.25 s later, the rotor has progressed to a contact free orbit. The final recovery force amplitude $|F_r| = 175\,\mathrm{N}$ was slightly larger than predicted by the simulation results shown in Figures 5.11 and 5.15. This is most likely caused by a larger unbalance in the experiment and a small error in the estimate of $\angle F_d$.

Displacement amplitudes after recovery were quite large due to the high unbalance forces. To allow a safe run-down, conventional unbalance compensation techniques could be applied to get accurate estimations of the unbalance distribution and reduce the vibration at selected locations, if desired.

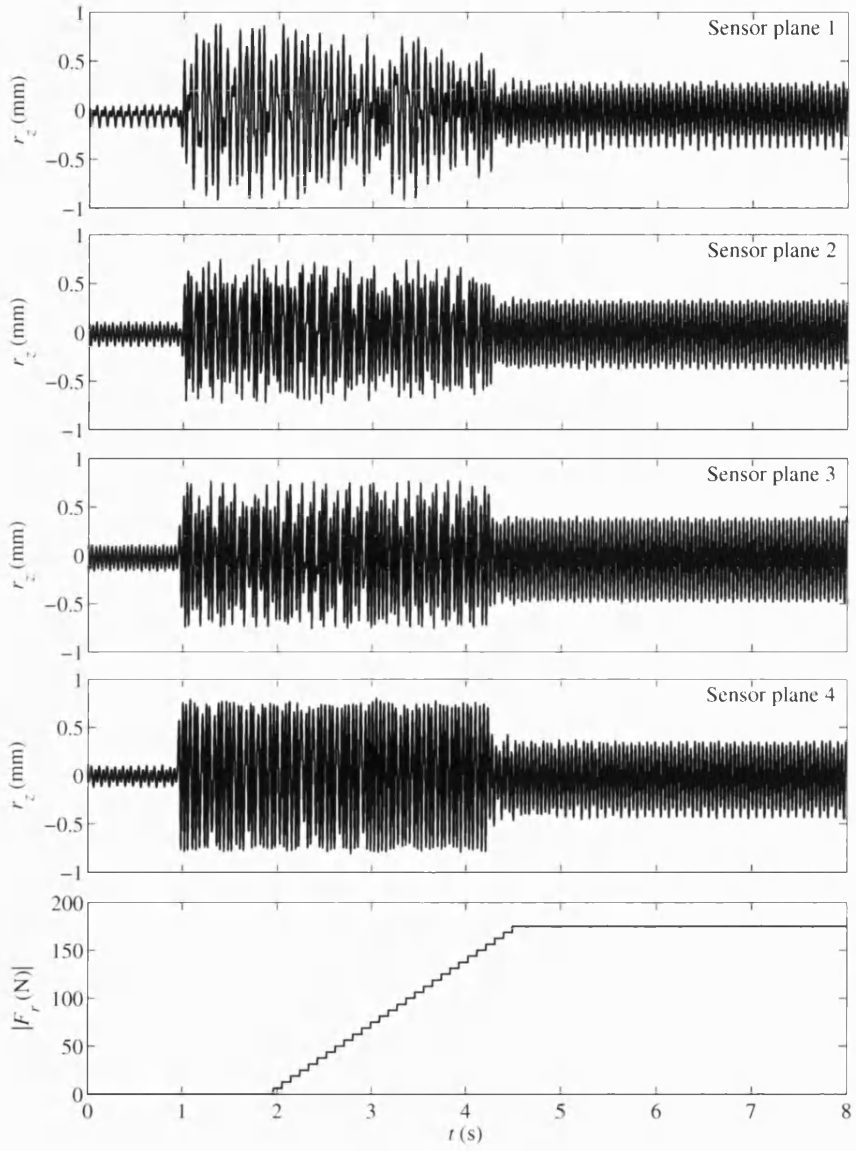

Figure 5.19: Rotor response and applied contact recovery forces after mass loss of 520 g cm at $t = 1$ s. The rotational speed was $\Omega = 151$ rad/s.

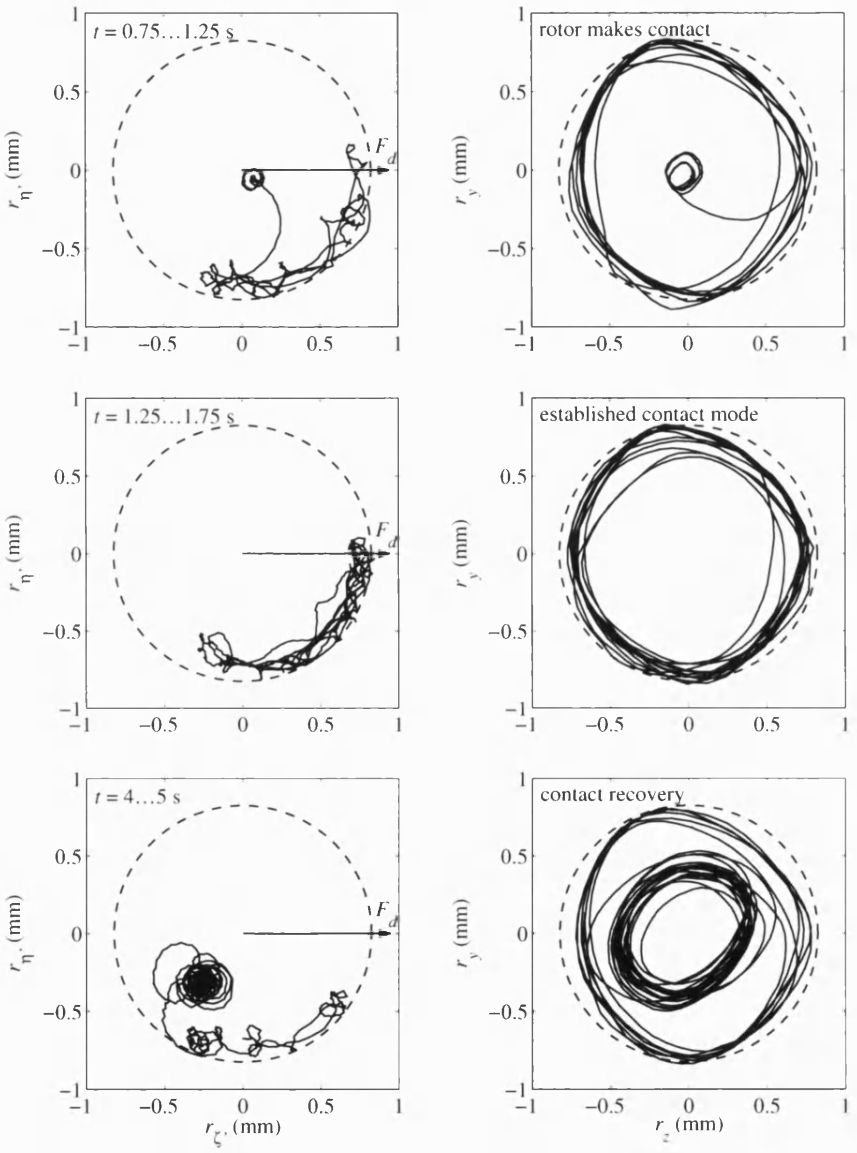

Figure 5.20: Rotor motion at selected times in the rotating and stationary frames during the mass loss experiment showing successful recovery.

5.5.3 Allowable Bounds on the Recovery Force Phase

Two experiments were performed in which the phase of the disturbance force was deliberately set to be 60° larger/smaller than estimated, before F_r was calculated. The simulation results in Figures 5.11 and 5.15 suggest that recovery should fail in both cases.

If 60° is added to the measured $\angle F_d$, the rotor contact free position was recovered nevertheless, as shown in Figures 5.21 and 5.22. However, it takes some time for the rotor to come off, and the required compensation force is large. The vibration amplitudes after recovery are similar to those obtained in the previous section.

If $\angle F_d$ is set to be 60° smaller value than estimated, the recovery fails as shown in Figures 5.23 and 5.24. The recovery force is increased to the limit of $|F_{r\,max}| = 500\,\mathrm{N}$, which causes contact at both magnetic bearings in addition to the original contacting auxiliary bearing. Furthermore, the contact point location in the rotating frame swings anti-clockwise by about 70°. This is similar to the simulation result shown in Figure 5.10.

It could be assumed, that in practice ψ is slightly larger than in theory. Some experiments with modified values have been performed. However, the results of Section 5.5.2, in particular the recovery time, force amplitude, and displacements after recovery could not be improved.

5.6 Contact Recovery for H_∞ Controlled Systems

Contact phenomena of H_∞ controlled rotor/magnetic bearing systems have been discussed in Section 4.7. It was found that periodic contact modes can become established. Experimental testing was undertaken to establish whether the rotor can be recovered to a non-contacting state by applying appropriate synchronous forces through the magnetic bearings.

5.6.1 Recovery Control Parameters

Two values that have to be determined before contact recovery is attempted are the phase of the influence coefficients from magnetic bearing forces to virtual forces at the contact point, $\angle H_r$, and the angle between contact point and unbalance force direction, ψ. H_r can be obtained from the FE model as explained in Section 5.3.1.

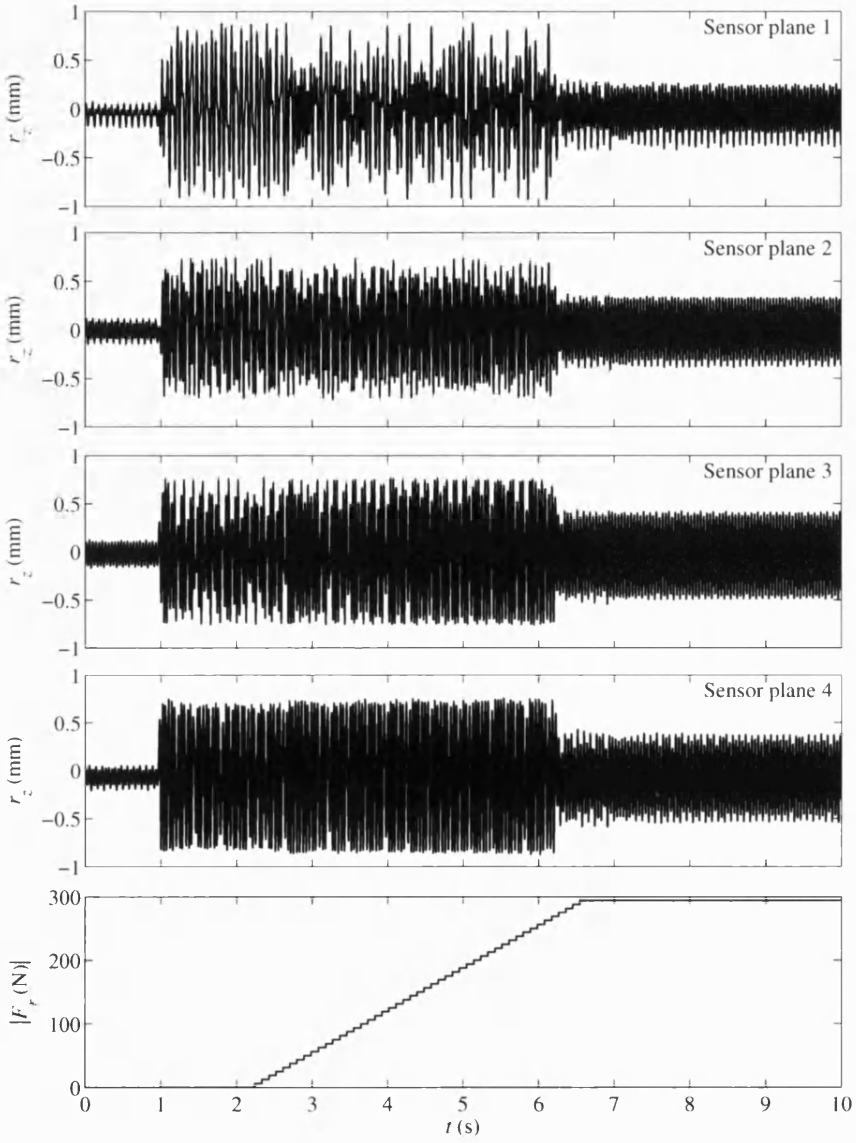

Figure 5.21: Recovery succeeds if $\angle F_r$ is chosen 60° larger than calculated, but the recovery time is longer and the applied forces are higher.

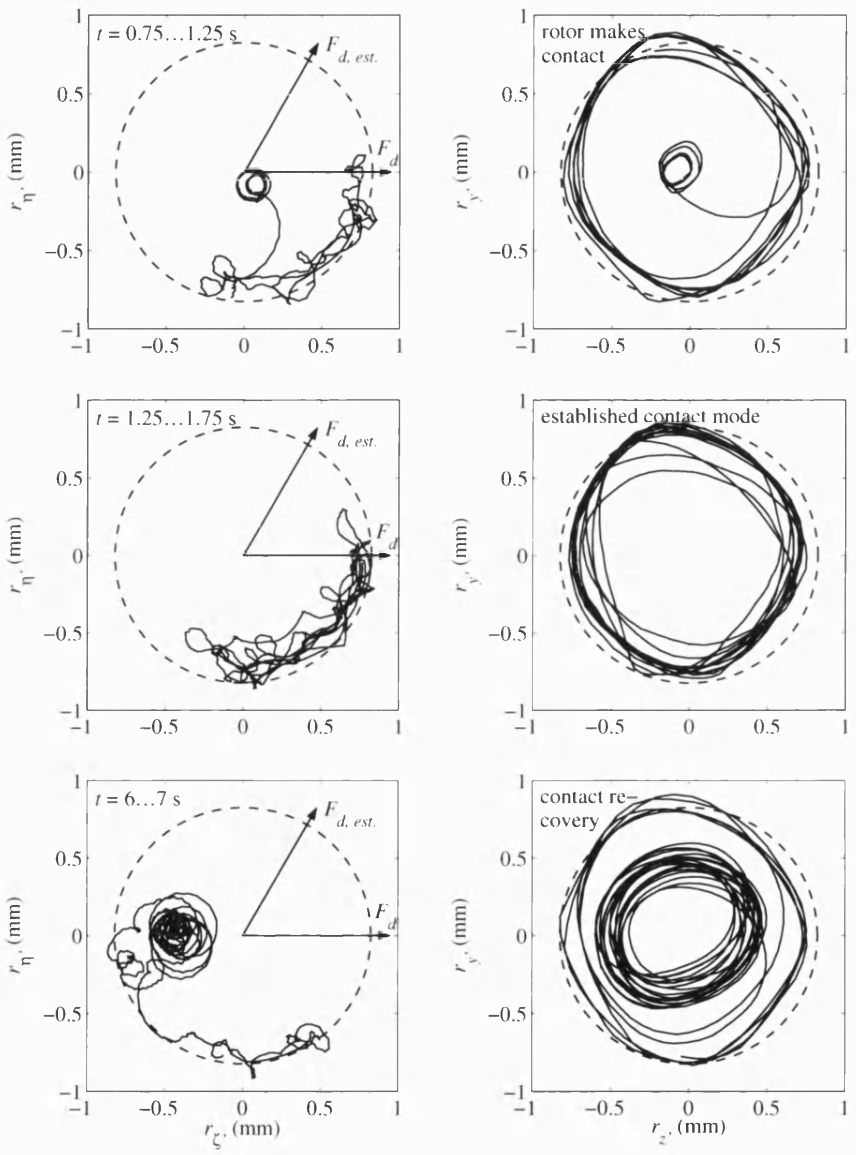

Figure 5.22: Rotating frame displacements corresponding to the responses shown in Figure 5.21.

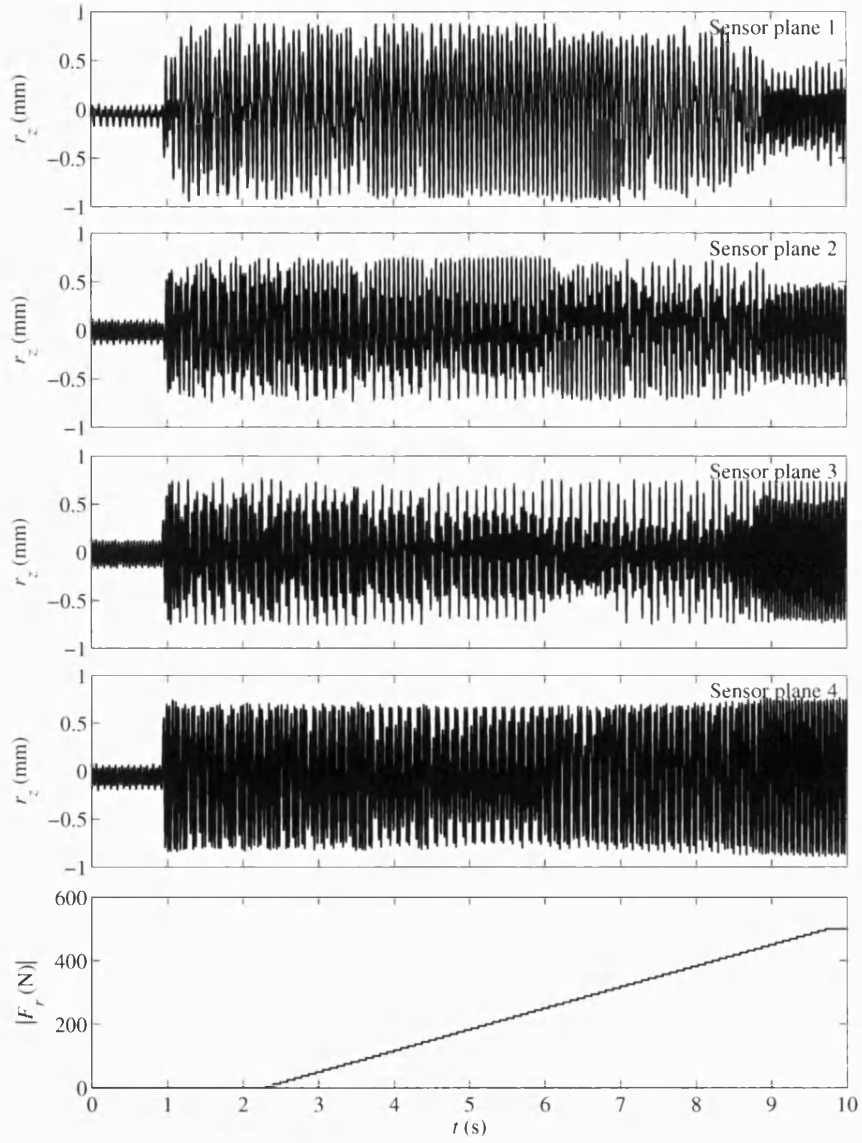

Figure 5.23: The recovery force phase is deliberately chosen 60° smaller than calculated, which leads to a failed recovery attempt.

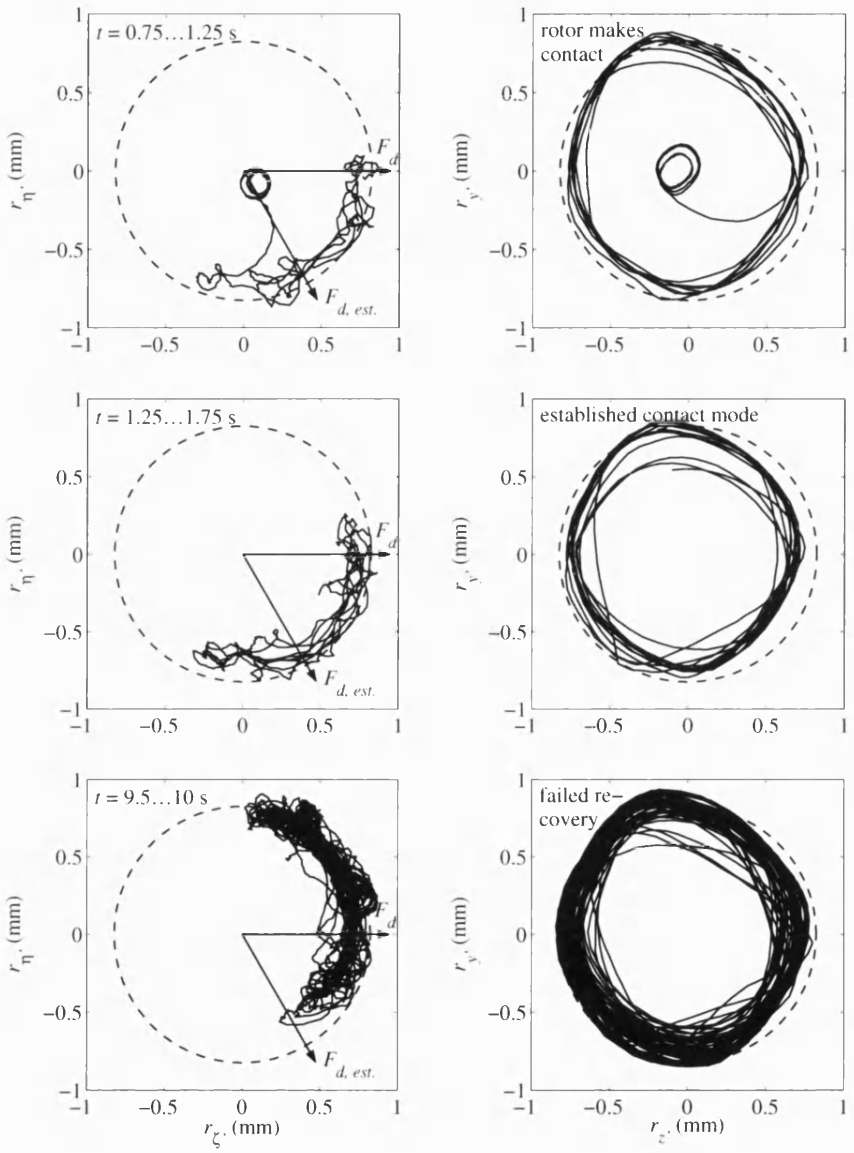

Figure 5.24: The angular contact point location in the rotating frame changes if $\epsilon_{\angle F_r}$ is too large.

TF	hard H_∞ controller	soft H_∞ controller
$H_{AJ,AJ}$	$6.76 \cdot 10^{-6}\,\mathrm{e}^{-\mathrm{j}1.44}$	$1.19 \cdot 10^{-5}\,\mathrm{e}^{-\mathrm{j}1.33}$
$H_{AJ,MB}$	$1.50 \cdot 10^{-6}\,\mathrm{e}^{-\mathrm{j}1.77}$	$2.54 \cdot 10^{-6}\,\mathrm{e}^{-\mathrm{j}2.19}$
H_r	$4.50\,\mathrm{e}^{\mathrm{j}0.32}$	$4.68\,\mathrm{e}^{\mathrm{j}0.86}$

Table 5.6: Evaluated transfer functions of the flexible rotor with H_∞ controlled magnetic bearings at $\Omega = 151\,\mathrm{rad/s}$.

The influence coefficient data for the hard and soft H_∞ controlled systems at $\Omega = 151\,\mathrm{rad/s}$ are listed in Table 5.6.

ψ can be calculated for PD controlled plants, but if MIMO model based controllers are used it must be determined from simulations or experiments. Here, the rather crude estimates $\psi_e^{\mathrm{hard}} = \frac{2}{3}\pi$ and $\psi_e^{\mathrm{soft}} = \frac{1}{2}\pi$ are used. They follow from the experimental data shown in Figures 4.30 and 4.31, respectively.

As pointed out earlier, measured displacements close to the contact point are significantly smaller than the bearing clearance for the H_∞ controlled rotor. Hence, the contact detection threshold s_t is set to only 0.6 mm. All other recovery control parameters are the same as for the PD system.

5.6.2 Experimental Results

The measured data of the contact recovery experiment with a hard H_∞ controller are presented in Figures 5.25 and 5.26. After a mass loss at $t = 1\,\mathrm{s}$ causing an unbalance of 650 g cm at the non-driven end disk, the rotor quickly adopts a stable contact mode with a fixed contact point in the rotating frame. This was detected by the recovery algorithm, which computes the phase $\angle F_r$. At roughly $t = 2\,\mathrm{s}$, $|F_r|$ was gradually increased until $|w| < s_t$.

The recovery is successful, but the contact-free orbit is quite large. As soon as $|F_d|$ is reduced to a level at which the contact-free orbit is smaller than the clearance, the rotor loses contact. It does not "stick" to the stator at small unbalance forces as the PD controlled systems did.

5.7 Closure

It was shown in this chapter that a rotor established in a stable periodic contact mode can be recovered to a non-contacting orbit by applying appropriately phased

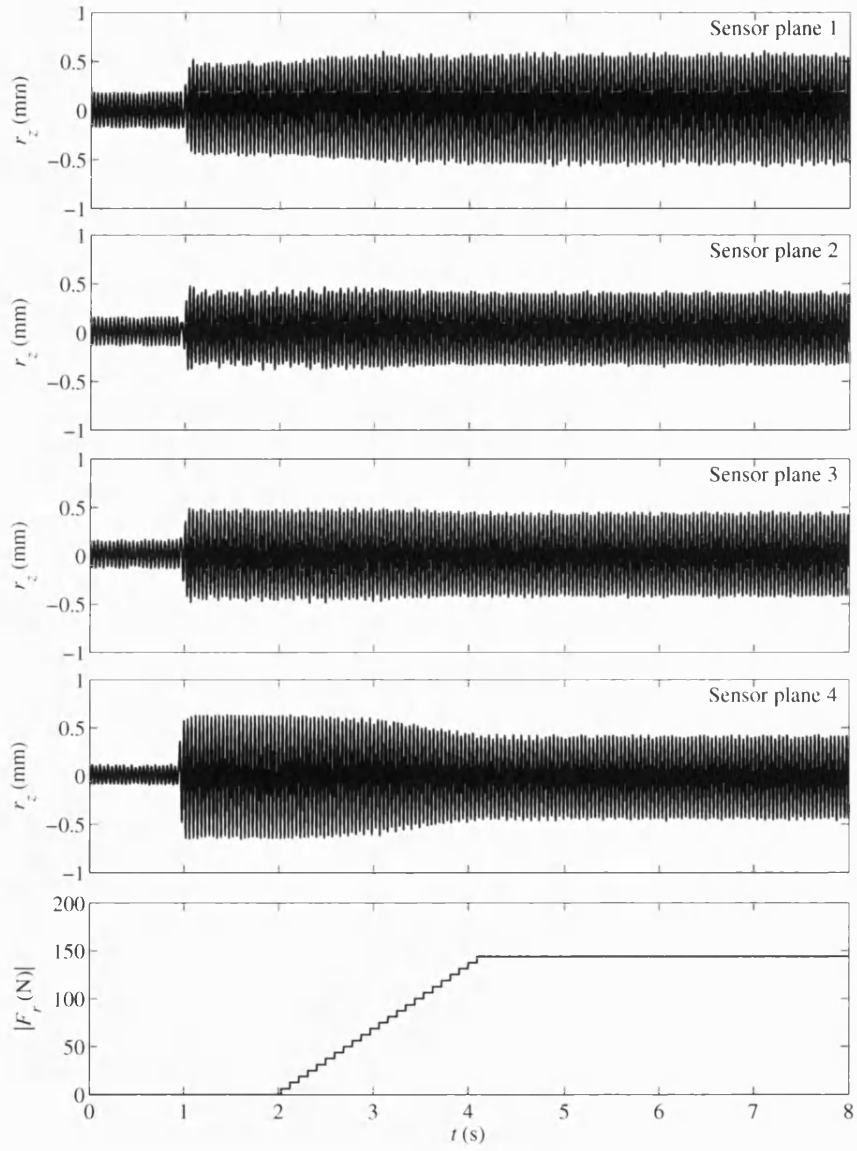

Figure 5.25: Rotor response and applied contact recovery forces after mass loss at $\Omega = 151\,\text{rad/s}$ with a hard H_∞ controller.

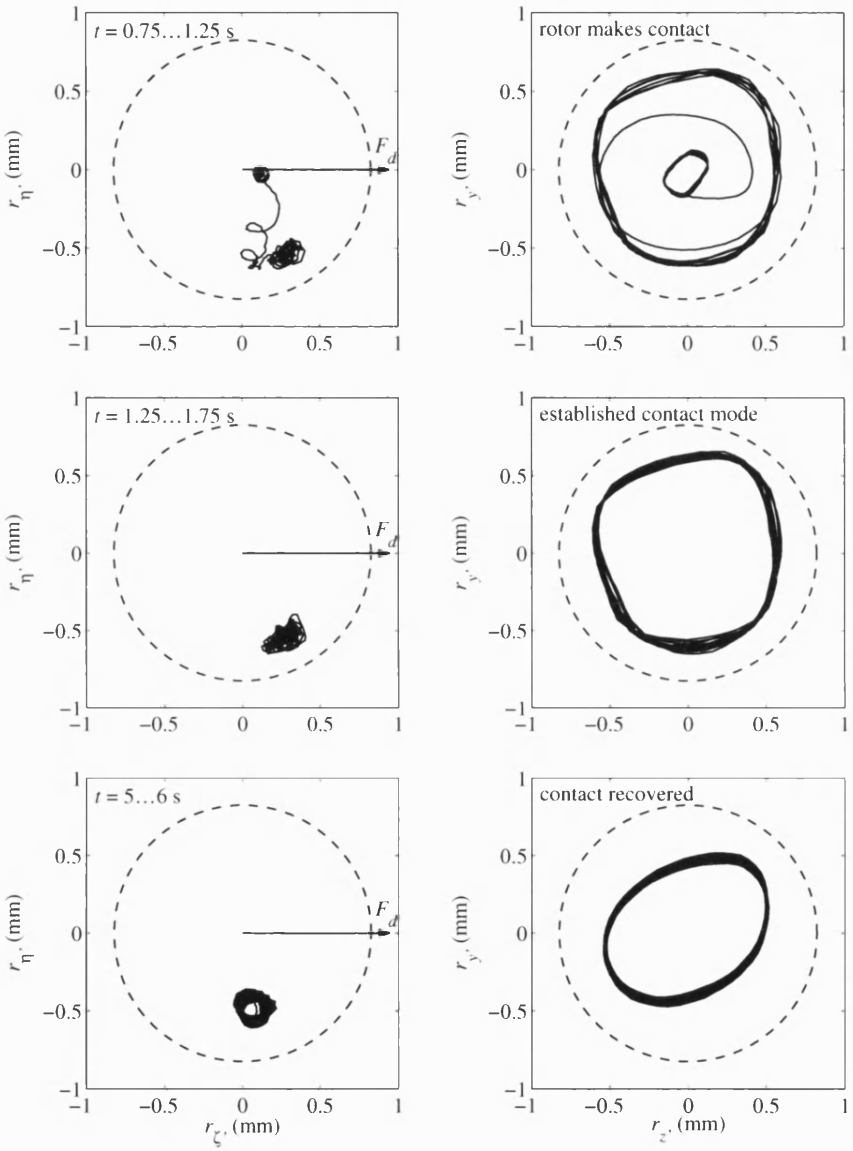

Figure 5.26: Rotor motion at selected times in the rotating and stationary frame during the mass loss experiment with a hard H_∞ controller.

synchronous forces with a magnetic bearing. Contact recovery is complicated because the unbalance forces causing contact are usually unknown and a direct measurement is not possible. However, by measuring the contact points in the rotating frame and knowing the phase ψ, sufficiently accurate estimates can be made. The proposed recovery strategy was successfully tested in simulations and experiments for PD and H_∞ controlled systems.

6 Conclusions

This thesis consists of two parts: In part one, robust control of flexible rotor/-magnetic bearing systems was examined. The second part focused on contact recovery control. For both tasks, an accurate model of the system is required and it was found that the FE method provides a suitable modelling framework. In order to use the FE models for control design, the high order of the dynamic equations has to be reduced with suitable reduction techniques. As only the lower frequency modes are of interest in practical applications, modal reduction was applied. An experimental system identification was carries out to get an estimate for the error between the model and the real system.

With a sufficiently accurate model and an estimate for the model error, robust magnetic bearing controllers can be derived. Properly designed model based MIMO controllers offer improved stability and performance over conventional decentralised PD controllers. In this project, the H_∞ synthesis method was used in which the closed loop properties are determined by user defined weight function matrices. With the common augmented plants the choice of these weights is difficult as they are abstract values. Here, a novel augmented plant has been proposed, which takes the physical structure of rotor/magnetic bearing systems into account. This significantly facilitates the design process.

It was shown that LTI controllers can cause instability if the plant dynamics vary with time. However, the proposed LMI based gain-scheduling synthesis techniques guarantee closed loop stability if system parameters, in particular the rotational speed, change during operation. Simulations and experiments verified that the presented algorithm computes reliable LPV controllers with good stability and performance for flexible rotor/magnetic bearing systems in the whole operating range. Other measurable varying parameters such as base motion could be considered in the design process if necessary in a particular application. However, the computational effort increases proportionally with the number of gain-scheduling parameters, which can be problematic with relatively large order H_∞ controllers. Modern control design is an active area of research, and future work could in-

clude to tackle the problem of the high computational complexity of controllers for flexible structures.

Currently, PD controllers are still used in most applications mainly because of the simple implementation. Their relatively poor disturbance rejection makes rotor-stator contact likely if a mass loss or base motion occurs. After a few initial impacts, PD controlled rotors may adopt stable periodic contact modes for a wide range of unbalance levels. An analytical description of the steady-state contact dynamics has been presented, based on the FE equations of flexible rotors. It was found that information about the unbalance causing contact can be obtained from displacement measurements in the rotating frame. With this information, appropriate synchronous unbalance compensation forces can be applied through the magnetic bearings, which recover the rotor to a non-contacting state. Both the analytical description of contact dynamics and the contact recovery strategies have been successfully verified by simulations and experiments which showed a good match between theory and practice. It is believed that the proposed method will increase the safety and reliability of a wide range of industrial machinery.

The theoretical framework covers all rotor systems suspended by bearings with an approximate linear spring/damper characteristic. It is therefore not directly applicable for H_∞ controlled rotor/magnetic bearing systems. However, simulations and experiments showed that even these plants can exhibit a similar contact dynamic response, although contact is less likely because of the better disturbance rejection. An analytical description the rotor/stator contact of systems with model based controllers is difficult due to the complex controller dynamics. It is certainly an interesting topic for future work. Maybe the results presented in this thesis can help to develop "intelligent" robust (gain-scheduled, non-linear) controllers, which detect contact and recover the rotor automatically without explicitly applying synchronous forces. The benefit of such a closed loop approach would be a higher reliability compared to the presented open-loop strategy.

7 References

[1] European Research Project. Magnetic bearings for smart aero engines. Technical report, EC GROWTH, Project G4RD-CT-2001-00625, 2001–2005.

[2] S. D. Garvey, I. A. Jones, W. K. S. Khoo, and I. C. D. Care. On the mechanical stability of circular discs in high specific load capacity magnetic bearings. In *Proceedings of the 5th International Conference on Modern Practice in Stress and Vibration Analysis*, volume 440–441, pages 481–488, 2003.

[3] G. Schweitzer, A. Traxler, and H. Bleuler. *Magnetlager*. Springer-Verlag, 1993.

[4] C. R. Burrows, N. Sahinkaya, A. Traxler, and G. Schweitzer. Design and application of a magnetic bearing for vibration control and stabilization of a flexible rotor. In *1st International Symposium on Magnetic Bearings*, pages 159–168. Springer Verlag, 1988.

[5] M. Schlotter. Unbalance compensation by active magnetic bearings. Diplomarbeit, Technische Universität Darmstadt, February 2004.

[6] X. Zhang. *Aktive Regel- und Kompensationsstrategien für magnetgelagerte Mehrfreiheitsgrad-Rotoren*. Dissertation, Technische Universität Darmstadt, 2002. GCA-Verlag Herdecke.

[7] R. Herzog, P. Bühler, C. Gähler, and R. Larsonneur. Unbalance compensation using generalized notch filters in the multivariable feedback of magnetic bearings. *IEEE Transactions on Control Systems Technology*, 4(5):580–586, September 1996.

[8] K. Glover and J. C. Doyle. State-space formulae for all stabilizing controllers that satisfy an H_∞ norm bound and relations to risk sensitivity. *Systems and Control Letters*, 11:167–172, 1988.

[9] J. C. Doyle, K. Glover, P. P. Khargonekar, and B. A. Francis. State-space solutions to standard H_2 and H_∞ control problems. *IEEE Transactions on Automatic Control*, 34(8):831–847, August 1989.

[10] P. Gahinet and P. Apkarian. A linear matrix inequality approach to H_∞ control. *International Journal of Robust and Nonlinear Control*, 4:421–448, 1994.

[11] P. Gahinet. Explicit controller formulas for LMI-based H_∞ synthesis. *Automatica*, 32(7):1007–1014, July 1996.

[12] C. Scherer, P. Gahinet, and M. Chilali. Multi-objective output-feedback control via LMI optimization. *IEEE Transactions on Automatic Control*, 42(7):896–911, July 1997.

[13] A. Packard. Gain-scheduling via linear fractional transformations. *Systems and Control Letters*, 22(2):79–92, 1994.

[14] G. Becker and A. Packard. Robust performance of linear parametrically varying systems using parametrically-dependent linear feedback. *Systems and Control Letters*, 23(3):205–215, 1994.

[15] P. Apkarian and P. Gahinet. A convex characterization of gain-scheduled H_∞ controllers. *IEEE Transactions on Automatic Control*, 40(5):853–864, May 1995.

[16] P. Apkarian, P. Gahinet, and G. Becker. Self-scheduled H_∞ control of linear parameter-varying systems: a design example. *Automatica*, 31(9):1251–1261, 1995.

[17] S. Sivrioglu and K. Nonami. LMI approach to gain scheduled H_∞ control beyond PID control for gyroscopic rotor-magnetic bearing system. In *Proceedings of the 35th Conference on Decision and Control*, pages 3694–3699, December 1996.

[18] P. Tsiotras and S. Mason. Self-scheduled H_∞ controllers for magnetic bearings. In *Proceedings of the 1996 ASME International Mechanical Engineering Congress and Exposition*, volume 91, pages 151–157, November 1996.

[19] P. Tsiotras and C. Knospe. Reducing conservatism for gain-scheduled H_∞ controllers for AMB's. In *Proceedings of MAG'97, Industrial Conference and Exhibition on Magnetic Bearings*, pages 290–299, 1997.

[20] M. O. T. Cole, P. S. Keogh, and C. R. Burrows. Vibration control of a flexible rotor/magnetic bearing system subject to direct forcing and base motion disturbances. *Proceedings of the Institution of Mechanical Engineers. Part C - Journal of Mechanical Engineering Science*, 212:535–546, October 1998.

[21] M. A. Fumagalli. *Modelling and Measurement Analysis of the Contact Interaction between a High Speed Rotor and its Stator.* PhD thesis, ETH Zürich, 1997. `http://e-collection.ethbib.ethz.ch`.

[22] A. R. Bartha. *Dry Friction Backward Whirl of Rotors.* PhD thesis, ETH Zürich, 2000. `http://e-collection.ethbib.ethz.ch`.

[23] R. G. Kirk, E. E. Swanson, F. H. Karavana, and X. Wang. Rotor drop test stand for AMB rotating machinery, Part 1: Description of test stand and initial results. In *Proceedings of the 4th International Symposium on Magnetic Bearings*, pages 207–212. ETH, Zurich, Switzerland, August 1994.

[24] R. G. Kirk. Evaluation of AMB turbomachinery auxiliary bearings. *Transactions of the ASME, Journal of Vibration and Acoustics*, 121(2):156–161, April 1999.

[25] J. Schmied and J. C. Pradetto. Behavior of a one ton rotor being dropped into auxiliary bearings. In *Proceedings of the 3rd International Symposium on Magnetic Bearings*, pages 145–156, 1992.

[26] U. Ehehalt and R. Markert. Rotor motion during stator contact. In *Proceedings of the the 6th IFToMM Conference on Rotor Dynamics*, volume 2, pages 913–920, February 2002.

[27] U. Ehehalt, E. Hahn, and R. Markert. Experimental validation of various motion patterns at rotor stator contact. In *Proceedings of the 11th International Symposium on Transport Phenomena and Dynamics of Rotating Machinery*, February 2006.

[28] L. Ginzinger and H. Ulbrich. Control of a rubbing rotor – experiments and theory. In *Proceedings of the 11th International Symposium on Transport Phenomena and Dynamics of Rotating Machinery*, February 2006.

[29] P. S. Keogh and M. O. T. Cole. Rotor vibration with auxiliary bearing contact in magnetic bearing systems – Part 1: Synchronous dynamics. *Proceedings of the Institution of Mechanical Engineers. Part C – Journal of Mechanical Engineering Science*, 217:377–392, April 2003.

[30] M. O. T. Cole and P. S. Keogh. Asynchronous periodic contact modes for rotor vibration within an annular clearance. *Proceedings of the Institution of Mechanical Engineers. Part C – Journal of Mechanical Engineering Science*, 217:1101–1115, October 2003.

[31] P. S. Keogh, M. O. T. Cole, M. N. Sahinkaya, and C. R. Burrows. On the control of synchronous vibration in rotor/magnetic bearing systems involving auxiliary bearing contact. *Transactions of the ASME, Journal of Engineering for Gas Turbines and Power*, 126:366–372, April 2004.

[32] P. S. Keogh and M. O. T. Cole. Rotor vibration with auxiliary bearing contact in magnetic bearing systems – Part 2: Robust synchronous control for rotor position recovery. *Proceedings of the Institution of Mechanical Engineers. Part C – Journal of Mechanical Engineering Science*, 217:393–409, April 2003.

[33] N. K. Rutland and P. S. Keogh. Design of an experimental rotor and active magnetic bearing rig. Technical Report 030/1994, University of Bath, Department of Mechanical Engineering, October 1994.

[34] N. K. Rutland and P. S. Keogh. Design procedure for an active magnetic bearing. Technical Report 029/1994, University of Bath, Department of Mechanical Engineering, October 1994.

[35] K.-J. Hoffmann. *Integrierte aktive Magnetlager.* Dissertation, Technische Universität Darmstadt, 1999. GCA-Verlag Herdecke.

[36] D. Laier. *Nichtlinearitäten magnetgelagerter Rotorsysteme.* Dissertation, Technische Universität Darmstadt, 1998. Fortschritt-Berichte VDI, Reihe 11, Nr. 273.

[37] N. K. Rutland and P. S. Keogh. Experimental validation of active magnetic bearing force characteristic. Technical Report 032/1995, University of Bath, Department of Mechanical Engineering, May 1995.

[38] R. J. Astley. *Finite Elements in Solids and Structures.* Chapman & Hall, 1993.

[39] P. Hagedorn. *Technische Schwingungslehre II.* Springer Verlag, 1989.

[40] E. S. Zorzi and H. D. Nelson. Finite element simulation of rotor-bearing systems with internal damping. *Transactions of the ASME, Journal of Engineering for Power*, pages 71–76, January 1977.

[41] H. D. Nelson and J. M. McVaugh. The dynamics of rotor-bearing systems using finite elements. *Transactions of the ASME, Journal of Engineering for Industry*, pages 593–600, May 1976.

[42] A. L. Kimbal, Jr. Internal friction theory of shaft whirling. *General Electric Review*, 27(4):244–251, April 1924.

[43] F. M. Dimentberg. *Flexural Vibrations of Rotating Shafts.* Butterworths, London, 1961.

[44] R. Markert. Schwingungsmeßtechnik. Lecture Notes, Technische Universität Darmstadt, Department of Mechanics, 2003.

[45] VDI-Gesellschaft. Werkstoff- und Bauteildämpfung. Technical Report VDI 3830, Blatt 5, Verein Deutscher Ingenieure, 2003.

[46] J. M. Maciejowski. *Multivariable Feedback Design.* Addison-Wesley, 1989.

[47] K. Zhou, J. C. Doyle, and K. Glover. *Robust and Optimal Control.* Prentice Hall, 1995.

[48] The MathWorks, Inc. *Robust Control Toolbox User's Guide*, third edition, October 2004.

[49] A. Muszynska and P. Goldman. Chaotic responses of unbalanced rotor/-bearing/stator systems with looseness or rubs. *Chaos, Solitons and Fractals*, 5(9):1683–1704, 1995.

[50] H. F. Black. Interaction of a whirling rotor with a vibrating stator across a clearing annulus. *Journal of Mechanical Engineering Science*, 10(1):1–12, 1968.

[51] H. Xie, G. T. Flowers, L. Feng, and C. Lawrence. Steady-state dynamic behavior of a flexible rotor with auxiliary support from a clearance bearing. *Transactions of the ASME, Journal of Vibration and Acoustics*, 121:78–83, 1999.

[52] A. Muszynska. Rotor-to-stationary part full annular contact modeling. In *Proceedings of 9th International Symposium on Transport Phenomena and Dynamics of Rotating Machinery, Honolulu, Hawaii*, 2002.

[53] D. W. Childs. Rub induced parametric excitation in rotors. *Transactions of the ASME, Journal of Mechanical Design*, 10:640–644, 1979.

[54] A. Muszynska. Partial lateral rotor to stator rubs. In *Proceedings of 3rd International Conference on Vibrations in Rotating Machinery, University of York*, 1984.

[55] F. F. Ehrich. High order subharmonic response of high speed rotors in bearing clearance. *Transactions of the ASME, Journal of Vibration, Acoustics, Stress and Reliability in Design*, 110:9–16, 1988.

[56] A. R. Bartha. Dry friction induced backward whirl: Theory and experiment. In *Proceedings of 5th IFToMM Conference on Rotor Dynamics, Darmstadt, Germany*, pages 756–767, 1998.

Appendix

A Notation

This chapter gives an overview of all symbols in the report. It is unavoidable that some symbols are assigned more than once; their meaning should always be clear from the context, however.

A.1 Symbols

l, R, A, V	length, radius, area, volume
m, d, k	mass, damping, stiffness parameter
I, Θ	moment of area, moment of inertia
E, G, ν, ρ	Young's modulus, shear modulus, Poisson's ratio, density
ϕ, κ	transverse shear factor, shear form factor
η	internal damping parameter
μ	dry friction coefficient
ε, α	static, dynamic unbalance parameter
s, δr	gap between rotor–magnet, rotor–auxiliary bearing
i, u	current, voltage
H, B, Φ, μ	magnetic field strength, flux density, flux, permeability
U, V, W	potential, kinetic, field energy
r, φ	translational, rotational displacement
v, a	velocity, acceleration
p, q	modal, generalised coordinate
$\mathbf{p}$, $\mathbf{q}$	modal, generalised coordinate vector
$\boldsymbol{q}$	generalised coordinate vector for contact analysis
F, τ, f	force, torque, generalised force
$\mathbf{f}$, $\mathbf{u}$	force, unbalance vector
$\mathbf{M}$, $\mathbf{D}$, $\mathbf{K}$, $\mathbf{G}$	mass, damping, stiffness, gyroscopic matrix
$\mathbf{P}$, $\mathbf{Q}$, $\mathbf{R}$	Boolean position matrix, constraint matrix, distribution matrix
N, $\mathbf{N}$	shape function, shape function matrix

s	position in finite element
$\mathbf{A}$, $\mathbf{B}$, $\mathbf{C}$, $\mathbf{D}$	state-space matrix
$\mathbf{x}$, $\mathbf{y}$, $\mathbf{u}$	state, output, input vector
λ, α, ω	complex eigenvector, real, complex part
ω_0, ξ	undamped natural frequency, Lehr's damping factor
ψ, $\mathbf{\Psi}$	eigenvector, modal matrix
f, T	frequency, time step
ω, Ω	circular frequency, rotation speed
S, γ^2	power spectrum, coherence
$\mathbf{G}$, $\mathbf{P}$, $\mathbf{Q}$	plant, augmented plant, general transfer matrix
$\mathbf{K}$, $\mathbf{R}$	controller, rotor
$\mathbf{T}_{y,u}$	closed loop transfer function from u to y in augmented system
$\mathbf{H}$	closed loop transfer function from nodal forces to rotor displacements
$\mathbf{J}$	closed loop TF from nodal displacements or forces to actuator forces
$\mathbf{\Delta}$	uncertainty
$\mathbf{W}$, $\mathbf{w}$	weighting function, weight scaling matrix
$\mathbf{S}$, $\mathbf{T}$	sensitivity, complementary sensitivity function
$\mathbf{MB}$, $\mathbf{PD}$	magnetic bearing, PD controller transfer matrices
$\boldsymbol{\theta}$, $\mathbf{\Theta}$	varying parameter, parameter polytope
γ	performance/optimisation parameter
$\mathbf{X}$	positive definite solution to LMI
$\mathbf{M}$, $\mathbf{N}$, $\mathbf{R}$, $\mathbf{S}$	temporary matrix variables
$\mathbf{w}$, $\boldsymbol{\xi}$	complex coordinates, displacement states in rotating frame
$\mathbf{\Xi}$	Fourier coefficients of $\boldsymbol{\xi}$
Π	characteristic equation for contact frequency
Υ, $\aleph$, $\beth$	substitution variables
ψ	phase between unbalance force and contact location
α, β	bounce amplitude factor, energy dissipation coefficient
ϵ	error
i, k, n	integer number or quantity
α, ϕ, θ	angle or factor

A.2 Subscripts

$\square_0$	default or nominal
$\square_{+,-}$	positive, negative direction
$\square_{min,\,max}$	minimum, maximum
$\square_{lin,\,lim}$	linearised, limited
$\square_{r,\,rel}$	relative
$\square_{m,\,meas}$	measurement
$\square_{e,\,est}$	estimate
$\square_{avg,\,calc}$	average, calculation
$\square_{OP}$	operating point
$\square_{cut}$	cut-off
$\square_{fft}$	Fast-Fourier transformation
$\square_{o,\,i}$	output, input
$\square_{y,\,u}$	output, input signal
$\square_{l,\,u}$	lower, upper
$\square_{a,\,m}$	additive, multiplicative
$\square_{r,\,m}$	real, modal
$\square_{s,\,c}$	sine, cosine
$\square_{r,\,t}$	radial, tangential
$\square_{d,\,p}$	diametral, polar
$\square_{a,\,b,\,c}$	axial, bending, circulatory
$\square_{x,\,y,\,z}$	x-, y-, z-direction
$\square_{\eta,\,\zeta}$	η-, ζ-direction
$\square_w$	rotating frame
$\square_\phi$	angle
$\square_s$	control
$\square_{d,\,u}$	disturbance, unbalance
$\square_{a,\,r}$	compensation, recovery
$\square_g$	gravity
$\square_c$	contact
$\square_t$	threshold
$\square_G$	gyroscopic
$\square_{d,\,f}$	displacement, force

$\square_{i,s}$	current, displacement component
$\square_{h,v}$	hysteretic, viscous
$\square_{B,S,D,AJ}$	base, shaft, disk, auxiliary journal bearing
$\square_{M,MB}$	magnetic, magnetic bearing
$\square_{A,Fe,C}$	air gap, iron core, coil
$\square_{P,I,D}$	proportional, integral, derivative component
$\square_{PD,PID}$	PD-, PID-controlled
$\square_{i,j,k,l,m,n}$	general numbering indices

A.3 Superscripts

$\square^{N}$	Newtonian
$\square^{B,S,D,AJ}$	base, shaft, disk, auxiliary journal bearing
$\square^{MB}$	magnetic bearing
$\square^{PD,PID}$	PD-, PID-controlled
$\square^{e,d,pd}$	shaft-, disk-, PD-controlled magnetic bearing element

A.4 Accents

$\widetilde{\square}$	normalised
$\overline{\square}$, $\underline{\square}$	largest, smallest

A.5 Operators

$\mathrm{Re}(\cdot)$, $\mathrm{Im}(\cdot)$	real, imaginary part
$\sigma(\cdot)$, $\mu(\cdot)$	singular value, structured singular value
$\mathrm{F}(\cdot,\cdot)$	linear fractional transformation
$\mathrm{Co}\{\cdot\}$	convex hull
$\lvert\cdot\rvert$	absolute value
$\lVert\cdot\rVert_\infty$	infinity norm

A.6 Constants

j	imaginary unit: $\mathrm{j} = \sqrt{-1}$

e	Euler's number: $\mathrm{e} = 2.7182\ldots$
π	area of a circle of radius 1: $\pi = 3.1415\ldots$
$\mathbf{I}$	identity matrix: $\mathbf{I} = \mathrm{diag}(1, 1, \ldots, 1)$
μ_0	magnetic permeability in vacuum: $\mu_0 = 4\pi \cdot 10^{-7}\ \frac{\mathrm{N}}{\mathrm{A}^2}$
g	gravity constant: $\mathrm{g} = 9.81\ \frac{\mathrm{m}}{\mathrm{s}^2}$

B Finite Element Beam Matrices

The Euler-Bernoulli and the Timoshenko finite element matrices for homogeneous, cylindrical beam elements, defined in equations (2.32) and (2.36) are listed here. For thin disks, the moments of inertia are $\Theta_d = \frac{\rho A R^2}{4}$ and $\Theta_p = \frac{\rho A R^2}{2}$. The second moment of area for circular cross shapes is $I = \frac{\pi R^4}{4}$.

B.1 Euler-Bernoulli Beam Elements

$$\mathbf{M}^e_{tz} = \frac{\rho A l}{420}\begin{bmatrix} 156 & -22l & 54 & 13l \\ -22l & 4l^2 & -13l & -3l^2 \\ 54 & -13l & 156 & 22l \\ 13l & -3l^2 & 22l & 4l^2 \end{bmatrix}$$

$$\mathbf{M}^e_{ty} = \frac{\rho A l}{420}\begin{bmatrix} 156 & 22l & 54 & -13l \\ 22l & 4l^2 & 13l & -3l^2 \\ 54 & 13l & 156 & -22l \\ -13l & -3l^2 & -22l & 4l^2 \end{bmatrix}$$

$$\mathbf{M}^e_{rz} = \frac{\Theta_d}{30l}\begin{bmatrix} 36 & -3l & -36 & -3l \\ -3l & 4l^2 & 3l & -l^2 \\ -36 & 3l & 36 & 3l \\ -3l & -l^2 & 3l & 4l^2 \end{bmatrix}$$

$$\mathbf{M}^e_{ry} = \frac{\Theta_d}{30l}\begin{bmatrix} 36 & 3l & -36 & 3l \\ 3l & 4l^2 & -3l & -l^2 \\ -36 & -3l & 36 & -3l \\ 3l & -l^2 & -3l & 4l^2 \end{bmatrix}$$

$$\mathbf{K}^e_{bz} = \frac{2EI}{l^3}\begin{bmatrix} 6 & -3l & -6 & -3l \\ -3l & 2l^2 & 3l & l^2 \\ -6 & 3l & 6 & 3l \\ -3l & l^2 & 3l & 2l^2 \end{bmatrix}$$

$$\mathbf{K}^e_{by} = \frac{2EI}{l^3}\begin{bmatrix} 6 & 3l & -6 & 3l \\ 3l & 2l^2 & -3l & l^2 \\ -6 & -3l & 6 & -3l \\ 3l & l^2 & -3l & 2l^2 \end{bmatrix}$$

$$\mathbf{K}^e_{az} = \frac{F_a}{30l}\begin{bmatrix} 36 & -3l & -36 & -3l \\ -3l & 4l^2 & 3l & -l^2 \\ -36 & 3l & 36 & 3l \\ -3l & -l^2 & 3l & 4l^2 \end{bmatrix}$$

$$\mathbf{K}^e_{ay} = \frac{F_a}{30l}\begin{bmatrix} 36 & 3l & -36 & 3l \\ 3l & 4l^2 & -3l & -l^2 \\ -36 & -3l & 36 & -3l \\ 3l & -l^2 & -3l & 4l^2 \end{bmatrix}$$

$$\mathbf{K}^e_{c} = \frac{2EI}{l^3}\begin{bmatrix} 6 & -3l & -6 & -3l \\ 3l & -2l^2 & -3l & -l^2 \\ -6 & 3l & 6 & 3l \\ 3l & -l^2 & -3l & -2l^2 \end{bmatrix}$$

$$\mathbf{G}^e = \frac{\Theta_p}{30l}\begin{bmatrix} -36 & 3l & 36 & 3l \\ -3l & 4l^2 & 3l & -l^2 \\ 36 & -3l & -36 & -3l \\ -3l & -l^2 & 3l & 4l^2 \end{bmatrix}$$

B.2 Timoshenko Beam Elements

The transverse shear factor, which appears in the Timoshenko matrices, is $\phi = 24EI(1+\nu)/\kappa EAl^2$ with $\kappa \in [0.75, 0.9]$. The mass, stiffness, and gyroscopic matrices are splitted in parts, the full matrices are given by $\mathbf{M}^e_{(\cdot)} = \mathbf{M}^e_{0(\cdot)} + \mathbf{M}^e_{1(\cdot)} + \mathbf{M}^e_{2(\cdot)}$, $\mathbf{K}^e_{(\cdot)} = \mathbf{K}^e_{0(\cdot)} + \mathbf{K}^e_{1(\cdot)} + \mathbf{K}^e_{2(\cdot)}$, $\mathbf{G}^e_{(\cdot)} = \mathbf{G}^e_{0(\cdot)} + \mathbf{G}^e_{1(\cdot)} + \mathbf{G}^e_{2(\cdot)}$, respectively.

$$\mathbf{M}^e_{0tz} = \frac{1}{(1+\phi)^2}\frac{\rho Al}{420}\begin{bmatrix} 156 & -22l & 54 & 13l \\ -22l & 4l^2 & -13l & -3l^2 \\ 54 & -13l & 156 & 22l \\ 13l & -3l^2 & 22l & 4l^2 \end{bmatrix}$$

$$\mathbf{M}^e_{1tz} = \frac{\phi}{(1+\phi)^2}\frac{\rho Al}{420}\begin{bmatrix} 294 & -38.5l & 126 & 31.5l \\ -38.5l & 7l^2 & -31.5l & -7l^2 \\ 126 & -31.5l & 294 & 38.5l \\ 31.5l & -7l^2 & 38.5l & 7l^2 \end{bmatrix}$$

$$\mathbf{M}^e_{2tz} = \frac{\phi^2}{(1+\phi)^2}\frac{\rho Al}{420}\begin{bmatrix} 140 & -17.5l & 70 & 17.5l \\ -17.5l & 3.5l^2 & -17.5l & -3.5l^2 \\ 70 & -17.5l & 140 & 17.5l \\ 17.5l & -3.5l^2 & 17.5l & 3.5l^2 \end{bmatrix}$$

$$\mathbf{M}^e_{0ty} = \frac{1}{(1+\phi)^2}\frac{\rho Al}{420}\begin{bmatrix} 156 & 22l & 54 & -13l \\ 22l & 4l^2 & 13l & -3l^2 \\ 54 & 13l & 156 & -22l \\ -13l & -3l^2 & -22l & 4l^2 \end{bmatrix}$$

$$\mathbf{M}^e_{1ty} = \frac{\phi}{(1+\phi)^2}\frac{\rho Al}{420}\begin{bmatrix} 294 & 38.5l & 126 & -31.5l \\ 38.5l & 7l^2 & 31.5l & -7l^2 \\ 126 & 31.5l & 294 & -38.5l \\ -31.5l & -7l^2 & -38.5l & 7l^2 \end{bmatrix}$$

$$\mathbf{M}^e_{2ty} = \frac{\phi^2}{(1+\phi)^2}\frac{\rho Al}{420}\begin{bmatrix} 140 & 17.5l & 70 & -17.5l \\ 17.5l & 3.5l^2 & 17.5l & -3.5l^2 \\ 70 & 17.5l & 140 & -17.5l \\ -17.5l & -3.5l^2 & -17.5l & 3.5l^2 \end{bmatrix}$$

$$\mathbf{M}^e_{0rz} = \frac{1}{(1+\phi)^2}\frac{\Theta_d}{30l}\begin{bmatrix} 36 & -3l & -36 & -3l \\ -3l & 4l^2 & 3l & -l^2 \\ -36 & 3l & 36 & 3l \\ -3l & -l^2 & 3l & 4l^2 \end{bmatrix}$$

$$\mathbf{M}^e_{1rz} = \frac{\phi}{(1+\phi)^2}\frac{\Theta_d}{30l}\begin{bmatrix} 0 & 15l & 0 & 15l \\ 15l & 5l^2 & -15l & -5l^2 \\ 0 & -15l & 0 & -15l \\ 15l & -5l^2 & -15l & 5l^2 \end{bmatrix}$$

$$\mathbf{M}^e_{2rz} = \frac{\phi^2}{(1+\phi)^2}\frac{\Theta_d}{30l}\begin{bmatrix} 0 & 0 & 0 & 0 \\ 0 & 10l^2 & 0 & 5l^2 \\ 0 & 0 & 0 & 0 \\ 0 & 5l^2 & 0 & 10l^2 \end{bmatrix}$$

$$\mathbf{M}^e_{0ry} = \frac{1}{(1+\phi)^2}\frac{\Theta_d}{30l}\begin{bmatrix} 36 & 3l & -36 & 3l \\ 3l & 4l^2 & -3l & -l^2 \\ -36 & -3l & 36 & -3l \\ 3l & -l^2 & -3l & 4l^2 \end{bmatrix}$$

$$\mathbf{M}^e_{1ry} = \frac{\phi}{(1+\phi)^2}\frac{\Theta_d}{30l}\begin{bmatrix} 0 & -15l & 0 & -15l \\ -15l & 5l^2 & 15l & -5l^2 \\ 0 & 15l & 0 & 15l \\ -15l & -5l^2 & 15l & 5l^2 \end{bmatrix}$$

$$\mathbf{M}^e_{2ry} = \frac{\phi^2}{(1+\phi)^2}\frac{\Theta_d}{30l}\begin{bmatrix} 0 & 0 & 0 & 0 \\ 0 & 10l^2 & 0 & 5l^2 \\ 0 & 0 & 0 & 0 \\ 0 & 5l^2 & 0 & 10l^2 \end{bmatrix}$$

$$\mathbf{K}^e_{0az} = \frac{1}{(1+\phi)^2}\frac{F_a}{30l}\begin{bmatrix} 36 & -3l & -36 & -3l \\ -3l & 4l^2 & 3l & -l^2 \\ -36 & 3l & 36 & 3l \\ -3l & -l^2 & 3l & 4l^2 \end{bmatrix}$$

$$\mathbf{K}^e_{1az} = \frac{\phi}{(1+\phi)^2}\frac{F_a}{30l}\begin{bmatrix} 60 & 0 & -60 & 0 \\ 0 & 5l^2 & 0 & -5l^2 \\ -60 & 0 & 60 & 0 \\ 0 & -5l^2 & 0 & 5l^2 \end{bmatrix}$$

$$\mathbf{K}^e_{2az} = \frac{\phi^2}{(1+\phi)^2}\frac{F_a}{60l}\begin{bmatrix} 60 & 0 & -60 & 0 \\ 0 & 5l^2 & 0 & -5l^2 \\ -60 & 0 & 60 & 0 \\ 0 & -5l^2 & 0 & 5l^2 \end{bmatrix}$$

$$\mathbf{K}^e_{0ay} = \frac{1}{(1+\phi)^2}\frac{F_a}{30l}\begin{bmatrix} 36 & 3l & -36 & 3l \\ 3l & 4l^2 & -3l & -l^2 \\ -36 & -3l & 36 & -3l \\ 3l & -l^2 & -3l & 4l^2 \end{bmatrix}$$

$$\mathbf{K}^e_{1ay} = \frac{\phi}{(1+\phi)^2}\frac{F_a}{30l}\begin{bmatrix} 60 & 0 & -60 & 0 \\ 0 & 5l^2 & 0 & -5l^2 \\ -60 & 0 & 60 & 0 \\ 0 & -5l^2 & 0 & 5l^2 \end{bmatrix}$$

$$\mathbf{K}^e_{2ay} = \frac{\phi^2}{(1+\phi)^2}\frac{F_a}{60l}\begin{bmatrix} 60 & 0 & -60 & 0 \\ 0 & 5l^2 & 0 & -5l^2 \\ -60 & 0 & 60 & 0 \\ 0 & -5l^2 & 0 & 5l^2 \end{bmatrix}$$

$$\mathbf{K}^e_{0bz} = \frac{1}{(1+\phi)^2}\frac{2EI}{l^3}\begin{bmatrix} 6 & -3l & -6 & -3l \\ -3l & 2l^2 & 3l & l^2 \\ -6 & 3l & 6 & 3l \\ -3l & l^2 & 3l & 2l^2 \end{bmatrix}$$

$$\mathbf{K}^e_{1bz} = \frac{\phi}{(1+\phi)^2}\frac{2EI}{l^3}\begin{bmatrix} 0 & 0 & 0 & 0 \\ 0 & l^2 & 0 & -l^2 \\ 0 & 0 & 0 & 0 \\ 0 & -l^2 & 0 & l^2 \end{bmatrix}$$

$$\mathbf{K}^e_{2bz} = \frac{\phi^2}{(1+\phi)^2}\frac{2EI}{l^3}\begin{bmatrix} 0 & 0 & 0 & 0 \\ 0 & l^2/2 & 0 & -l^2/2 \\ 0 & 0 & 0 & 0 \\ 0 & -l^2/2 & 0 & l^2/2 \end{bmatrix}$$

$$\mathbf{K}^e_{0by} = \frac{1}{(1+\phi)^2}\frac{2EI}{l^3}\begin{bmatrix} 6 & 3l & -6 & 3l \\ 3l & 2l^2 & -3l & l^2 \\ -6 & -3l & 6 & -3l \\ 3l & l^2 & -3l & 2l^2 \end{bmatrix}$$

$$\mathbf{K}^e_{1by} = \frac{\phi}{(1+\phi)^2}\frac{2EI}{l^3}\begin{bmatrix} 0 & 0 & 0 & 0 \\ 0 & l^2 & 0 & -l^2 \\ 0 & 0 & 0 & 0 \\ 0 & -l^2 & 0 & l^2 \end{bmatrix}$$

$$\mathbf{K}^e_{2by} = \frac{\phi^2}{(1+\phi)^2}\frac{2EI}{l^3}\begin{bmatrix} 0 & 0 & 0 & 0 \\ 0 & l^2/2 & 0 & -l^2/2 \\ 0 & 0 & 0 & 0 \\ 0 & -l^2/2 & 0 & l^2/2 \end{bmatrix}$$

$$\mathbf{K}^e_{0c} = \frac{1}{(1+\phi)^2}\frac{2EI}{l^3}\begin{bmatrix} 6 & -3l & -6 & -3l \\ 3l & -2l^2 & -3l & -l^2 \\ -6 & 3l & 6 & 3l \\ 3l & -l^2 & -3l & -2l^2 \end{bmatrix}$$

$$\mathbf{K}^e_{1c} = \frac{\phi}{(1+\phi)^2}\frac{2EI}{l^3}\begin{bmatrix} 0 & 0 & 0 & 0 \\ 0 & -l^2 & 0 & l^2 \\ 0 & 0 & 0 & 0 \\ 0 & l^2 & 0 & -l^2 \end{bmatrix}$$

$$\mathbf{K}^e_{2c} = \frac{\phi^2}{(1+\phi)^2}\frac{2EI}{l^3}\begin{bmatrix} 0 & 0 & 0 & 0 \\ 0 & -l^2/2 & 0 & l^2/2 \\ 0 & 0 & 0 & 0 \\ 0 & l^2/2 & 0 & -l^2/2 \end{bmatrix}$$

$$\mathbf{G}^e_0 = \frac{1}{(1+\phi)^2}\frac{\Theta_p}{30l}\begin{bmatrix} -36 & 3l & 36 & 3l \\ -3l & 4l^2 & 3l & -l^2 \\ 36 & -3l & -36 & -3l \\ -3l & -l^2 & 3l & 4l^2 \end{bmatrix}$$

$$\mathbf{G}^e_1 = \frac{\phi}{(1+\phi)^2}\frac{\Theta_p}{30l}\begin{bmatrix} 0 & -15l & 0 & -15l \\ 15l & 5l^2 & -15l & -5l^2 \\ 0 & 15l & 0 & 15l \\ 15l & -5l^2 & -15l & 5l^2 \end{bmatrix}$$

$$\mathbf{G}_2^e = \frac{\phi^2}{(1+\phi)^2}\frac{\Theta_p}{30l}\begin{bmatrix} 0 & 0 & 0 & 0 \\ 0 & 10l^2 & 0 & 5l^2 \\ 0 & 0 & 0 & 0 \\ 0 & 5l^2 & 0 & 10l^2 \end{bmatrix}$$